

Part I

The "anomalous" energy production



Evolution and Progress in Material Science for Studying the Fleischmann and Pons Effect (FPE)

V. Violante¹, E. Castagna¹, S. Lecci¹, M. Sansovini¹, G. Hubler², D. Knies², K. Grabowski², M. McKubre³, F. Tanzella³, C. Sibilìa⁴, Z. Del Prete⁴, T. Zilov⁵, F. Sarto

¹ *ENEA Frascati Research Center, Frascati (Rome) 00044 Italy*

² *Naval Research Laboratory, Washington DC 20375 USA*

³ *SRI International, Menlo Park CA USA*

⁴ *University of Rome La Sapienza, Dept. of Energetics, Rome, Italy*

⁵ *Energetics Technologies, Omer, Israel*

Abstract. Calorimetric experiments have revealed a crucial role of the metallurgy and surface characteristics for reproducing the FPE. A material status to have an improved probability to observe the effect under electrochemical loading of deuterium in palladium has been identified by means of statistical approach. The evolution of the research approach is described in this work.

1. Introduction

The threshold effect of the deuterium concentration into the palladium lattice was identified as condition for observing the excess of power during electrolysis of palladium cathodes with LiOD electrolyte [1-2], i.e. Fleischmann&Pons effect [3].

Such an experimental evidence created a broad interest in identifying the mechanisms controlling hydrogen isotope dissolution into the palladium lattice during the loading process.

A material science study allowed to define a metallurgical treatment to have the most appropriate metallurgy to facilitate absorption and hydrogen mass transfer into the palladium lattice [4].

The most significant outcome of the study was an increasing of the loading reproducibility, near 100%, in achieving a deuterium concentration larger than 0.9 (atomic fraction), that was considered to be the threshold value to observe the effect.

The high loading reproducibility was the condition to demonstrate that the loading threshold is a necessary condition but not sufficient to have the excess of power production [5].

A research effort was performed for identifying others necessary features of the material correlated with the excess of power production and, for such a reason, the focus of the research was mainly oriented on metallurgy, crystallography, triggering, and interface - surface physics.

2. Experimental results

A mass flow calorimeter and closed electrochemical cells equipped with a catalytic fixed bed to recombine the gas produced by the electrolysis have been conceived and operated to directly measure the output power.

The calorimetric system is composed by a Memmert thermostatic box (± 0.05 °C), Haake thermostatic bath for coolant water, Bronkhorst high precision mass flow meter and controller (0.3-0.1 cc/s), read by the data acquisition system in order to have a precise measurement of the output power. Inlet and outlet temperatures of the coolant are measured with two Pt 100 thermometers (four wires measurement). The closed electrochemical cell is equipped with a recombiner. Cell power supply is an AMEL galvanostat. Output power is measured by means of the mass flow rate and coolant temperatures, R/Ro measurement is done by means of an HP- 4284 (four wires measurement). The calorimeter efficiency is 97.5% and was estimated by using LiOH electrolyte in several experiments. No excess of power production has been observed by using H₂O despite a very high loading (H/Pd=0.97) was achieved.

Palladium cathodes, loaded above the deuterium concentration threshold (D/Pd =0.9: atom. frac.) gave a different behavior:

- 1) Excess of power larger than 100% of the input power.
- 2) Excess of power lower than 20% of the input power.
- 3) No excess.

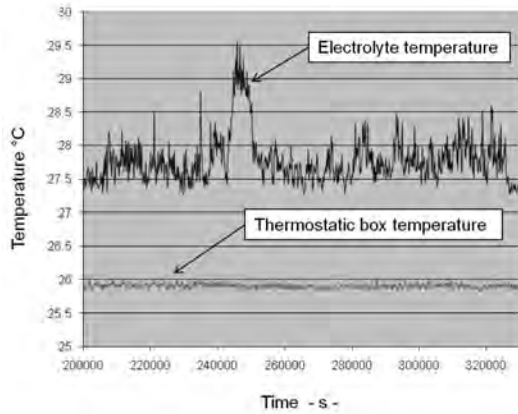


Fig. 1. – Input, output and excess power in the experiment L17.

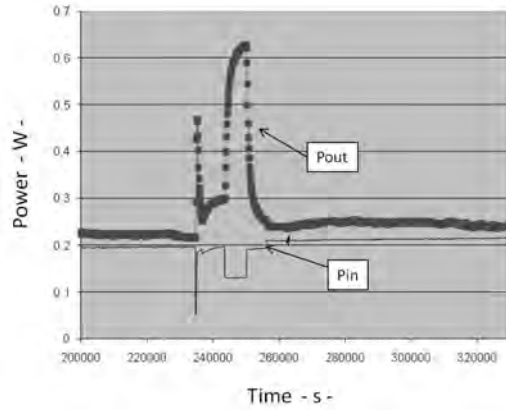


Fig. 2. – Increasing of the electrolyte temperature during the production of excess of power.

We identified some differences in two palladium lots received from the same producer. Both lots were 99.95% pure Pd. The first lot gave a reproducibility larger than 60% with signal amplitudes well above 100%. Fig.1 shows the input, output and excess power in the experiment L17 performed with a sample belonging to the first lot; Fig.2 shows the increasing of the electrolyte temperature in this experiment during the excess production. During the experimental campaign performed with the second palladium lot the reproducibility reduced below 20% and the excess amplitude was always below 20-25% of the input power.

A systematic work, to improve the knowledge about the status of the material that is required to have the effect, was conceived on the basis of such a different behavior of the two lots.

The experimental data highlighted that high loading is a necessary, but not sufficient condition to have the production of excess of heat, for such a reason the focus was moved on other features of the samples correlated with the occurrence of the excess of power production.

The most significant evidence, to be correlated to the different behavior in terms of excess of power production from these two lots, was the different spectrum of contaminants. It is well known from physics metallurgy that contaminants may have several effects on the metal characteristics; in fact, contaminants may act on grain size, crystal orientation and grain boundaries shape and depth.

The figures 3 and 4 show the typical grain size distribution of samples obtained from the first and second lot, undergone to the same metallurgical treatment. In addition samples belonging to the first and the second lot showed a different crystallographic orientation: the first lot was mainly oriented $\langle 100 \rangle$ while the second lot was $\langle 100 \rangle$ and $\langle 110 \rangle$ 50% oriented. Excess of power was mostly observed with samples having a dominant $\langle 100 \rangle$ orientation.

The difference in the spectrum of contaminants produced also a different effect of the chemical etching because of the different reactivity of the surface. The consequence was a different surface morphology between samples belonging to the two lots.

We selected the Power Spectral Density Function (PSD) as merit figure to identify the status of the surface.

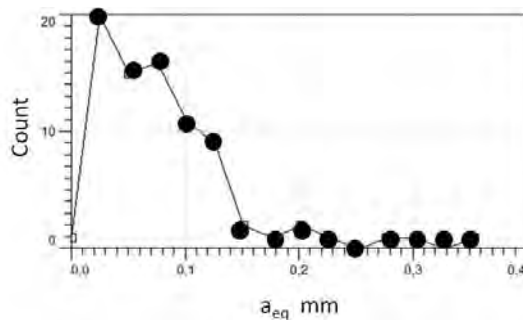


Fig. 3. – First lot grains size distribution.

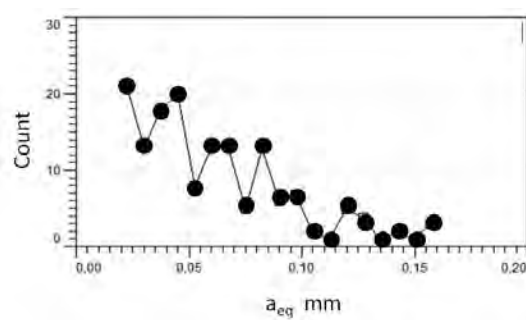


Fig. 4. – Second lot grains size distribution.



Fig. 5. - Microscopy of #64 sample surface.

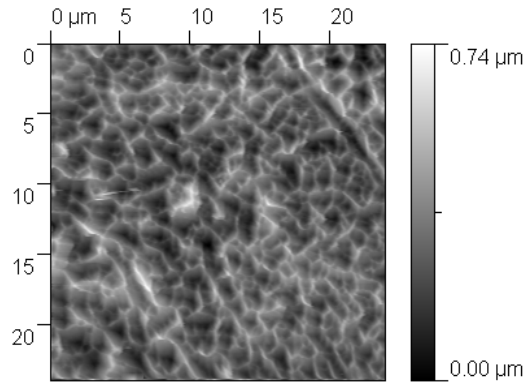


Fig. 6. - Microscopy of L25 sample surface.

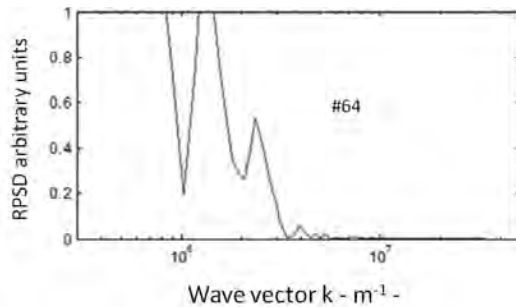


Fig. 7. - PSD of #64 sample.

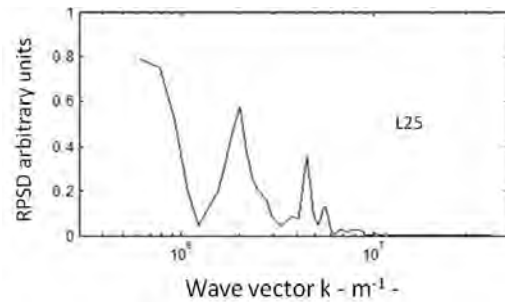


Fig. 8. - PSD of L25 sample.

Fig. 5 and Fig. 6 show the surface microscopy of samples #64 (sample #64 was produced at ENEA and experienced at Energetics) and L25 respectively; both gave a significant excess of power production but the effect was stronger for lot #64. Samples #64 and L25 gave an excess of power larger than 1000% and 200% respectively. Figures 7 and 8 show the power spectral density function for lot #64 and for lot L25 respectively. One may observe that the structure of the PSDF are quite similar but the larger the amplitude of the PSD peaks the larger the produced excess of power. This correlation, highlighting a significant role of the surface, was also found in other measurements.

3. A designed material

The experimental correlations presented in the previous paragraph led to produce a material having characteristics close to the ones described above.

A lot of Pd having a spectrum of contaminants approaching the one of lot 1 was undergone to the treatment leading to: dominant <100> orientation and an appropriate metallurgy.

A surface morphology quite similar to the labirintic one of sample #64 and L25 was produced by the chemical etching.

Fig. 9 shows the PSD for such a sample that results to be similar to the one of samples #64 and L25 even if the peaks amplitude is lower. A small excess was expected from such a sample. The experimental behavior gave a satisfactory agreement with the expectation. Fig. 10 show the produced excess of power up to 12% of the input.

A material designed to have excess of power production was replicated successfully by using the approach described above. Fig. 11 and 12 show the excess of power and the PSD for another designed sample.

An increased control of the effect is achieved even if not yet satisfactory, in particular if we compare the amplitude of the signals with the values observed experiencing the samples obtained from the first palladium lot. However a correlations between the amplitude of the power spectrum and the amplitude of the excess of heat turns out. This result is pointing into the direction of a crucial role of the surface status

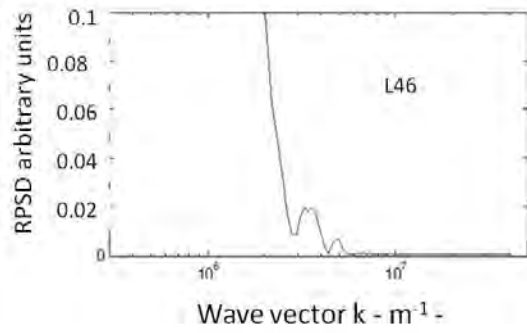


Fig. 9. – PSD of a material designed to produce excess of power.

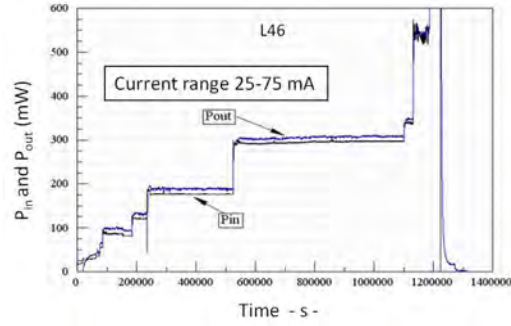


Fig. 10. – Excess of power produced by the designed material.

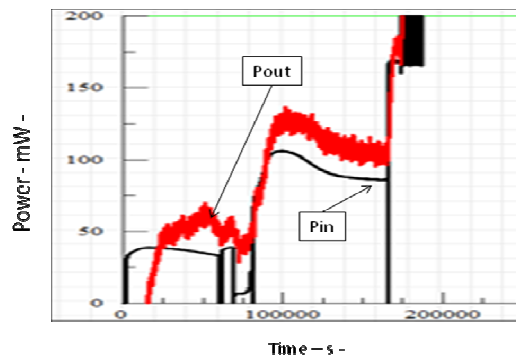


Fig. 11. – Excess of power produced by a designed sample.

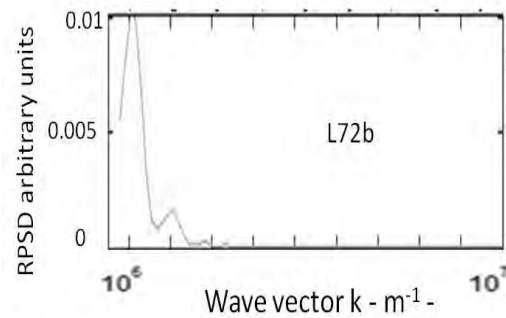


Fig. 12. – Designed material PSD.

to observe the effect; in other words an appropriate surface morphology is confirmed to be an additional condition to observe the effect. A certain reproducibility has been achieved in preparing “designed materials”; however the samples produced with the “designed material” and the ones obtained from the first lot are similar but not equal to each other. In other words the broad effort in the material science remains a crucial point for enhancing the level of knowledge in this field.

4. Conclusions

Reproducing the characteristics of the palladium cathodes that have been identified to be correlated with the excess of power production during electrochemical deuterium loading allowed to obtain the effect. This effect correlation was observed in several experiments performed with a designed material.

The enhancement of the probability to have excess of power is given by:

- 1) Easy loading at low current density due to proper metallurgy.
- 2) $\langle 100 \rangle$ mostly oriented material.
- 3) Labirintic surface giving a defined shape of the power spectral density function.

The correlation of the amplitude of the excess of power with the amplitude of the PSD is pointing in the direction of a crucial role of the surface under electrochemical conditions.

References

- [1] K. Kunimatsu, N. Hasegawa, A. Kubota, N. Imai, M. Ishikawa, H. Akita and Y. Tsuchida, Proc. Third Int. Conf on Cold Fusion, Nagoya (Japan) October 20-25, 1992, p.31.
- [2] M. C. H. McKubre, S. Crouch-Baker, A. M. Riley, S. I. Smedly, F. L. Tanzella, Proc. Third Int. Conf on Cold Fusion, Nagoya (Japan) October 20-25, (1992), p.5.
- [3] M. Fleishmann, S. Pons, J. Electroanal. Chem. Vol. 261, (1989) p. 301.
- [4] V. Violante et al., Phys. Rev. B, Vol. 56, (1997) pp. 2417-2420.
- [5] V. Violante et al., Proc. ICCF-14 Washington DC 10-15 August 2008, Vol. 2 p. 429.

Excess Power Observations in Electrochemical Studies of the D/Pd System; the Operating Parameter Space

M.C.H. McKubre

SRI International, Menlo Park, California.

Abstract. The research activity into the Fleischmann-Pons Effect, FPE [1] at SRI has now accumulating more than 60 man-years of research. Here we focus attention on aspects of that work that lead to an improved understanding of the parameter space in which the FPE occurs.

1. Introduction

Researchers at SRI first focused attention on the critical importance of deuterium loading, the role of chemical poisons and additives in controlling the electrochemical interface, in order to achieve and maintain high D/Pd loading. We studied the correlation of excess power production with loading and reported simultaneously with IMRA-Japan [2,3] the threshold onset of the FPE reproduced as Figure 1. We designed and built a novel, high-accuracy, fully automated mass flow calorimeter, and set out to perform replication studies of the Fleischmann and Pons heat effect, first to confirm the existence the effect and second to better define the physical conditions under which it can be observed.

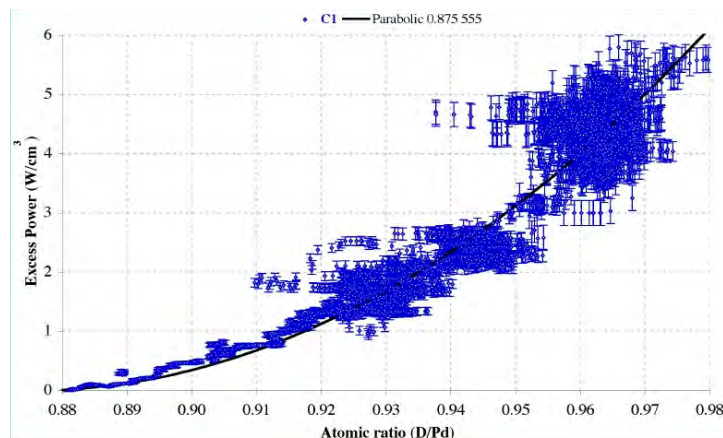


Fig. 1. - Excess power density in W/cm^3 versus average D/Pd atomic ratio measured from the axial resistance for a Johnson Matthey wire cathode 30 cm long and 1 mm diameter in 1.0 M LiOD containing 200 ppm Al.

As a second thrust of activity SRI embarked on a formal program of laboratory replication already discussed in several papers [4-7]. We successfully replicated:

- i. calorimetric evidence of the Fleischmann and Pons heat effect [8,9],
- ii. pioneering Miles/Bush FPE heat/helium correlations [4,10],
- iii. heat (and helium) results of gas loading studies reported initially by Case [10],
- iv. Arata & Zhang double structured cathode electrolysis heat (and helium) results [10],
- v. Energetics Technologies startling amplification of the power and energy gain of the FPE using innovating current (and other) modulation first elucidated by Dardik [7,11].

To accomplish these tasks the SRI team encouraged and contributed in a number of scientific partnerships. Obviously in approaching any difficult problem it is important to attract a critical mass of all the people who might contribute to the resolution of these effects. Specifically and ongoing we have a long established collaboration with Peter Hagelstein and his colleagues at MIT and over a decade of continuous, active, formal collaboration with Vittorio Violante and his group at ENEA Frascati. The Energetics team we have been collaborating actively with since about 2006, and more recently with the Naval Research Laboratory, NRL.

2. Experimental

At SRI, it was decided in early experiments to pursue excess power measurements based on flow calorimetry so that measurements of thermal power were obtained from measurements of the input and output (water) temperature, mass flow rate, and knowledge of the (water) heat capacity. In the SRI calorimetry of the early 1990s, about 95% of the thermal power was captured in the flow. The power not captured by the flow calorimetry was estimated using a Fick's law measurement, resulting in total power measurements with errors on the order of 0.5% in the case of 95% capture by the flow. In later designs, specifically the Labyrinth (L) and helium leak tight (M) calorimeter designs greater than 99% of the evolving heat was captured in the convecting fluid flow resulting in accuracies better than $\pm 0.35\%$.

To perform excess power measurements in this kind of calorimeter, closed cell operation was required, which necessitated the recombination of all gases generated in association with the electrochemistry. A further advantage of this choice is the retention of D_2O and products for analysis. It is worth noting that mass flow calorimetry and closed cell operation were not the methods adopted by Fleischmann and Pons. Much has been made of this difference but these choices reflected no disapproval of earlier principles and procedures of calorimetry. Although we were not aware of the details at the time, Fleischmann and Pons designed and built a beautiful calorimeter. It was very subtle and very sophisticated, requiring a sophisticated analysis and understanding. Unfortunately most of the people who remained skeptical in 1898 and 1990 had no means of achieving that sophisticated understanding.

In order to achieve high loading values (D/Pd ratios $\gg 0.9$) one needs to take strong control of the impurity aspects of the electrochemical cell. At SRI the various elementary constraints evolved a particular cell design shown in Figure 2. We employed mostly one molar $LiOD$, where the original work [1] employed 0.1 M. Again, no judgment is implied. We selected the electrolyte we believed best able to test our hypothesis that high D/Pd loadings prompted or promoted the excess heat effect. Most early SRI experiments were performed with 1 and 3 mm diameter wires, either 3 or 5 cm long. Loading is inferred from measurements of the resistance in the axial direction, expressed as a ratio of the unloaded resistance.

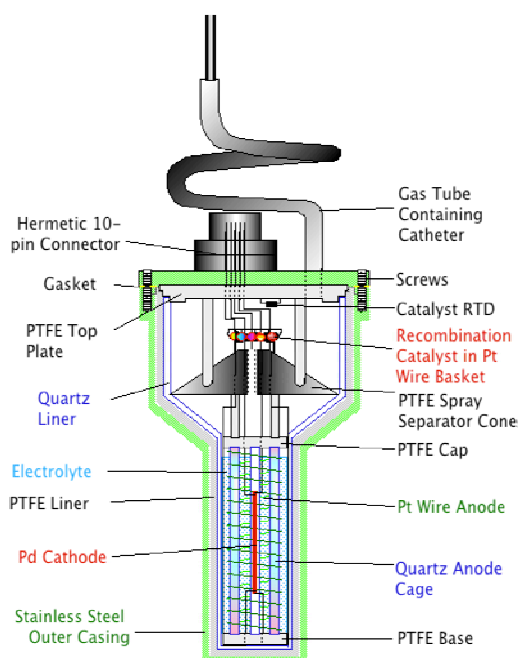


Fig. 2. - SRI Degree of Loading (DoL) electrochemical cell shown in hermetic closure.

In its calorimetric use the cell of Figure 2 is placed inside the calorimeter as shown in Figure 3. The calorimeter was submerged inside a large ($\sim 1 \text{ m}^3$), water bath that was well stirred and well regulated. This bath was placed in the center of an isolated, temperature controlled room. The mass flow fluid (water) was drawn from the bath past two inlet RTD sensors placed directly in the flow stream, past the submerged

electrochemical cell and emerges past outlet temperature sensors situated within the axial outflow channel, directly in contact with the outgoing fluid. Two outlet RTD sensors were used, identical to the two at the inlet, to provide a redundant measurement of ΔT ¹.

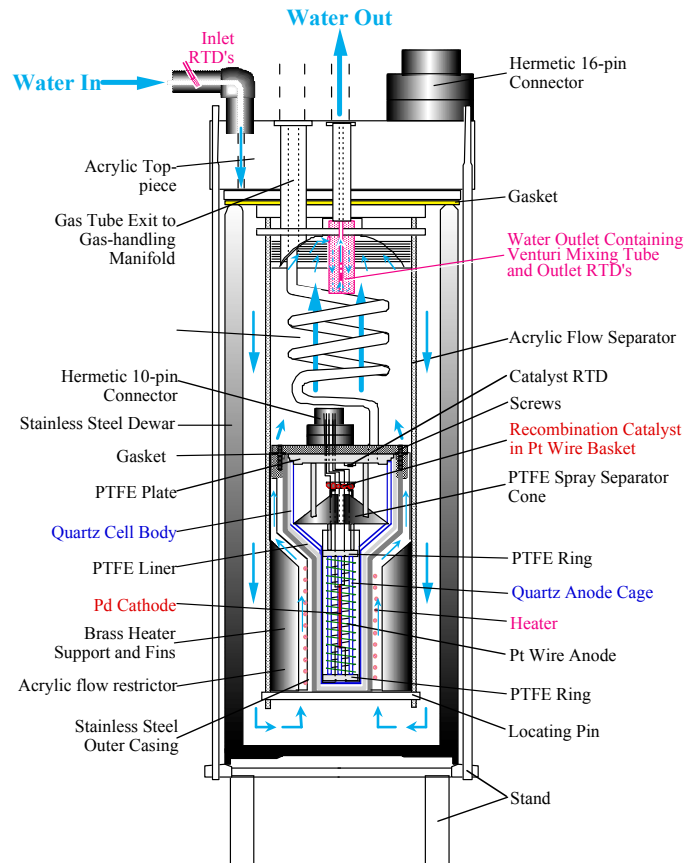


Fig. 3. - SRI Labyrinth (L) Mass Flow Calorimeter showing internal hermetically sealed electrochemical cell.

Many excess heat bursts were detected over the years in Fleischmann Pons experiments run in the SRI flow calorimeters. An example is illustrated in Figure 4, where two cells (a light water cell and a heavy water cell) were run electrically in series. Excess power was observed in heavy water cells at SRI, but not in light water cells, consistent with the results presented in this figure. In addition, the excess power effect appears to vary in response to the current density applied as shown in Figure 5. One observes a threshold in current density, where no excess power is present below 270 mA/cm^2 , and where the excess power appears to increase roughly linearly above this threshold. The appearance of a threshold in current density is typical in FPE experiments, although the specific current threshold is different for different cathodes, and depends strongly on whether the cathode is a rod or foil [12].

¹ In some experiments two additional thermistor sensors were used at the outlet to provide an alternative measurement method.

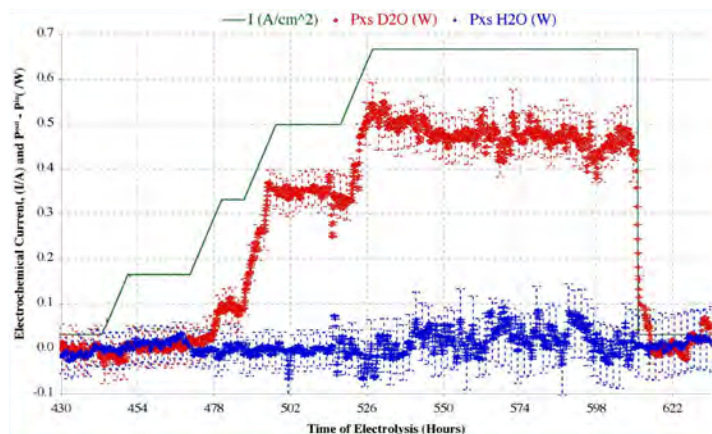


Fig. 4. - Excess power in Fleischmann-Pons experiments as a function of time in twin cells and calorimeters, driven with a common current, one with heavy water (upper data points) and one with light water (lower data points). The applied current density is shown as a solid line.

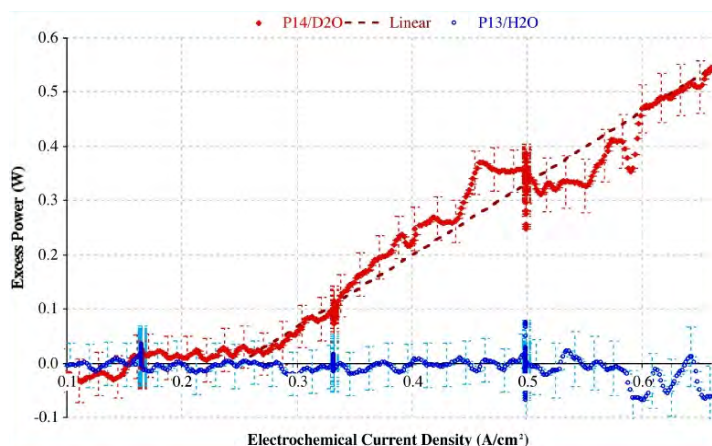


Fig. 5. - Excess power as a function of current density for Fleischmann-Pons cells with heavy water (upper data points) and with light water (lower data points).

Figure 6 presents not a typical result but a good result from later series SRI FPE experiments. With total input power² 12 W, we observe the output power increasing up to 6 W, with peak excess power of 50% with respect to the total input power. Also plotted is a pseudo-reference voltage exhibiting structure and detail reflecting extreme and at times bi-stable conditions at the electrochemical interface of the cathode, somewhat correlated to excess power. The period from ~700 hours onwards was more or less steady electrochemically, but the thermal and voltametric responses are dynamic.

It was found that changes in the operating parameters could initiate a heat burst in addition to the apparently self-stimulated dynamics of the cathode overvoltage and excess power. This observation may be related to a more general correlation between excess heat and a net deuterium flux either into or out of the metal. Figure 7 plots loading and excess power for a 24 hour period of constant electrochemical condition for (temperature and current density) a 1 mm dia. Pd wire wire cathode exhibiting variable excess power. The loading can be seen to vary in a somewhat sinusoidal “breathing” mode with ~2 hour period as the cathode apparently spontaneously absorbs and desorbs deuterium.

² Experiments were operated in pseudo-isothermal condition by holding the sum of the electrochemical and joule heater input power constant.

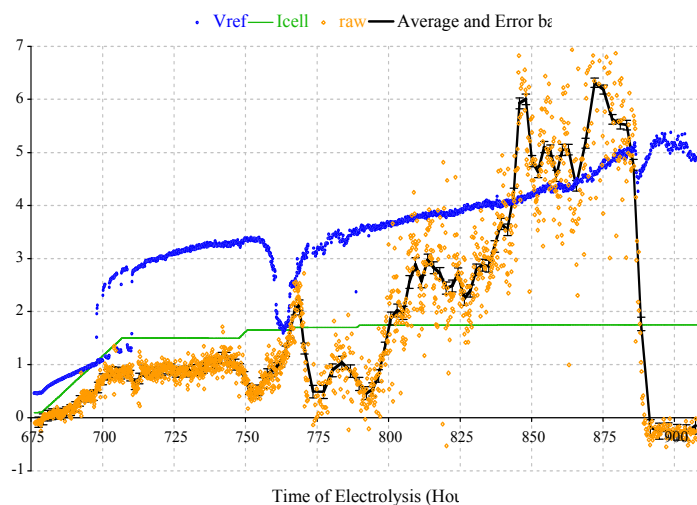


Fig. 6. - Excess power as a function of time for Fleischmann-Pons cells with LiOD electrolyte containing 200 ppm Al. The solid green line plots electrochemical current density, the square blue points are cathode voltage measured vs. proximate open-circuit Pt pseudo-reference electrode. The solid black line is the average excess power raw data points plotted in orange.

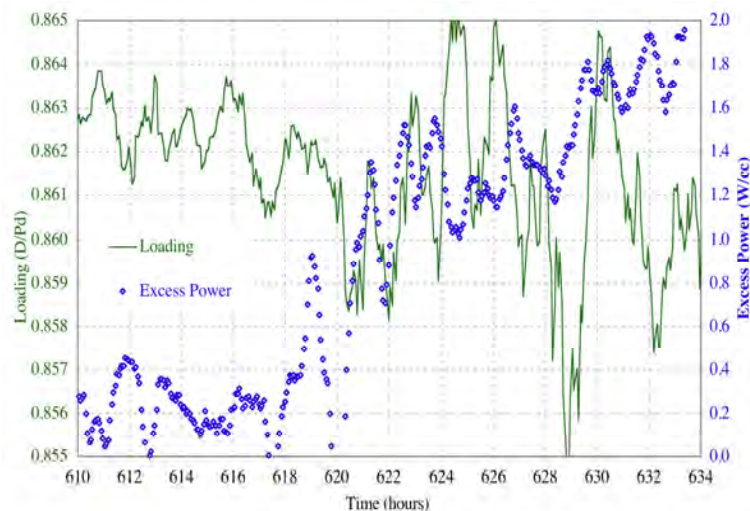


Fig. 7. - Correlation of the amplitude of loading oscillations with the magnitude of excess power in experiment M4.

While the frequency remains fixed, the amplitude of this “breathing” closely correlates with the amplitude of the excess power signal. We do not have an accurate knowledge of the diffusion coefficient of D under the prevailing loading condition but a time constant of 2 hours corresponds with a diffusion coefficient of $\sim 5 \times 10^{-7} \text{ cm}^2 \text{ s}^{-1}$ traversing the full radius of the electrode. We do not know what caused this to occur, and all attempts to stimulate such oscillatory fluxing in the high loading condition have failed (with one notable exception discussed below).

3. Conclusions

The clear evidence of both intense and extended experimental investigation is that the FPE heat effect occurs as a consequence of four conditions in the electrochemical palladium-deuterium system:

- i. electrodes must attain and maintain D/Pd loading above a (high) threshold value, for
- ii. periods longer than an initiation time that is long compared to deuterium in-diffusion
- iii. while being subjected to a high electrochemical current that is in general larger than the current density of maximum loading
- iv. maintaining an electrode/electrolyte interface kinetically free enough to facilitate high rates of deuterium absorption/desorption (flux).

This set of observations prompted the development of an empirical expression for the simplest and most widely observed mode of excess heat production (designated by us as Mode A).

$$P_{xs} = M (x-x^{\circ})^2 (i-i^{\circ}) |i_D| \quad [1]$$

where $x = D/Pd$, x° is the threshold value typically ~ 0.875 , the current density threshold i° for wire cathodes typically falls in the range $75 < i^{\circ} < 450 \text{ mA cm}^{-2}$, the deuterium interfacial flux $i_D = 2\text{-}20 \text{ mA cm}^{-2}$.

In conclusion it should be noted that the simultaneous attainment of the above specified conditions has been found to require patient and rigorous attention to: system electrochemistry; bulk palladium metallurgy; electrode surface morphology and crystal orientation. Much, if not all of the apparent and “famous” irreproducibility of the Fleischmann-Pons heat effect can be traced directly to the failure to recognize and meet one or more of these conditions.

References

- [1]. M. Fleischmann, S. Pons and M. Hawkins, *J. Electroanal Chem.*, **201**, p.301 (1989); Errata, **263**, p. 187 (1990). See also M. Fleischmann, S. Pons, M.W. Anderson, L.J. Li and M. Hawkins, *J. Electroanal. Chem.*, **287**, p. 293 (1990).
- [2]. K. Kunimatsu, N. Hasegawa, A. Kubata, N. Imai, M. Ishikawa, A. Akita and Y. Tsuchida, “Deuterium Loading Ratio and Excess Heat Generation during Electrolysis of Heavy Water by a Palladium Cathode in a Closed Cell Using a Partially Immersed Fuel Cell Anode”, in *Frontiers of Cold Fusion*, H. Ikegami, Ed., proceedings of the 3rd International Conference on Cold Fusion, Nagoya, Japan, p. 21, October 1992.
- [3]. M.C.H. McKubre, S. Crouch-Baker, A. M. Riley, S. I. Smedley and F. L. Tanzella, “Excess Power Observations in Electrochemical Studies of the D/Pd System; the Influence of Loading”, in *Frontiers of Cold Fusion*, H. Ikegami, Ed., proceedings of the 3rd International Conference on Cold Fusion, Nagoya, Japan, p. 5, October 1992.
- [4]. M.C.H. McKubre, F. L. Tanzella, P. Tripodi and V. Violante “Progress towards replication”, in *The 9th International Conference on Cold Fusion, Condensed Matter Nuclear Science. 2002*. Tsinghua Univ., Beijing, China, X. Z. Li Ed., Tsinghua Univ. Press.
- [5]. P.L. Hagelstein, M.C.H. McKubre, D.J. Nagel, T.A. Chubb, and R.J. Hekman, “New Physical Effects in Metal Deuterides”, *Proceedings of the 11th International Conference on Cold Fusion, Marseilles, France, November 2004*, J.P. Biberian Ed., World Scientific, p. 23 (2006).
- [6]. M.C.H. McKubre, “The Importance of Replication”, accepted for publication in proceedings of the 14th International Conference on Cold Fusion, D.J. Nagel Ed., Washington, D.C., USA, October 2008.
- [7]. M. C. H. McKubre, , F. L., Tanzella, I. Dardik, A. El Boher, T. Zilov, T., Greenspan, C. Sibilina, and V. Violante, “Replication of Condensed Matter Heat Production”, in *Low-Energy Nuclear Reactions Sourcebook*, J. Marwan Ed., ACS Symposium Series 998, Oxford University Press, 2008, p. 219.
- [8]. M.C.H. McKubre, S. Crouch-Baker, R.C. Rocha-Filho, S.I. Smedley, and F.L. Tanzella, “Isothermal Flow Calorimetric Investigations of the D/Pd System”, in *Second Annual Conference on Cold Fusion, "The Science of Cold Fusion"*. 1991. Como, Italy: Societa Italiana di Fisica, Bologna, Italy.
- [9]. M.C.H. McKubre, S. Crouch-Baker, R.C. Rocha-Filho, S.I. Smedley, and F.L. Tanzella, “Isothermal Flow Calorimetric Investigations of the D/Pd System” *J. Electroanal Chem.*, **368**, p. 55 1994.
- [10]. M.C.H. McKubre, F. L. Tanzella, P. Tripodi and P. L. Hagelstein “The Emergence of a Coherent Explanation for Anomalies Observed in D/Pd and H/Pd System: Evidence for ⁴He and ³He Production”, in *8th International Conference on Cold Fusion. 2000*. Lerici (La Spezia), Italy: Italian Physical Society, Bologna, Italy.
- [11]. M. C. H. McKubre, and F. L. Tanzella, “New Physical Effects in Metal Deuterides”, Final Report on DARPA contract HR0011-05-C-0089, SRI Project P16816, 2006.
- [12]. E. Storms, *The Science of Low Energy Nuclear Reactions*, World Scientific, Singapore, 2007.

Differential Thermal Analysis Calorimeter at the Naval Research Laboratory

D.L. Knies, K.S. Grabowski, D.A. Kidwell and V.K. Nguyen

*Materials Science and Technology Division, Naval Research Laboratory,
Washington, DC 20375*

M.E. Melich,

*Wayne E. Meyer Institute of Systems Engineering, Naval Postgraduate School,
Monterey, CA 93943*

Abstract Differential thermal analysis (DTA) is a standard thermoanalytic technique used widely in industry and research. Drawing on this concept, DTA based calorimeters are under development at the Naval Research Laboratory (NRL) for the study of hydrogen in metals. The design goals are: high sensitivity, linear response, short time constant, tolerant to ambient temperature variations, easy to adapt to experimental constraints and low cost. In this paper we detail basic design requirements, and show a number of examples of their implementation.

1. Introduction

Since the announcement of thermal anomalies in the palladium-deuterium system reported by Fleischmann & Pons [1] in 1989, now referred by many as the Fleischmann Pons Effect (FPE), the veracity of their results have been questioned by the wider scientific community. Much of this criticism has been leveled at the calorimetry and its interpretation. Since then, the complexity of calorimeters used to confirm or refute the original isoperibolic calorimeter results has added to the confusion. One example of calorimeters applied is a first principles mass flow calorimeter, as was reviewed by McKubre et al. [2]. These are complicated systems requiring a large capital investment, and are not well suited for broad materials studies. To circumvent these limitations, we investigated commercially available calorimeters and analyzed their operating principles. None was found that met all our needs to study materials related to FPE. However, the basic operating principle for the differential thermal analysis (DTA) class of calorimeters held the promise of meeting this need. This paper describes the operating principle of DTA and our prototype implementations of DTA concepts specifically geared for the study of FPE-related materials.

2. Approach

The rejection of common mode signals is an integral part of the design of a DTA calorimeter. The technique relies on using two nearly identical thermal masses connected to a thermal reference (Fig. 1). The ability to reject common mode signals is dependent on the careful physical layout and shielding of the measurement channels. In our case, one of the thermal masses is an inert cell, while the other is the active cell. The analog electric circuit equivalent is a common mode amplifier, in this case, used to remove stray thermal signals generated by fluctuations in the ambient or reference temperature. In the ideal case

$$V_{\text{out}} = A*(V_{\text{inert}} - V_{\text{active}})$$

where A is the difference gain, and V is the voltage generated by thermoelectric modules. Thermoelectric modules (TEM) monitor the flow of heat from the inert and active cells to the common thermal reference. The cell output voltages are given by

$$V = \alpha N(T_{\text{cell}} - T_{\text{ref}})/(1 + 2rl_c/l)$$

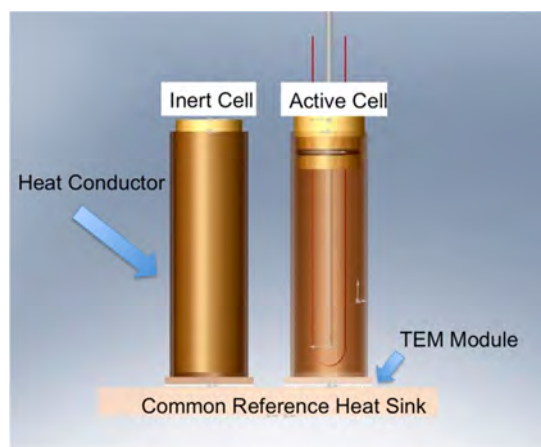


Figure 1. Conceptual drawing of a DTA calorimeter.

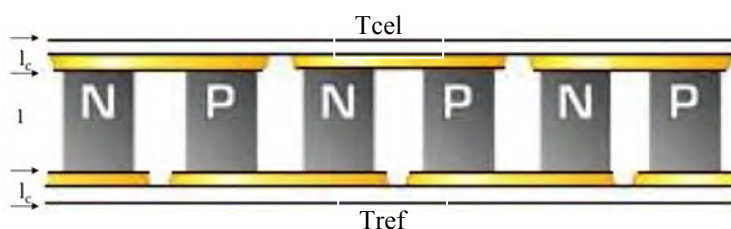


Figure 2. Graphical representation of thermoelectric module.

according to Rowe et.al. [3], where α is the Seebeck coefficient of the thermoelectric material, N the number of thermocouples, l is length of the thermoelement, l_c , the thickness of the contact layer, T_{cell} , and T_{ref} , are temperatures at the cell and reference sides of the module and $r = l/\lambda_c$, where λ the thermal conductivity of the thermoelement and λ_c the contact thermal conductivity as shown in Fig. 2.

Rather than paneling the inside of a box with many TEMs as was done by Stroms [4], only two TEMs were used - one for the active cell and one for the inert cell (Fig 1). Heat flow was directed to the TEM by surrounding the active cell volume by a good heat conductor. A finite element analysis calculation was done to understand the steady state heat flow pathway for this approach. The result of this study can be seen in Fig. 3. The largest temperature gradient is across the TEM, thus, that is where the bulk of the heat flows. The time constant of the cell can be adjusted by the thermal mass and thermal properties of the cell. The cells should be surrounded by a constant temperature bath of very low thermal mass. This can be accomplished by surrounding the cell with a large thermal mass at the reference temperature, and leaving a small air gap between it and the cell. These basic principles have been used to tailor calorimetric systems to specific tasks since the invention of the thermocouple.

3. Experimental

The basic DTA concept can have nearly unlimited variations and can be tailored to satisfy specific applications. We tested two basic test tube designs. The first DTA is built around a disposable BD Falcon™ 50 ml conical tube. It can house either a simple cathode and anode assembly for electrolytic loading or a gas bottle for gas phase experiments. The heat transfer tubes were machined from two pieces of aluminum such that the 50 ml test tubes fit tightly. A large scrap piece of aluminum (26 cm x 21.6 cm * 3.81 cm) was used as the reference heat sink. The bottoms of the heat transfer tubes and the top of the reference heat sink were polished where the TEM's where to be attached. Two Custom ThermoElectric 40 mm x 40 mm TEM modules (part# 12711-5L31-03CQ) were silver printed to both the heat transfer tubes and the reference heat sink. The heat transfer tubes were then insulated using Armacel AP/Armaflex Microban 25/50 pipe insulation. Identically insulated hand wound 23 ohm nichrome wire heaters were

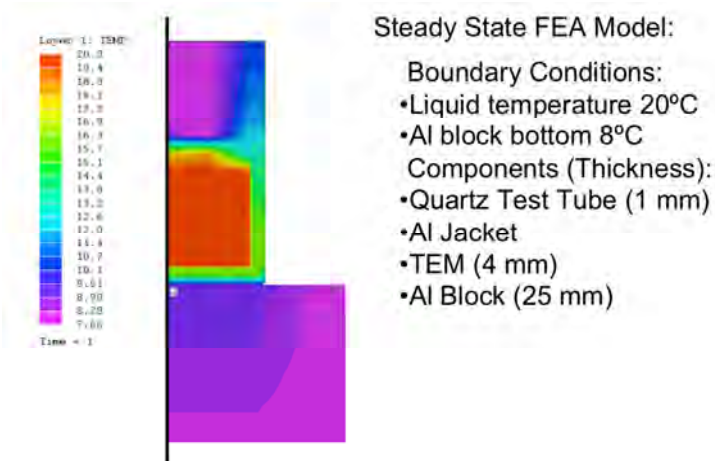


Figure 3. - Steady state FEA model of active cylindrical cell. One-half of symmetric cell is shown in cross section.

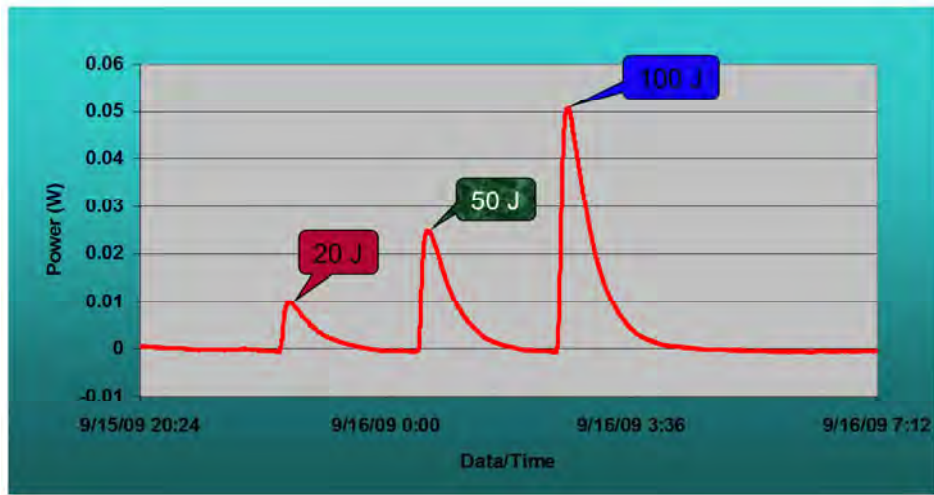


Figure 4. - DTA baseline stability and pulse response.

Table 1. - DTA response to a gas loading simulation

Impulse	Measured	Error
20 J	19.8 J	1% / 0.2 J
50 J	46.1 J	8% / 3.9 J
100 J	94.6 J	5% / 5.4 J

installed in both the reference and active cells. RTDs for temperature measurement were installed along the centerline of the cells. The completed system was then placed inside an incubator.

The DTA was tested for baseline stability and pulsed heat response to simulate our typical gas loading experiment [5]. The performance was evaluated by programming a Bio-Logic USA, LLC Model VSP potentiostat / galvanostat in constant power mode to produce 20, 50, and 100 joule pulses. Shown in figure 4 and table 1 are the results of this test. The agreement between the measured response and the delivered power is comparable to commercially produced instrumentation.

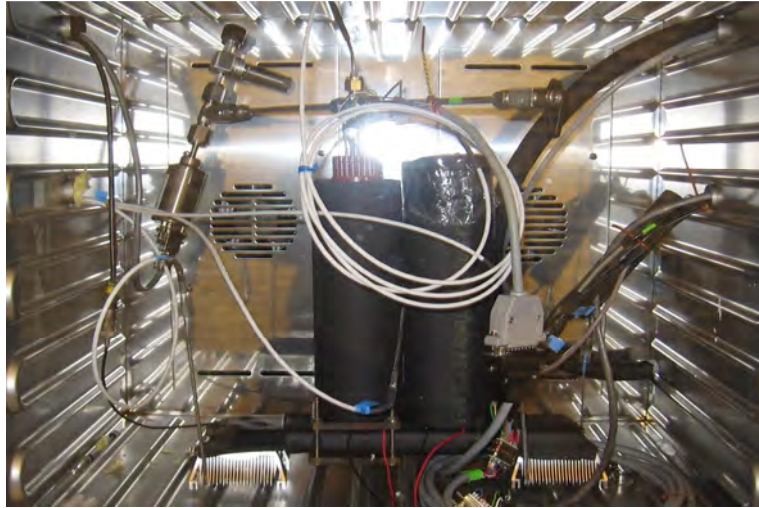


Figure 5. - Fully assembled DTA Calorimeter.

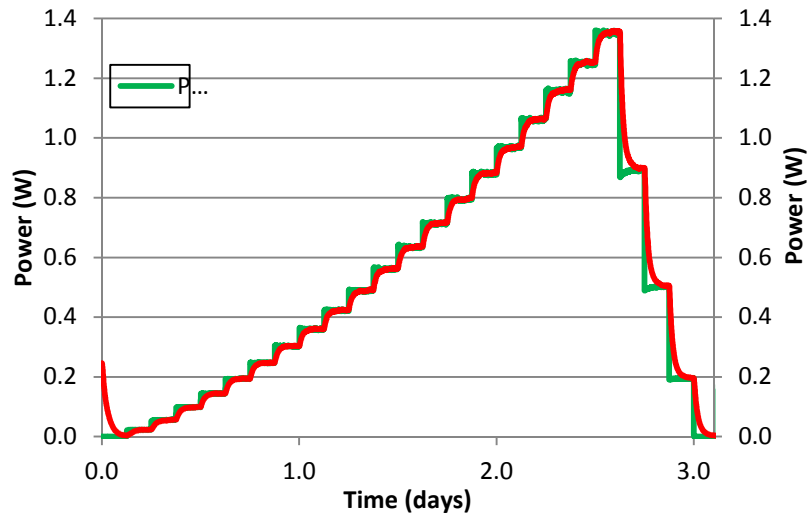


Figure 6. - Calibration run of DTA designed to match ENEA cell.

The second proof of principle DTA system was built to match the ENEA Violante closed cell design [6]. The design concept is basically the same as the first. The heat transfer tubes are built from commercially available copper pipe machined to match the outside dimension of the ENEA electrolytic cell. The fully assembled DTA is shown in Fig. 5. Results of a 3 day calibration run using light water are shown in Figure 6, where the current was stepped under galvanostatic control over a typical operating range. A single linear combination of the inert and active cell TEM voltages fit the input power of the tested range. The maximum power is limited by the heat sink's capability to transfer heat to the incubator. The inside temperature of the cell was monitored by RTDs, and also correlates with the input power as expected. Two heat sinks on either end of the thermal reference were also monitored. Their temperatures were also well correlated with the input power.

4. Conclusions

These proof of principle tests clearly demonstrate that one can build a very capable calorimeter that satisfy the needs of a rapid materials development and screening program, to gain insight underlying the requirements for the FPE. These simple systems proved to be stable (1% over 5 days) with good

sensitivity (1% absolute) comparable in many ways to our commercial Hart Heat Conduction calorimeter. The concepts can readily be modified to include, for example, external stimuli of time varying magnetic or electric fields, laser stimulation and programmable temperature ramps. This makes this design an ideal platform to test the validity of FPE claims in both liquid and gas phases. The linear response obtained over the tested operating range from a few Joules of impulse heat to long-term hours of operation at several watts DC makes the interpretation of results straightforward.

References

- [1] M. Fleischmann, S. Pons and M. Hawkins, J. Electroanal. Chem. **261** (1989) 301; *Errata* 263 (1989) 187.
- [2] McKubre, M.C.H. and F. Tanzella, Mass Flow Calorimetry, in ICCF-14 International Conference on Condensed Matter Nuclear Science. 2008. Washington, DC.
- [3] D.M. Rowe, G.Min, IEE Proc.-Sci. Meas. Technol. **143** (1996) 351.
- [4] Storms, E., 12th International Conference on Condensed Matter Nuclear Science. 2005. Yokohama, Japan.
- [5] D.A. Kidwell, A.E. Rogers, K.S. Grabowski, D.L. Knies, 15th International Conference on Cold Fusion, Rome, Italy, October 5-9, 2009
- [6] Violante, V., Sarto, F., Castagna, E., McKubre, M. C. H., Tanzella, F. L., Hubler, G. K., Knies, D., Dardik, I., Sibilial, Joint Scientific Advances in Condensed Matter Nuclear Science. in 8th International Workshop on Anomalies in Hydrogen / Deuterium Loaded Metals. 2007. Sicily, Italy.

Electrochemical models for the Fleischmann-Pons experiment

P.L. Hagelstein¹, M.C.H. McKubre², and F.L. Tanzella²

¹Research Laboratory of Electronics, MIT

²SRI International, Menlo Park, CA

E-mail: plh@mit.edu

Abstract. The loading of Pd by hydrogen isotopes in the Fleischmann-Pons experiment does not seem to be well described by the hydrogen/deuterium evolution reaction model that is commonly used for hydrogen in metals. We consider modified versions of the model that may be more relevant to the loading of deuterium in Pd.

1. Introduction

The need for high deuterium loading in Pd in the Fleischmann-Pons experiment as a prerequisite for the development of excess heat has been emphasized by McKubre and coworkers repeatedly over the years [1-3]. We are interested in modeling the cathode loading in order to understand the associated physics, and to simulate excess heat production.

The loading of deuterium in palladium can be understood simply enough in a broad sense in terms of individual reactions that constitute the hydrogen/deuterium evolution reaction model. Deuterium is brought to the surface through the Volmer reaction



Deuterium on the surface can recombine through the Tafel reaction to make D₂ gas



Adsorbed deuterium can move into the cathode to occupy more tightly bound sites associated with adsorbed deuterium



Other things can happen as well (as we will discuss below). However, these three basic reactions provide a simple picture which allows for a quantitative description of the cathode loading at low current density (in the Volmer-Tafel regime).

In this reduced picture, the electrochemical current is dominated at the Pd surface by the Volmer reaction. When this occurs, one deuterium atom is deposited on the cathode surface as an adsorbed atom per charge transferred. In this regime, we can load the cathode simply by applying a current.

As deuterium accumulates on the surface (and hence in the bulk), the deuterium chemical potential increases, making D₂ gas formation more likely. The loading is determined in the Volmer-Tafel regime by matching the incoming deuterium from the Volmer reaction to the outgoing deuterium gas associated with the Tafel reaction.

Although there are technical issues, this simple picture can account for important features of cathode loading in the Fleischmann-Pons experiment at low current density. Unfortunately, at higher current density the situation becomes more complicated. One can find publications in the literature which make use of the hydrogen/deuterium evolution equations to describe the loading at higher current density [4,5]. Unfortunately, these models do not work particularly well when used systematically for different experiments. For example, Zhang et al [5] used such a model to account for a decrease in the loading at high current density observed in an experiment reported by Kunimatsu's group. In this model, the Heyrovsky mechanism



accounted for this loss of loading. The Heyrovsky mechanism decreases the loading by one deuterium per unit charge in the electrochemical current, in contrast to the Volmer mechanism that increases the loading by one deuterium per unit charge. The problem is that the kinetics rate associated with the Heyrovsky mechanism increases exponentially with loading. Hence, such a model would not predict a loading significantly higher than the maximum loading for that experiment (D/Pd of about 0.85), where there are now many reports of experiments where significantly higher loading is seen.

2. Volmer reaction kinetics model

We start with a model for the Volmer current density j_V given by

$$j_V = r j_{V0} \left(\frac{1-\theta}{1-\theta_0} \right) e^{-(1-\beta_V) f \eta} + d.b. \quad (5)$$

Here r is a roughness factor, θ is the fraction of available surface sites with adsorbed deuterium, β_V is an asymmetry factor, f is $e/k_B T = F/RT$, and η is the overpotential. The notation d.b. denotes the counter term required for detailed balance. Our notation is most closely related to that of Zhang et al [5].

There are two free model parameters here (the quantity $r j_{V0}/(1-\theta_0)$, and β_V). The asymmetry factor β_V can be obtained from experiment, and we have used 0.49 as given by Green and Britz [6] for 0.1 M LiOD. For simplicity, we have adopted $r=2$ from this work. We are able to approximately match the data given in [6] with $j_{V0} = 1.63 \times 10^{-5}$ A/cm² and $\theta_0=0.70$. This choice in our models approximately reproduces the overpotentials that are reported.

3. Tafel reaction model

In the case of the Tafel reaction, we can begin with a model for the equivalent Tafel current density j_T given by

$$j_T = r^2 j_{T0} \left(\frac{\theta}{\theta_0} \right)^2 e^{2u(\theta-\theta_0)} + d.b. \quad (6)$$

Here u is a Frumkin adsorption isotherm parameter [7], which takes into account the change in the chemical potential of the deuterium with loading. In the beta phase, we have made use of the measurements of Chun and Ra [8], which leads to $u = 20.0$ at room temperature. In the mixed phase region below a loading of about 0.60, the chemical potential does not change with loading, so that $u=0$ would be appropriate. It seems that there is one remaining free parameter, j_{T0} . It is possible to obtain a reasonable fit to different data sets in the Volmer-Tafel regime, but only if we adopt a different value for j_{T0} for each experiment separately. Individual values in this case can be different by two orders of magnitude.

For the purposes of model development here, we will adopt the point of view that the reason for this variation is that there are internal surfaces where deuterium gas can evolve via the Tafel reaction, and that this gas can subsequently find its way to the outer surface. This point of view is discussed by Storms [9]. To implement this, we will augment the Tafel reaction to read

$$j_T = r^2 [1 + a(\theta)] j_{T0} \left(\frac{\theta}{\theta_0} \right)^2 e^{2u(\theta-\theta_0)} + d.b. \quad (7)$$

where $a(\theta)$ is the ratio of the square of the internal surface area to the square of the outer geometrical surface area. In anticipation of arguments to follow, we assume that the amount of internal surface area depends on the loading.

While such a model seems to allow for a description of the effect, there is the problem that to determine j_{T0} , we require experiments carried out on cathodes that we know have no internal leaks at low loading. In this respect we draw attention to a set of experiments reported by Green and Quickenden [10] where the cathode loading was found to increase up to 0.93 for cathodes that were vacuum annealed and then etched in acid. Within the framework of the model, this pre-treatment produced a smaller value for the internal surface area. In recent experiment at ENEA Frascati with thin foils (which initially are single crystals transverse to the surface), D/Pd loadings above 1.0 have been obtained.

As a result, a low value of j_{T0} is probably appropriate. A value which seems to be in the right regime in this regard is 2.0×10^{-8} A/cm². Tafel current densities as a function of loading for different assumed internal areas are shown in Figure 1. According to this plot, the cathodes reported in Green and Britz have an internal area greater than the surface area by four orders of magnitude or so.

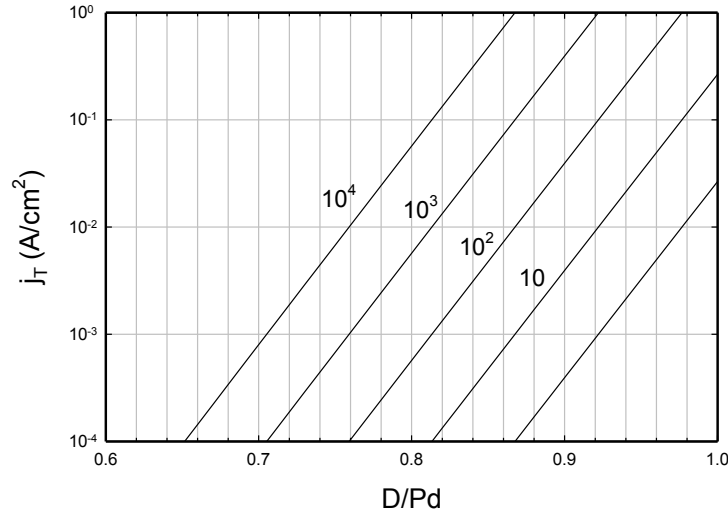


Fig. 1 – Tafel equivalent current density j_T versus loading for different values of a ; the rightmost curve is for $a=0$.

4. Lithium model

Experiments carried out in heavy water electrolytes with LiOD show that lithium enters the cathode [11,12] in significant amounts. We assume that lithium is transported to the surface through the analog of the Volmer reaction in acid



Adsorbed lithium probably comes off of the surface through a version of the lithium-water reaction



If we assume that in steady state the adsorbed lithium is determined from a balance between these reactions, then we obtain the following adsorption isotherm

$$\frac{\theta_{\text{Li}}^2}{1 - \theta - \theta_{\text{Li}}} e^{2v\theta_{\text{Li}}} = C [\text{Li}^+] e^{-(1-\beta_{\text{Li}})f\eta} \quad (10)$$

The measurements of the near-surface absorbed lithium concentrations of Yamazaki et al [11] can be fit well using this adsorption isotherm. The overpotentials in [11] are determined relative to a reference hydrogen electrode (RHE), which seems to give rather different results than the method used by Green and Britz [6]. If we substitute these overpotentials matching currents, then we can fit the near-surface absorption data using $\beta_{\text{Li}} = 0.53$ and $v = 19.4$.

5. Lattice expansion effects

As the cathode loads, the lattice constant increases. One would expect this to have an impact on the internal surface area. The loading curves of Green and Britz [6] show a reduction of loading at the higher current densities over what would be predicted from a simple Volmer-Tafel regime model (which would give the loading approximately proportional to the log of the current density). Near 0.5 mA/cm², the Volmer-Tafel kinetics matches the data well, but up at 50 mA/cm² a pronounced reduction in loading from the Volmer-Tafel model can be seen.

There is not agreement as to why the loading should decrease with increasing current density. From the discussion above, the cathode loading is determined by a balance between incoming deuterium (which is provided by the electrochemical current via the Volmer reaction) and the outgoing deuterium (which leaves as molecular D₂ via the Tafel reaction). As the current initially increases, there is no reason to believe that the efficiency of producing adsorbed deuterium somehow decreases (which might be the case if reactions occurred via the Heyrovsky mechanism). Measurements in this regime searching for evidence of the Heyrovsky mechanism showed that it is not present [6]. It seems unlikely that some new reaction mechanism kicks in that removes deuterium more efficiently than the Tafel mechanism.

We will assume that the loading decreases because additional internal surfaces become available as the lattice expands with increased loading. This point of view seems generally consistent with Storms [8], McKubre [10], and Zhang [13].

Once we adopt this approach, then technical questions arise as to how to implement a model which works this way. Intuitively, one would expect that the surfaces and channels that open as the lattice expands constitute physical changes in the lattice that might be expected to remain if the loading is subsequently reduced. This would show up as hysteresis in the loading curve. Although there is some hysteresis present in the loading curves, it seems that the effects are largely reversible. As such, it seems reasonable to begin with a reversible model that can sensibly be parameterized. To model the initial increase in the internal area, we have found reasonable agreement with a fit of the form

$$a(\theta) = a(0.60) \left(1 + e^{w(\theta - \theta_a)^7} \right) \quad (11)$$

The idea is that the internal Tafel leak rate at the beta-phase boundary (near D/Pd=0.60), when large, dominates the loading curves in the Volmer-Tafel regime. The subsequent increase in the internal Tafel rate is then assumed to depend only on the loading, and not on the current density or overpotential. The experimental curves seem to show a similar shape that has an offset in θ . A more highly loaded cathode suffers a similar reduction in loading as compared to the Volmer-Tafel model as the loading increases. To capture this effect, we require a characteristic loading at which the increases start. This is accomplished most naturally within the model by defining a characteristic loading θ_a , which satisfies

$$\theta_a = \theta_0 + \frac{1}{2u} \ln \frac{j_{V0}}{rj_{T0} [1 + a(0.60)]} \quad (12)$$

With this definition, the parameter w is fitted to be 6.0×10^5 . This model seems to account well for the data of Green and Britz [6] up to 50 mA/cm².

5. Effects at higher current density

The model discussed above seems to be capable of extending the hydrogen/deuterium evolution reaction model to current densities up to about 50 mA/cm². To go higher in current density, we require further modifications of the model, for which there is even less consensus.

To proceed, we focus on three relevant experimental observations. The first is that the loading curves as a function of current density generally become flat with increasing current [9], and can show a decrease in

loading at current densities approaching 1 A/cm² [14]. A reversible decrease in the loading cannot be accounted for by the model above that we introduced to account for lattice expansion effects. The second observation is that the Tafel plot (overpotential as a function of current density) can show a distinct change of slope at higher current density [15]. This effect can also be seen in the data of Ref. [14]. The third observation of interest here is that the catalytic activity of Pd and other catalysts is strongly dependent on the local surface morphology, so that atoms on edges and corners are more active [16]. There is a growing literature on this issue, but we have so far not found papers yet which consider this effect specifically in the case of the Volmer reaction.

We consider first the overpotential anomaly as reported by Bockris et al [15]. In the Bockris measurement, the (negative) overpotential is seen to increase with current density at a rate of 157 mV/decade of current density between 20 μA/cm² and 5 mA/cm². At higher current density, the slope changes to 357 mV/decade. In essence, more overpotential is required to maintain the electrochemical current density. In the data of Akita et al [14], the same effect is observed, except that the slope increases near 100 mA/cm².

What physical process is capable of changing the slope on a Tafel plot? Usually a change of slope signals the onset of a different reaction becoming important. Such an interpretation doesn't work here because the slope increases rather than decreases. If the slope had decreased instead, then a plausible explanation is that the relative strength of a different reaction increased compared to the Volmer reaction, overtaking it at more negative overpotential where the current density is higher.

For the slope to increase, we need instead some mechanism that makes it harder to get the current to flow as the current increases. Perhaps the simplest approach is to assume that sites at which the Volmer reaction occur are getting blocked, so that more overpotential is needed to support a higher current per unit site at the remaining unblocked sites.

We can show that this approach can work in principle through a simple example. Assume that whatever blocks the active sites has an adsorption isotherm something like that of lithium given above in Equation (10). In the limit that the blocking is sufficiently efficient that most of the sites are occupied, the number of unblocked sites is exponential in the overpotential

$$1 - \theta - \theta_{Li} = \frac{\theta_{Li}^2 e^{2v\theta}}{C[Li^+]} e^{(1-\beta_{Li})f\eta} \quad (13)$$

The current density of the Volmer reaction in this limit would then acquire a different dependence on the overpotential

$$j_V = rj_{V0} \left(\frac{1 - \theta - \theta_{Li}}{1 - \theta_0} \right) e^{-(1-\beta_V)f\eta} \rightarrow \frac{rj_{V0} \theta_{Li}^2 e^{2v\theta}}{(1 - \theta_0) C[Li^+]} e^{-(\beta_{Li} - \beta_V)f\eta} \quad (14)$$

In this limit, there will be an increased value for the change in overpotential per decade of current, as long as β_{Li} is greater than β_V . The increased slope in this model would be matched to the difference in asymmetry parameters

$$\beta_{Li} - \beta_V = \frac{\ln 10}{0.357f} = 0.167 \quad (15)$$

In our two-parameter fit of the Yamazaki data using the Green and Britz overpotential numbers, we obtained 0.53 for β_{Li} . But β_{Li} would need to be about 0.66 to be consistent with the measurements of Bockris et al given this interpretation. An approximate fit to the Yamazaki data is possible if such a large value for β_{Li} is assumed.

Now, the amount of lithium computed to be absorbed near the surface is in the few per cent range, so that we would not expect complete coverage. However, suppose that the Volmer reaction occurs primarily at edge or corner sites, and suppose further that these sites are also targets for adsorbed lithium, then this mechanism could account for the Bockris and Akita observation. If so, then the offset in current density where the slope changes could be related to the number of active Volmer sites.

There remains the question of why the loading is reduced at high current density. Given the picture above, one might conjecture that inhomogeneities are responsible for loss of loading at high current density. The basic problem with the Heyrovsky mechanism in this model is that the Heyrovsky current density has such a strong dependence on the loading. But if we assume that the loading is high close to a small number of active Volmer sites, then the local loading might be high, leading to the appearance of a Heyrovsky current density that is not connected with the average bulk loading.

6. Conclusions

We have described issues involved in the development of a new electrochemical model to describe the loading of Pd cathodes in the Fleischmann-Pons experiment. The basic hydrogen/deuterium evolution reaction kinetics model fails in this case, and we are working to develop a modified version of the model which works better. To account for the data, we have to assume that D₂ molecules are formed at internal surfaces inside that cathode. The loss of this gas is responsible according to the new model for the low loading observed in most cathodes in early experimental work. Lithium is adsorbed on the surface, and can be fit using an adsorption isotherm that results from a balance between Li⁺ deposition and the lithium water reaction. The change in slope observed at high loading is attributed in the model to a blocking of a limited number of active Volmer sites by lithium (or perhaps by some other impurity that is adsorbed as a singly charged species). The decrease in loading is conjectured to be caused by a modified Heyrovsky current density that depends on local high loading near active Volmer sites. These modifications address the primary experimental issues, and it remains to develop connecting relations between the adsorbed and absorbed deuterium and lithium fractions.

7. References

- [1] M.C.H. McKubre, S. Crouch-Baker, A.M. Riley, S.I. Smedley, *Proceedings of ICCF3*, Nagoya, 1992, Nagoya, edited by H Ikegami, page 5 (Universal Academy Press, Tokyo, 1993).
- [2] M.C.H. McKubre, S. Crouch-Baker, R.C. Rocha-Filho, S.I. Smedley, F.L. Tanzella, T.O. Passell, J. Santucci, *J Electroanal. Chem.* **368** 55 (1994).
- [3] M.C.H. McKubre and F.L. Tanzella, *Proceedings of ICCF12*, Yokohama, edited by A Takahashi, K.-I. Ota, and Y Iwamura, page 392 (World Scientific, Singapore, 2005) .
- [4] S. Szpak, C.J. Gabriel, J.J. Smith, and R.J. Nowak, *J. Electroanalytical Chem.* **309** 273 (1991).
- [5] W.-S. Zhang, X.-W. Zhang, and H.-Q. Li, *J. Electroanalytical Chem.* **434** 31 (1997).
- [6] T. Green and D. Britz, *J. Electroanalytical Chem.* **412** 59 (1996).
- [7] E. Gileadi, *Electrode kinetics for chemists, chemical engineers, and materials scientists*, Wiley-VCH (1993).
- [8] J. H. Chun and K. H. Ra, *J. Electrochem. Soc.* **145** 3794 (1998).
- [9] E. Storms, *J. Alloys and Compounds* **268** 89 (1998).
- [10] T. A. Green and T. I. Quickenden, *J. Electroanalytical Chem.* **368** 121 (1994).
- [11] O. Yamazaki, H. Yoshitake, N. Kamiya, K. Ota, *J. Electroanalytical Chem.* **390** 127 (1995).
- [12] H. Uchida, M. Sato, W. Cui, T. Tabata, M. Kumagai, H. Takano, and T. Kondo, *J. Alloys and Compounds* **293-295** 30 (1999).
- [13] W.-S. Zhang, private communication.
- [14] H. Akita, Y. Tsuchida, T. Nakata, A. Kubota, M. Kobayashi, Y. Yamamoto, N. Hasegawa, N. Hayakawa, and K. Kunimatsu, *Proceedings of ICCF4*, Lahaina, 1993, edited by T.O. Passell, page 21-1 (EPRI, Palo Alto, 1994).
- [15] J.O'M. Bockris, D. Hodko, and Z. Minevski, *Proceedings of ICCF2*, Lake Como, 1991, edited by T. Bressani, E. Del Giudice, and G. Preparata, page 337 (Italian Physical Society, 1991).
- [16] R. Narayanan and M.A. El-Sayed, *Nano Letters* **4** 1343 (2004).

New approaches to isoperibolic calorimetry

M.H. Miles¹ and M. Fleischmann²

¹*Dixie State College, St. George, UT 84770, U.S.A.*

²*Bury Lodge, Duck Street, Tisbury, Salisbury, Wilts SP3 6LJ, U.K.*

Email: melmiles1@juno.com

Abstract. Relatively inexpensive isoperibolic calorimeters have been designed and constructed with the goal of obtaining a constant heat transfer coefficient that is insensitive to normal changes in the electrolyte level during electrolysis. Four prototypes were constructed from copper tubing and used different insulating materials. Preliminary tests on two of these new calorimeters show excellent stability for the cell temperature measurements, stable heat transfer coefficients during electrolysis, and precise power measurements.

1. Introduction: design considerations for isoperibolic calorimeters

An important goal for isoperibolic calorimeters is a constant heat transfer coefficient that does not change as the electrolyte level decrease due to the electrolysis and evaporation. All measurements could then be evaluated with a single, predetermined value for the heat transfer coefficient. The placement of the thermistors in a secondary compartment outside the cell has been shown to minimize the cell electrolyte level effect [1-4]. This type of calorimeter can then be modeled as a fluid in which the electrochemical cell serves as a heating element for the substance in the adjacent compartment.

The size of the calorimetric system must be carefully considered in the design. Large systems give slower electrolyte level changes along with larger heat capacities and time constants. Small calorimetric cells yield faster electrolyte level changes and smaller heat capacities and time constants, but their small cell volumes require more frequent makeup of H₂O or D₂O additions. The heat transfer coefficient will also increase with the surface area of the calorimetric system. Adequate stirring of the cell contents by the electrolysis gases requires thin, tall cells where the cell diameter does not exceed 3 or 4 cm. All these factors were carefully considered in selecting design features for these new isoperibolic calorimeters.

2. Experimental details of the calorimetric design

Four prototype isoperibolic calorimeters (A, B, C, D) have been constructed from commercial copper tubing and copper end caps, and two (A, B) have been tested. Each calorimeter consisted of two completely isolated copper cylinders. The outer copper cylinder for each calorimeter had a 5.1 cm (2.0 inch) diameter and a 28 cm height. The inner copper cylinder (3.2 cm x 20 cm) was completely separated from the outer cylinder by the insulating material consisting of either pipe foam insulation (Cell A) or of tightly packed Oregon timber sawdust (Cell B). The glass electrochemical cell (2.5 cm x 20 cm) was a large commercial glass test tube (Kimax). This test tube cell was positioned inside the inner copper cylinder and filled 2/3 full using 50.0 mL of the selected electrolyte. Two thermistors were positioned on opposite sides of the outer wall of the glass tube with each thermistor level with the center of the cathode used. Thermal contact between the glass cell and the inner copper tube was provided by Mobil-1 (5W-30W) synthetic motor oil (50 mL) as the heat conducting fluid. This Mobil-1 oil has a reported density of 0.80 g/mL at 15°C and a heat capacity of 2.10 J/g.K at 80°C. This 50 mL of Mobil-1 oil filled the secondary chamber well above the cell electrolyte level. It is expected that this calorimetric design will provide for high cell operating temperatures up to the boiling point of the selected electrolyte solution. Photographs of the calorimetric cell and experimental arrangements are available electronically (http://iccf15.frascati.enea.it/ICCF15-PRESENTATIONS/S1_O9_Miles.pdf).

3. Review of equations for isoperibolic calorimetry

The mathematical equations that model isoperibolic calorimetry have been fully presented elsewhere [5-8], thus this will only be a brief review. The fundamental modeling equation is

$$P_{calor} = P_{EI} + P_H + P_X + P_C + P_R + P_{gas} + P_W \quad (1)$$

where these individual power terms have all been defined elsewhere [5-8]. Equation 1 represents a differential equation because

$$P_{calor} = C_p M dT/dt \quad (2)$$

where $C_p M$ is the heat capacity of the total calorimetric system expressed in terms of the heat capacity (C_p) and the equivalent moles (M) of H₂O or D₂O.

It is useful in initial calculations to assume that there is no anomalous excess power, $P_X=0$, thus Eq. 1 becomes

$$P_{calor} = P_{EI} + P_H + 0 + P_C' + P_R + P_{gas} + P_W \quad (3)$$

The simple subtraction of Eq. 3 from Eq. 1 yields

$$0 = P_X + P_C - P_C' = P_X - k_C \Delta T + k_C' \Delta T \quad (4)$$

or

$$P_X = (k_C - k_C') \Delta T \quad (5)$$

where $\Delta T = T - T_b$. Therefore, the difference between the true conductive heat transfer coefficient (k_C) and the pseudo heat transfer coefficient (k_C') obtained by assuming $P_X = 0$ provides for a simple calculation of the actual excess power via Eq. 5. All of the power terms in Eq. 1, however, should be considered in the determination of k_C' .

4. Initial experimental results

The use of this new isoperibolic calorimetric design requires the evaluation of the conductive heat transfer coefficient, k_C , and the heat capacity, $C_p M$, of the calorimetric system. Several experiments using H₂O control electrolytes yielded $k_C = 0.164$ W/K for Cell A and $k_C = 0.133$ W/K for Cell B. These cells differ only by the use of foam insulation in Cell A and packed sawdust insulation in Cell B.

The experimental cooling curve obtained by simply turning off the cell current provides a convenient method for determining the heat capacity, $C_p M$, of the calorimetric system. For a H₂O control experiment at zero current, Eq. 1 becomes

$$C_p M dT/dt = -k_C (T - T_b) \quad (6)$$

This differential equation can be rearranged to

$$dT/(T - T_b) = -(k_C/C_p M) dt \quad (7)$$

and then integrated to yield

$$-\ln (T - T_b) / (T_0 - T_b) = (k_C/C_p M) t \quad (8)$$

This integrated equation is of the form $y = mx$ where the slope (m) is given by $m = k_C/C_p M$.

The experimental cooling curve for Cell B using a H₂O control is present in Figure 1 where T_2 is the cell temperature measured by thermistor 2. This figure shows the expected exponential decrease of $T_2 - T_b$ with time. Figure 2 shows the same data using the integrated Eq. 8. The slope $m = 0.01752 \text{ min}^{-1} = 2.920 \times 10^{-4} \text{ s}^{-1}$. Therefore $C_p M = k_C/m = 456$ J/K. The heat capacity of the system can also be calculated using the differential equation (Eq. 6) directly, but this is considerably less accurate because of the estimate of dT/dt . From Eq. 6, $C_p M = -k_C (T - T_b) / dT/dt$. Table 1 presents the value for $C_p M$ obtained directly from Figure 1 at 10, 30, and 65 minutes. The three values calculated for $C_p M$ range from 427 J/K to 485 J/K with a mean of 457 ± 29 J/K. It is obvious that more

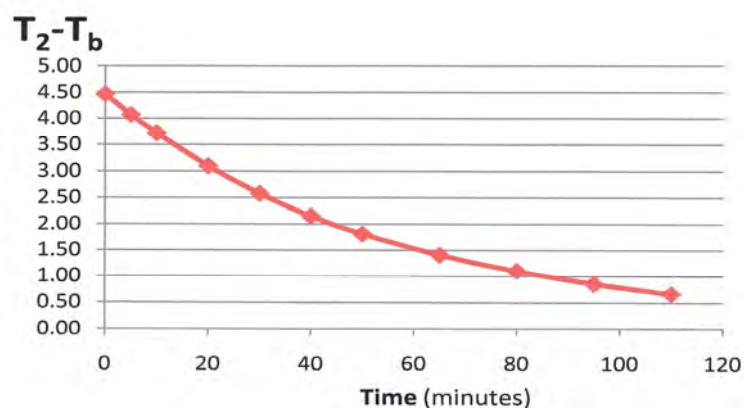


Fig. 1. - Experimental cooling curve for Cell B.

Table 1. Heat capacity (C_pM) for Cell B calculated from the cooling Curve of Fig. 1 using the differential equation (Eq. 8).

T (minutes)	dT_{cell} / dt (K/min)	T - T _b (K)	C_pM (J/K)
10	-10.8×10^{-4}	3.72	458
30	-8.03×10^{-4}	2.58	427
65	-3.87×10^{-4}	1.41	485
Mean $C_pM = 457 \pm 29$ J/K			

accurate results for C_pM are obtained by use of the integrated equation (Eq. 8) where the results can be displayed in a straight line form (Fig. 2). The same is true for all isoperibolic calorimetric results using Eq. 1. Numerical integration of the experimental calorimetric data along with casting them into the straight line form, $y=mx+b$, gives the most accurate results as previously reported [6-9].

The heat capacity of the cell can also be estimated by considering the heat capacity of all materials in the cell or in contact with the cell that undergo the same temperature changes. These calculations give 200 J/K for the 50.0 mL of H₂O used, 133 J/K for the 344 g of the inner copper cylinder, 84 J/K for 50 mL of Mobil-1 oil, 38 J/K for 52 g of the glass cell, and 3 J/K for the copper cathode, platinum wire, palladium and nickel present. The calculated total of 458 J/K is close to the measured value for C_pM .

The time constants for Cells A and B can be readily calculated once k_C and C_pM are known because $\tau = C_pM/k_C$. This yields $\tau = 3420$ s or 57 minutes for Cell B and 46 minutes for Cell A.

It should be noted that cooling curves such as Fig. 1 and 2 provide a useful method for determining lingering excess power effects or “heat-after-death” when electrolysis ceases in active D₂O/Pd experiments. Cell cooling that departs from Eq. 8 or Fig. 2 would be readily apparent. Such studies of cooling curve behavior is planned for future D₂O/Pd experiments. A previous study of Pd-B/D₂O in a Dewar type cell showed marked deviations from the expected cooling curve behavior (see pp. 22-23 and Figs. A.23 and A.24 of Ref. 6).

Although potassium nitrate (KNO₃) has been widely used for years by electrochemists as an inert supporting electrolyte, it has been proposed that shuttle reactions involving nitrates may give false excess power effects [10]. Theoretically, the nitrate ion may be reduced at the cathode to form various gaseous nitrogen oxides, nitrite ions (NO₂⁻), or even N₂ or NH₄⁺. With the use of special electrocatalysts and conditions, some electrochemical reduction of nitrates is possible [11]. In molten nitrates (LiNO₃-KNO₃) at elevated temperatures (250°C), there exists a large 4.5 V electrostability region between the reduction of lithium ions and the oxidation of nitrate ions [12, 13]. This demonstrates the stability of the nitrate ion even at high temperatures. This extreme anodic limit for the nitrate melt is the oxidation of the nitrate ion, $\text{NO}_3^- \rightarrow \text{NO} + \text{O}_2 + \text{e}^-$, followed by the further reaction of NO with oxygen to form brown NO₂ gas [12].

Because of the proposed shuttle reactions involving nitrates [10], an initial study using this new isoperibolic calorimeter was the investigation of 0.154 M KNO₃ in Cell B. This study used a platinum wire cathode

(1mm x 15mm) and a platinum coil anode. The $\text{H}_2\text{O} + 0.154 \text{ M KNO}_3 / \text{Pt}$ system was investigated over several days of electrolysis at currents of 80, 100, and 150 mA. These were no measurable excess power effects. The correct value of $k_C' = 0.133 \text{ W/K}$ was obtained using Cell B and assuming $P_X = 0$. Therefore $k_C - k_C' = 0$ and $P_X = 0$ from Eq. 5. Recent cyclic voltammetric studies on $\text{KNO}_3 + \text{NaNO}_2$ have confirmed that there are no reversible reactions involving nitrates or nitrites that could act as shuttle reactions.

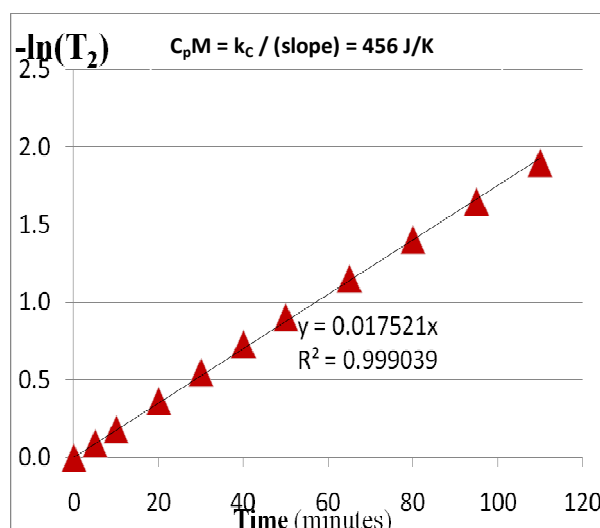


Fig. 2. - Cooling curve data of Fig. 1 using the integrated equation where $-\ln(T_2)$ represents the left-hand side of Eq. 8.

The measured pH of the 0.154 M KNO_3 solution, however, changed from near neutral initially ($\text{pH} = 7.02$) to $\text{pH} = 10.24$ at the end of this study. Any electrochemical reaction of a NO_3^- ion to form a neutral product such as N_2H_2 or N_2 results in the production of OH^- ion to maintain electroneutrality. For the total of 27,626 coulombs used in this study, the observed pH change could be explained by 0.003% of the current being consumed by the reaction of NO_3^- . Therefore, 99.997% of the current was consumed by the expected H_2O electrolysis. The electrochemical reaction of nitrates would, therefore, change the thermoneutral potential (E_{H}) by only $4.4 \times 10^{-5} \text{ V}$. At the highest current used (150 mA), this nitrate reaction would give a calorimetric error of $(4.4 \times 10^{-5} \text{ V})(0.150 \text{ A}) = 6.6 \times 10^{-6} \text{ W}$ or less than 0.007 mW. Therefore, based on this study of 0.154 M KNO_3/Pt , the use of KNO_3 as an inert electrolyte in calorimetric studies would be justified. In a related experiment using 0.158 M $\text{KNO}_3 + 0.0577 \text{ M NaNO}_2$, 99.992% of the current (90,720 coulombs) was consumed by H_2O electrolysis. There are no shuttle reactions involving nitrates or nitrites that would give a false excess power effect. In both experiments, the volume of H_2O consumed was larger than the theoretical amount based on Faraday's Law.

This new calorimeter was also used to study the 0.15 M $\text{NH}_4\text{Cl} + 0.15 \text{ M NH}_4\text{OH} + 0.025 \text{ M PdCl}_2$ co-deposition system in H_2O . Complete results are given elsewhere [14]. In this case, a chemical excess power effect was detected early in the experiment due to the solution becoming acidic ($\text{pH} = 1.25$) resulting in chlorine evolution and the formation of nitrogen trichloride (NCl_3). Similar excess power effects were measured by NRL for this same system using a Seebeck calorimeter [15]. With further electrolysis, the solution becomes more basic, chlorine evolution ceases, the NCl_3 dissipates, and normal calorimetric results are observed [14].

In a new study, $\text{NH}_4\text{Cl} + \text{NH}_4\text{OH} + \text{PdCl}_2$ co-deposition was repeated, but following the palladium co-deposition onto a copper cathode, sufficient LiOH was added to maintain a basic pH. This provided a very stable electrolysis system with no chlorine or NCl_3 formation. The electrolysis of this system using a high current of 400 mA gave evidence for a stable cell constant that was independent of the electrolyte level. The results for this study in Cell B is given in Table 2. The mean cell constant over almost five hours of electrolysis was $\langle k_C \rangle = 0.1324 \pm 0.000069 \text{ W/K}$. The cell constant never varied by more than $\pm 0.0001 \text{ W/K}$ from the mean value. This is the best evidence to date for an isoperibolic calorimetric cell where the electrolyte level does not affect the cell constant. We were, therefore, successful in attaining our major goal for this new isoperibolic calorimeter.

Table 2. Calorimetric data summary for Cell B with I = 400 mA using the PdCl₂ + NH₄Cl + NH₄OH + LiOH electrolyte.

Time	-E _{cell} (V)	P _{El} (W)	ΔT ₂ (K)	k ₂ (W/K)
2:29	5.122	1.4564	11.000	0.1324
2:44	5.121	1.4560	10.995	0.1324
4:01	5.110	1.4516	10.970	0.1323
4:53	5.103	1.4488	10.935	0.1325
5:51	5.094	1.4452	10.915	0.1324
6:46	5.088	1.4428	10.900	0.1324
7:19	5.083	1.4408	10.890	0.1323

$$\langle k_2 \rangle = 0.1324 \pm 0.000069 (\pm 0.052\%)$$

5. Summary of results

New isoperibolic calorimeters that are relatively inexpensive have been designed, constructed, and tested using several different electrolyte systems. These calorimeters show stable heat transfer coefficients that do not change during electrolysis at high cell currents over long time periods.

Acknowledgements

Financial help in the design and construction of these new calorimeters is acknowledged by M.H.M. from an anonymous fund at the Denver Foundation via Dixie State College. Steve Tetz of Wolf Creek, Oregon performed the actual construction of the four calorimetric cells. The authors also thank William Wilson of DTRA and Michael Melich of the Naval Postgraduate School for their support of this work.

References

- [1] M.H. Miles, K.H. Park and D.E. Stillwell: *J. Fusion Energy* **9** 333 (1990)
- [2] M.H. Miles, K.H. Park and D.E. Stilwell: *J. Electroanal. Chem.* **296** 409 (1990)
- [3] M.H. Miles, B.F. Bush and D.E. Stilwell: *J. Phys. Chem.* **98** 1948 (1994)
- [4] M.H. Miles: *J. Electroanal. Chem.* **482** 55 (2000)
- [5] M. Fleischmann, S. Pons, M.W. Anderson, L.J. Li and M. Hawkins: *J. Electroanal. Chem.* **287** 293 (1990)
- [6] M.H. Miles, M. Fleischmann and M.A. Imam: *Calorimetric Analysis of a Heavy Water Electrolysis Experiment Using a Pd-B Alloy Cathode*, NRL/MR/6320-01-8526 (March 26, 2001)
- [7] M. Fleischmann and M.H. Miles: *Proceeding of ICCF-10*, edited by P.L. Hagelstein and S.R. Chubb, pp. 247-268 (Cambridge, 2003)
- [8] M.H. Miles and M. Fleischmann: *Low-Energy Nuclear Reactions Sourcebook*, edited by J. Marwan and S.B. Krivit, pp. 153-171, ACS Symposium Series 998 (2008)
- [9] M.H. Miles and M. Fleischmann: *Proceedings of ICCF-14* (Washington D.C., 2008) submitted
- [10] D.A. Kidwell: email communication (2009)
- [11] F.V. Andrade, L.J. Deiner, H. Varela, J.F.R. de Castro, I.A. Rodrigues and F.C. Nart: *J. Electrochem. Soc.* **154** F159 (2007)
- [12] M.H. Miles, J.R. Alston, A.J. Davenport and A.A. Grumet: *Low Melting Electrolytes for Thermal Batteries*, SBIR Phase I Final Report (October 31, 2007)
- [13] M.H. Miles: *Chloride-Free Thermal Batteries Using Molten Nitrate Electrolytes*, U.S. Patent No. 7,629,075 B2, December 8, 2009
- [14] M.H. Miles: *Proceedings of ICCF-15* (Rome, Italy 2009) submitted
- [15] D. Knies: email communication (2009)

Characteristics of Excess Heat in Pd|D₂O+D₂SO₄ Electrolytic Cells Measured by Seebeck Envelope Calorimetry

W.-S. Zhang

Institute of Chemistry, Chinese Academy of Sciences, P.O. Box 2709, Beijing 100190, China

E-mail: wszhang@iccas.ac.cn

Abstract. Pre-electrolysis at the boiling point in open Pd|D₂O cells is an effective method to activate a palladium cathode, which can produce excess power in subsequent electrolysis in closed systems for several months. The reproducibility is 23/45. Another characteristic of excess heat is the apparent resistance of electrolytic cell changes irreversibly with temperature.

1. Introduction

In previous works [1–3], anomalous excess thermal power in Pd|D₂O cells was observed using Seebeck Envelope Calorimetry (SEC). Two phenomena were found for reproducibility of excess heat. One is that the temperature increment during electrolysis must be high enough; otherwise no excess heat will be produced [2]. Another is that the second run always gives more excess heat than in the first under the same condition as shown in Table V in Ref. [2]. After reviewing the data of past experiments, it is found that the samples Pd-A and Pd-E in Ref. [2], which gave the maximum excess power (~ 1 W, about one order greater than others), have the same histories. Both of them had been electrolyzed at the boiling point in open cells due to mistakes (Exp. #041110 for Pd-A and Exp. #050829 for Pd-E). After that, these two samples become active in excess heat production in electrolysis. All these phenomena inspire the author to intentionally use pre-electrolysis at the boiling point in open cells to activate samples. Experimental results show that this procedure is effective to some extent as reported below. At the same time, it is found that the apparent cell resistance changes irreversibly with temperature when excess heat occurs.

2. Experimental set-up

Electrolytic cells used in most experiments described in this paper are modified versions of pervious experiments [3]. Copper tube leads were replaced with platinum wires to avoid contamination, and H₂SO₄ is replaced with D₂SO₄ for a similar reason. A schematic and a photo of the electrolytic cell are shown in Figs. 1(a) and 2(a), respectively. The cell is a cylinder of borosilicate glass (ϕ_{in} 42 × ϕ_{out} 45 × 142 mm³, capacity ~190 ml). A PTFE male cap has three parts: the top part is ϕ 41 × 4 mm² for fixing the cell by a metal frame as shown in Figs. 1(b) and 2(b); the middle part is a hexagonal prism with side length 32 mm and thickness 13 mm; the bottom part is ϕ 41 × 24 mm² with a groove of 4 mm width and 2.5 mm depth in the middle for O-ring. The O-ring (ϕ_{in} = 31.5 mm, width = 3.55 mm) made of nitrile butadiene rubber (NBR, resistant to acid) is used to seal the cap against the inner wall of glass cylinder. The cap has two holes, 1 mm diameter each and 20 mm apart, for the electrode lead wires. A PTFE plate (ϕ 41 × 8 mm²) is used to suspend the recombination catalyst. It has 57 holes of ϕ 2 mm to pass gases (D₂ and O₂) and vapors (D₂O). A PTFE rod (ϕ 6 × 40 mm²) is fastened to the perforated plate and the cap. This ensures that the perforated plate being at a fixed distance above the electrolyte. Before and after every electrolysis, the cell was weighed with a Mettler balance (PM1200, 0.001 g readability) since June 06, 2009 (Exp#090605). Before that time, cells were weighed only with chemical balances.

The metal frame is used to clamp the PTFE cap into the cell as shown in Figs. 1(b) and 2(b). These arrangements ensure that the electrolytic cell is a closed system. The metal frame and cell is partly embedded in a Styrofoam base (ϕ 15 × 12 cm²), which is placed in an enamel jar (ϕ 15 × 16 cm²). The enamel jar can weaken the impact of cell explosions in the calorimeter and prevent corrosion caused by

the acidic electrolyte after an explosion. Three explosions occurred during the past year. These were caused by incomplete recombination, due to variability in the effectiveness of the recombination catalyst. The polystyrene box shown in Fig. 2(b) of Ref. [3] was broken into pieces in one explosion (Exp. #090219) earlier this year.

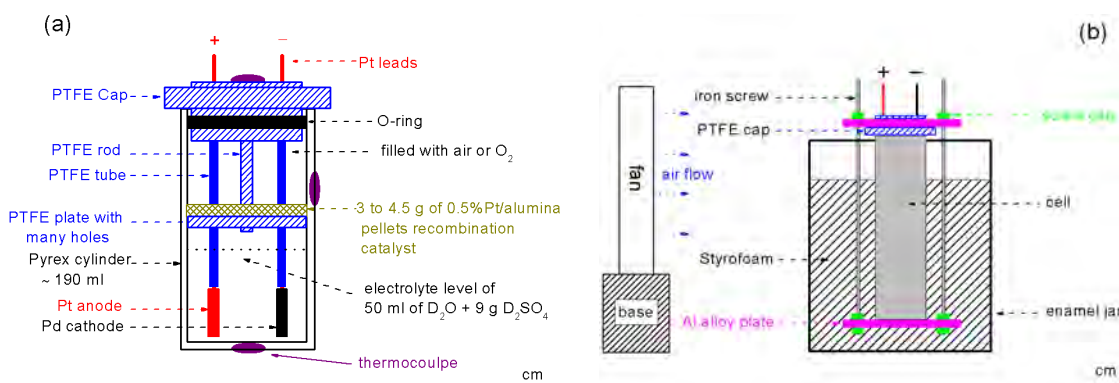


Fig. 1. - Schematics of electrolytic cell (a) and parts outside the cell (b).



Fig. 2. - Photos of bare electrolytic cell (a), cell in the SEC (b), fresh Pd #1 (c) and Pd#1 after electrolysis as cathode for 285 hours and anode for 14 hours at 3 to 3.5 A (d).

Four different palladium samples are used as listed in table 1. Both Pd #1 (see Figs. 2(c) and (d)) and #2, provided by John Dash, Portland State University, are from Alfa Aesar, Stock #11514, Lot #G15Q17, 99.9% purity. Pd #3 is from General Research Institute for Nonferrous Metals (GRINM), 99.95% purity. Pd #4, provided by Da-Lun Wang, Institute of Nuclear Physics and Chemistry, CAEP, is from Kunming Institute of Precious Metals (KIPM). All these samples are weighed using an Ohaus AR2140 balance. Before the first electrolysis, all Pd samples were immersed in concentrated sulfuric acid to remove surface contamination, and then washed with de-ionized water several times.

Table 1. Parameters of different palladium samples used in experiments.

Pd #	Exp. #	size / mm ²	area / cm ²	mass / g	source	metallurgical treatment
1	081220-091002	25 × 25 × 0.3	12.5	2.1891	Alfa Aesar	30% cold rolled
2	090219-090612	25 × 25 × 0.3	12.5	2.1831		
3	090620-090624	11 × 31 × 0.05	7.25	0.2271	GRINM	cold rolled
4	090625-090723	10 × 30 × 0.5	6.28	1.7836	KIPM	unknown

The anode is a platinum foil, 31 × 43 × 0.02 mm³ with area of 26.7 cm². Two electrode lead wires made of Pt (ϕ 0.8 × 145 mm²) are covered with heat-shrink Teflon tubing. The Pt foil and wires are from GRINM (99.95% purity). These were annealed for easy machining. Ethyl α -cyanoacrylate instantaneous adhesive (502 glue) is filled into the gaps between the leads and the cap in order to prevent escape of the off gases from electrolysis. The cap is cooled with flowing air during electrolysis to prevent the failure of the glue at high temperature, as shown in Fig. 1(b).

The electrolyte is ~ 50 ml heavy water mixed with 8 to 10 g D₂SO₄. Both deuterium reagents are from Beijing Chemical Reagent Company (> 99.9% isotopic purity). The quantity of recombination catalyst varied from 3 to 4.5 g (~ 60 to 90 pellets), depending on its history and the applied current. In some cases, O₂ gas at 1 atmosphere is flowed into the cell to accelerate catalysis.

The calorimeter, power supply and data logging system are the same as before [3–5]. These will not be discussed here, except for some recent modifications.

3. Experimental results

3.1. Calibration of calorimeter and contrast experiments

The calibration was conducted with a 3.6 Ω electric heater, starting on May 19, 2009 (Exp. #090519). The heater is made of Tophet® alloy A wire (ϕ 0.3 mm) wound around cylindrical heat sink fins, which are located at the center of the measuring vessel of the calorimeter. The calorimeter was calibrated from 2 to 50 W (55 sets of data) 16 times in 13 months. It gives good stability and linearity between thermal powers and responses, as shown in Fig. 3(a) and the simulation equation (1) below:

$$P = -0.0355 \pm 0.0161 + (5.8961 \pm 0.0118)E - (0.0020 \pm 0.0016)E^2 \quad (1)$$

with $\chi^2 = 0.1661$, $R^2 = 0.9997$, mean square = 0.0031. P is the input power in Watts and E is the output electromotive force of the SEC in Volts. This equation gives less accuracy than in Ref. [3] because the period is more than one year. Fluctuations of room temperature at different seasons affect the long term precision; however this calorimeter is calibrated every 2 to 3 weeks during experiments and it is enough accurate to give the real signal of excess power within the error of 20 mW for every calorimetry.

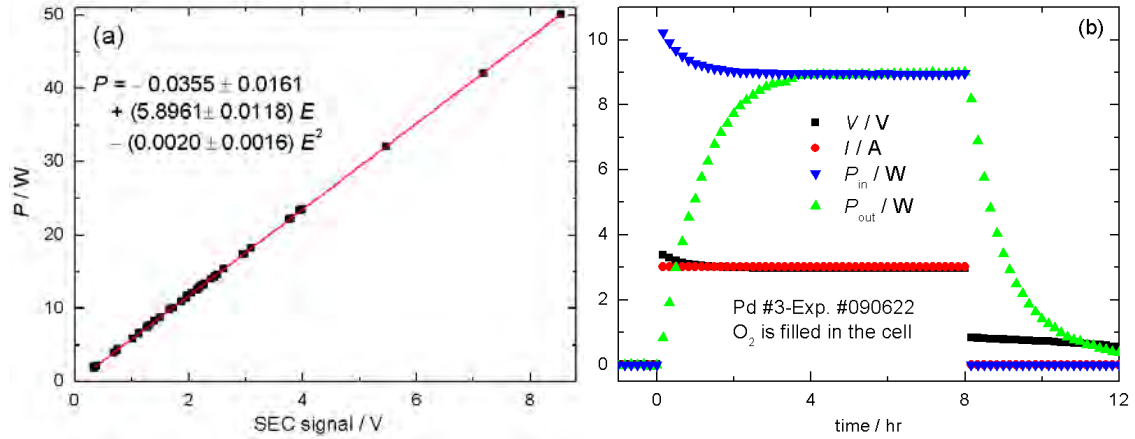


Fig. 3. - (a) Calibration of the calorimeter from 2 to 50 W, 55 sets of data, in 13 months; (b) Comparison of input electrolytic power with output thermal power of a Pd-D₂O cell. The fan's power is deducted from the total power.

Before presentation of anomalous excess heat, sample experiments are introduced to demonstrate the accuracy of the calorimetry and the reality of excess heat afterwards. Three types of experiments, i.e. Pt-D₂O, Pd-H₂O and dead Pd-D₂O electrolytic systems, were carried out. Each of them has only one component, i.e. cathode or electrolyte, being replaced with that in the active cell. All of Pt-D₂O (Pt cathode is a foil of 22 × 28 × 0.02 mm³) and Pd-H₂O systems were designed for contrast and did not give excess heat as shown in table 2. The inactive Pd cathodes also did not give excess heat especially for Pd #3 and #4.

Table 2. Parameters of different sample experiments carried out at 25 °C, 3 A.

Pd#-Exp#	system	t / hr	P_{in} / W*	P_{ex} / mW	Q_{in} / kJ*	Q_{ex} / kJ	Δm / g	$Q_{ex} + \Delta H$ / kJ
Pt-090824	Pt-D ₂ O	7	10.819(7)	1±24	278.20(6)	-0.29±1.25	0.084	0.95±1.26
1-091002	Pd-H ₂ O	9	8.824(4)	6±29	287.98(6)	-0.51±1.16	0.038	0.06±1.17
3-090622	Pd-D ₂ O	8	8.956(3)	0.4±26	262.38(5)	-0.55±0.90	0.022	-0.22±0.90

* The number in one set parentheses is the uncertainty of the last figure of the quantity before the parentheses.

Fig. 3(b) shows an example of calorimetric results for dead-Pd-D₂O electrolysis. The input and output powers are $P_{in} = 8.9556 \pm 0.0029$ and $P_{out} = 8.9552 \pm 0.0264$ W, respectively, during the steady state (5 to 8 hours of electrolysis time). They are consistent with each other within 0.004% although the calorimetric error is 0.29%. The input, output and excess energies are $Q_{in} = 262.38 \pm 0.05$, $Q_{out} = 261.83 \pm 0.88$ and $Q_{ex} = -0.55 \pm 0.90$ kJ, respectively. The mass loss of the cell in this run is $\Delta m = 0.022$ g. If this loss was caused by poor catalytic recombination, the corresponding energy correction (enthalpy change) is $\Delta H = 0.33 \pm 0.03$ kJ. The output energy after correction is $Q_{out} + \Delta H = 262.16 \pm 0.90$ kJ; the resulting excess energy is $Q_{ex} + \Delta H = -0.22 \pm 0.90$ kJ, corresponding to $(-0.08 \pm 0.34)\%$ of the input energy. It means

there was no excess heat produced in the electrolytic cell and this calorimeter gave good accuracy (better than 0.1%) at power around 9 W running for 8 hours. Because this calorimeter is designed for power measurement, it gives higher precision for power than for energy, as shown in table 2.

3.2. Excess heat

As mentioned in the Introduction, effects of pre-electrolysis on excess heat are the main objective of this work. Seven runs with pre-electrolysis were carried out for 4 samples as shown in table 3. An example is shown in Fig. 4; this experiment was conducted at the end of 2008 using the cell described in Ref. [3]. Pd #1 was activated by pre-electrolysis on Dec. 20, 2008. The applied current was increased step by step: firstly 3.5 A for 2 hr, then 3.7 A for 1.5 hr and 3.9 A for 1 hr, 4 A for 0.5 hr at the end, as shown in Fig. 4(a). During the pre-electrolysis, the cell temperature was increasing and the electrolyte was boiling. The electrolyte level was lowering and the cathode surface was becoming exposed to the air. On the second day (Exp. #081221), more heavy water was added, and the cell was closed and electrolyzed. However, the excess heat was uncertain because of a poor seal and a great mass loss of 17.3 g. Two days later (Exp. #081223), the system was tested again and excess power was produced, as shown in Fig. 4(b). After electrolysis for 3 hr at 3 A, the calorimeter showed excess heat and its amplitude reached the maximum value of $P_{ex,max} = 220 \pm 16$ mW in 4.5 to 5 hr. After 5 hr electrolysis, P_{ex} keep the steady value of 120 ± 18 mW till the end of this experiment. In this experiment, there was no mass loss, within the error of measurement.

Another example for sample Pd #2 is shown in Fig. 5. The current applied during pre-electrolysis was: firstly 3.5 A for 3 hr, then 3.7 A for 1 hr, 3.9 A for 1.3 hr, 4 A for 2.7 hr at the end, as illustrated in Fig. 5(a). Four days later, calorimetry with a closed cell was carried out. This sample gave excess power of $P_{ex} = 0.120 \pm 0.020$ W during 5 to 6 hr of electrolysis, as shown in Fig. 5(b).

Table 3. Summary of pre-electrolysis and subsequent excess heats.

Pd #	pre-electrolysis			excess heats			total reproducibility
	Exp. #	I_{max} / A	$T_{max} / ^\circ C$	Exp. #	$P_{ex,max} / mW$	reproducibility	
1	081220	4	110	081223	220 ± 16	8/15	17/35
	090808	4.5	97	090810	146 ± 24	4/4	
	090814	3	98	090828	66 ± 24	3/8	
	090915	4.5	108	090916	17 ± 22	0/1	
	090917	4.5	145	090919	31 ± 22	0/2	
	090921	4.5	127	090922	20 ± 15	0/1	
	090923	4.2	114	090927	152 ± 24	2/5	
2	090521	4	99	090525	120 ± 20	6/10	6/10
3	090620	3	97	090621	5 ± 24	0/3	0/3
4	090629	3	99	090721	3 ± 13	0/3	0/3

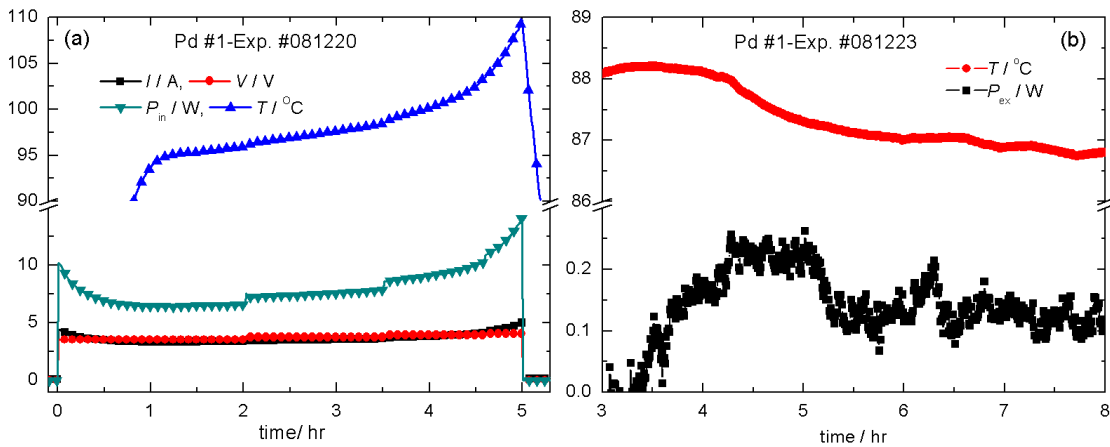


Fig. 4. - Example of effects of pre-electrolysis in an open cell in the first run on the excess heat production on the subsequent run in a closed cell. (a) Pre-electrolysis; (b) Excess power after activation. Parameters: $T_{SEC} = 25$ °C, 3 A \times 8 hr, $P_{ex,max} = 220 \pm 16$ mW (4.5 to 5 hr); $P_{ex,stable} = 120 \pm 18$ mW (7 to 8 hr), $Q_{ex} = 2.46 \pm 0.33$ kJ. The mass loss during electrolysis $\Delta m = 0.0 \pm 0.2$ g.

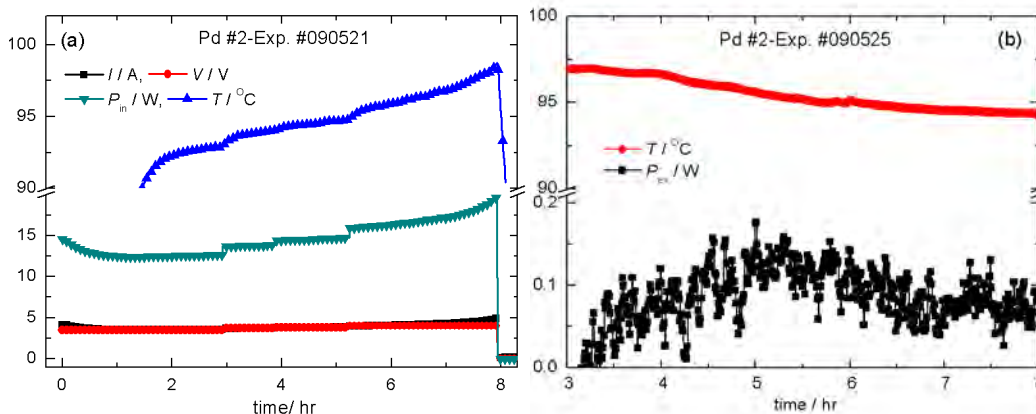


Fig. 5. - Another example of effects of pre-electrolysis in an open cell in the first run on the excess heat production in a closed cell in the subsequent run. (a) Pre-electrolysis; (b) Excess power after activation. Parameters: $T_{SEC} = 25\text{ }^{\circ}\text{C}$, $3\text{ A} \times 8\text{ hr}$, $P_{ex} = 120 \pm 20\text{ mW}$ (5 to 6 hr). The mass loss $\Delta m = 0.05 \pm 0.02\text{ g}$ is not included in calculation of excess power.

Not every pre-electrolysis for every sample can stimulate excess power in subsequent experiments, as shown in table 3. For sample Pd #1, the effective ratio of pre-electrolysis is 4/7. For the other 3 samples, only one pre-electrolysis was tested and only one sample gave excess power; therefore, further research is necessary to determine other unknown factors which affect reproducibility.

Besides pre-electrolysis, other methods were used in attempts to stimulate increased excess heat production. These include reverse current activation in pre-electrolysis (Exp. #090814, 090915, 090921 for Pd #1), modifying cell temperature through changing the thickness of Styrofoam layers shown in Fig. 1(b) (85 to 102 $^{\circ}\text{C}$, Exp. #090725 to #090731), stepwise increasing (ladder-like) current (Exp. #090825) were also tested to stimulate excess heat production as done before [1–3]; however, all these methods did not show clear evidence of positive effects. More work is needed.

From the history of Pd #1 shown in table 3, it seems excess heat from boiling-point electrolysis can be switched on or off like a light bulb. Another question is the lifetime of excess heat activity after pre-electrolysis. Pd #1 kept the activity for at least 7 months (Exp. #081220 to 090807). Sample Pd-A had kept the activity for at least 2 months (Exp. #041110 to #050111) and Pd-E kept the activity for at least 10 months (Exp. #050829 to #060706) in Ref. [2]. Therefore, pre-electrolysis should be an effective way to activate a Pd sample for several months.

3.2. Irreversible change of cell's resistance with temperature

During the emergence of excess heat, it was noticed that P_{ex} and cell temperature T approach to their maximum amplitudes and then decrease to the stable values as shown in Figs. 4(b) and 5(b). It means that

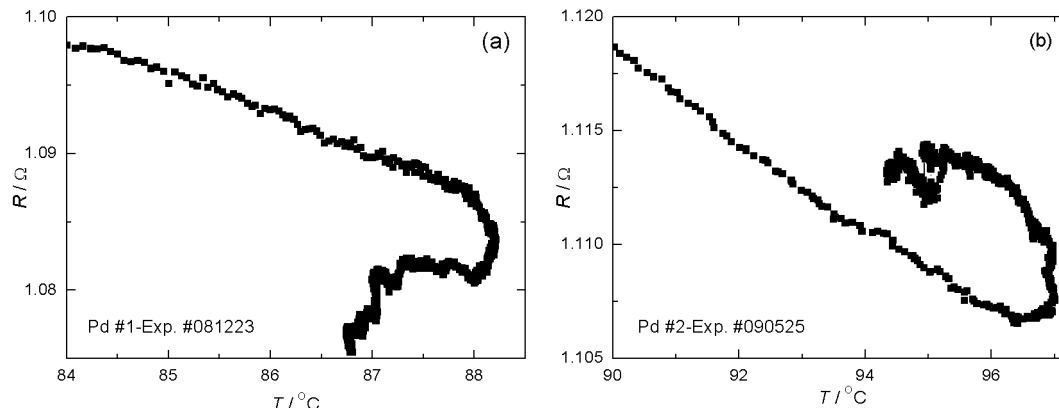


Fig. 6. - Apparent cell resistance R vs. temperature T for experiments in which excess power was produced.

increment of excess power is suppressed in electrolysis due to a changing cell parameter. This parameter is the apparent cell resistance R . R vs. T with excess heat is shown in Fig. 6 and without excess heat in Fig. 7. It is found that there is obvious irreversible change of R vs. T when excess heats occur. These results indicate this change can be a collateral evidence of excess heat besides the calorimetry. However, this irreversible change is not fully understandable and predictable at present; it may be negative or positive as shown in Fig. 6(a) and (b), respectively.

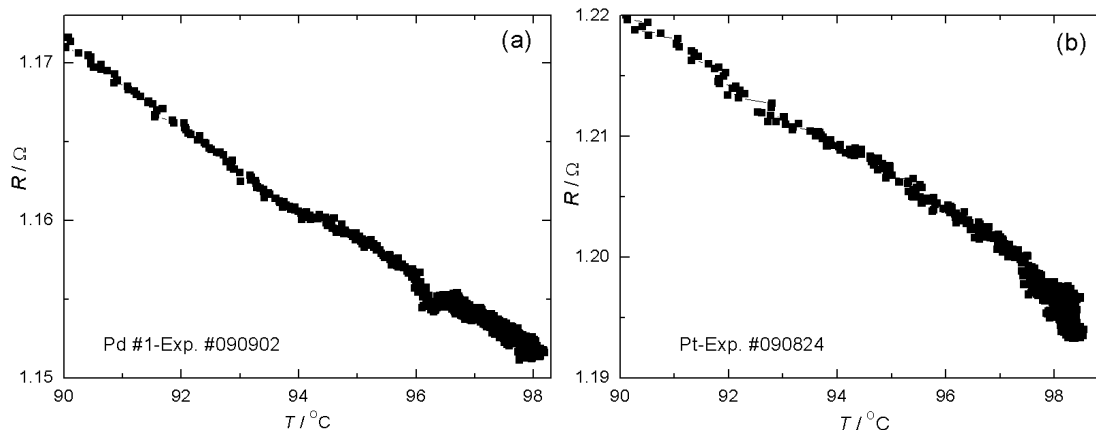


Fig. 7. - Apparent cell resistance R vs. temperature T without excess power.

4. Discussion

Pre-electrolysis activation of excess heat production reported here is similar to the heat-after-death effect observed by Fleischmann and Pons [6]; both situations work at the boiling point of the electrolyte. This phenomenon must be explainable by some mechanism which is activated by the high temperature. As concerns the irreversible change of cell resistance, it should be the intrinsic nature of excess heat because the state of cathode polarization must change in excess heat production at the cathode hot spots observed by Mosier-Boss and Szpak [7], and positive feedback of voltage and temperature observed by Fleischmann et al [8]. The author will study all these interesting phenomena in future work.

5. References

- [1] W.-S. Zhang, J. Dash, Q. Wang: *Condensed Matter Nuclear Science, Proceedings of the 12th International Conference on Cold Fusion*, Yokohama, Japan, Nov 27 to Dec 2, 2005. Edited by A. Takahashi, K.-I. Ota and Y. Iwamura, (World Scientific Pub., Singapore, 2006), p. 86.
- [2] W.-S. Zhang, J. Dash: *Proceedings of the 13th International Conference on Condensed matter Nuclear Science*, Dagomys, Sochi, Russia, June 25 to July 1, 2007. Edited by Y. Bazhutov, (Moscow, MATI, 2008), p. 202.
- [3] W.-S. Zhang, J. Dash, Z.-L. Zhang: *Proceedings of the 14th International Conference on Condensed matter Nuclear Science*, Washington DC, USA, Aug 8 to 10, 2008.
- [4] W.-S. Zhang: *China Patent Application # 200910085862*.
- [5] W.-S. Zhang: *Thermochim. Acta* (accepted)
- [6] M. Fleischmann, S. Pons: *Phys. Lett. A* **176** 118 (1993)
- [7] P.A. Mosier-Boss, S. Szpak: *Nuovo Cimento A* **112** 577 (1999)
- [8] M. Fleischmann, et al.: *J. Electroanal. Chem.* **287** 293 (1990)

Acknowledgments

Thanks to Prof. John Dash and Zhong-Liang Zhang for valuable discussions. This work was supported by NSFC (20673129 & 20973185), 973 Program of MOST in China (2009CB226113), Innovation Project of CMS (CMS-CX200816) and SRF for ROCS, SEM.

Investigations of co-deposition systems

M.H. Miles

Jacobs Technology, Inc., Naval Systems Group, Ridgecrest, CA 93555, U.S.A.

Email: melmiles1@juno.com

Abstract. Electrochemical studies of co-deposition show that the palladium deposited onto a copper substrate produces very high capacitance values (370 Farads/g) equal to those of supercapacitor materials. This large electrode capacitance causes a collapsing and tilting of the cyclic voltammograms that approaches Ohm's Law behavior. Results for the electrochemistry, chemistry, and calorimetry of the 0.025 M PdCl₂+0.15 M NH₄Cl+0.15 M NH₄OH system and its deuterium analog are reported.

1. Introduction: selection of co-deposition systems

The observation of Fleischmann-Pons effects (FPE) for co-deposition systems was first reported by Szpak and Mosier-Boss using the PdCl₂+LiCl/D₂O system [1, 2]. Improved reproducibility of the excess power effect was obtained with the PdCl₂+ND₄Cl+ND₄OD/D₂O system [3-5]. In fact, all three initial experiments using this ammonia-based system produced large excess power effects [3]. This system was selected because the H₂O analog is commonly used for commercial palladium plating [6]. However, the extended electrolysis at the higher currents required for FPE studies leads to a black dendritic hydride deposit, large pH changes, chlorine evolution, and other unknown processes in this ammonia-based co-deposition system.

2. Experimental methods used for investigations of co-deposition systems

Electrochemical studies included cyclic voltammetry (CVA), electrochemical impedance spectroscopy (EIS) and various galvanostatic methods. The solution pH was periodically measured using a pH meter (± 0.01 pH units). Commercial chlorine detectors were used to monitor the gases escaping from the cell. A new isoperibolic calorimeter was used to determine any excess power produced by the electrochemical cell [7].

3. High capacitance produced by co-deposited palladium

The 0.025M PdCl₂+0.15M NH₄Cl+0.15M NH₄OH/H₂O system was investigated at various stages of the co-deposition onto a copper cathode. Figure 1 shows the cyclic voltammogram after the initial co-deposition at -6.00 mA for two hours (43 coulombs). This trace shows the normal features of a palladium surface with PdO formation at 0.25V and PdO reduction at -0.48V along with probable palladium deposition at -0.90V. Hydrogen and oxygen evolution occurs at the negative and positive vertexes, respectively.

Further electrolysis at -6.00 mA for 28.45 hours, I= -20 mA for 22.70 hours, then I= -50 mA for 22.95 hours (6423 coulombs total) gradually gave the completely tilted and collapsed cyclic voltammogram presented in Figure 2. Furthermore, the pH changed from pH=8.87 for the initial solution to pH=1.25, and chlorine evolution was readily detected at this electrolysis stage.

The striking contrast between Figure 1 and 2 has been previously observed for supercapacitor materials [8]. As shown in the Appendix, the exact equation for cyclic voltammetric studies yields Ohm's Law, $I \approx E/R_s$, for extremely high electrode capacitances ($R_s C_d \gg t$). From the EIS measured cell resistance ($R_s=0.9945 \Omega$) and

the time for a single scan in Figure 2 ($t=38$ s), it is estimated that the electrode capacitance (C_d) must be at least 50 Farads (F) or about 370 F/g for the deposited palladium. Typically, electrode capacitances are about $50 \mu\text{F}/\text{cm}^2$, thus the deposited palladium has an effective surface area of 10^6 cm^2 . Chronopotentiometry was used to confirm the unusually large RC time constant for the palladium deposited onto the copper cathode [8]. Similar experiments were conducted on the $\text{PdCl}_2+\text{LiCl}/\text{H}_2\text{O}$ co-deposition system and similar high capacitance values were observed. The electrochemical literature today relating to supercapacitor materials does not generally realize how large RC time constants distort cyclic voltammograms as shown in Figure 2 and explained in the Appendix.

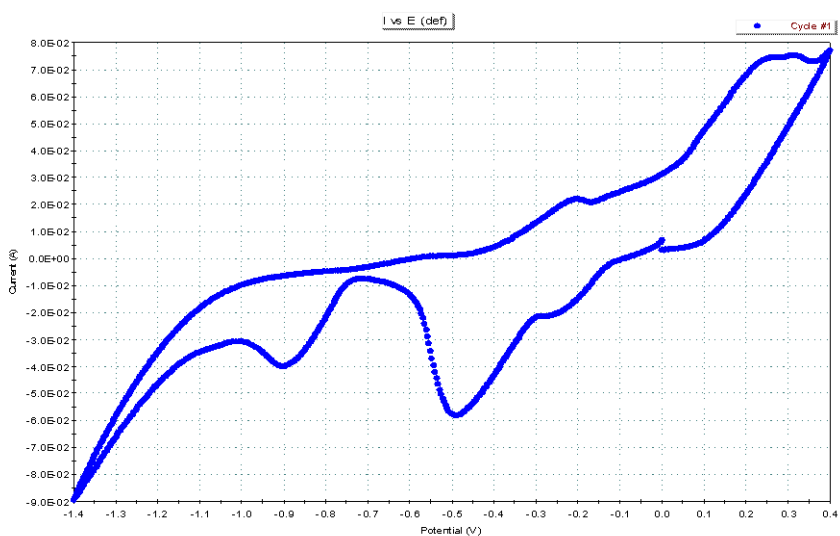


Fig. 1 - Early cyclic voltammetric study of co-deposition ($v = 50$ mV/s).

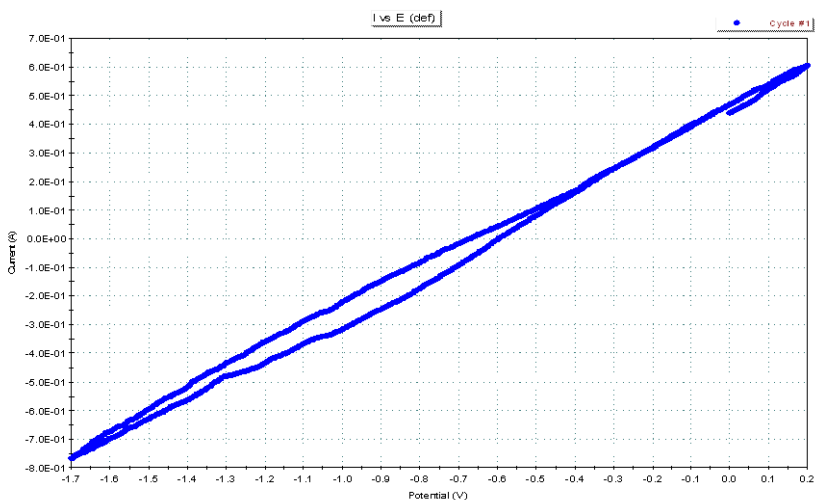
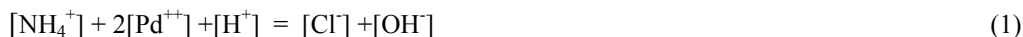


Fig. 2 - Later cyclic voltammetric study of co-deposition ($v = 50$ mV/s).

4. Complex chemistry of ammonia co-deposition system

Solution pH measurements were the key to unraveling the complex chemistry of the 0.025 M PdCl₂+0.15 M NH₄Cl+0.15 M NH₄OH co-deposition system. The electroneutrality expression for molar (M) ionic concentrations



along with the equilibrium $\text{NH}_4\text{OH} = \text{NH}_4^+ + \text{OH}^-$, $K_b = 1.81 \times 10^{-5}$ M, were also very useful. The reaction of palladium ions with NH₄OH produces insoluble palladium hydroxide



thus Pd⁺⁺ ions are initially replaced by additional ammonium ions (Eq. 1). The resulting low activity of palladium ions explains the stability of the copper cathode and other metals towards displacement reactions such as $\text{Cu} + \text{Pd}^{++} \rightarrow \text{Cu}^{++} + \text{Pd}$ in this initial solution. The cell reaction for the palladium deposition can be expressed as



with the solution remaining basic as observed experimentally. However, the generated electrolysis gases (H₂, O₂) gradually drive off the ammonia by the net reaction $\text{NH}_4^+ \rightarrow \text{NH}_3 + \text{H}^+$ and the solution becomes acidic, $[\text{H}^+] = 0.050$ M, pH = 1.30 from Eq. 1. Acidic solutions make chlorine evolution thermodynamically more feasible, and a portion of the cell reaction becomes



instead of H₂O electrolysis. A readily observable decrease in the cell voltage magnitude clearly defines when the solution becomes acidic and chlorine evolution commences as also shown by chlorine detectors.

The introduction of chlorine into an acidic NH₄Cl solution is known to produce nitrogen trichloride, $\text{NH}_4\text{Cl} + 3 \text{Cl}_2 \rightarrow \text{NCl}_3 + 4 \text{HCl}$. The net electrochemical cell reaction for this NCl₃ production is



with hydrogen formed at the cathode. The enthalpy change for this reaction is 864 kJ/mol, thus the thermoneutral potential for Eq. 5 is nearly the same as for water electrolysis (1.49 V vs. 1.48 V). The consumption of acidic HCl by both Eqs. 4 and 5 produces an increase in the pH and an end to the Cl₂ and NCl₃ production. Therefore, only normal water electrolysis occurs after the first few days, and this is marked by a significant increase in the solution pH and an observable increase in the cell voltage as well as the end of any chlorine detection. In previous experiments, most of the excess power was observed after the third day when the chlorine evolution and NCl₃ production had ceased [3-5].

5. Calorimetric measurements of co-deposition systems

The PdCl₂ + NHCl + NH₄OH system was developed for palladium plating [6] and was not designed for the extended electrolysis at high currents required for the Fleischmann-Pons effect (FPE). However, this ammonia system can readily be converted to a very stable electrolysis system with no Cl₂ or NCl₃ formation if sufficient LiOH is added following the palladium co-deposition to maintain a basic pH. The required amount of LiOH or LiOD is given by $[\text{LiOH}] > [\text{NH}_4\text{Cl}] + 2[\text{PdCl}_2]$, or a LiOH concentration greater than 0.20 M in these experiments. Following the LiOH addition, all NH₃ is driven off by the electrolysis gases, and the solution consists of only LiCl + LiOH. Initial studies of the PdCl₂ + NH₄Cl + NH₄OH system with the LiOH

addition produced a very stable electrolysis process that was used in calibration of a new isoperibolic calorimeter [7].

Two calorimetric experiments have been completed using $\text{PdCl}_2 + \text{ND}_4\text{Cl} + \text{ND}_4\text{OD}/\text{D}_2\text{O}$ with LiOD addition following the completion of palladium deposition. Both experiments initially gave excess power effects of 70 to 100 mW at $I = -100$ mA. However, the excess power gradually diminished to near zero with further electrolysis. In both experiments, almost all of the deposited palladium somehow became detached from the cathode and settled to the cell bottom where it was electrochemically inactive. Further experiments are needed to determine if the LiOD addition destabilizes the palladium deposit.

Calorimetric studies of $\text{PdCl}_2 + \text{NH}_4\text{Cl} + \text{NH}_4\text{OH}/\text{H}_2\text{O}$ without the LiOH addition gave a chemical excess power effect reaching 50 mW during the acidic period of Cl_2 and NCl_3 formation. Nitrogen trichloride is a volatile, yellow oily liquid of high density (1.653 g/cm^3) and explosive in pure form. It could be observed experimentally as a small yellow pool at the cell bottom and as a yellow solution coloration during the Cl_2 evolution period. This NCl_3 substance is only slightly soluble in water, but this dissolved NCl_3 would readily react with the hydrogen generated by electrolysis to produce a chemical excess power effect by the reverse of Eq. 5. Because of the NCl_3 formation, it is recommended to keep the cell behind a safety shield with adequate ventilation and to wait until the chlorine evolution ceases and the yellow color clears before performing calorimetric measurements.

6. Investigations of chlorates, nitrates and nitrites

Chlorates, nitrates and nitrites are possible electrochemical products from the oxidation of chloride and ammonium ions. Therefore, effects of these substances on the electrochemistry and calorimetry were investigated. Cyclic voltammetric studies of 0.1505 M NaClO_3 using a platinum electrode showed only water electrolysis and no reversible reactions involving chlorates. The EIS studies showed that any chlorate reactions would be very slow with an exchange current density of $i_0 = 10^{-6} \text{ A/cm}^2$. Constant current pulse methods proved that any electrochemical reactions of chlorates could not sustain currents above 0.5 mA/cm^2 in 0.1505 M NaClO_3 . A calorimetric study of the 0.1505 M NaClO_3 in H_2O gave no measureable excess power effects. Based on pH measurements, it is estimated that more than 99.999% of the total current (48474 coulombs) was consumed by H_2O electrolysis. The volume of H_2O consumed in this chlorate calorimetric experiment was larger than calculated from Faraday's Law (6.5 mL vs. 4.5 mL). These studies all rule out any measurable shuttle reactions involving chlorates. Related investigations involving KNO_3 and NaNO_2 showed that there were no shuttle reactions involving nitrates or nitrites that would give false excess power effects [7].

7. Evidence for a palladium volume effect

Based on the measured capacitance of the deposited palladium, the effective surface area increased by a factor of 10^6 during co-deposition. The presence of H^+ or D^+ within the deposited palladium likely contributes to these high capacitance values. Because the excess power observed in co-deposition experiments scales much more closely with the palladium volume, it appears that the FPE is a volume effect in co-deposition systems. A secondary double layer consisting of D^+ within the deposited palladium is likely a region rich in both electrons and deuterons and a prime location for near surface fusion reactions.

Acknowledgments

The author thanks William Wilson of DTRA and Michael Melich of the Naval Postgraduate School for their support of this work. Financial help is also acknowledged by M.H.M. from an anonymous fund at the Denver Foundation via Dixie State College.

8. Appendix

The exact equation for a voltage scan for an electrical circuit of a resistor, R_s , and a capacitor, C_d , is given by

$$I = \nu C_d + (E_i/R_s - \nu C_d) \exp(-t/R_s C_d) \quad (\text{A.1})$$

where I is the current (A), ν is the voltage scan rate (V/s), and E_i is the initial scan voltage at $t=0$ seconds [9]. Generally $R_s = 1 \Omega$ and $C_d = 50 \mu\text{F}$ (approximately) for electrochemical studies, thus the exponential term falls to zero within about 250 μs , and Eq. A.1 becomes $I = \nu C_d$. This simplified equation is generally used in cyclic voltammetric studies of supercapacitor materials [8]. However, $R_s C_d \gg t$ for high capacitance materials, thus $\exp(-t/R_s C_d) \approx 1 - t/R_s C_d$, and Eq. A.1 becomes

$$I \approx \nu C_d + (E_i/R_s - \nu C_d)(1 - t/R_s C_d) \quad (\text{A.2})$$

or

$$I \approx E_i/R_s - E_i t/R_s^2 C_d + \nu t/R_s \quad (\text{A.3})$$

Introducing $\nu t = E - E_i$ for a potential scan yields

$$I \approx E/R_s - (E_i/R_s)(t/R_s C_d) \quad (\text{A.4})$$

but $E > E_i$ and $R_s C_d \gg t$, hence $I \approx E/R_s$ which is Ohm's Law as observed experimentally in Figure 2.

9. References

- [1] S. Szpak, P.A. Mosier-Boss and J.J. Smith: *J. Electroanal. Chem.* **302** 255 (1991)
- [2] P.A. Mosier-Boss and S. Szpak: *Nuovo Cimento Soc. Ital. Fis. A* **112** 577 (1999)
- [3] M.H. Miles: *NEDO Final Report*, Sapporo, Japan (March 31, 1998)
- [4] S. Szpak, P.A. Mosier-Boss and M.H. Miles: *Fus. Technol.* **36** 234 (1999)
- [5] S. Szpak, P.A. Mosier-Boss, M.H. Miles and M. Fleischmann: *Thermochimica Acta* **410** 101 (2004)
- [6] R. Le Penven, W. Levason and D. Pletcher: *J. Applied Electrochem.* **20** 399 (1990)
- [7] M.H. Miles and M. Fleischmann: *Proceedings of ICCF-15* (Rome, Italy 2009) submitted
- [8] M.H. Miles, T.J. Groshens and C.E. Johnson: *Batteries and Supercapacitors*, edited by G.A. Nazri, E. Tekeuchi, R. Koetz and B. Scrosati, pp. 602-608, The Electrochemical Society Proceedings Volume 2001-21 (2001)
- [9] A.J. Bard and L.R. Faulkner: *Electrochemical Methods: Fundamentals and Applications*, pp. 10-15 (John Wiley, New York, 1980)

Anomalous Silver on the Cathode Surface after Aqueous Electrolysis

J. Dash, Q. Wang

Eugene F. Mallove Laboratory for New Energy Research, Portland State University, Portland, OR 97207

E-mail: dashj@pdx.edu

Abstract. The presence of localized concentrations of anomalous elements (gold and silver) on the surfaces of palladium cathodes after electrolysis in either light water or heavy water electrolyte was first reported in 1994 [1]. Similarly, anomalous elements in surface pits were reported for titanium cathodes after electrolysis in heavy water electrolyte [2]. More recently, off-the-shelf battery fluid (Sp.G. 1.26) was substituted for analytical-grade H₂SO₄ (Sp.G. 1.84) in the electrolyte. Silver was found in localized concentrations on palladium cathodes after electrolysis. These results are consistent with a thermal neutron mechanism proposed previously [1].

1. Introduction

A demonstration of our excess heat experiment was performed in Salt Lake City (SLC) at an American Chemical Society conference on March 23, 2009, the 20th anniversary of the announcement by Fleischmann and Pons that they had achieved nuclear fusion in a bottle. The apparatus for this demonstration was shipped from our Portland State University (PSU) laboratory. The electrolyte, containing sulfuric acid, a hazardous chemical, was to be shipped separately, with required precautions. However, the electrolyte did not arrive in SLC in time for the demonstration. Rather than cancelling the demonstration, commercial battery fluid was substituted for our electrolyte.

2. Experimental methods and Results

The battery fluid contained dilute sulfuric acid (Sp.G. 1.265). This was further diluted with tap water. Therefore, the diluted electrolyte contained no heavy water. This was the electrolyte for the control cell (C cell). This cell contained a Pt foil anode, a Pd foil cathode, and hydrogen and sulfate ions in the electrolyte. The experimental cell (E cell) was identical except that it contained the same commercial battery fluid diluted with heavy water instead of tap water. This cell also contained a Pt foil anode and a Pd foil cathode, but the electrolyte contained both hydrogen ions and deuterium ions, in addition to sulfate ions. The cell components are given in Table 1.

The two cells were connected in series to a direct current power supply which supplied constant current to both cells at almost the same voltage. Thus, the power input was almost identical for the two cells (about 14 watts), but the power output was at least one watt higher for the C cell compared with the E cell. This result was totally unexpected. The experiment in SLC was repeated, and the result was the same, i.e. the C cell produced more than one watt greater thermal power than the E cell.

Our previous experiments used deionized water and pure sulfuric acid (Sp.G. 1.84) for the C cell electrolyte, and pure heavy water and the same sulfuric acid for the E cell electrolyte. A typical excess heat result was about 0.8 watt higher power output from the E cell. This was the result which we demonstrated at ICCF10 in Cambridge, MA in 2003.

After electrolysis for about two hours, the demonstration was stopped, the electrolyte was removed, and the apparatus was shipped back to PSU. The C cell cathode was removed from the cell and examined. Whereas it originally was a flat, silvery foil, it is now black and bent lengthwise to a curved surface which was concave to the anode during electrolysis. It was then examined with a scanning electron microscope (SEM) equipped with an energy dispersive spectrometer (EDS). Fig. 1 shows the pitted topography on the concave side of a Pd cathode after electrolysis for about two hours in light water electrolyte. A characteristic x-ray spectrum was taken by scanning the electron beam over the entire area of Fig. 1. The only elements detected in this spectrum were C, O, Al, Pd, and Pt. The origin of C is not known, O, Al, and Pt are thought to result from the Pt-Al₂O₃ recombination catalyst suspended above the electrolyte. Pt could also be produced by electroplating Pt dissolved from the anode.

Table 1. Cell components for experiment on 3-23-09 in SLC.

	E-cell	C-cell
	50ml D2O (99.9%, 151882-250g, Aldrich)	75ml H2O (tap water)
	50ml H2SO4 (Battery Fluid, S.G. 1.265, UN2796)	25ml H2SO4 (Battery Fluid, S.G. 1.265, UN2796)
Anode	Pt=1.2798g (25mm*24mm*0.1mm)	Pt=1.3503g(25mm*24mm*0.1mm)
	Stock #11509 Lot # C25Q28	Stock #11509 Lot # C25Q28
Cathode	Pd=0.5355g cold rolled (29mm*8mm*0.2mm)	Pd=0.6167g cold rolled (29mm*8mm*0.2mm)
	Stock #11514 Lot # IO5S014	Stock #11514 Lot # IO5S014
Catalyst	20ml	20ml
	Alfa Aesar 0.5% Pt on alumina	Alfa Aesar 0.5% Pt on alumina

In Fig. 1 the gray areas contain mostly Pd, the white areas contain mostly electroplated Pt, and the black holes contain mostly Pd with statistically significant Ag. The ratio Ag/Pd averages 0.06 for 9 black holes. This Pd/Ag ratio for each of these nine black holes is given in Table 2.

The area shown in Fig. 1 was chosen for intensive study because it is highly pitted. One possible explanation for the pitting is that localized melting and vaporization occurred. Such events seem unlikely with only 14 watts input energy. Another possibility is that chemical dissolution occurred. If so, a more uniform topography would be expected instead of the pitted surface shown in Fig. 1. In previous research localized concentrations of anomalous elements were found on surface asperities [1] and in pits [2] The SEM electron beam, less than 1 μ m diameter, was focused on the asperity or pit. This resulted in the emission of characteristic x-rays from all of the elements present. The x-rays were detected and processed to produce a spectrum from each pit. Carbon, atomic number 6, and all elements of higher atomic numbers, could be detected and quantified by this method.

Table 2. Silver content at various locations in the black pits shown in Fig. 1. Statistically significant (>3 sigma) amounts of Ag were found in nine of 14 pits which were analyzed. The spectrum obtained by scanning the electron beam over the whole area of Fig. 1 (wa) did not contain Ag.

Atomic %-041409	Pd	Ag	Ag/Pd
Shu-SLC-C-Cell-Pd-CC-0.5k-wa		0.0	
Shu-SLC-C-Cell-Pd-CC-0.5k-s1	94.8	5.2	0.06
Shu-SLC-C-Cell-Pd-CC-0.5k-s2	95.3	4.7	0.05
Shu-SLC-C-Cell-Pd-CC-0.5k-s3	90.6	9.4	0.10
Shu-SLC-C-Cell-Pd-CC-0.5k-s4	92.7	7.3	0.08
Shu-SLC-C-Cell-Pd-CC-0.5k-s5	94.8	5.2	0.05
Shu-SLC-C-Cell-Pd-CC-0.5k-s7	95.8	4.2	0.04
Shu-SLC-C-Cell-Pd-CC-0.5k-s8	94.7	5.3	0.06
Shu-SLC-C-Cell-Pd-CC-0.5k-s10	95.4	4.6	0.05
Shu-SLC-C-Cell-Pd-CC-0.5k-s11	92.2	7.8	0.08

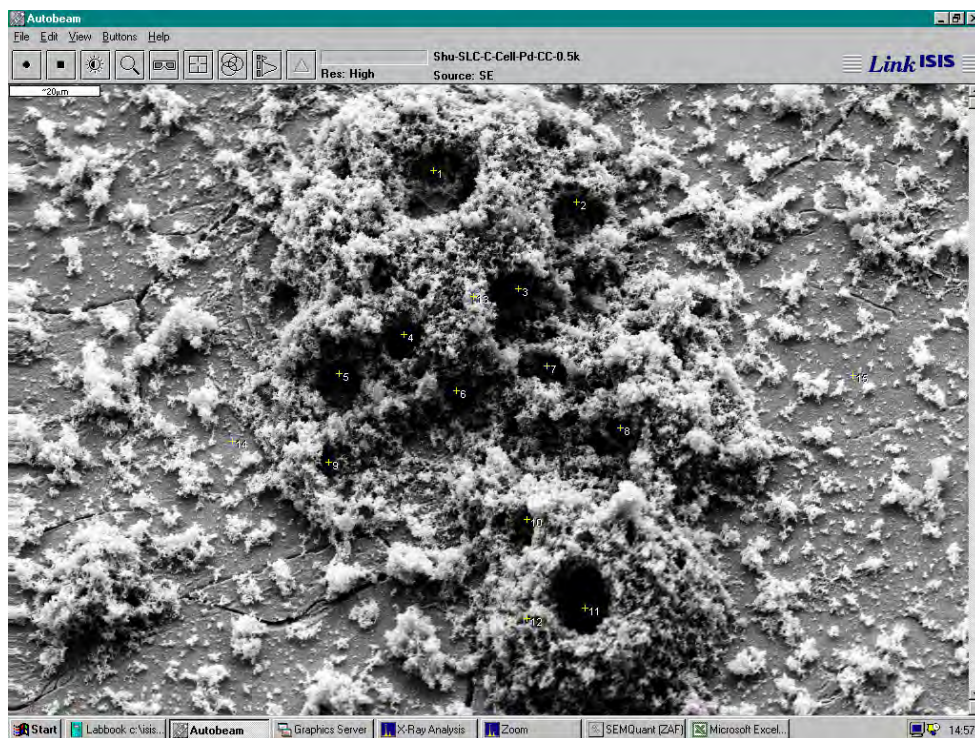


Fig. 1 - Micrograph of the concave side of the Pd cathode after about two hours electrolysis in light water electrolyte.

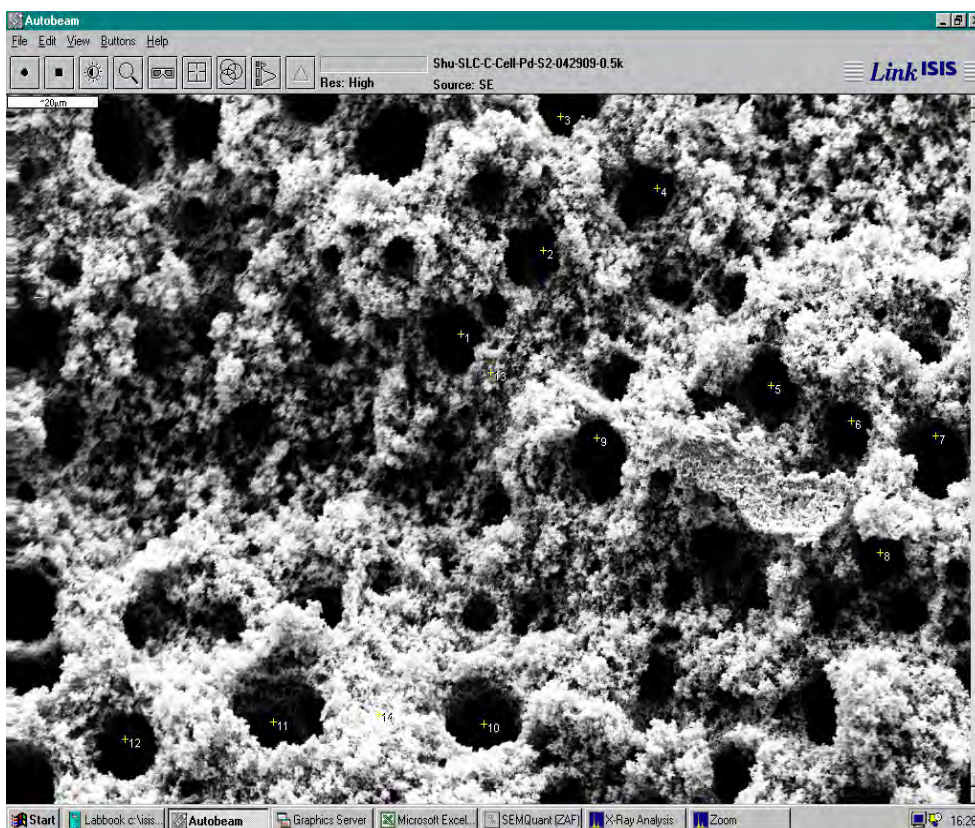


Fig. 2 - Topography of a hotspot on the convex side of a Pd cathode after electrolysis for about two hours in light water electrolyte, SLC 3-23-09. Twelve of 14 black holes contained statistically significant Ag (>3 sigma). The average ratio Ag/Pd was 0.09, and the range was 0.06 to 0.14.

3. Discussion

We now examine the possibility that the silver detected in the black holes originated from environmental contamination, such as impurities from the tap water. This seems unlikely because deposition occurs preferentially on asperities, not in pits. The black holes in figures 1 and 2 are rimmed with white particles which are almost pure platinum. We suggest that miniature explosions occurred, leaving behind pits containing Ag, which resulted from thermal neutrons absorbed by Pd. The unstable Pd isotopes then beta decayed to form Ag and heat sufficient to form a localized pit. Pt then electroplated from the electrolyte onto the rims, which were elevated above the original surface.

EDS measurements were also performed on the cathode from the E cell. Topography was similar to that found on the C cell cathode, and anomalous Ag was found in the pits. Our efforts were concentrated on the light water C cell cathode because it produced more heat than the heavy water E cell.

We are currently using secondary ion mass spectrometry (SIMS) before and after electrolysis to determine if there are changes in Pd isotopic abundance in our cathodes.

4. Conclusions

Excess heat was obtained from electrolysis with palladium cathodes in cells containing acidified H₂O electrolyte compared with cells containing palladium cathodes and acidified D₂O electrolyte.

Statistically significant, localized concentrations of silver were found in pits on the surfaces of palladium cathodes after electrolysis.

The results for the light water cells were obtained using commercial battery acid diluted with tap water, suggesting that highly purified chemicals are not necessary for LENR.

Acknowledgements

Our research began in April 1989. It was performed with the assistance of 36 high school apprentices and nine graduate students (seven M.S. theses and two doctoral dissertations).

Funds were provided by Portland State University, the U.S. Army Research Office, The Drexler Foundation, the New Energy Foundation, and the New York Community Trust.

5. References

- [1]. J. Dash, G. Noble, and D. Diman, *Trans. Fusion Tech.* **26**, 299(1994).
- [2]. J. Warner and J. Dash, *Conf. Proc.* **70**, ICCF8, F. Scaramuzzi (Ed), SIF, Bologna, 2000, p.161.

Calorimetry Of Pulse Electro-Melting of PdD_x Wires

F.L. Tanzella, M.C.H. McKubre

SRI International

E-mail: francis.tanzella@sri.com

Abstract. Several groups have reported anomalous effects (heat and nuclear products) in thin PdD_x materials stimulated by different forms of electro-diffusion. We have designed and tested a calorimeter utilizes an “exploding wire” technique to examine the effect of a destructive electro-diffusion on a highly loaded PdD_x wire. We have shown that highly loaded PdD_x wires can be formed using high voltage electrolysis of very high purity D₂O with a very thin Pd wire cathode and a thin Pt wire anode. The addition a partial monolayer of a recombination poison yields a highly loaded PdD_x cathode. Following that step with the addition of a larger amount of that same poison seals the loaded wire and allows transfer to a cryogenic calorimeter. Our liquid nitrogen boil-off cryogenic calorimeter has been shown to have an accuracy of less than 0.4J.

1. Introduction

Several groups[1, 2] have reported anomalous effects (heat and nuclear products) in thin PdD_x materials stimulated by different forms of electro-diffusion. The ultimate extrapolation of this technology is the electrical heating of thin PdD_x wires resulting in destructive high-speed melting - “exploding wires”. Exploding wire technology has been used for over 150 years to make fine metal particles[3]. Celani *et al*[4-5] have reported loading thin Pd wires electrochemically up to high loading and sealing their surface electrochemically. Tripodi[6] reported that such sealed wires can be immersed in liquid nitrogen (LN) and analyzed for anomalous effects at those temperatures or soon after warming up. As such, electrically exploding such loaded wires while immersed in LN should release the deuterium and cause the evolution of gaseous N₂ equal to the electrical energy passed through the wire due to the heat capacity and enthalpy of vaporization of LN.

Since considerable attention has been directed toward demonstrating a correlation between the rates of excess heat and ³He and ⁴He production [7, 8], we will analyze the off gases for excess He and non-natural isotopic He ratios.

2. Experimental

Although some experiments have been performed, the primary effort during this year has been to design, build, and test the equipment necessary to load deuterium into palladium, seal the deuterium inside, measure the energy released during electrical stimulations, and measure He-4 products produced both in the electrolytic cell and during the stimulated energy release.

We have adapted the original H₂O high loading/sealed cathode technique to D₂O. This is not a trivial effort since the loading process requires ultra-clean materials and ultra-pure reagents. Unfortunately, most available D₂O is chemically impure when compared to 18 MΩ-cm de-ionized H₂O. We have been using high-purity D₂O (Sigma-Aldrich #P192341), which also provides the high isotopic purity necessary to yield high D loading. In order to maintain this isotopic purity all transfers are performed under dry N₂ or Ar.

5 x 10⁻⁵ M SrSO₄ in D₂O is prepared under dry conditions. Approximately 5 ml of Hg₂SO₄ saturated D₂O is similarly prepared and stirred overnight. After cleaning all components are rinsed with deionized H₂O, followed by pure ethanol before drying. ~ 5 cm length of 0.050 mm diameter Pd wire (Alfa # 40730) is

attached to 4 lengths of 0.25 mm Pt wire and attached to the cell shown diagrammatically in Fig. 1. This allows for *in situ* accurate 4-wire resistance measurements of the Pd cathode. This cell is closed with its silica quartz vessel and the Pd resistance measured.

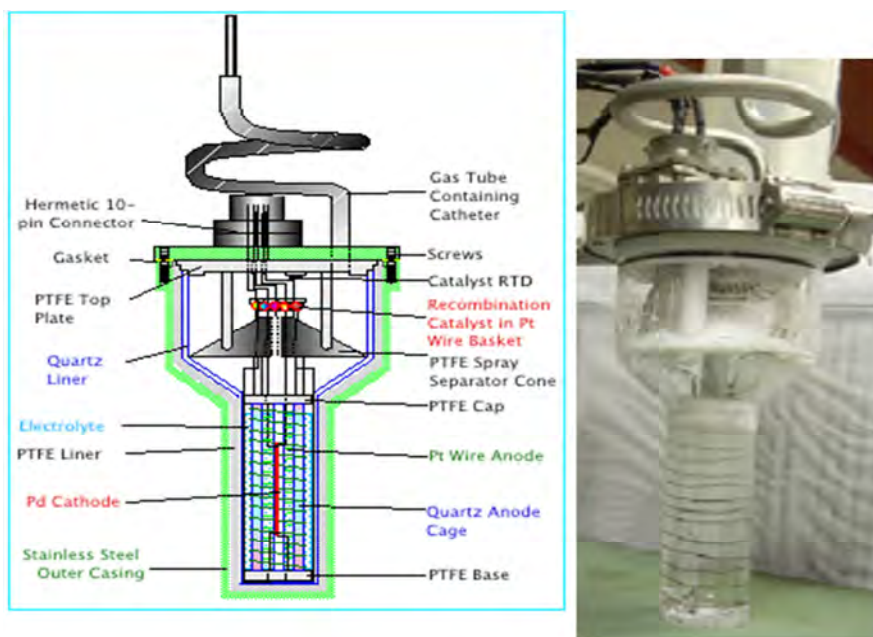


Fig. 1 - Degree of loading cell used to load and seal thin wires.

A current is passed along the length of the Pd to resistively heat the wire and anneal it in place. The current is raised slowly to $\sim 0.75\text{A}$ where the wire glows a bright orange color. Experience has shown this to be adequate to properly anneal the wire. The current is then lowered slowly to 0A at room temperature where the resistance is again measured. This procedure is repeated until the Pd resistance does not change upon annealing. This final resistance is considered R_0 .

After a stable resistance is obtained, the cell assembly is again rinsed with DI water and ethanol and dried. Then $\sim 20\text{ ml}$ of $5 \times 10^{-4}\text{ M SrSO}_4/\text{D}_2\text{O}$ is added to the cell. After measuring a stable resistance with electrolyte present, $\sim 2.5\text{ mA}$ is applied across the cell. After a stable resistance value is obtained, the current is doubled to 5.0 mA . After the resistance has stopped coming down on the right side of the maximum (see the R/R_0 versus $H(D)$ loading curve in Fig.4), $\sim 1\text{ ml}$ of $\sim 5 \times 10^{-5}\text{ M Hg}_2\text{SO}_4$ is added to the cell. R/R_0 is often reduced at this point possibly due to the partial recombination poisoning of the Pd surface. Hg_2SO_4 solution is added, one ml at a time, until the resistance stops coming down. The electrolytic current is then reduced in steps to see if the resistance stabilizes at a value below $R/R_0=1.6$. If not, more Hg_2SO_4 is added. When R/R_0 is unchanged and below 1.6, the electrolysis is stopped, the Pd cathode removed and moved to the calorimeter.

The wires are then immersed in liquid nitrogen in a cryogenic nitrogen boil-off calorimeter, shown in Fig. 2. The measured input energy from the pulse boils off a known amount of nitrogen, which is measured by a calibrated thermal mass flow meter (MFM). By using different length pulses into a current shunt immersed in the LN calorimeter we calibrated the volume of N_2 evolved at different input energies. In the case of PdD_x , the energy from the input pulse and any excess energy produced from the extremely fast electro-migration inside the PdD_x will boil off a known given volume of nitrogen. Fig. 2 also shows the cathode connection blocks to be immersed in the LN. The copper probes hold the sample via a set-screw in each probe. This probe is then immersed in the LN, sealed with a low temperature O-ring, and held tight with two clamps. All of the vaporized gas is measured using an electronic mass flowmeter. The calorimeter is calibrated using a 50 watt 1 ohm resistor. The voltage, current, and time are measured using a high-speed data acquisition system and transferred digitally to the computer. The analog output of the MFM is also measured by the high-speed data acquisition systems.

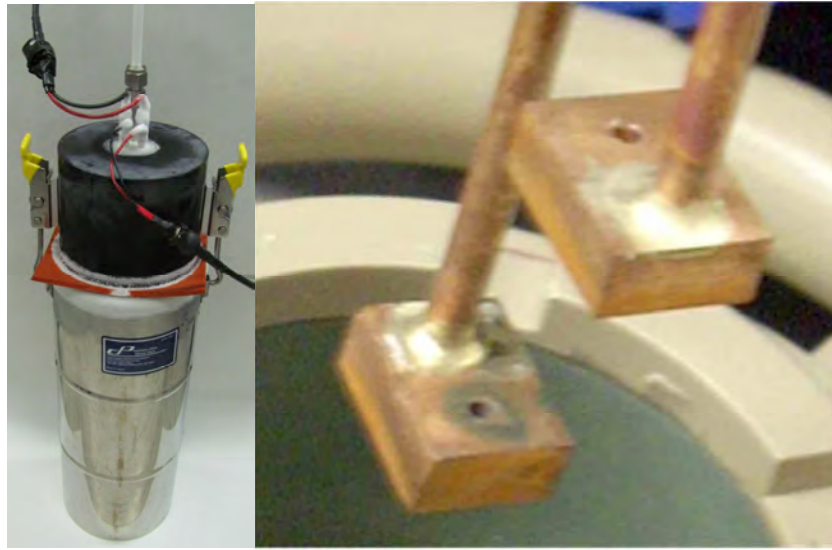


Fig. 2 - Photographs of the cryogenic calorimeter and its cathode connection blocks.

3. Results

The data collected and a photograph of the Pd wire during this annealing process are shown in Fig. 3. The blue line shows the voltage, the blue the current steps and the green line shows the R/R_0 measured

Low while the current is off. molarity Pd/SrO₄/D₂O electrolysis experiments have been performed using 50 μ m wires. These wires were then sealed electrolytically using Hg₂SO₄. A typical cell response to current steps and Hg₂SO₄ additions is shown in Fig. 4. R/R_0 goes through a maximum very quickly as you would expect for such a thin wire. Then small amounts of Hg₂SO₄ are added to enhance the loading and seal the wire. Finally the current is reduced in step with little or no loss of loading. These wires have been successfully transferred to a liquid nitrogen (LN) vessel without loss of loading. Calibration of the cryogenic calorimeter is shown in Fig. 5 as joules electrical input versus N₂ volume evolved. The red dot at ~ 0.4 J represents exploding wire results from a 50 μ m diameter pure Pd wire.

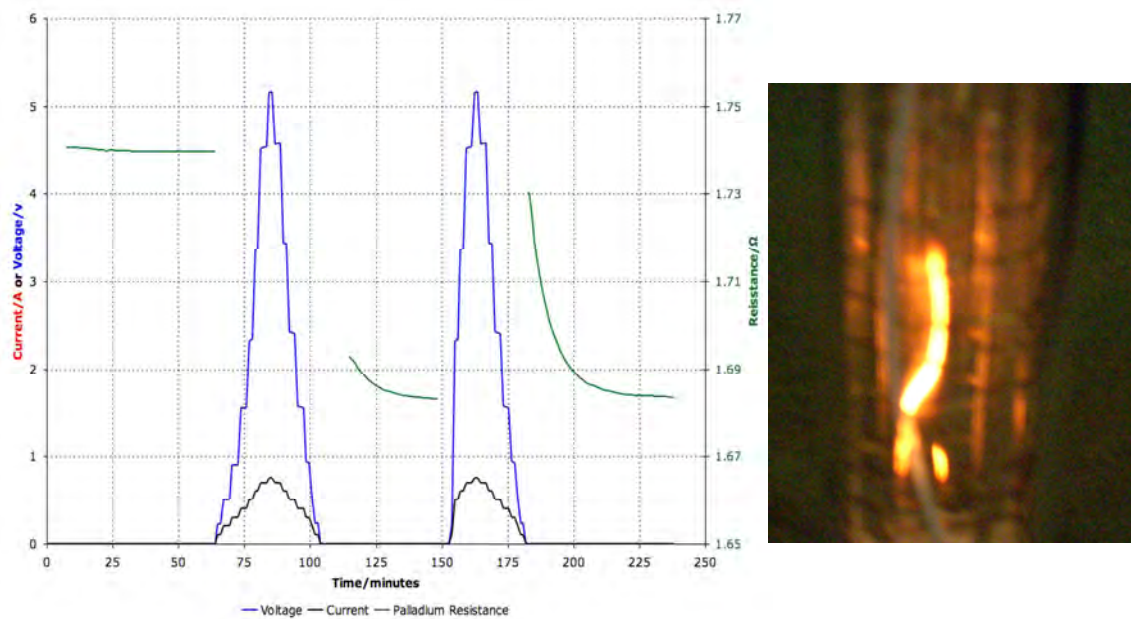


Fig. 3 - Plot of R/R_0 , current and voltage and photograph during Pd wire annealing.

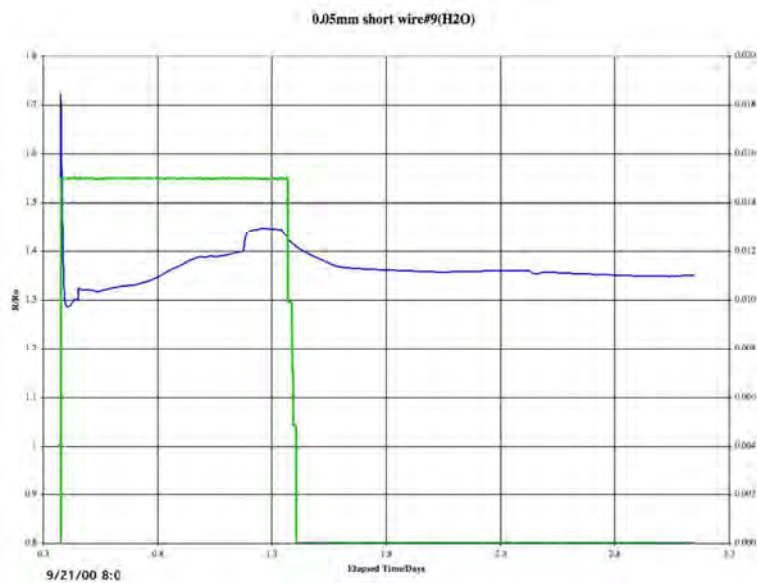


Fig. 4 - Plot of R/R_0 (blue) and Current (green) for H loading of Pd wire.

In addition to the input pulse the gas volume measured may be affected by the enthalpy of melting/volatilizing the wire as well as the gas evolution from the desorption of any hydrogen/deuterium. For these reasons, the results from PdD_x wires will be compared the energy released from pure Pd or Pt wires as well as the results from PdH_x .

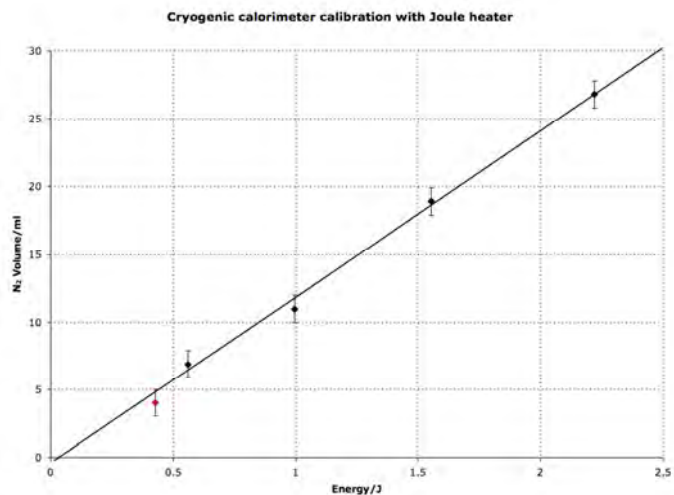


Fig. 5 - Calibration of cryogenic calorimeter and exploding pure Pd wire result (red dot)

4. Conclusions and Future Work

We have shown that we can load and seal 50 μ m diameter PdH_x and PdD_x wires electrolytically. We have shown that we can transfer those wires to a cryogenic calorimeter without loss of loading. We have shown that we can measure as little as 400 mJ of input energy in the cryogenic calorimeter.

We have performed gas phase measurement of He isotopes from the headspace of various cells and are planning to perform this on most electrolysis cells' headspace gas and low-temperature stimulated wire effluent. We will also use a metal vaporization inlet to the He isotope mass spectrometer to analyze any Pd fragments for anomalous He isotopic ratio.

He insertion will be done by heating the Pd (or other wire) resistively in a tube to appropriate temperatures using sealed feed-throughs and selected pressures of He for a selected time. He insertion will be used to form defects in the Pd cathodes, which may facilitate anomalous effects.

Acknowledgements

We gratefully acknowledge the support of the Basic Research Program of Defense Threat Reduction Agency.

5. References

- [1] E. Del Giudice, et al., ICCF8 Conference Proceedings - Italian Physical Society, Vol. 70, pages. 47-54, (2000).
- [2] C. Manduchi, et al., Nuovo Cimento della Societa Italiana di Fisica, A Nuclei, Particles and Fields, Vol. 108A, pages. 1187-1205, (1995).
- [3] M. Faraday, Philos. Trans. Royal Society London, Vol. 147, pages. 145-181, (1857).
- [4] F. Celani, et al., ICCF8 Conference Proceedings - Italian Physical Society, Vol. 70, pages. 181-190, (2000).
- [5] F. Celani, et al., Fusion Technology, Vol. 29, pages. 398-404, (1996).
- [6] P. Tripodi, et al., Physics Letters A, Vol. 276, pages. 122-126, (2000).
- [7] Y. Arata and Y-C. Zhang, Proc. Japan Acad. 73B, 1 (1997).
- [8] D. Gozzi, R. Caputo, P. L. Cignini, M. Tomellini, G. Gigli, G. Balducci, E. Cisban, S. Frullani, and F. Garibaldi, Proc. ICCF4 Conference Proceedings, 1, 2-1 (1993).

Confirmation of Heat Generation during Hydrogenation of Oil

T. Mizuno

*Hydrogen Engineering Application & Development Corporation, 4-3-9-102,
Minamimach Makomanai Minamiku, Sapporo 001-0016, Japan*

E-mail: mizuno@qe.eng.hokudai.ac.jp

Abstract The study was devoted to replicating and controlling that excess heat effect during hydrogenation of hydrocarbon. The reactant is phenanthrene, a heavy oil fraction, which is reacted with H₂ gas of high pressure and high temperature in the presence of a metal catalyst. This results in the production of excess heat and radiation. After the reaction, an analysis of residual gas reveals a variety of hydrocarbons, but it seems unlikely that these products can explain the excess heat. Most of them form endothermically, and furthermore heat production reached 60 W. Overall heat production exceeded any conceivable chemical reaction by two orders of magnitude.

1. Introduction

This study was stimulated by a liquefying reaction to change the heavy oil to light oil. Abnormal heat generation was observed during the hydrogenation experiments when heated in high-pressure hydrogen gas. The amount of heat generated was abnormally large considering the expected chemical reaction between a few drops of heavy oil and a little hydrogen gas. Based on their estimate, they concluded the heat generated had not come from a conventional chemical reaction.

2. Experimental

2.1 Cell

Figure 1 shows a schematic of the reaction cell and the experimental set up. The reaction chamber is cylindrical. It is constructed from Inconel 625. It has a 16-mm outer diameter, a 10-mm inner diameter, a 300-mm height, and has a 0.01-*l* capacity. It can sustain a pressure of 500 atm, and it can be heated to 850°C. The reactor has a plug for the hydrogen inlet and outlet, and housing for an internal temperature sensor. A platinum catalyst is placed inside the cell. The temperature inside the cell is measured with an R-type thermocouple, 1.6 mm in diameter, 30 cm long, which is enveloped in a 0.3 mm thick SS314 stainless steel shield and grounded to reduce noise. The thermocouple range is from -200 to 1,300°C. Moreover, another thermocouple of the same type is inserted between the outer reactor wall and the inner wall of the electric furnace, to measure the temperature of the outside wall of the reactor cylinder. Thermocouple data is collected by a data logger (Hewlett Packard HP3497A), with a temperature sensitivity of 0.1°C. The error ranges of the temperature measurement system is determined by the resistivity of the thermocouples (4 Ω), the insulation (100 MΩ), and the data logger (100 MΩ). In this case, the error works out to be 0.03% of the instrument reading. At a temperature of 800°C the error is 0.03°C.

2.2 Measurement system

As shown in Fig. 1, the cell is placed in the electric furnace, and hydrogen gas is introduced into the cell through a 6 mm diameters stainless steel pipe. The pipe is fitted with high pressure Swagelok valves which are used to introduce gas into the cell, or to evacuate it. Hydrogen is stored in a tank at 135 atm. It passes through a piezoelectric pressure transducer (Kyowa P-100KA) and amplifier (Shinko Tsushin 603F) and the flow rate is recorded in the data logger. Gas purity is more than 99.999%. The gas line is connected to the vacuum pump and mass spectrometer (ULVAC REGA201) that detects mass numbers up to 400.

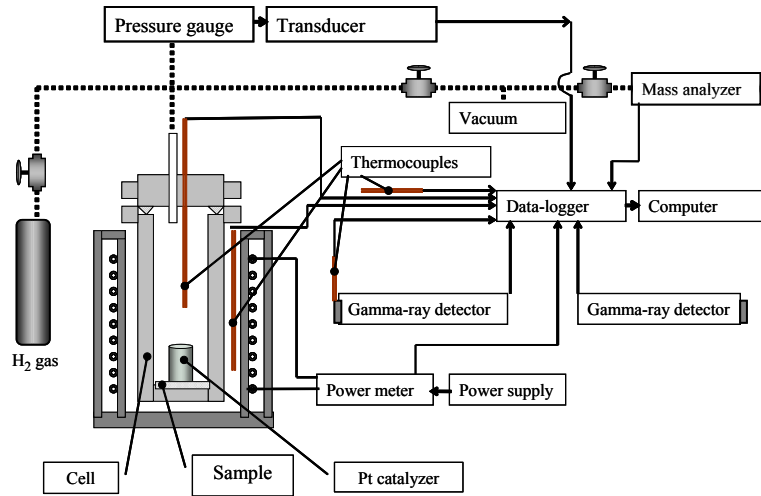


Fig. 1 - Cell and experiment configuration.

The electric furnace is custom made (Tokyo Technical Lab. PH, Mo13763A1). It is 200 mm outside diameter, 65 mm inside diameter and 200 mm high. A direct current regulated power supply is used (Takasago Electric EX-1500H), that produces up to 240 V at 6 A (1.5 kW). The heater power is monitored with high precision meter (Yokogawa PZ4000), which measures amperage and voltage every millisecond, sending averaged data to the data logger at 5-second intervals. The combined error for amperage and voltage is 0.0015%.

Radiation emissions are detected by a γ -ray detector (Aloka ICS-311) that is located 15 cm from the reactor. Its output is recorded continuously by the computer through a digital multimeter (Advantest TR-6845). The ionization chamber has a 14 cm long electrode, a correction plate 1 cm long, a window 0.5 cm thick, and it is pressurized with air at 1 atm. This detector can detect x-rays, γ -rays and β -rays. It can detect x-rays and γ -rays in the range of 30 keV ~ 2 MeV with an efficiency of 0.85 ~ 1.15 calibrated with ^{137}Cs .

This output is sent to the data logger and recorded in the computer. The detection of radiation emission employed a gamma-ray detector, which was calibrated by a 3.7×10^5 Bq ^{226}Ra check source that was positioned at various distances from the gamma-ray detector. Before the experiment, the check source was placed inside the reactor cylinder to obtain a gamma-ray reading. The background radiation level surrounding the system was 0.05 ± 0.008 $\mu\text{Sv/h}$.

The radiation data was further processed with OriginPro software (OriginLab) to analyze multiple peaks. A Gaussian distribution analysis was performed to fit of multiple peaks, with the following equation:

$$y = y_0 + A(w(\pi/2)^{-1/2})\exp(-2(x-x_0)^2/w^2)$$

where, y_0 = Baseline offset, A = Total area from baseline to curve, X_0 = Midpoint of peak, $W = 2\sigma$. Full width at half maximum $\cong 0.849$

The midpoint X_0 is the average, where $w/2$ is the standard deviation. To reduce the difference between the fitted curve and original data, additional peaks were plotted, and the following peak analysis was performed. To analyze multiple peaks, a function with multiple dependent variables and independent variables was defined in the following equations:

$$y_1 = f(x_1, x_2, \dots, a, b, c, \dots)$$

$$y_2 = f(x_1, x_2, \dots, d, e, f, \dots)$$

$$\dots$$

$$y_n = f(x_1, x_2, \dots, o, p, q, \dots)$$

Here, x_1, x_2 are independent variable and a, b, c, \dots, o, p, q are coefficient for the variables.

The Gaussian peaks derived with these functions are closest to the original data.

2.3 Materials

Fluorescent grade (98.0% pure) phenanthrene ($C_{14}H_{10}$; MW 178.23) was used in this study. It was supplied by the Kanto Chemical Co. LTD. The Pt catalyst was a high purity (99.99%) Pt mesh (Tanaka Noble Metal Co. LTD.) The catalyst is rectangular and is 5-cm high, is 10-cm wide, and weighs 50 g. Before the experiment, the Pt catalyst was activated once in an atmosphere of hydrogen gas for 1 hour at 850°C.

2.4 Experimental procedures

One gram of phenanthrene and the Pt catalyst were put in the reactor; the reactor cell was then sealed with the lid, which was secured in place with bolts. The reactor was connected to the vacuum system and evacuated to 10^{-3} mmHg. The vacuum system exhaust valve was left open for several minutes to remove the residual air from the reactor. The exhaust valve was then closed, and the gas was supplied to the reactor at the set pressure. After gas filled the reactor, the gas supply valve was closed. The temperature of the gas in the reactor then was increased to the starting temperature. Calibration of temperature versus pressure was performed by changing the hydrogen gas pressure from a vacuum to 80 atm.

2.5 Temperature calibration

The amount of excess heat is determined by comparing input heater power to a stable temperature in the cell on a calibration curve.

3. Results

3.1 Excess heat generation

Figure 2 shows an example of anomalous excess heat. In this test, 1 g of phenanthrene was exposed to a 70 atm of hydrogen gas. Furnace heater power was set for 60 W. The furnace heater temperature rose faster than the cell temperature. As shown in the calibration curve when there is no anomalous heat, by 10 ks both temperatures stabilize at around 640°C. However, in this test they both soon begin to rise above the stabilization point. After 5 ks, large perturbations begin and the temperatures continue rising. Also, at this point the cell temperature exceeds the furnace heater temperature. This temperature reversal is proof that heat was being produced inside the cell. The cell temperature reaches 800°C, which is 200°C higher than the calibration curve predicts. Since input power is 60 W, we extrapolate that roughly 60 W of anomalous heat is being produced. Because of the extreme fluctuation in heat, total energy is more difficult to estimate than power, but because the excess power persisted for 10 ks it was at least 120 kJ in this test.

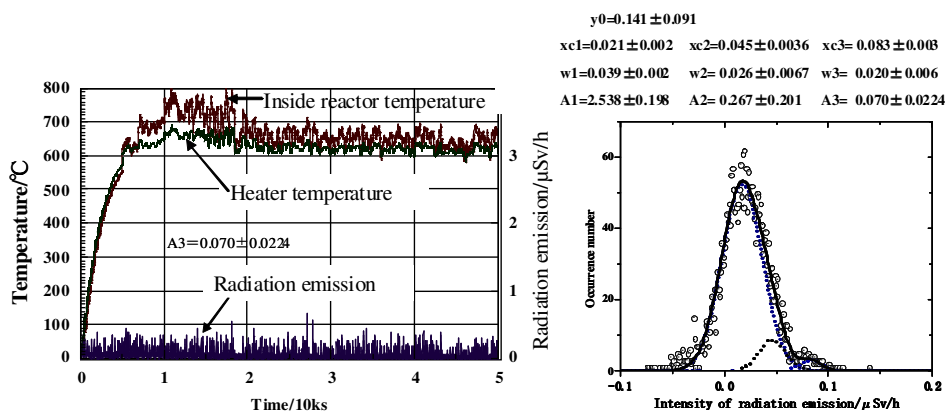


Fig. 2 - An example of anomalous heat. Fig. 3 - Intensity spectrum of radiation emission from Fig. 2.

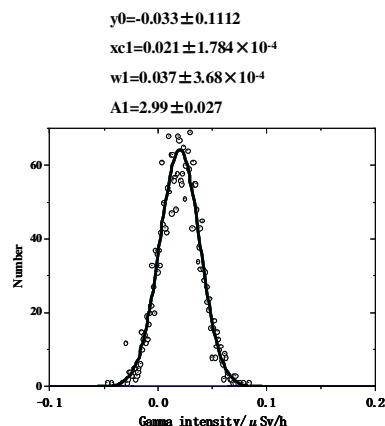
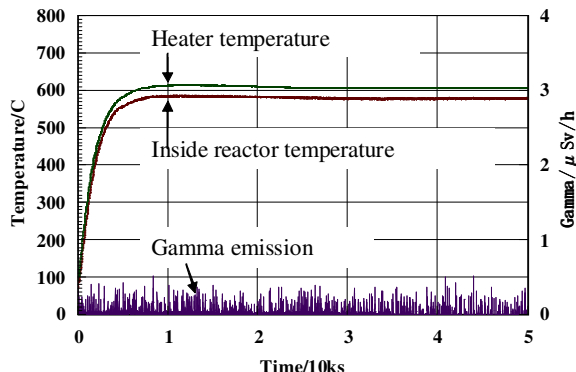


Fig. 4 - An example with no anomalous heat.

Fig. 5 - Intensity spectrum of radiation emission from Fig. 4.

Total heat production can be estimated from the calibration curve and total duration of excess heat production which started around 18 ks and continued to 50 ks. Over this period, the average temperature was 50°C above the calibration point continuing for 40 ks. Based on the calibration point of 600°C (in Fig 3) the excess was roughly 5 W on average, so total heat production was roughly 160 kJ for the entire run.

Figure 3 shows the intensity distribution of gamma-ray emission from the ionization chamber detector. Two peaks are shown, 0.05 μSv/h and 0.09 μSv/h of the background by calculated peak analysis. These are clearly differentiated from the background of 0.02 μSv/h. Gamma-ray emissions were weak but they were clearly observed when intense excess heat was generated.

Figure 4 shows an example of a test with no excess heat. As in the test shown in Fig. 2, 1 g of phenanthrene was exposed to a 70 atm of hydrogen gas, and furnace heater power was set for 60 W. However, the Pt catalyst was not placed in the cell. By 10 ks, the temperature stabilized at about 600°C. After that the temperature remained stable and settled.

Figure 5 shows the intensity distribution of gamma-ray emission for the test shown in Fig. 4. Only the background peak is observed. Calculated peak analysis reveals no other peaks.

4. Discussion

In these experiments, a 1 g sample of phenanthrene was used, which is 5.6×10^{-3} moles. Oxidation, reduction and other chemical reactions can produce at most a few kilojoules from this much material, whereas this reaction produced on the order of 100 kJ of heat. That is roughly 100 times larger than a chemical reaction. Therefore, a chemical reaction as the source of this heat is conclusively ruled out. Furthermore, during the experiment weak radioactivity was observed, probably γ or x-rays. If these are γ -rays that is proof this is a nuclear reaction; if they are x-rays then they were generated by some other mechanism. The detector used in this study can detect an energy range starting from 20 keV up to high levels. The cell wall is 3 mm thick stainless steel. The x-ray mass absorbent coefficient for 20 keV x-rays is 100 cm²/g, so most of the radiation would not penetrate the cell wall. However, if these are γ -rays at around 1 MeV, 80% of the radiation would pass through the cell wall. Therefore, although we cannot be certain it is very likely these are γ -rays

The excess heat and radiation were not strongly correlated, but they both indicate that some sort of nuclear reaction occurred. With additional research to understand the mechanism of the reaction, this reaction might possibly become a practical source of energy.

5. Conclusions

The anomalous energy generation cannot be the product of a conventional chemical reaction for the following reasons:

- At these temperatures, hydrogenation reactions are endothermic, not exothermic.
- Based on this massive reaction and the mass of the reactants, the total heat release far exceeded any known chemical reaction.
- There was no chemical fuel in the reactor cells.
- There were no chemical reaction products. Except the platinum screen that was coated with carbon, the components and chemical species in the cell, including phenanthrene and hydrogen gas, remained essentially as they were when the experiment began,
- Gamma-ray emissions were detected. These emissions are characteristic of a nuclear reaction. These emissions might have been x-rays but this is unlikely.

The reaction is reliably triggered by raising temperatures above the threshold temperature of ~ 580°C and hydrogen pressures above 60 atm. The reaction can be quenched by lowering the temperature inside the cell to below ~ 500°C. When the required conditions are satisfied excess heat is generated with high reproducibility, but the rate of heat production is not stable. There is only a small amount of reactant in the cell, and it is likely that the accompanying ordinary chemical reactions that occur in the cell soon consume it all.

Acknowledgements

The author would like to acknowledge financial support from the Hokkaido Gas Foundation in 2007, and from Mr. Brian Scanlan of Kiva Labs. The author would also like to express thanks to those who provided assistance, samples, analysis, and consultation in these experiments, including Mr. Hiroshi Yamakawa of Honda Technology Research, and Mr. Toshiyuki Sanpo, Dr. Yuji Yamauchi, Dr. Fumiyuki Fujita of the Department of Engineering, Hokkaido University. Finally, author would like to express thanks for the effort of translation to Mr. Jed Rothwell.

Abnormal excess heat measured during Mizuno-type experiments: a possible artefact?

J-F. FAUVARQUE, P. P. CLAUZON, G. J-M. LALLEVE

CNAM Laboratoire d'Electrochimie Industrielle 2 rue Conté 75003 PARIS

G. LE BUZIT

CNAM Laboratoire des Sciences Nucléaires 2 rue Conté 75003 PARIS

« Anyone who has never made a mistake has never tried anything new » A. Einstein

Abstract. Recently performed Mizuno-type experiments confirmed generation of excess heat but not at the rate reported in ref. 2 (Sotchi -ICCF13). The main reason for the discrepancy is now clear; the bandwidth of our Unigor wattmeter, used in old experiments, was insufficient for correcting measurements of highly fluctuating electric energies.

1. Introduction

Using the boiling water calorimeter, described in reference 2, we measured excess heat generated during high voltage electrolysis. The experimental setup is shown in Figure 1. The input electric energy was measured with a D6000 Norma Goerz wattmeter, rather than with simple Unigor instrument. Note that the frequency bandwidth of the Goerz wattmeter is significantly wider than that of the Unigor wattmeter (see below). The new setup, containing the boiling water calorimeter, allowed us to eliminate two additional artifacts that could possibly be responsible for systematic errors:

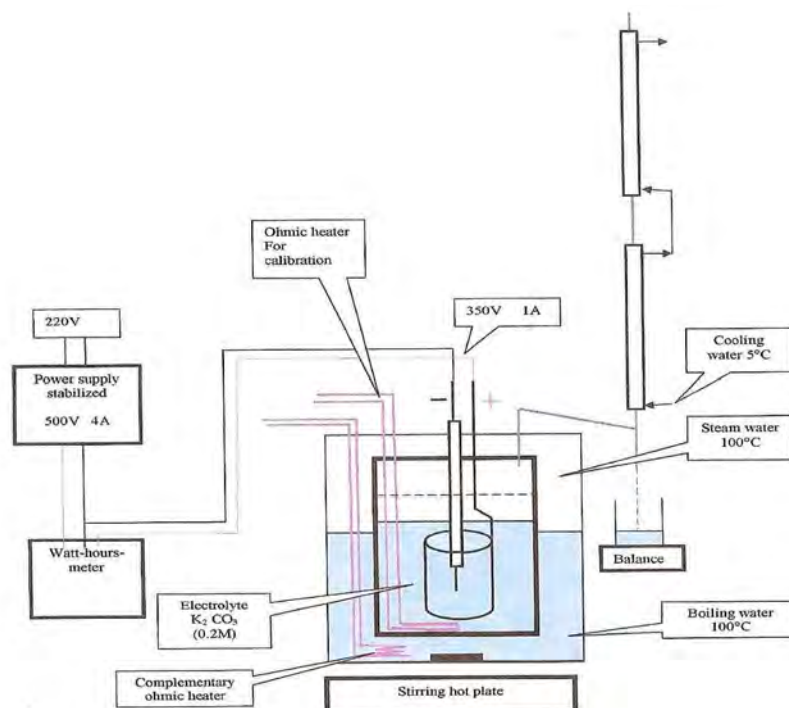


Fig. 1 - Experimental setup.

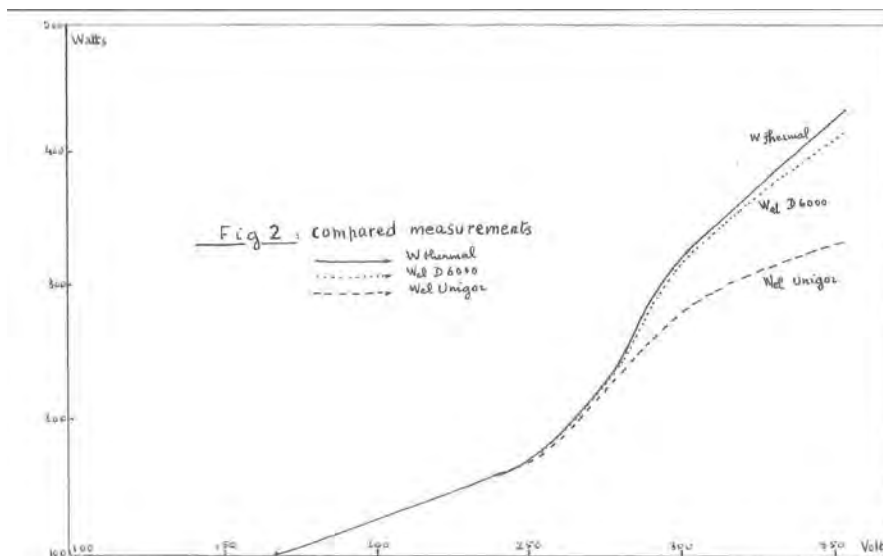


Fig. 2 – Comparison of power measurements

- storage and destorage (the internal reactor temperature remains always at 100°C and then do not allow any stored heat)
- electrolyte droplets losses (the condensed steam gives an easy chemical way to check up if electrolyte droplets are carried on)

Let us elaborate on the issue of electric power measurements. In the early experiments, they were performed by using the Unigor wattmeter. Its readings were shown to be reliable when the electrolytic cell was replaced by an ohmic resistor, that is when the current was constant. But the current in the electrolytic cell rapidly fluctuated between zero and approximately ten amperes. Wide fluctuations of the current, observed with the oscilloscope, were responsible for wide fluctuations of the voltage between the anode and the cathode. Unlike the Unigor 390M (bandwidth up to 0.1 MHz), the Goerz D6000 instrument (bandwidth up to 2 MHz) is designed to function properly at such fluctuations.

As seen in Fig. 2 (curves normalized at 200 volts), the measurements made with the D6000 wattmeter were very close to the thermal values. On the contrary, the Unigor values did not agree with the D6000 values, specially in the 280-300 volts region. This explains the discrepancy between our now results and results reported in (2). Oscilloscopic measurements of electric energy were essentially the same as those performed by using the D6000 wattmeter (even at 300 V, where arcing was very intense). The previously-reported excess heat was not observed in our new experiments.

2. Return to our Yokohama type experiments (ref. 1)

Therefore, we tried to understand why the abnormal excess heat seemed to have disappeared. We have then thought that the reactor in our boiling water calorimeter, was not large enough (only 1 liter) for the electrolysis to be made in and that violent moves of the electrolyte consequently disrupted the plasma around the cathode. Thus, we suspect that this phenomenon is responsible for the disappearance of the abnormal excess heat.

We decided to return to the experimental set-up presented in ref.1 (Yokohama - ICCF12), in which the volume of the beaker was 5 times larger for the electrolysis, but we replaced this 5 liters beaker by a Dewar flask of the same volume. See fig 3.

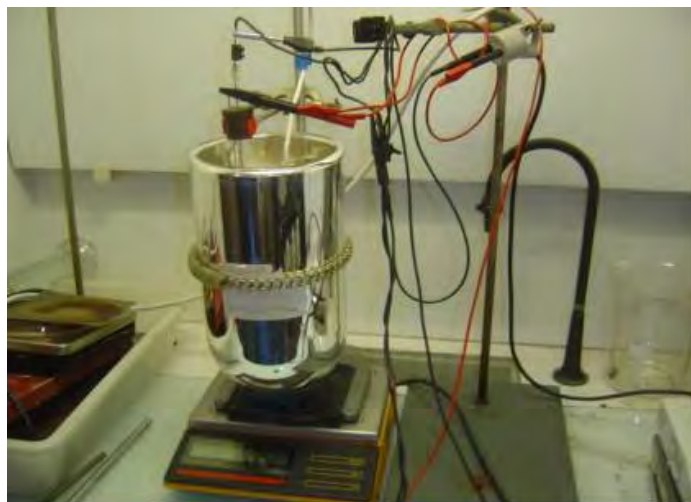


Fig. 3 - Experimental Yokohama (ICCF12) set up.

Essential parameters of experiments described in ref. 1 and ref. 2 were as follows:

- a Sartorius balance, measuring up to 6 kg at an accuracy of 0.1 g
- a continuous current electricity supply (500 volts, 4 amperes)
- a tungsten cathode of 2.4 mm
- a wire in platinized titanium for anode
- an electrolyte made with K_2CO_3 at 0.2 M

Calibration tests, made with a thermal resistance (~ 150 ohm), showed that in the range of 250 w to 700 w the thermal losses (escaping heat) were very small and constant.

Our first electrolysis experiments were perturbed by the storage and destorage problem. We found out that the problem was due to non uniform temperature distribution (not 100°C everywhere) inside the Dewar flask due to electrolyte stratification. We solved this problem by leaving inside the Dewar flask a thermal resistance giving a continuous power at about 300 watts. Convection of hot electrolyte inside the Dewar flask is sufficient to establish the uniform temperature distribution (100°C) within the flask. Of course, we have to take into account the continuous loss of water due to this 300 watt extra power.

Thanks to our quite deep Dewar and also to a well arranged perforated Teflon screen just above the electrodes, we did not notice any electrolyte droplets losses. Moreover, the storage and destorage problem was solved and verified by measurements made with an auxiliary thermal resistance.

3. Results obtained:

First, we will give an example of our experimental procedure, as done in our run of July 17th 2008.

Voltage applied was 300 Volts.

Duration of the run : 25 minutes.

T minutes (min)

M: water mass (g) .

Wh : Electric energy furnished (Wh).

(Water loss due to the auxiliary thermal heater for 2.5 minutes : 22g)

Table 1.

T	M	Wh
0	-150	545
2.5	-183	560.6
5.0	-240	575.1
7.5	-276	589.6
10.0	-328	602.8
12.5	-375	615.9
15	-416	628.9
17.5	-447	641.8
20	-493	654.7
22.5	-530	667.3
25	-585	679.7

The mean **COP** (coefficient of productivity) during this run may be obtained as following :

Mean thermal energy produced by electrolysis for **2.5 minutes** between 2.5 and 25 minutes (9 intervals of 2.5 minutes):

$(585-183)/9 - 22 = 22.7$ g , that is to say : $22.7 \times 2260 = 51302$ joules.

Electric energy furnished for **2.5 minutes** between 2.5 and 25 minutes :

$(679.7-560.6)/9 = 13.2$ Wh, that is to say : $13.2 \times 3600 = 47520$ joules

Mean COP value: $51302/47520 = 1.08$

The preliminary results obtained by the end of July 2008, tests that, up to now, we were not able to pursue due to the lengthy reorganization of our society are the following:

Table 2.

Voltage applied	COP values			
200 V	1.00			
250 V	1.09	1.00	1.10	0.97
300 V	1.06	1.08	1.04	1.01

The accuracy of our measurements is fairly good (2 to 3 % max. error margin), as we have a measurement made every 2.5 minute during about 20 to 30 minutes duration for a given test. On the other hand, in this type of experiment, it is difficult to imagine to have negative thermal losses (destorage problem has been solved) and usually, the COP values are under 1.00. One can however notice that the positive COP values larger than one are not very large and that they are not as reproducible as formerly announced in ref.2.

4. Conclusion

After a severe doubt due to the use of a wattmeter without a sufficiently large bandwidth, we were able to find again values for the ratio of outlet thermal energy to inlet electric energy (COP) larger than 1.00 . We think that these values are meaningful. For the time being, these values are not very large and do not occur as often as we wrote in ref. 2. We may add that we get an hypothesis for the disappearance of the excess heat : the size of the reactor in our boiling water calorimeter was too small and the violent moves of the electrolyte inside disrupted the plasma around the cathode and the abnormal excess heat disappeared.

However, although we think that these results are quite encouraging, they need to be confirmed and we need a bigger involvement of new sponsors in the future studies because the hope of a clean, cheap and abundant energy deserves it, even if some uncertainties cannot be completely avoided.

Acknowledgements

We want to thank Didier NOËL (EDF – Etudes et recherches) very much for his advice and his lent of the D6000 Norma Goerz wattmeter. We also thank Jean-Louis NAUDIN very much for his advice during our work.

5. References

- [1] « Abnormal excess heat observed during Mizuno-type experiments » by J.F. Fauvarque- P.P. Clauzon- G.J-M. Lallevé – Service d'électrochimie Industrielle du CNAM – Paper given at Yokohama – Nov.2005 – ICCF12 meeting.
- [2] « A boiling-water calorimeter for the study of the abnormal excess heat observed during MIZUNO-like experiments » by J.F. Fauvarque – P.P. Clauzon – G. J-M. Lallevé – G. Le Buzit (CNAM Paris) paper given at Sochi – Nov 2007 – ICCF 13 meeting.

Sonofusion Produces Tritium That Decays to Helium Three

R. S. Stringham
First Gate Energy

E-mail: firstgate@earthlink.net

Abstract. Three main points are covered that are unique to Ti sonofusion target foils. These are surface modification to TiO_x shown by photos and scanning electron microscope, SEM, photos, and the decay measurement of tritium, T, by mass spectrum analysis, MS, to 3He , the Ti target foils, and the unexplained production of $1\mu m$ Ti hollow tubes shown in SEM photos.

1. Introduction

A collection of D^+ implanted Ti sonofusion data, $D_2O \rightarrow 2D^+ \rightarrow T + H + 17 \text{ MeV}$, are measured and described as $T \rightarrow ^3He$. The cavitation bubble jet implants into a Ti target foil producing fusion and heat. Along with T some 4He was also detected but will not be covered here. This work was spread over several years of sonofusion laboratory work. All experiments described here used $100 \mu m$ Ti target foils in M II and M III reactors. Experiments show some fusion products, the observed small but high temperature events in the foil, ejecta sites, and induced MHz acoustic standing waves in the target foils. The Ti foil behaves differently than most other target foils in that it forms a bonded hydride that stops the deep loading found in mobile D^+ lattices. The Ti shows very colorful markings due to thin film build-up of TiO_x on its surface. The unique formation of hollow Ti $1 \mu m$ tubes, atoms thick, were observable by SEM photos.

2. Experimental and data

Two Ti target foils are described, one exposed to 20 KHz, foil Ti 3A (4-2) and the other to 46 KHz, foil Ti 17. Ti 3A was run at Los Alamos National Lab., LANL. The other foil, Ti 17, was run at the EQuest laboratory on 2/09/95. The Ti 3A run in the MII reactor was a dual cavitation system, Fig. 1,2,3. The configuration of the dual concentric cavitation reactors was powered by a 5cm diameter Ti horn. The top reactor circulated D_2O ; the bottom reactor H_2O . The reactors were separated by 0.6 cm thick x 7 cm diameter stainless steel reactor volume. The acoustic energy was transferred through the disk producing the transient cavitation bubbles that implanted plasma jets into these foils. The experiments were run with the assistance of Tom Claytor, Dale Tuggle, and Russ George, The gas sample was collected from over the circulating D_2O in the MII reactor by gas transfer to an evacuated 50 cc sample volume on 4/29/94. Fig. 2.

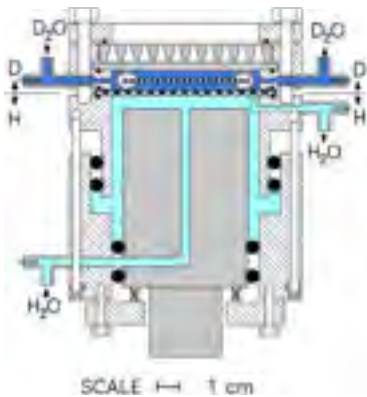


Fig.1- MII, reactor 20 KHz was used in the tritium and 3He experiment with a heater for calibration.



Fig.2 - 50 cc sample volume was used for MS analysis.



Fig.3 - MIII, 46 KHz reactor, had two opposing piezos with a calibration heater.

Table 1. The table of mass spectral, MS, data produced by Brian Oliver. Days represent days after gas collection.

Sample Volume 4-2.	Analysis Date.	Days.	T in Volume, atoms.	³ He in Volume, atoms.
2-0	4/29/94	0	Leak ?	0+
2A	9/14/94	139	1.13E+15	1.71E+13
2B	9/14/94	139	1.10E+15	1.67E+13
2C	9/14/94	139	1.08E+15	1.63E+13
2D	2/06/95	285	1.03E+15	3.89E+13
2E	2/06/95	285	1.00E+15	3.80E +13
2F	2/08/95	287	9.76E+14	3.73E+13

Shown in table 1 is the experimental sonofusion data, Ti 3A (4-2) tritium, analyzed for T via the evolution of ³He that was identified by mass spectrometry, MS. From this experiment at LANL, the 4-2 sample was chosen. The exposed Ti target foil, 5x5x0.01 cm, in a controlled flow of D₂O and Ar at 200 ml/min was cavitated for 18 hours. The 200-watt acoustic input into a 35 cc reactor volume was driven at 20 KHz by a Heat Systems 5 cm diameter Ti horn. The steady state temperature was 61°C, the external pressure of Ar at 30 psig. The lower H₂O reactor was pressurized by N₂ gas to reduce the population of cavitation bubbles (high pressure stops the formation of cavitation bubbles). The dual sonofusion reactor MII was vacuum tight. The gas samples were collected by vacuum transfer in evacuated 50 cc stainless steel sample volumes. Sample 4-2 was collected at the end of the run on 4/28/94. All these dates are very important for measurements as $T \rightarrow {}^3\text{He} + \beta + \nu$ at a decreasing rate of ³He production in the sample volume. T has a half-life of 4475 days and $\lambda = 1.56 \times 10^{-4}/\text{days}$. The MS data is shown in column 5 in atoms. Brian Oliver of the DOE using his tested methodology for ³He analysis performed the mass spectrometry. Column 2 shows 3 dates and column 3 shows days between measurements. These measurements show a disintegration constant that was consistent with the decay of T to ³He. A plot of this data shows the T decay rate in the sample volume to be $\Delta(\text{To} - {}^3\text{He})/\Delta t$ is λ and $\text{To} - {}^3\text{He} = T$, where To is initial tritium. The calculated decay of T is shown as circles in Fig. 4 a,b (4b shows expanded scales).

In the experiment the hypothetical addition of less than 0.66×10^{13} atoms to the initial ³He alters the To, initial titanium atoms, and corrects the data for a possible storage leak. The data in the graph shows that there is a good fit that incorporates the day the gas sample was collected, See table 1. The date produced by the uncorrected data was 30 days later and is shown by the squares in Fig. 4a. With this correction there is a good fit to Brian Oliver's data (in Fig. 4b the circles are calculated data). Brian's data has the right slope but the wrong intercept. Correction for a leak remedies that problem.

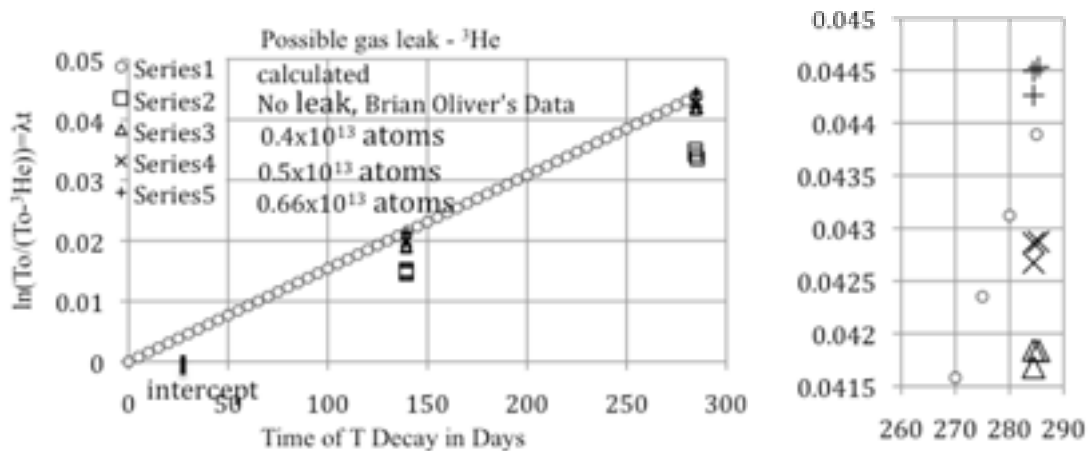


Fig. 4a,b - Graph of the MS data. Leak of gas during storage of 139 days (leaked atoms of ³He corrects the data)

The 50 cc sample volume shown in Fig. 2 may have had a slow leak in its valve, a Nupro (SS 4BK TW-VA), during its storage.

Ti target foil Ti 17 was run at EQuest Laboratory in Mountain View, CA. USA at 46 KHz. The reactor MIII consisting of opposing dual piezo ceramic disks produced smaller cavitation bubbles, same energy density, in circulating D₂O. The configuration of the concentric dual piezo stacks bonded to opposing stainless steel disks held about 0.5 cm gap with 5x5x.01 cm Ti target foil centered in the 6 cm diameter reactor. A controlled flow of D₂O passed through the 14 ml reactor volume at a rate 60 ml/min. Cavitation bubbles formed at the target foil surface were implanted via the plasma jets of deuterons and electrons into the target lattice. The MIII reactor run was pressurized with 3 atmospheres of Ar. The calorimetry was a flow through type calibrated by a variable resistance heater and measured at steady state temperatures and D₂O flow rates. Most of the acoustic activity occurred in the center 50% of the target foil.

3. Discussion

The graph, Fig. 4a, of the MS data was gathered over a period of 284 days with an assumed 0 atoms of ³He on the day the 50 cc gas cylinder 4-2 was filled via vacuum transfer with the gas from the reactor. This transfer effectively removed 50% of the reactor gas. The gas in the sample volume was flown from LANL to the EQuest laboratory where it spent most of the 139 days in storage. The sample volume was mailed to Brian Oliver at the Rocketdyne DOE facility for the 4-2 mass spectrum analyses. Table 1 of the data from the MS of Brian's gas analysis from sample volume Ti 3A (4-2) was on the 9/14/94 for samples A, B, and C and was repeated 145 days later on the 2/06/95 for samples D, E, and F. The intercept of these two points with the timeline in Fig. 4a should be the time the sample was collected, 4/27/94. However, this is not the case. Brian Oliver's calculated sample volume collection date shows an intercept 30 days later; data shown by squares, Fig. 4a. The intercept should be moved to the earlier collection date, 0 days, not 30 days later. The initial storage time was 139 days. This can be done if one assumes a small leak of gas, T and ³He, from the sample volume during that period. It is enough to identify T decay as a straight line from the two MS measurements shown in Fig. 4a, at 139 days and 285 days, that has the slope of the disintegration constant λ for T. But it is better to show that the intercept point was on the day of the gas collection. A leak during the initial storage period, valve later closed at 139 days, can explain the shift in the timeline intercept. Or possibly doping of the sample volume with DTO might be the explanation for Brian Oliver's intercept date. Tritium is obviously there in the sample volume. If the sample was spiked, it happened before the sample was mailed to Brian Oliver about 30 days after the sample collection. In any case Brian Oliver's data is a good example showing the presence of T in the sample volume Ti 3A (4-2).

The photo Fig. 5 of the Ti 3A target foil shows interesting colorful visual modification of its surface produced by the sonofusion process. Similar observations in Ti 17 are shown in Fig. 6. These colorful standing wave patterns are produced by thin layers of TiO_x deposited during cavitation that is unusual in an apparent reducing environment of D⁺. These standing waves appear to be associated with the Ti target foil's mass and thickness producing an induced MHz resonance frequency via the primary 20 KHz resonance reactor frequency. The Ti surface lattice and D⁺ form stable bonds and the surface is covered with thin layers of mostly TiO_x and TiD_x [1,2]. The jets that implant leave their bulky ionic oxygen atoms combined with the surface Ti of the target foil. The D⁺ and e⁻ are implanted into the Ti lattice and form the transient imploding cluster, the cluster model [3,4,5]. Surface color and erosion patterns are not unique to Ti target foils [6].

The SEM of the surface of the two Ti target foils, Ti 3A and Ti 17, are very informative via SEM photos, Fig. 7 and Fig. 8. The two are almost indistinguishable from each other. The 20 to 50 nm nodule surface of sonofusion Ti target foils are different from those foils that have mobile D⁺ in their lattice [5]. The very mobile D⁺ ejecta from the lattice matrix as found in Pd and Ag target foils [3,5,6]. The SEM of the surface of Ti 3A shows the presence of very small hollow 1 μ m diameter tubes of Ti. They appear as a complex network of black lines on the target foil surface, see Fig. 9. SEM photos discovered these several years after Ti 3A foil removal from the M II reactor. Further SEM magnification shows that these tubes are only a few Ti atoms thick and about a micrometer in diameter, Fig. 10. The Energy Dispersive X-ray Spectroscopy, EDS analysis, shows a degree of transparency and perhaps shadows, Fig. 10. These tubes were thought to be fragile and certainly would not last long in the cavitation environment so their existence would be limited to a time period just before the reactor was turned off. The SEM photos, Figs. 7, 8, and 9, were taken by Jane Wheeler of Evans Lab, Sunnyvale, CA, and six months later Ti 3A was reanalyzed by Lorenza Moro of SRI, Menlo Pk., CA., Fig. 10.

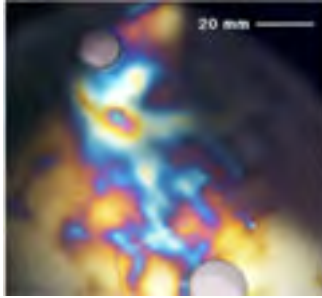


Fig. 5 - surface Ti 3A (20 KHz).



Fig. 6 - surface Ti 17 (46 KHz).

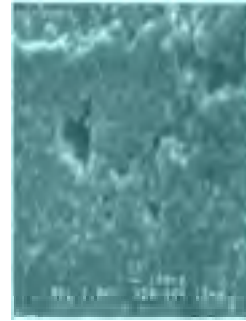


Fig.7 - SEM photo of Ti 3A.

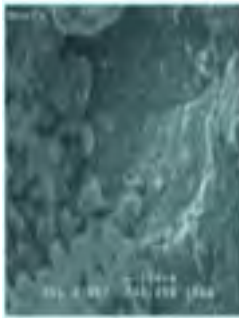


Fig. 8 - SEM photo of Ti 17



Fig. 9. - SEM; tube network

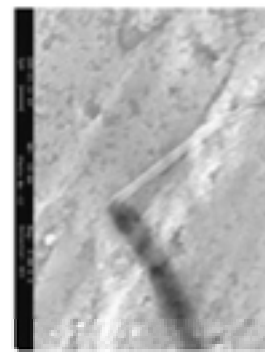


Fig. 10 - SEM of 1 μm

4. Summary

The Ti experiments are worth repeating and the many unanalyzed foils are worth analyzing [6]. T was measured and definitely decaying in the sample volume. The MS analysis showed a 30-day shortfall of the true collection date that can be corrected by assuming a small initial leak from the sample volume before the first MS measurement. Introducing a phantom leak improves the data to the correct time line. The TiO_x and TiD_x surface appearance for the two Ti target foils at different frequencies were the same except that the pattern was larger for the 20 KHz foil. The Ti tubes defy explanation at this point. Collapsing bubbles, their implanting jets, and D^+ clusters produce heat and nuclear products and exist in other systems [5].

Acknowledgements

Tom Passell of EPRI funded Brian Oliver's DOE MS analysis, $T \rightarrow {}^3He$ and $2D^+ \rightarrow {}^4He$.

5. References

- [1] W. Lisowski, E. G. Keim, et al, *Analytical and Bioanalytical Chemistry*, Vol 2, Num. 4, (June 2006).
- [2] SEM and EDS analysis by Jane Wheeler, Charles Evans Lab., Sunnyvale, CA, (2001).
- [3] R. S. Stringham, *Proceedings ICCF 8*, ed. F. Scaramuzzi, Italy, SIF. vol. 70, 299, (21-26 May 2000).
- [4] R. S. Stringham, *Proceedings ICCF 10*, ed. Hagelstein, Chubb, USA, CMNS. 233, (24-29 Aug 2003).
- [5] R. S. Stringham, ACS book, *LENR sourcebook, vol. 2*, ed. by Steve Krivit and Jan Marwan, (2009).
- [6] First Gate's collection of sonofusion exposed target foils dating from 1989 to 2005, over 50 foils.

Diurnal Variations in LENR Experiments

D. J. Nagel¹, T. Mizuno², D. Letts³

¹The George Washington University, Washington DC USA

²Hokkaido University, Sapporo Japan

³Lettslab, Austin TX USA

E-mail: nagel@gwu.edu

Abstract. Two very different LENR experiments exhibited daily variations in their characteristics or outputs. Comparison of the variations for the experiments forces the conclusion that the measured variations are artifactual. That is, they are not due to the influence of an external diurnal mechanism such as cosmic rays. However, the causes of the observed variations are not understood. Such understanding is important for the conduct of robust LENR experiments to obtain credible data. It is also critical to the reliable operation of eventual LENR power sources.

1. Introduction

Diurnal variations occur over the course of a day, and typically recur every day. Daily variations in light and temperature due to the rotation of the earth are familiar examples. Low Energy Nuclear Reaction (LENR) experiments should not be subject to diurnal variations. However, there have been reports of daily cyclic changes in the conditions and output of LENR experiments. The purpose of this paper is to report and examine such variations in two experiments, one in Hokkaido, Japan, and the other in Texas, U. S.

2. Mizuno Experiment

The first experiment, which exhibited long term diurnal variations, was aimed at the study of transmutation reactions [1]. Some of the equipment for that electrochemical experiment is shown in Fig. 1. The experiment was pressurized to about 7.4 atmospheres and operated at temperatures near 375K. The D/Pd loading ratio was measured for the duration of the experiment (about 800 hours).

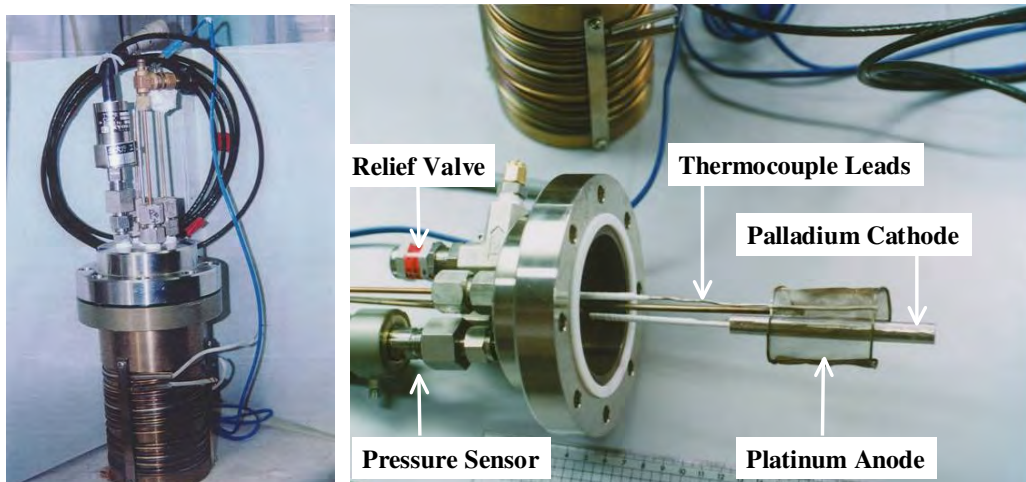


Fig.1 – Exterior and interior of the pressure vessel for a search for transmutation products in Hokkaido.

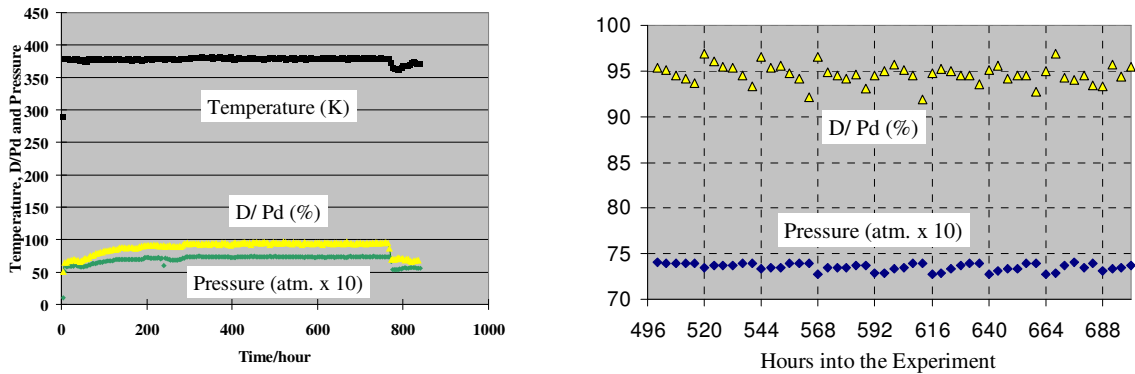


Fig. 2. Time histories of the pressure, loading and temperature for the high-pressure transmutation experiment.

The long-term record of the pressure, loading and temperature for the experiment is given in Figure 2. A blow up of the data from 500 to 700 hours is also in that figure. It can be seen that the pressure (P) and loading (L) vary inversely with each other on a 24 hour cycle. The degree of the two modulations is small in both cases, with $\Delta P/P$ and $\Delta L/L$ both being a few percent. The variations have sawtooth shapes, with the discontinuity occurring at midnight local time. The regularity of the sawtooth shapes evolved during the experiment. Variations in the ambient temperature in the laboratory cannot account for the measured variations because the temperature of the experiment was much greater than the laboratory temperature.

3. Letts-Cravens Experiment

The experiment in Texas was run for a much shorter time than the one in Hokkaido. It involved the use of laser stimulation and the measurement of excess heat. The experiment was controlled remotely via the internet from Cambridge MA during the 10th International Conference on Condensed Matter Nuclear Science [2]. Figure 3 shows the equipment for the experiment.

Figure 4 shows the excess power (mW) for somewhat over 2.5 days of the experiment. It is seen that the signal-to-noise for the excess power measurement is about 10. The power varies with a cycle time of about one day, although the shape of the daily variation is not the same on each of the days. The peaks of maximum output power occur in the range of 1800 to 2000 local time. The most remarkable aspect of the

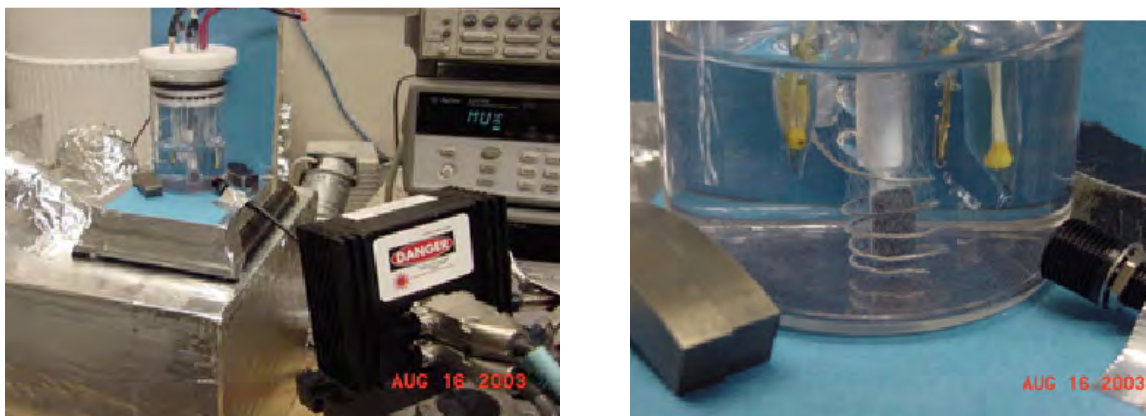


Fig.3. Overall photograph of the excess power experiment and close-up of the electrochemical cell in Texas.

power data in Figure 3 is the depth of the modulation. The variation the first day is from a low near 50mW to a peak at 450 mW. The corresponding variation the second day is from 200 to 600 mW. The third day exhibits a variation of about five-fold from 150 to 750 mW.

The time history of the laboratory temperature during the experiment in Texas is also in Figure 4. It is seen that the magnitude of the noise decreases noticeably when the excess power is high. However, the temperature variations both during and between episodes of peak excess power is 0.5 C or less. These are small changes compared to the large modulation of the excess power. Nonetheless, the clear changes in the noise of the temperature measurements over the course of this experiment are interesting.

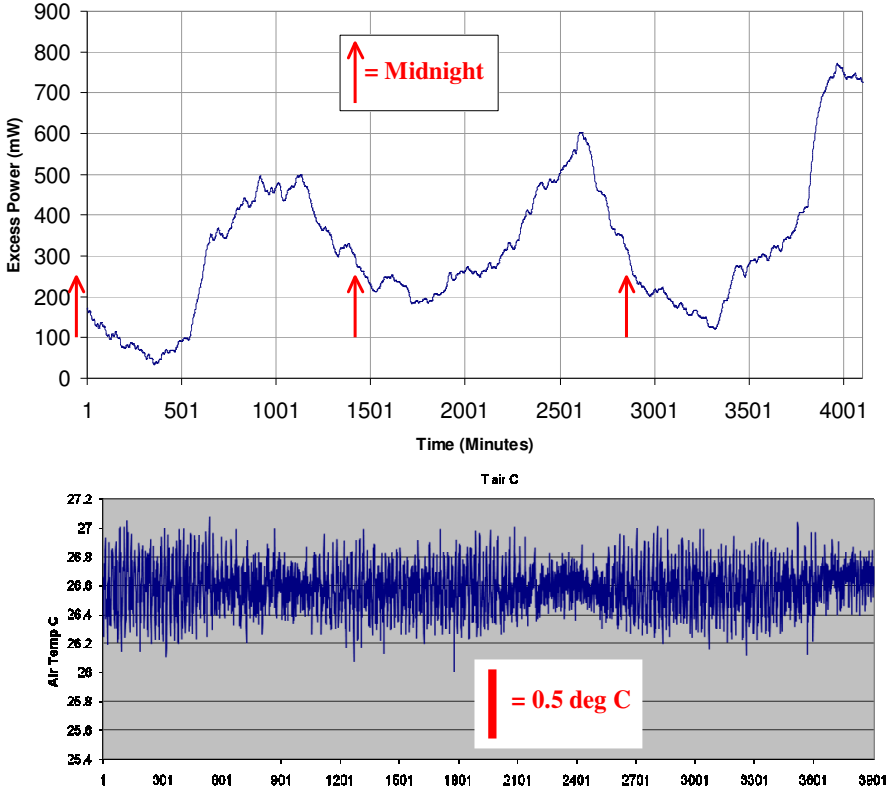


Fig. 4. Time histories of the excess power and the laboratory temperature in the laser-stimulation experiment. The two time traces are aligned vertically to permit comparison of power excess and temperature variations.

4. Discussion and Conclusion

One of the primary motivations for this study was to learn if the observed diurnal variations in LENR experiments could be due to cosmic ray particle bombardment. That was not thought to be likely because of two reasons. First, the fluxes of cosmic rays at sea level are relatively small, save for neutrinos, for which the interaction cross section in experiments, such as the two of concern here, is negligible. Second, if globally-present cosmic rays were involved in LENR experiments, diurnal variations would be more widely observed in the field. However, if a connection between observed variations in LENR experiments and cosmic rays could be made, then LENR experiments might be made to serve as cosmic ray detectors. In that case,

comparing the responses of LENR experiments on the surface of the earth and in deep mines would take on another significance.

What if the case can be made for the fundamental reality of diurnal variations in LENR experiments can be made? Then, there would arise the need for their theoretical and computational explanations. This would further complicate the understanding of LENR.

Contrasting the daily variations in the Hokkaido and Texas experiments is instructive, as shown in Table 1.

Table 1. Comparison of the Characteristics of Two LENR Experiments Exhibiting Diurnal Variations

Factors	Mizuno	Letts-Cravens
Duration of experiment (Days)	35	2.7
Shape of Daily Variation Curve	Sawtooth	Pseudo-Sinusoidal
Peaks (Local Time)	Midnight	1800-2000
Depth of Modulation (% of Average)	About 2	> 50

The major variations in the shapes, local times for peak values and extent of daily swings in Table 1 indicate that the variations are probably not due to some external cause, such as daily variations in cosmic ray neutron or other fluxes [3]. That is, the variations appear to be artifactual. It remains to be seen if an explanation for the observed variations can be found for either experiment.

Understanding and explaining uncontrolled variations in the behavior and output of LENR experiments is important for two reasons. The first is the ability to conduct scientific experiments that yield reproducible, reliable and credible data. Given the large daily variations in the excess power in the Texas experiment, the controllability, and hence the utility of potential engineered commercial LENR power sources, are at stake.

Acknowledgements

Interesting discussions and email exchanges on diurnal variations with Jean-Paul Biberian, Dieter Britz, Xing Zhong Li, Michael C. H. McKubre, Michael E. Melich, Peter Mobberley and Mahadeva Srinivasan are recalled with pleasure.

5. References

- [1] Mizuno, T., *Transmutation Reaction in Condensed Matter* in J. Marwan & S. B. Krivit (Editors), Low-Energy Nuclear Reactions Sourcebook, American Chemical Society symposium Series 998 (2008) 271-294, DC Oxford University Press
- [2] Letts, D., and Cravens, D., *Laser Stimulation of Deuterated Palladium: Past and Present* in Peter L. Hagelstein and Scott R. Chubb (Editors), Condensed Matter Nuclear Science, Proceedings of the 10th International Conference on Cold Fusion, pp. 159-170, World Scientific (2006)
- [3] Chilingarian, A. and Mailyan, B., *Investigation of Daily Variations of Cosmic Ray Fluxes in the Beginning of 24th Solar Activity Cycle*, Proceedings of the 31st International Cosmic Ray Conference, pp. 104, Lodz 2009, <http://us.aragats.am/files/Conferences/2009/Investigations.pdf>

Can Water be the Origin of Excess Energy?

A. K. Al Katrib and David J. Nagel

The George Washington University, Washington, DC, USA

E-mails: amk12@gwu.edu

Abstract. This study was initiated due to the concern of some critics of LENR research that small energy changes in many H₂O or D₂O molecules in electrochemical cells can explain observed excess heat. More than three hundred LENR papers from 1989 to 2008 that reported excess energy were acquired and reviewed to extract quantitative results and other information. Excess energies and cell volumes were found in 17 papers. These data were used to compute eV per water molecule values. Most experiments showed excess energy outputs that would lead to ratios below the vibrational energy of water molecules at room temperature (0.04 eV/molecule). However, 65% of the papers, which reported both excess energies and cell volumes, indicated values significantly higher. The highest reported value was 42.6 eV/molecule. Eleven ratios are far beyond what is plausible for water to be the source of anomalous heat. Therefore, it is concluded that some unknown rearrangement of water molecules in many LENR experiments is not the source of excess heat.

1. Introduction

Ever since first publically announced in 1989 by the two chemists, Martin Fleischmann and Stanley Pons, the discovery of Cold Fusion has caused great controversy. Criticism stems partly from the lack of theoretical understanding. And, there are substantial implications of the field, which promises abundant and distributed energy sources with little radiation, in competition with other developing energy sources. One main criticism that faced this field throughout its past 20 years has been the source of reported excess energy, whether or not it can be attributed to nuclear mechanisms, chemical reactions, or molecular rearrangements. Excess energy is defined as the final energy output in excess to the energy applied to an experimental cell.

Several papers have been published in the defense of LENR. Their main objectives were to explain the validity of the observed excess heat to rebut critics and minimize skepticism. One such paper published in 1989 was the “Eight Chemical Explanations of The Fleischmann-Pons Effect” [1]. It highlighted possible factors responsible for the 3W/cm³ observed in the author’s experiments. In another response to critics, it was shown that energy stored in defects in an electrode could not account for observed excess energies.

This study was designed to quantitatively examine the possibility that small energy changes in the many water molecules in electrochemical LENR experiments could account for measured excess heat. Lists of scientific papers, articles, and reviews were thoroughly screened to create a database of reports of excess heat. Cell volumes and excess energy data from these papers were tabulated and graphed. The results counteract claims that attribute excess energy to water molecule rearrangements. A secondary goal of this work was to create a database for additional useful information. Later publications will be based on that information.

2. Water Energies

Water is arguably the most important chemical on earth. As a result, it might be the most studied. And, it is also a very unusual substance. For example, water is most dense at about 4 C above its melting point, unlike most substances that are denser in the solid phase rather than in the liquid phase. Hence, water ice floats. Were that not true, the world would be very different. Despite its unusual and complex properties, there are only two component elements in water, and its structure is simple. The water molecule is polar, with more negative character on the side with the oxygen atom and more positive character on the sides with the two hydrogen atoms. This enables electrostatic hydrogen bonding, as indicated in Fig. 1. The attraction between any two neighboring molecules is very transient due to the constant thermal motions of the water molecules.

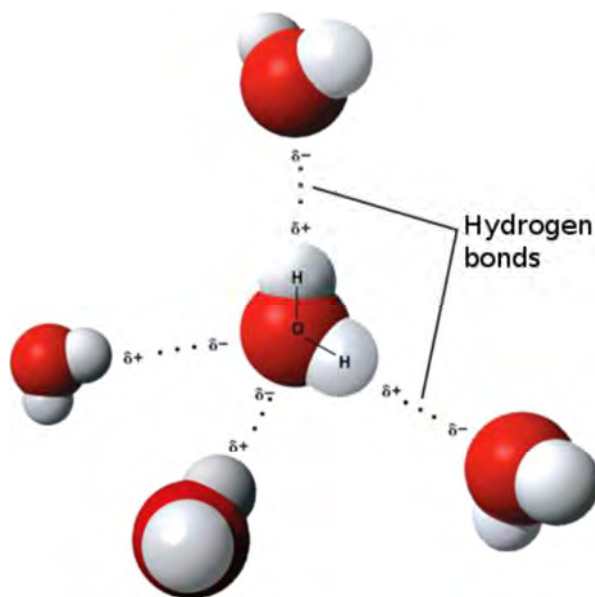


Fig.1 - Schematic of five water molecules, showing the 104.5 degree H-O-H angle and the hydrogen bonding between molecules. [2]

However, despite the chaotic dynamics, there is a net time-averaged attractive force between nearby molecules. It is such hydrogen bonding which is responsible for the relatively high boiling point and large heat of vaporization of water.

Some critics still attribute the perceived excess heat to the recombination of free hydrogen or deuterium with oxygen, as given off by electrolysis, to form liquid water. It is known that, in the presence of a catalytic material, those gases can easily recombine. This recombination gives off the heat of formation of water and can result in the erroneous appearance of excess heat. However, recombination is not the source of excess heat for two reasons. First, a properly conducted experiment will spend energy to electrolyze water and then recapture that energy when electrolysis occurs. And, very high values of measured excess energy cannot be due to recombination of atoms that were in the experiment at its outset.

Besides the heat of formation there are other characteristic energies for water molecules. They include the heat of vaporization, which is the energy to cause a molecule to transition from the liquid to the gas phase. The heat capacity of water is high, and there is an energy associated with raising the temperature of water. And, at a given temperature, there is a thermal vibrational energy associated with each water molecule. Some of the energies of water in table 1 provide a baseline for assessment of the eV/molecule values measured in LENR experiments.

Table 1. Water Molecule Energetics.

Heat of Formation (Recombination)	1.48 eV/molecule
Heat of Vaporization	0.42 eV/molecule
Energy to Heat Water from "room T" to boiling	0.06 eV/molecule
Vibrational Energy ($3kT/2$) at "room T"	0.04 eV/molecule

Rearrangement of water molecules involves energies from a few percent to almost half of 1 eV. Such energies are very low in comparison to those due to nuclear reactions, which are in the order of mega-electron Volts. The lowest value in Table 1, the vibrational energy of water at room temperature, will be used for comparison with eV/molecule values reported from LENR experiments. It will be seen that many measured

eV/molecule values fall below the vibrational energy. However, some values are well beyond even the molecular heat of formation.

3. Methodology

Several lists of Cold Fusion papers were examined to generate a broad and unbiased database for the study. Those lists included: (a) the Craven-Letts tabulation for ICCF-14, (b) Rothwell's website (www.lenr-canr.org) [3], (c) the Britz compilation of Cold Fusion papers, and (d) a list of papers submitted for the proceedings of ICCF-14 [4]. For our purposes, only papers that reported incidents of temperature increases and generation of excess heat, rather than production of tritium, neutrons or atoms, were included.

In all, 335 papers were examined. The information extracted from them formed an Excel spreadsheet. Experimental parameters, such as cathode material and dimensions, reference electrode, anode characteristics, Pd loading ratio, electrolyte composition and volume, type of water, current density, operating and delta temperatures, operating time, applied voltage and current, power, and excess energy were tabulated. However, our main focus for this study was directed towards information pertaining to excess energies and cell volumes. These factors were either provided explicitly, or else calculated by subtracting the input energy from the total energy output to obtain "excess energy". Grams of heavy water were converted to milliliters, or cubic centimeters, for the "cell volume". Some of the papers included numerous experiments with varying outcomes. In such cases, values were averaged to obtain a single representative value. eV/molecule values were obtained using the conversions:

$$\frac{kJ}{ml D_2O} \times \frac{6.34 \times 10^{21} eV}{1kJ} \times \frac{1ml D_2O}{1g D_2O} \times \frac{18g D_2O}{1mol D_2O} \times \frac{1mol}{6.02 \times 10^{23} molecule}$$

4. Results and discussion

The documented values were used to create four plots. The first plot compares excess energy and water volume information on a logarithmic scale. It has two purposes. One is to provide an overall comparison of the excess energies and cell volumes. The second is to permit assessment of a possible correlation between the two factors. The other three plots are histograms: (a) one that represents the distribution of excess energies, (b) another that presents the distribution of cell volumes, and lastly, (c) one that shows the distribution of eV/molecule values. The first two histograms are used to exhibit the overall trend in reported values for both excess energies and cell volumes. The third histogram is essential to demonstrate the number of papers that reported values higher than the vibrational energy of water molecules at room temperature.

Excess energy and water volume values were available from only 17 papers. They are plotted in Fig. 2. The trend of the data points suggests a rough correlation between both factors, where higher cell volumes seem to result in higher excess energies.

Only 40 out of 335 papers provided quantitative results for the amount of excess energy achieved in LENR experiments. The rest either failed to report any information about the output or reported excess power instead of energy. 60% of the 40 papers, as indicated in Fig. 3, reported results of 200 kJ or below. 200 kJ is enough energy to light a 100W bulb for about half of one hour. Such low values are considered by many as insufficient evidence to properly address critics of LENR. Only 40% of the papers reporting values for excess energy showed results above 200 kJ, with the highest documented value being 200 MJ. Notably, excess energy values up to 900 MJ were reported in experiments involving hydrogen-loaded nickel systems.

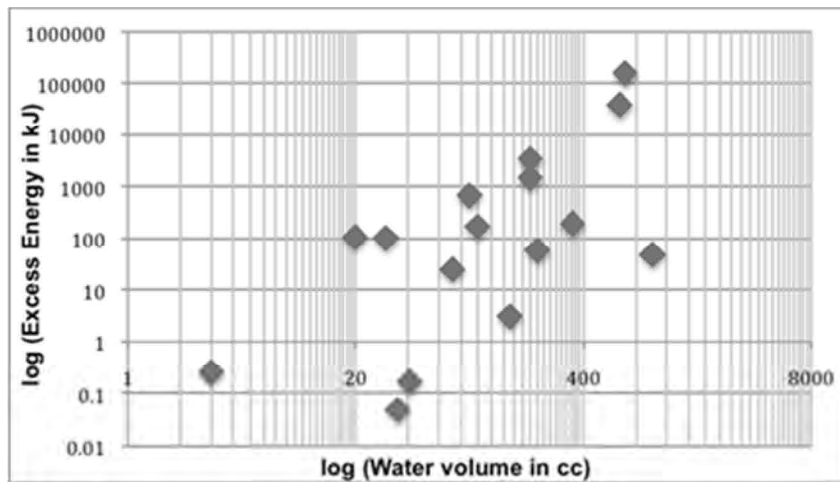


Fig.2 - The plot shows the relationship between excess energy and heavy water volume.

Only 57 out of 335 papers indicated the amount of heavy water or the amount of electrolyte used in the experiments, as can be seen in Fig. 4. Most experiments involved cells with volumes at or below 200 cc, with the highest volume used being 1000 cc in Lautzenhiser’s Amoco experiment in 1990 [5].

Lastly, excess energy per water molecule values were calculated from papers that reported both values and a histogram was created, as shown in Fig. 5. Many of the reports had high eV/molecule outputs. In fact, 11 of the papers resulted in energy per molecule values higher than that of the vibrational energy of water at room temperature. Those papers are listed in table 2. The highest value obtained is 42.6 eV/molecule. The fact that some of the papers had very high eV/molecules is enough to conclude that there is some other explanation of excess energy than new molecular rearrangements.

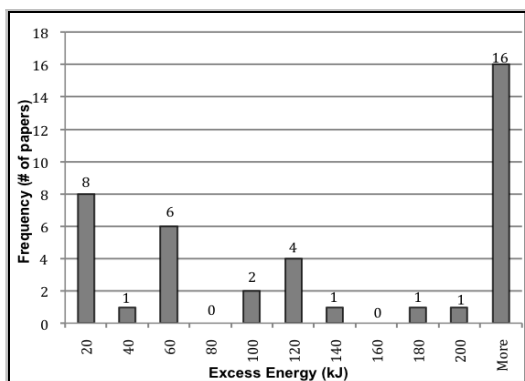


Fig. 3 - Histogram showing the distribution of excess energy values.

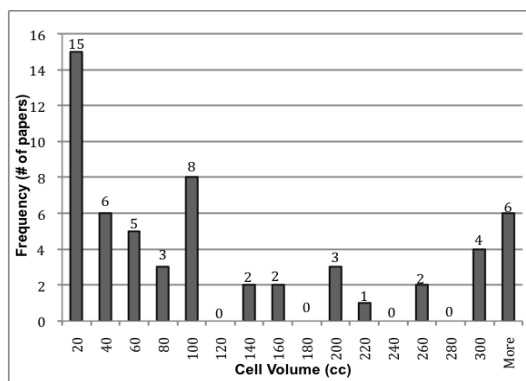


Fig. 4 - Histogram showing the distribution of experimental cell volumes.

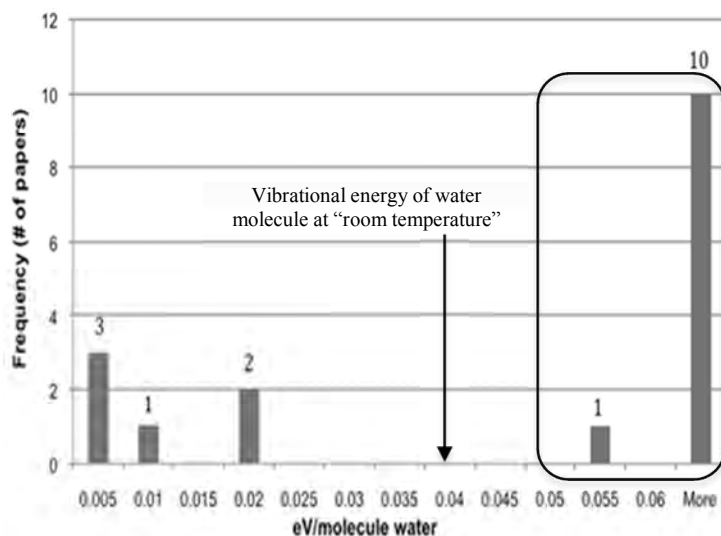


Fig. 5 - Histogram showing the distribution of eV/molecule values based on data provided by LENR papers.

Table 2. LENR articles that showed excess energy per water molecule values above the vibrational energy of water at room temperature.

Author	Reference	Year	eV/molecule
Oriani	6	1990	0.051 *
Lonchamp	7	1996	0.067 **
Takahashi	8	1998	0.106
Ohmori	9	1993	0.328
Storms	10	2006	0.659
Miles	11	1990	1.03
McKubre	12	1992	1.40
Miles	13	2001	1.45
Dardik	14	2008	3.27
Bockris	15	1993	11.2
Takahashi	16	1992	42.6

* highest value amongst 11 experimental runs.

** highest value amongst 6 experimental runs.

5. Conclusion

An extensive study of LENR papers has been performed to tabulate experimental conditions and data on excess energy. The goal was to address the question in the title of this paper. But, some unexpected results emerged during the course of the study. We summarize them, and then return to the question of the possible role of water in the production of excess energy.

Fewer than one out of five of the many papers examined reported the water volumes used in electrochemical experiments. More surprisingly, only one in eight papers gave the integrated excess powers, that is, the total excess energies for the experiments they described. Only 17 papers gave both the electrolyte volumes and the excess energies. After two decades of research on LENR, and thousands of experiments, it is noteworthy that the documentation of the experimental conditions and results is so sparse. There is clearly a need for more conscientious documentation of what was done and found in LENR experiments.

The second unexpected result is seen in Fig. 2, which shows the relationship between excess energy and heavy water volume. That plot is suggestive of a correlation between electrolyte volume and excess energy. Higher excess energy values tend to come from larger cells. However, there may be no basis for such a correlation, if the generation of excess energy occurs on or in the cathode and not in the volume of the electrolyte. Such a correlation might exist if the production of excess energy depended on some elements dissolved in the electrolyte. In that case, the greater the amount of electrolyte, the greater the amount of a reactant and the more excess energy, assuming adequate movement of the reactant elements to the reaction sites on or in the cathode.

Even if there were some reason for a correlation between excess energy and cell volume, the data in Fig. 2 are very scattered. Hence, it is not worth computing a correlation coefficient. However, it might be useful to conduct parametric experiments in which the same concentrations of the solutes in the electrolyte are used in cells of markedly different sizes. If one of the nuclear reactants is in solution at the start of an experiment, then the excess power might scale with electrolyte volume.

The range of cell volumes used in LENR experiments was quite well known. But, this study showed quantitatively that 44 of 57 cases had volumes of 200 cc or less. In fact, 37 of the 57 instances had electrolyte volumes equal to or less than 100 cc.

The experimental papers showed that 24 of the 40 reports of excess energy were equal to or below 200 kJ. Hence, only 16 were greater than 200 kJ. A few of the values of excess energy were in excess of 1 MJ. The more common and relatively small values for excess energy, some gotten during runs of days and weeks, emphasize the need for scaling up power and energy production in LENR experiments. Such scaling would also broaden the range of potential applications of LENR generators.

Returning to the motivating question for this study, we found that the values of eV per water molecule from some experiments are far beyond what is reasonable for water to be the source of observed excess heat. It is thus concluded that some unknown rearrangement of water molecules in an LENR experiment is not the source of anomalous heat production.

The mechanism(s) causing LENR remain mysterious. However, the experimental database evidencing the ability to trigger nuclear reactions using chemical energies is robust. That information has not been studied by most scientists in the physics community. The existence of LENR is still criticized occasionally, usually by people who have not read the available literature. Criticism is absolutely basic to scientific research and communications, as it brings up many useful questions. Nonetheless, it is crucial that scientists who think that LENR is real, even if not fully understood, respond to critics on the basis of experimental data. That motivated this study. It has shown that further experimentation, long-term and detailed data logging, and thorough documentation are required. Better experiments and reporting may render this field more acceptable to the broader scientific community.

Acknowledgements

This study was suggested by Graham Hubler. Lists of LENR papers were provided by Dennis Letts and Jed Rothwell. The administrative assistance of Mark Reeves and Gary Reynolds is appreciated. The study was funded by the U.S. Naval Research Laboratory Washington DC.

6. References

- [1] Kainthla, R. C., M. Szklarczyk, L. Kaba, G. H. Lin, O. Velev, N.J.C. Packham, J. C. Wass, and J. O'M Bockris. "Eight Chemical Explanations of the Fleischmann-Pons Effect." *Int. J. Hydrogen Energy* **14.11** (1989): 771-75. Print.
- [2] http://en.wikipedia.org/wiki/Properties_of_water.
- [3] Rothwell, Jed. LENR-CANR. Web.

- [4] Proceedings of The 14th International Conference on Condensed Matter Nuclear Science, Washington, DC. Print
- [5] Lautzenhiser, T. and D. Phelps, *Cold Fusion: Report on a Recent Amoco Experiment*. 1990, Amoco Production Company.
- [6] Oriani, R. A., John C. Nelson, Sung-Kyu Lee, and J. H. Broadhurst. "Calorimetric Measurements of Excess Power During the Cathodic Charging of Deuterium into Palladium." *Fusion Technology* **18** (1990): 652-58. Print.
- [7] McKubre, M.C. H., et al. *Excess Power Observations in Electrochemical Studies of the D/Pd System: The Influence of Loading. Proceedings of the Third International Conference on Cold Fusion. "Frontiers of Cold Fusion"*. 1992. Nagoya Japan: Universal Academy Press, In., Tokyo, Japan.
- [8] Bockris, J. O'M, Sundaresan, R., Minevski, Z., and Letts, D. *Triggering of Heat and Sub-Surface Changes in Pd-D Systems. Proceedings of the Fourth International Conference on Cold Fusion. "Transactions of Fusion Technology"*. 1993. Lahaina, Maui: Electric Power Research Institute.
- [9] Ohmori, Tadayoshi, and Enyo, Michio. "Excess Heat Evolution During Electrolysis of H₂O with Nickel, Gold, Silver, and Tin Cathodes." *Fusion Technology* **18** (1993): 293-95. Print.
- [10] Lonchampt, G., L. Bonnetain, and P. Hieter. *Reproduction of Fleischmann and Pons Experiments. Proceedings of the Sixth International Conference on Cold Fusion, Progress in New Hydrogen Energy*. 1996. Lake Toya, Hokkaido, Japan. New Energy and Industrial Technology Development Organization, Tokyo Institute of Technology, Tokyo, Japan.
- [11] Takahashi, Akito, Hirotake Fukuoka, Kenichi Yasuda, and Manabu Taniguchi. "Experimental Study on Correlation between Excess Heat and Nuclear Products by D₂O/Pd Electrolysis." *International Journal of The Society of Material Engineering for Resources* **6.1** (1998): 4-13. Print.
- [12] Miles, M., M.A. Imam, and M. Fleischmann, *Calorimetric analysis of a heavy water electrolysis experiment using a Pd-B alloy cathode*. Proc. Electrochem. Soc., 2001. **2001-23**: p. 194.
- [13] Storms, E., *Anomalous Heat Produced by Electrolysis of Palladium using a Heavy-Water Electrolyte*. 2007, LENR-CANR.org.
- [14] Focardi, S., et al., *Large excess heat production in Ni-H systems*. Nuovo Cimento Soc. Ital. Fis. A, 1998. **111A**: p. 1233.
- [15] Takahashi, A., et al., *Excess Heat and Nuclear Products by D₂O/Pd Electrolysis and Multibody Fusion*. Int. J. Appl. Electromagn. Mater., 1992. **3**: p.221.
- [16] Dardik, I., et al. *Ultrasonically-excited electrolysis Experiments at Energetics Technologies. Proceedings of the ICCF-14 International Conference on Condensed Matter Nuclear Science, 2008*, edited by D. J. Nagel & M.E. Melich, Washington, DC.

Production of Helium and Energy in the “Solid Fusion”

Y. Arata, Y.C. Zhang, and X.F. Wang

Center for Advanced Science and Innovation, Osaka University, 2-1 Yamadaoka, Suita, Osaka, 565-0871, Japan

E-mail: arata@casi.osaka-u.ac.jp

Abstract: In this paper, a new type “Solid Fusion Reactor” has been developed to test the existence of solid state nuclear fusion (“Solid Fusion”): reproducible experiments have been made at room temperature and without external power input. (Both of the energy and helium generation affected by the reactor structure, gas flow rate, powder weight, and cooling condition were studied.) Deuterium gas loading processes of two types of nano material (ZrO_2Pd_{35} and $ZrO_2Ni_{30}Pd_5$) were studied respectively in this paper. The results showed the energy produced in ZrNiPd powder is higher than in ZrPd powder. Helium as an important evidence of solid-state fusion was detected by mass analyzer “QMS”. As results, “Solid Fusion” has been confirmed by the helium existence.

1. Introduction

Though enormous reports [1-3] have been published on the deuterium nuclear fusion reactions, and scientists have hoped that “cold fusion” finally will solve the world’s energy problems. “Cold fusion”, however, has not been generally accepted due to the lack of experimental evidences on the stable and/or continuous generation of large amount of excess heat or nuclear reaction products [4]. It is well known that excess heat and Helium (or Tritium) have been considered the Solid Fusion Reaction’s products in Pd/D system [5].

It was studied that many factors having effects on the reaction heat in solid-state fusion, for instance: the gas flow rate, vessel structure and size, and cooling condition. Helium as an important evidence of solid-state fusion was detected by mass analyzer “QMS” in this paper.

Two kinds of powder were investigated under the same conditions in this paper: one is nano powder ZrO_2Pd_{35} (: ZrPd alloy), and the other is $ZrO_2 Ni_{30}Pd_5$ (: ZrNiPd alloy).

As shown in Fig.1, X-ray diffraction analysis was carried out for both of the nano powder ZrPd and ZrNiPd. From Fig.1 [A], we can see that almost all of the palladium elements exist as the palladium oxide (PdO) in the original nano powder (ZrPd). Based on these X-ray analysis results, to remove the Oxygen from the original ZrPd powder, a “deoxidization treatment” is very important for the nano powder ZrPd before the general pressurization of the powder with D_2 gas.

The process of “deoxidization treat” is as follows:

- (1) Firstly, the nano powder ZrPd was sealed inside the stainless vessel and then vacuumed at room temperature until the vacuum up to about 5×10^{-5} [torr]. Then the vessel (with the sample powder inside) was baked and vacuumed at $150[^\circ C]$, kept for 6 hours, then was cooled down to the room temperature. The vacuum degree of vessel was finally about 5×10^{-6} [torr] at room temperature;
- (2) Secondly, D_2 gas was loaded into the high vacuumed vessel with a fixed flow rate 20 [cc]/[min]. The total gas volume was decided by the sample weight (16.5 to 18 [cc]/ [g]). As results, this process made the PdO transmute into Pd, and D_2 gas into D_2O ;
- (3) Finally, exhausting the D_2O from the vessel: the reaction vessel was vacuumed at room temperature until the vacuum up to about 5×10^{-5} [torr], then baked and vacuumed at $150 [^\circ C]$ until the vacuum up to 2×10^{-6} [torr], kept for over 6 hours. Then the vessel was cooled down to room temperature.

Fig.1 [B] shows the X-ray analysis result of powder after “deoxidization treat”. The intensity of PdO got a big fall, but little PdO still exists in the powder. And Fig.1[C] is the X-ray analysis result of powder after fusion reaction (after D_2 gas loading), the intensity of PdO is about the same as the Fig.1 [B]’s. Accordingly, even if much more D_2 gas loaded, the PdO cannot be removed completely. This residual intensity of PdO in Fig. 1 [B] and [C] may be the limit contents of ZrPd powder.

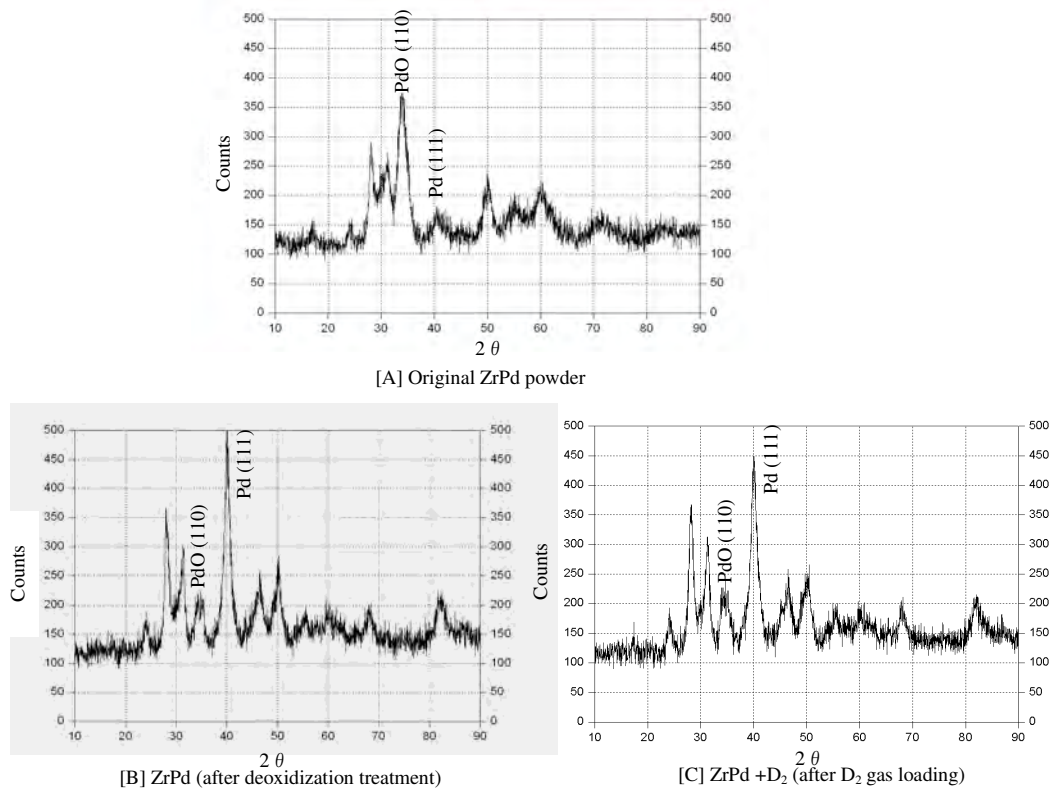


Fig.1 - X-ray diffraction analysis of ZrPd powder

Note: Based on the X-ray analysis results, the process of “deoxidization treat” is unnecessary for ZrNiPd powder. So only process (1) mentioned above is necessary when ZrNiPd powder is adopted.

2. Experiments and results

We used two kinds of material: nano powder (ZrPd) and powder (ZrNiPd) to investigate the process of D₂ gas loading at the same conditions: the stainless vessel; the weight of powder (16 [g]); the final pressure inside the vessel (P_{in}) is 10-16 [atm].

To make the powder's surface contact with D₂ gas as much as possible, we developed a small new plate shape device inside the reactor, as shown in Fig. 2. Powders are put in every plate with equal weight, and then the experiment is carried out according to the process as mentioned above, namely, process (1-3) and process (3) for nano powder (ZrPd) and powder (ZrNiPd) respectively. Within Fig.2, T_{in} is powder temperature, T_s ($T_{surface}=(T_{surface1}+T_{surface2})/2$) is the temperature of vessel surface and T_f (T_{flange}) is the temperature of the vessel flange and lid.

2.1 Experiment 1 (Energy generation):

Firstly, the above mentioned process (1)-(3) for ZrPd powder and process (1) for ZrNiPd powder was carried out; after that, pure D₂ gas was loaded into the closed vessel with a fixed flow rate ($v_G=20,50,70\text{cc/min, respectively}$) until the inner pressure (P_{in}) reaches at the range of 10-16[atm].

Fig. 3 [A] and [B] show the survey data of the temperature change with time applying nano powder (ZrPd) and the powder (ZrNiPd) respectively, using the above mentioned reactor vessel, as shown in

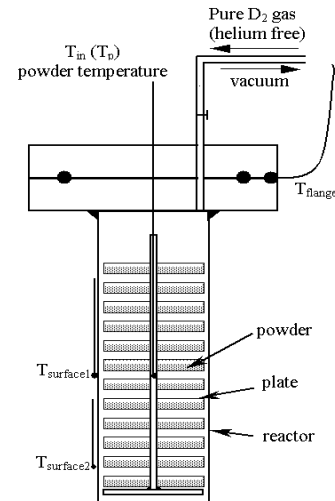


Fig.2 - Fusion reactor

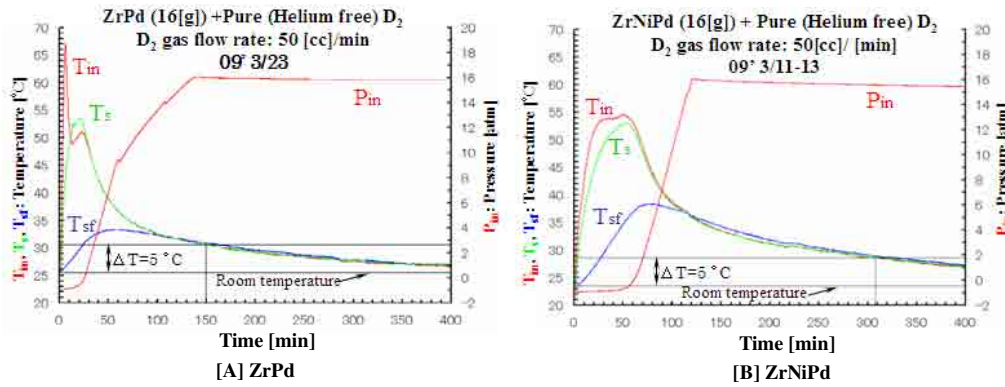


Fig.3 - Distribution of temperature and inner gas pressure

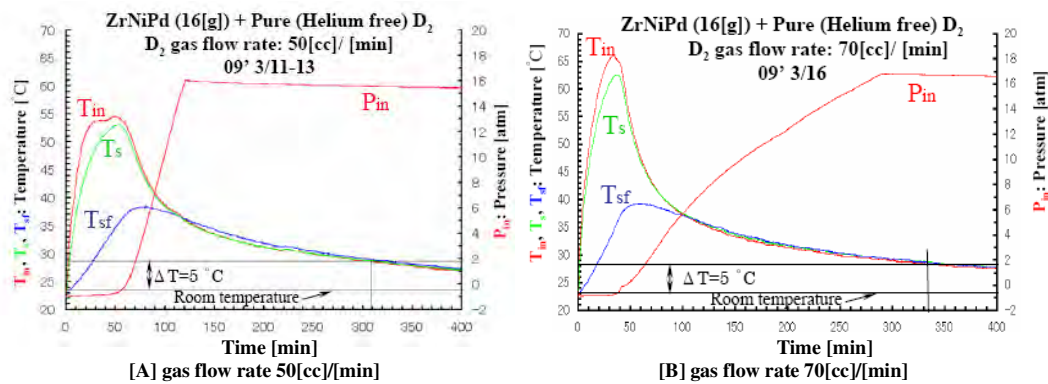


Fig.4 - Distribution of temperature and inner gas pressure

Fig.2. The reactor vessel is cooled in air with shelter during D₂ gas loading. Within Fig.3, T_{in} is powder temperature, T_s (T_{surface}=(T_{surface1}+T_{surface2})/2) is the temperature of vessel surface and T_f (T_{flange}) is the temperature of the vessel flange and lid, P_{in} is the pressure inside the reactor vessel.

As for a time interval of 5 [°C] of T_{in}, T_s and T_f above room temperature, Fig.3 [A] (nano powder (ZrPd)) lasts about 150 [min]; Fig.3 [B] lasts about 308 [min]. Namely, the heat that ZrNiPd powder generated is much more than nano powder ZrPd.

Fig. 4[A] and [B] are using the same powder (ZrNiPd (16 [g])), at the same conditions except D₂ gas flow rate. D₂ gas flow rate in Fig. 4[A] and [B] are 50 [cc]/[min] and 70 [cc]/[min] respectively. Comparing the time interval of 5 [°C] above room temperature between [A] and [B], the [B] lasts about 335 [min], it is longer than [A] (about 308 [min]).

Applying this cooling type, we can know the temperature change process of the powder (T_{in}) and the reactor vessel (T_s) during D₂ gas loading. However, the reaction temperature of powder cannot be controlled, so the reaction rate of powder is unable to be kept in a high range. Accordingly, the excess energy cannot be put into practice.

Therefore, to obtain a quantitative excess energy in solid fusion, three cooling type were applied. The sketch of these three cooling type is shown in Fig. 5.

Type-1, the reactor vessel is cooled down in air with shelter; the reaction energy was calculated on the basis of the data of the temperature change of T_{in}, T_s and T_f;

Type-2, the reactor vessel was put in a water bath with a constant water volume at room temperature, and the energy was calculated on the basis of the temperature change of the cooling water. This type makes to get excess energy easily but cannot be controlled for a stable output;

Type-3, the reactor vessel was enclosed by the copper tube, which was welded on the surface of the reactor vessel. During the D₂ gas loading, the reactor was cooled down by the water flowing through the copper tube with the constant water flow rate (40[cc] / [min]); the water was from a water chiller. And then the energy was calculated by the temperature difference between the outlet and inlet of cooling water.

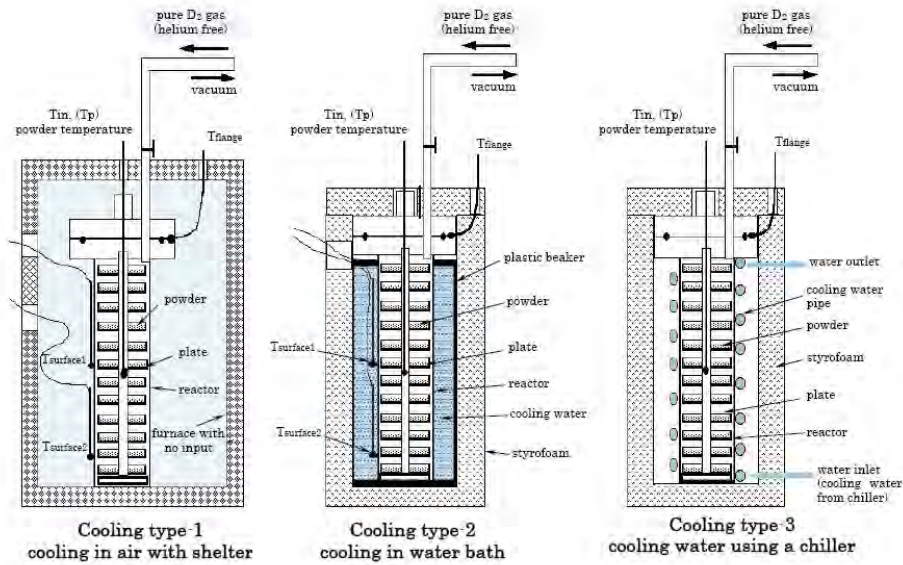


Fig.5 - Three kinds of cooling type during D₂ gas loading

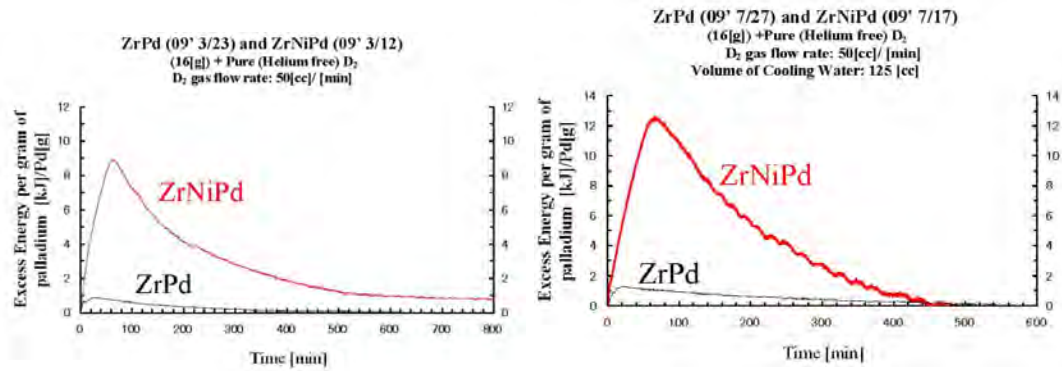


Fig. 6 - Excess Energy change with time (cooling type-1)

Fig. 7 - Excess Energy change with time (cooling type-2)

Among the three types, the cooling type-3 is the most useful one to get a stable excess power output.

Fig. 6 is one example of using the cooling type-1, which shows the distribution of reaction energy of both the ZrNiPd powder and ZrPd powder. Comparing the excess energy per one-gram palladium between the ZrNiPd powder (red line) and the ZrPd powder (black line), it can be found very clearly that the energy of ZrNiPd powder is larger than that of the ZrPd powder. Also, the same result was obtained by using cooling type-2 as shown in Fig. 7.

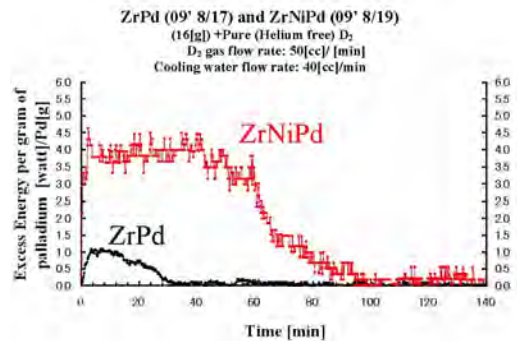


Fig. 8 - Excess Energy change with time (cooling type-3)

To obtain the output power change with time precisely, we applied the cooling type-3 for both of ZrNiPd powder and ZrPd powder. The sample weight was 16 [g], cooling water flow rate was 40 [cc] / [min]. Fig. 8 is an example showing the reaction power (per one gram palladium) change with time. In the case of ZrNiPd powder (red line), the generated power is 4 [watt] lasting 60 minutes, then the power dropped gradually with the time last. The total lasting time is about 100 minutes. For the case of ZrPd powder (black line), the generated power is only 1 [watt] lasting only 10 minutes, and the total lasting time is about 32 minutes.

Fig. 9 and Fig. 10 are the comparison of the measuring data among three cooling types. The two

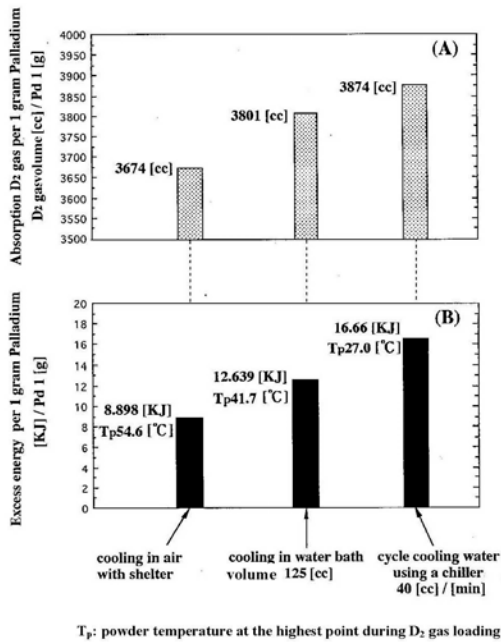


Fig.9 - Absorption volume of D₂ gas and excess energy of the ZrNiPd powder (16[g]) during the pure D₂ gas loading under the same conditions except for the cooling condition.

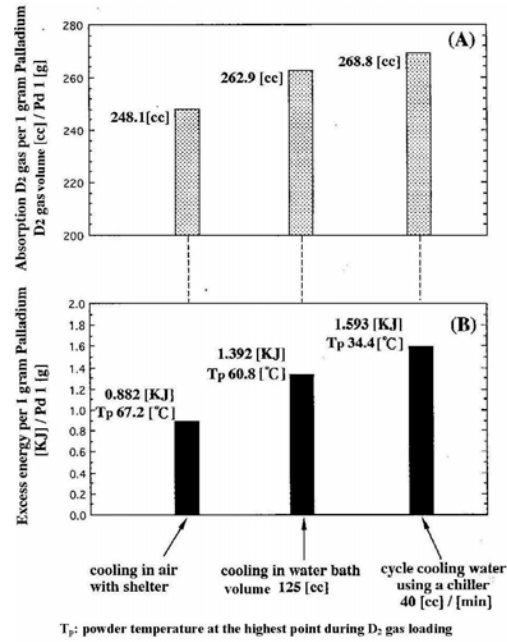


Fig.10 - Absorption volume of D₂ gas and excess energy of the ZrPd₃₅ powder (16[g]) during the pure D₂ gas loading under the same conditions except for the cooling condition.

figures show that the absorption volume of D₂ gas and excess energy changed with the different cooling conditions. Both of the powders, either ZrNiPd or ZrPd, when applying the cooling type-3, the absorption volume of D₂ gas and excess energy are higher while the powder's temperature is lower than other two cooling types during the D₂ gas loading.

Furthermore, the two powder's absorption capacity of D₂ gas and excess energy (per 1 gram palladium) are compared, as shown in Fig 11. Both of the powders, ZrNiPd and ZrPd, are tested with the same conditions and applying two kinds of D₂ gas flow rate. In Fig. 11, we can see, on the case of ZrNiPd powder, the absorption capacity of D₂ gas is fifteen times higher than that of the ZrPd applying the gas flow rate of both 50 [cc]/[min] and 70 [cc]/[min]. Also its excess energy is ten times higher than that of the ZrPd powder.

In the case of the cooling type-1, the reactor was cooled in air with shelter and the powder temperature rose up with the increase of the absorption volume of D₂ gas. The powder temperature cannot be controlled. While using the cooling type-3, the powder temperature can be stably controlled around 25 [°C] as shown in Fig.12.

As we known, the normal palladium absorption capacity of D₂ gas decreases with the rise of temperature. When using the cooling condition of type-1, the powder's temperature is higher than other two, so the absorption capacity of D₂ gas and excess energy is lower than other two types.

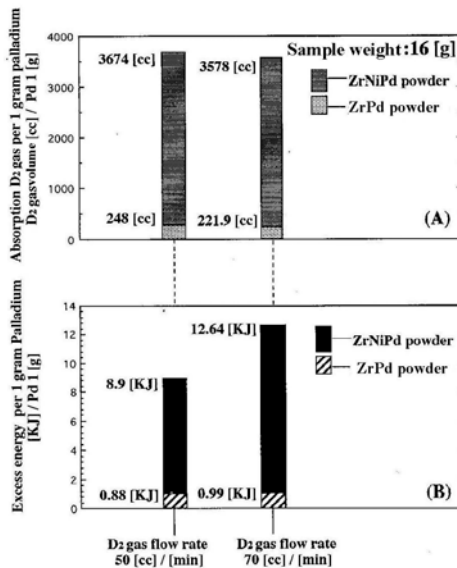


Fig.11 - Comparison of the absorbed D₂ gas volume and excess energy between ZrNiPd powder and ZrPd₃₅ powder under different gas flow rate.

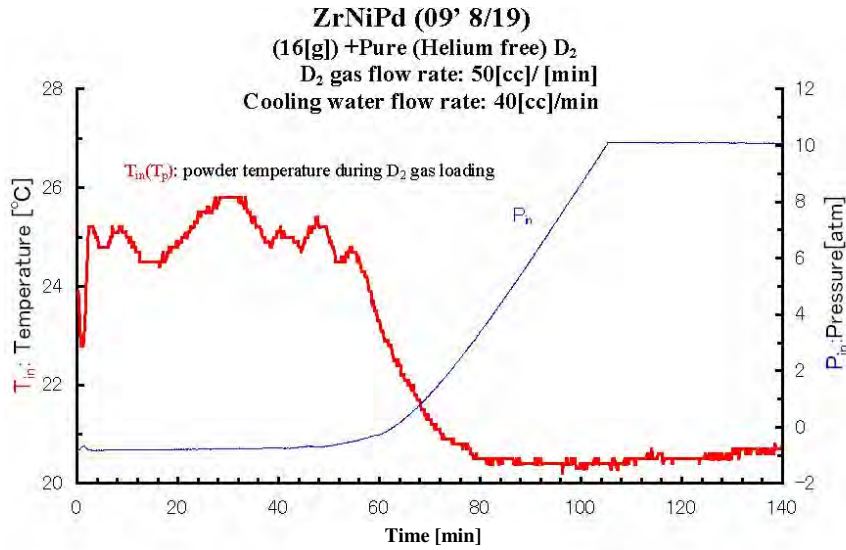


Fig.12 - Powder temperature change with time using the cooling type-3

Therefore, the change of the cooling condition not only decreases the energy losses, but also increases the powder's absorption capacity, which is in favor of increasing the solid fusion reaction rate. However, it must be confirmed by the fusion reaction products of helium.

2.2 Experiment 2 (Helium generation):

By using quadrupole mass spectrometer -"QMS", the helium can be detected for reacted powders and gas [6]. The helium has been detected many times for reacted powders and gas by using "QMS", as shown in Fig. 13. The "QMS" have two functions: normal resolution and high-resolution test. Both of the gas and powder can be analyzed by the "QMS". The helium can be identified by three kinds of analysis

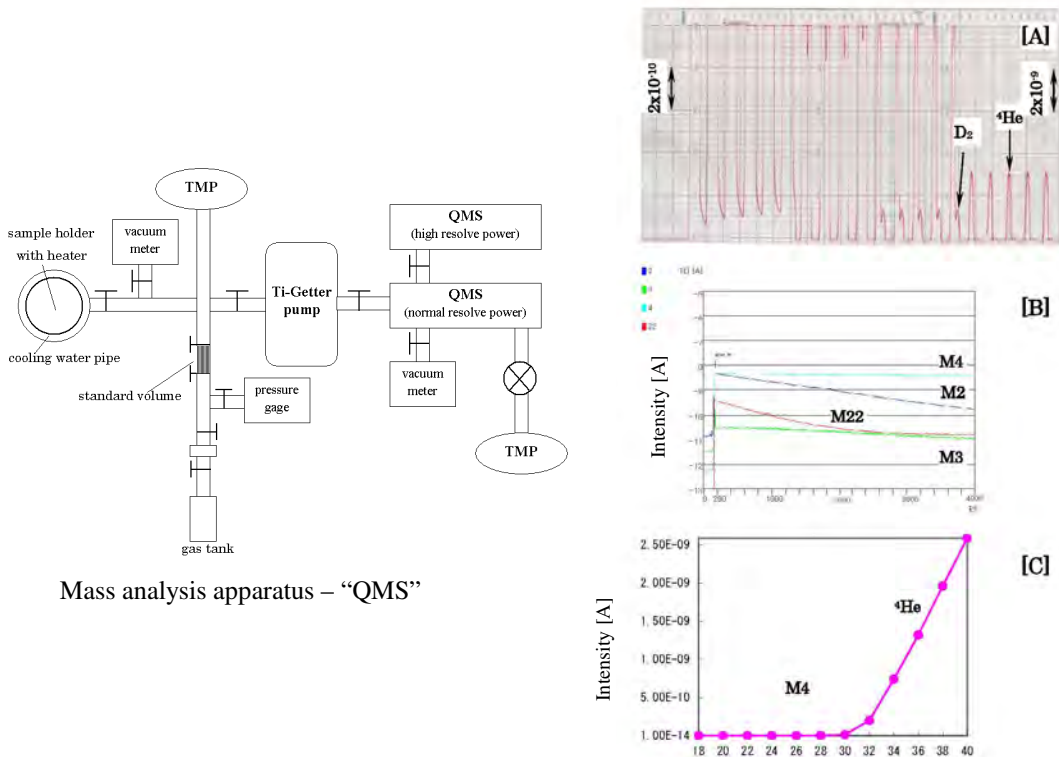


Fig.13 - QMS analysis principle and characteristic

methods. The first one is the normal resolution analysis; the second one is using the high-resolution test to separate the spectrum peak of helium from that of deuteron. During the analysis of gas, both functions of normal and high resolution were applied at the same time. At the right side of Fig. 13, an example of high resolution results is shown (Fig. 13 [A]), the helium (He4) and D_2 were separated clearly; Fig.13 [B] shows the normal resolution analysis result, many mass of element can be detected, because the Ti-getter has the absorption function of hydrogen system gas, but it can not absorb the helium. If the helium exists in the sample gas, the line of mass 4 will finally become parallel after most of D_2 gas absorbed.

The third one, Fig. [C] shows the result of measuring the ionization voltage of the main mass number 4 (helium, deuteron) and number 22 (neon-Ne22) by using ionization mechanism. The ionization voltage of hydrogen system is from 22 [volt] and that of He4 and Ne22 is about 28 ~ 30 [volt]. It can be confirmed whether the He4 or Ne22 exists or not, and the intensity of that element. As we know, the ratio of He4 per Ne22 is near 3 in the case of air gas. According to the measuring results of above mentioned three methods, the existence of helium can be confirmed clearly, and it also can be identified that helium is generated by solid fusion reaction not from air by calculated the element ratio of Helium / Neon 22.

But some people still have a prejudice, doubting it is true or not.

Recently, to make everyone understand clearly at a glance, we performed an interesting experiment: the concentration of helium from the fusion reacted gas. The apparatus's schematic diagram is shown in Fig. 14.

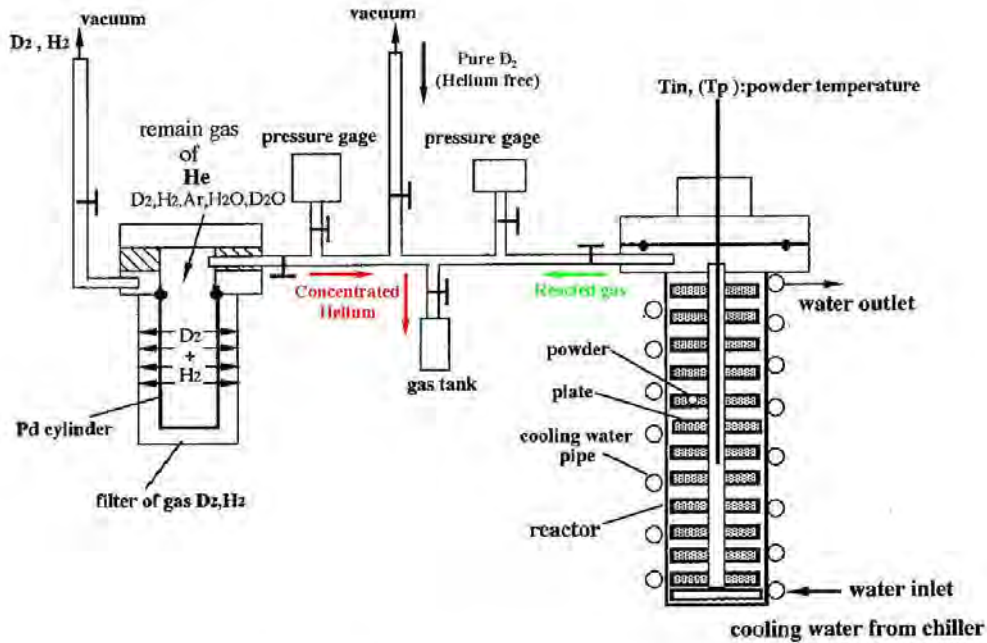


Fig.14 - Concentration apparatus of Helium from reacted gas and powders

By using the palladium filter, the D_2 and H_2 gas were removed from the fusion reacted gas. As results, if helium exists in the reacted gas, it will be concentrated, and we can control the concentration times of the gas easily by controlling the gas pressure.

Fig 15 [A] and [B] shows one example of the mass analysis of the fusion reacted gas of ZrNiPd powder and ZrPd powder (sample weight: 16 [g]). The measuring gas volume is 2.5 [torrcc]; the spectrum peak of Helium and D_2 gas analysis using high resolution mass analysis, the left one shows the reacted gas before concentration, and the right one shows the concentrated gas. You can see helium intensity of the concentrated gas of ZrNiPd is much higher than that of the ZrPd powder.

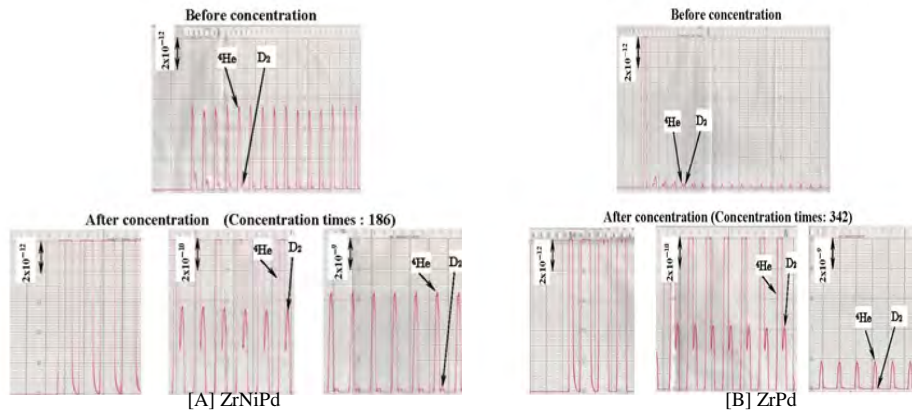


Fig.15 - Spectrum of reaction products by high resolution of mass analysis Helium intensity and the intensity ratio of Helium per Neon22 detected from reacted gas of ZrNiPd powder using “QMS” were shown in Fig.15[C].

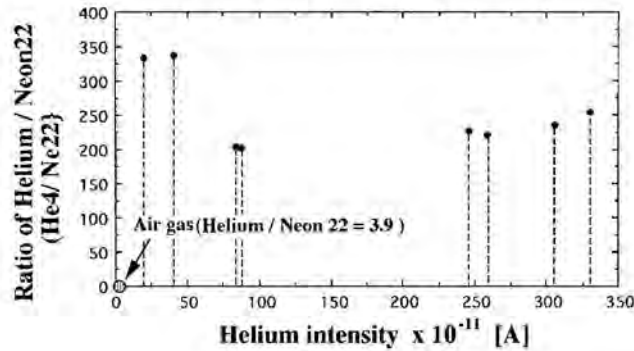


Fig.15[C] - Helium intensity and the intensity ratio of Helium per Neon22 detected from reacted gas of ZrNiPd powder using “QMS”

Fig 16 [A] and [B] is the graph of the mass analysis results of the fusion reacted gas of ZrNiPd powder and ZrPd powder respectively. Sample weight: 16 [g]), the measuring gas volume is 2.5 [torrcc].

Fig. 16 [A] shows the helium intensity relates to the concentration times of the ZrNiPd powder with D₂ gas loading. The helium intensity increases with the increase of the concentration times of the reacted gas. The highest helium intensity is up to 330x10⁻¹¹ [A] after 189 times concentration, which is 654 times of the gas before concentration

And Fig. 16 [B] is the results of ZrPd powder. Like the ZrNiPd powder, the helium intensity also increases with the increase of the concentration times of the reacted gas. The highest helium intensity is 116 x10⁻¹¹ [A] after 331 times concentrated.

Comparing Fig.16 [A] and [B], we can see that the highest helium intensity of the concentrated gas of ZrNiPd is much higher than that of the ZrPd powder, even if the concentration time of the former is less than the latter.

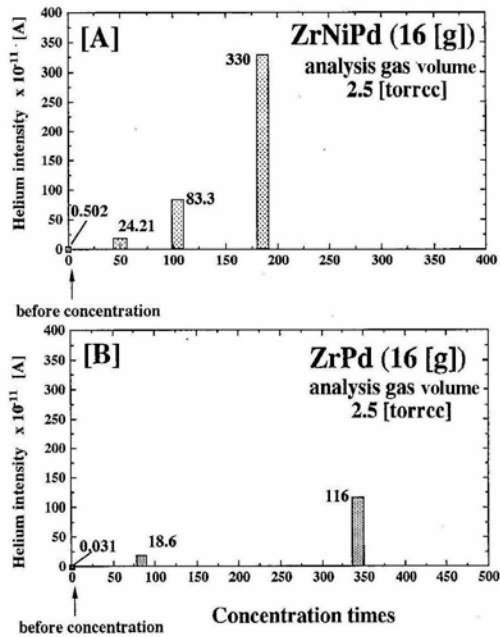


Fig.16 - Helium intensity relation to concentration Times with D₂ loading using cooling type-3

The comparison of the helium intensity of reacted gas with excess energy is shown in Fig. 17. It is the helium intensity per one gram palladium related to the excess energy per one-gram palladium, concentration times is also shown in this figure. We can see ZrNiPd powder generated not only the higher energy but also larger numbers of helium than the ZrPd powder. It indicated the helium intensity increases with the increase of the excess energy.

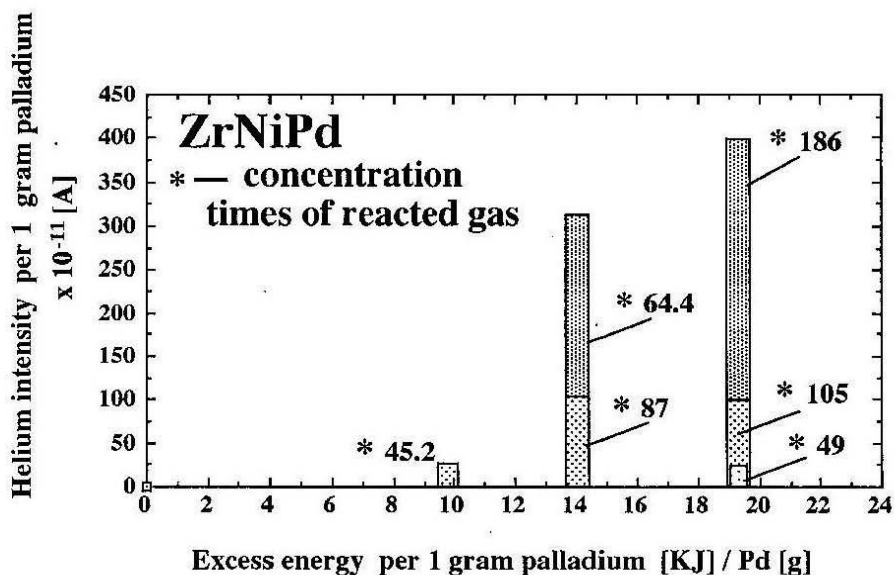


Fig.17 - Comparison of the helium intensity of solid fusion reacted gas with excess energy

3. Conclusions

(1) Both powder of ZrNiPd and ZrPd were used in solid fusion which generated the excess energy and the helium as products of fusion reaction, and the helium were measured many times by using mass analysis apparatus "QMS". As results, as for either excess energy or helium, the ZrNiPd powder is always about ten times higher than the ZrPd powder;

(2) Using the weight 16 [g] of the ZrNiPd powder, the excess power 4 [watt] continued stably for about one hour, and only consumed the palladium less than one gram, its cost is lower than the ZrPd powder and the experiment operation is easy with good reappearance, it is very useful of practical use, so we choose the ZrNiPd powder as a good material for the solid fusion at now;

(3) The concentration of helium was very successful; these results hint that the reacted gas of "solid nuclear fusion" will be a helium source as a helium production. However the powder is made in the ambient atmosphere, accordingly the original powder contains a little other composition like as air gas. Even if after the powder was baked at 150 [°C] for 16 ~20 hours to remove these gases before D₂ gas loading;

Though a trace of the gases still remain in the powder and these remained gases have a higher mass number than mass four, it maybe removed by a centrifugal separator. Of course it's not so easy, and these problems will be solved by a factory, but not by us in laboratory.

4. References

- [1] Belyavin, KE; Min'ko, DV; Kuznechik, OO, et al., Solid-state laser fusion of spherical titanium powders. POWDER METALLURGY AND METAL CERAMICS, 2008, 47(7-8): 500-504.
- [2] McKubre, M.C.H. and Tanzella F.L. Using resistivity to measure H/Pd and D/Pd loading: method and significance. The 12th International Conference on Condensed Matter Nuclear Science. 2005:392-403.

- [3] Grimshaw, T. Open Source Science Applied to CMNS Research: A Paradigm for Enhancing Cold Fusion Prospects and the Public Interest. ICCF-14 International Conference on Condensed Matter Nuclear Science. 2008. Washington, DC.
- [4] L. Kowalski, G. Luce, et al., New results and an ongoing excess heat controversy. The 12th International Conference on Condensed Matter Nuclear Science. 2005:171-177.
- [5] Y. Arata, Y C. Zhang. The establishment of solid nuclear fusion reactor, J. High Temp. Soc. Jpn 34(2008) , 2, 85-93.
- [6] Y.Arata, Y.C. Zhang. Helium (${}^4_2\text{He}$, ${}^3_2\text{He}$) within Deuterated Pd-black.Proc. Japan Acad., 73, Ser.B(1997).

Towards a High Temperature CMNS Reactor: Nano-Coated Pd Wires with D₂ at High Pressures.

F. Celani¹, P. Marini², V. di Stefano², M. Nakamura², O. M. Calamai¹, A. Spallone¹, E. Purchi², V. Andreassi¹, B. Ortenzi¹, E. Righi¹, G. Trenta¹, G. Cappuccio¹, D. Hampai¹, F. Piastra¹, A. Nuvoli¹

(1) *Istituto Nazionale di Fisica Nucleare, Laboratori Nazionali di Frascati, (INFN-LNF) Via E. Fermi 40, 00044 Frascati (Rome)-Italy.*

(2) *International Society of Condensed Matter Nuclear Science, Rome#1 ISCMNS_Group Via Lero 30, 00129 Rome-Italy.*

Collaboration with:

U. Mastromatteo.

STMicronics, Via Tolomeo 1, 20010 Cornaredo (Mi)-Italy.

A. Mancini. *ORIM SpA, Via Concordia 65, 62100 Macerata-Italy*

F. Falcioni, M. Marchesini, P. Di Biagio, U. Martini.

Centro Sviluppo Materiali, Via di Castel Romano 100, 00129 Roma-Italy

L. Gamberale, D. Garbelli.

Pirelli Labs, Viale Sarca 222, 20126 Milano-Italy

The work was partially supported by Lam.Ba. Srl Caluso (Turin)-Italy.

E-mail: francesco.celani@lnf.infn.it

Abstract. There were improved measurements on our reactor presented at ICCF14 (2008): long-thin Pd wires with surfaces nano-coated by multi-layers of several elements, D₂ at P<10bar; wires temp. <500°C; SS reactor wall temperature <100°C; longitudinal current density up to 45 kA/cm² (voltage drop up to 70V); transversal electric field up to 700V/cm. Previous ICCF14 results *confirmed*: anomalous excess power, stable over time and power cycling, up to 400 W/g of Pd. Made a new experiment with D₂-Ar mixture: demonstrated the role of high temperatures (into “nano” Pd-D) to enhance production of anomalous thermal effects. The combined effects of high concentration *and* mobility of D inside Pd seem the key points to get them: models based on **High Temperature** BEC Nuclear Fusion (Kim, Premuda) fits several of our experimental results. Experiments on the planned (new) High Pressure (60 bar) High Temperature (>600 °C) reactor wall are still in progress: experienced *heavy problems* coming out because degassing of impurities (specially S, P) from SS (304, 316) used in the reactor wall. The scavenger effect of H₂ (and D₂) on SS and other materials makes the impurities problem quite difficult to be overcome: designed and build a new, multiple layer wall (SS/Cu 3N), reactor that is now under the stage of final test.

1. Introduction

In the framework of experiments using Pd-based nano-materials and D₂ pressurised gas loading, we developed since 2004 an *hybrid* procedure that, in principle, takes advantage of several reproducible effects up to now introduced both from other Researchers and ourselves: Pd nano-particles, multi-layers, enhanced D diffusion (and D/Pd ratio) by flowing large current on thin Pd wires (with even transversal electric field up to 700V/cm). In short: high temperatures and D forced mobility through nano-Pd.

We recall that the Researcher that, in the field of Condensed Matter Nuclear Science, at first used concentrated Pd nano-particles to increase the D/Pd ratio was Prof. Yoshiaki Arata (Osaka University-Japan) since 1993 [1]; the first that developed multiple nano-layers of Pd-CaO was Dr. Yasuhiro Iwamura (Mitsubishi Heavy Industries, Yokohama-Japan) since 1999 [2]. Both used D₂ gas loading.

Our group applied (since 1995) the so-called *Preparata Effect* [3], to improve the D/Pd ratio on long and thin Pd wires by large voltage drop along the wire itself in electrolytic environments [4], i.e. with

maximum temperature $\ll 100^\circ\text{C}$ (cell not pressurised). In the experiment discussed in [4], was observed also the beneficial effect by coating thin layers of Ni, Li salts (the electrolyte), Pd to the main Pd wire due to side effects of both anodic corrosion of Ni (used as anode) and partial dissolution (and subsequent deposition) of Pd cathode itself due the specific pulsed operation ($T_w = \text{few } \mu\text{s}$) of the kind of electrolysis regime we developed (there was always present a little anodic component of the high power pulse, with voltage up to 200V and rise/fall time of less 100ns, due to inductive reasons). The main drawback of such procedure was that the kind of deposit and thickness was out of any control because both spontaneous and due to side effects (voltage undershoot) of pulses. Starting from 1999 we published several papers [5, 6] where was reported the beneficial effects of addition of soluble salts of alkaline earth elements (Ca, Sr, Ba), at very low concentration (10^{-4}M), in order to improve the D/Pd; moreover, the effect was magnified by several cathodic-anodic regimes: we observed (and published in 2003), by SEM, that Pd surface was similar to *fractals*. Later (2004) the effect to generate fractals was kept under better control by both deposition of proper elements (and subsequent heat treatments) before the use the Pd wire and using gaseous environments ($P = 6\text{bar}$) at wire temperatures of the order of $200\text{--}300^\circ\text{C}$. Since 2007 were made noticeable changing both to the procedure of preparation of the Pd wire and experimental set-up (Fig. 1, Fig. 2) in order to can operate up to about 500°C [7] and measure the Pd wire temperature/power emitted: by 2 similar wires (in Pt) one used as calibrator (Pt_cal) and the other as monitor (Pt_mon). For a deeper understanding of our paper, because of length constrains of the Proceedings, we suggest reading: the ICCF14 paper [7], the ICCF15 oral presentation at: http://iccf15.frascati.enea.it/ICCF15-PRESENTATIONS/S4_O3_Celani.pdf

2. Descriptions

We have made verifications, among others by instrumental improvements, of measurements previously presented at ICCF14 (2008, Washington D.C.-USA) on anomalous excess heat using thin ($\Phi = 50\mu\text{m}$) and long ($l = 65\text{cm}$) Pd wires with surface covered by *several multi-layers of nano-materials* Pd included (nominally: $\Phi = 6\text{--}9\text{nm}$, $S = 300\text{m}^2/\text{g}$; layers thickness $< 1\mu\text{m}$). The excess heat was at macroscopic levels (up to 5W at the highest wire temperature operated of 500°C); the power density was 400W/g of bulk Pd or even larger (up to 5000-15000 W/g) if it is supposed that the main excess heat is generated between the several nano-layers. The current flowing inside the bulk Pd wire was up to 900mA, equivalent to a DC current density of $45\text{ kA}/\text{cm}^2$. The contribution of nano-layers to the total electric conduction is just *supposed* to be negligible in respect to one of Pd bulk.

* We decided to modify further our previous preparation procedures (very shortly described also at ICCF14, [7]) of nano-coating proper (several) materials onto the Pd wire surface in order to make the nano-coated wire more “resistant” to aging effects due to several, *partial*, loading-deload cycles.

* In addition, the material of the braid was changed from glassy fibres to pure quartz (in order to can increase wire’s temperature, from about 520°C to 850°C): such changing, in principle, improves the thermal coupling between braids (thermal conductivity of pure SiO_2 is higher than mixed oxides of Si-Na-B glasses) but, at the same time, the overall thermal losses from the hot wires to the cold ($30\text{--}60^\circ\text{C}$) internal wall of the reactor increase (wire temperatures are lower at the same electrical input power).

The main instrumental improvements were: a) addition of another long Pt thermometer surrounding all the previous 3-wires braid (the length of such Pt thermometer was 190 cm, i.e. about 3 times longer in respect to the (Pd-Pt-Pt) wires inserted into the braid); b) addition of others 2 thermocouples inside the pressurized SS chamber; c) external cooling (flow rate of 3-4 cc/s) water’s bath (volume 15 l) temperature made more homogeneous by bubbling air inside it from the bottom. All the data acquired, after correction by calibrations using ^4He , were consistent each-others.

According to our measurement procedures, we made experiments in ^4He (calibrations, Fig. 3) and subsequently in D_2 (Fig. 4) gas atmospheres (both at 6.5 bar). Some crosscheck tests were performed also under vacuum conditions (P about 10^{-3}bar), pure Ar (1-5.5bar), dry air (1-7bar).

We made new experiments also with a mixture of $\text{D}_2\text{--Ar}$ ($P = 4.62\text{--}1.68\text{bar}$; Fig. 5). The reason was to study if the effect of larger temperature of Pd wire, at same input power, could compensate for lower pressure of D_2 ($6.5 \rightarrow 4.6\text{ bar}$) or even increase anomalous heat production. Thermal conductivity of Ar is over 7 times lower in respect to D_2 ($T = 35\text{--}90^\circ\text{C}$): in the case of mixture $\text{D}_2\text{--Ar}$ [8], adding 24% of Ar to pure D_2 , the thermal conductivity is reduced (at 95°C) of 56% (from 151 to $96\text{mW}\cdot\text{m}^{-1}\cdot\text{K}^{-1}$).

The answer was that the increase of temperature improved, in a large way, the anomalous heat production and overcame the deleterious effect of D_2 partial pressure reduction. Such important result pushed us to increase the efforts to overcome the technological problems of high temperatures: we get strong indications that, at least in our experimental conditions, the Pd- D_2 system has a “*positive feedback*”

behaviour from the point of view of anomalous heat generation with the increasing of Pd wire temperature. Moreover, after some temperature threshold value has been overcome (about 200°C in our experimental conditions), the energy gain slope looks *larger* than linear versus temperature increase.

3. Key characteristics of nano-coated Pd wires

The loading time to get a 0.8 D/Pd ratio (of the *bulk Pd*) at RT, using pressure of Hydrogen or Deuterium gas of 6.5bar, was of the order of 10-20 second. The gas addition time, from vacuum condition, was 4-5 s. The deloading time, using vacuum and high temperatures, is quite long and depends on the “quality” of nanomaterials deposited on the Pd surface: as a general behaviour, as short was the loading time as long, and difficult, will be the deloading procedure. Several times it was necessary to reach, under vacuum, by Joule heating, temperature as high as 350-400°C for time as long as 1-2 hours, to get an almost “full” deloading. Anyway, we had indications that even such “heavy” procedures did not assure always a fully 100% Deuterium (or Hydrogen) out-gassing from Pd.

The whole effect was observed since 2002 even in electrolytic experiments: we named it the *DIODE EFFECT*. In other words, the good wires adsorb very easily the H₂ or D₂ and such gases, once absorbed, are very difficult to be desorbed.

In addition, we have some indications that the de-loading by direct heating of Pd wire (by Joule effect, and as a consequence some large voltage drop along the long Pd wire) is more difficult than of the deloading in indirect heating conditions (by the Pt_{cal} wire, near the Pd, used as heater, [6]). An innovatively speculative interpretation of such experimental behaviour is that the voltage drop along the Pd wire is operating against the D₂ deloading (possible experimental proof, of *Preparata Effect*).

4. Figure description.

The description of five figures are shortly reported as following:

Fig. 1. Photo of the three wires, each of $\Phi=50\mu\text{m}$ and $l=65\text{cm}$, before insertion in the SS reactor. Each wire (Pd, Pt, Pt) is inserted inside a quartz flexible sheath: they are closely braided each other. The braid is surrounded by several sheets of thermal insulating material (Superwool 607). It is high temperature annealed in air, before the use, to burn the several impregnating oils. Later it is vacuum degassed at 900°C. Similar treatments, at lower temperatures (700°C), are performed to the quartz sheaths.

Fig. 2. Photo of the whole experimental set-up with the SS pressurised reactor surrounded by water tank. The temperature of the water is kept stable by large cooling.

Fig. 3. Diagram of calibrations by ⁴He (at 6.5bar). The wire temperature of Pd is lower (e.g. about 30°C at a Pt temperature of about 480°C) because the increased power dissipation ability of Pd surface due to the nanomaterials coated. Moreover, the apparent detected power is lower (over 1W at an input power of 75W) because nanomaterial effect. The temperature detected by the third Pt wire (Pt_{mon.}), used as monitor, is about 40% of the temperature emitted by the Pd or Pt_{cal} calibration wires.

Fig. 4. Typical experiment with pure D₂ gas at a pressure of 6.5bar at RT. There are shown the behaviours of R/Ro of Pd, versus the power applied, both for the power applied to Pd (orange line, direct heating of Pd) and to the Pt_{cal} wire (blue colour). It is noticeable the larger maximum value of R/Ro (e.g. 2.3) of Pd, with direct heating, in respect to the maximum value with indirect heating (e.g. 2.18). We stress that, in all of our experiments, the maximum value of R/Ro in direct heating condition is *always* larger in respect to the indirect one. Such behaviour, taking into consideration that the R/Ro is directly related to D/Pd ratio, can suggest that the large voltage drop along the Pd wire (the so called “*Preparata Effect*”) due the current flowing inside the wire and/or the (new) transversal electric field toward the Pt wires (almost at zero potential) can be the reasons of such completely unexpected (and quite interesting) behaviour. Moreover, the energy gain increases at larger temperatures of Pd wires are due to both the combined effect of transition from β to α phase (larger diffusion coefficient, from $1.8 \cdot 10^{-3}$ to about $4 \cdot 10^{-3}$ cm²/s) and larger temperatures itself (the diffusion speed increase largely increasing the temperature). Such combined effects overcome the reduction of D/Pd ratio (from about 0.8 to about 0.1) that, according to several Authors, will affect negatively the anomalous heat production in D/Pd systems.

Fig. 5. The experiment is like that described in Fig. 4 but with a gas mixture (D₂+Ar) optimised to increase, at the same input power, the wires temperatures. Because of larger temperatures, in spite of reduction of D₂ pressure (from 6.5 to down 4.64 bar), the energy gain increased of about 50% in comparison with pure D₂ experiments. Such behaviour, together with other observation in other our

experiments, suggested us that the *anomalous energy gain*, once overcome the threshold value (about 200°C in such experiments) has a *behaviour larger than linear increasing in Pd wire temperature*.

Fig. 6. Because of the evidence about the relative maximum of R/Ro may be important both for the understanding of the phenomenon of anomalous heat emission (in our experimental conditions) and even for basic studies (like *High Temperature Bose-Einstein Condensate*, see later), *after the Conference*, we assembled a new experimental set-up devoted to study deeper it and rule out the possibility of experimental artefacts. In short, the braid has been wrapped around a small diameter (6/4 mm) Cu tube with a thermocouple inside (called Tc_inA): we build a sort of furnace heated externally by the Pd or Pt_cal wires. In Fig. 6, apart the temperature measured inside the tube by the insulated thermocouple, it is shown (at high data acquisition rate of 1s) the behaviour of R/Ro of Pd when the power (i.e. under electromigration regime) is applied to Pd itself (R/Ro_max=2.33) or to the Pt_cal (R/Ro=2.28).

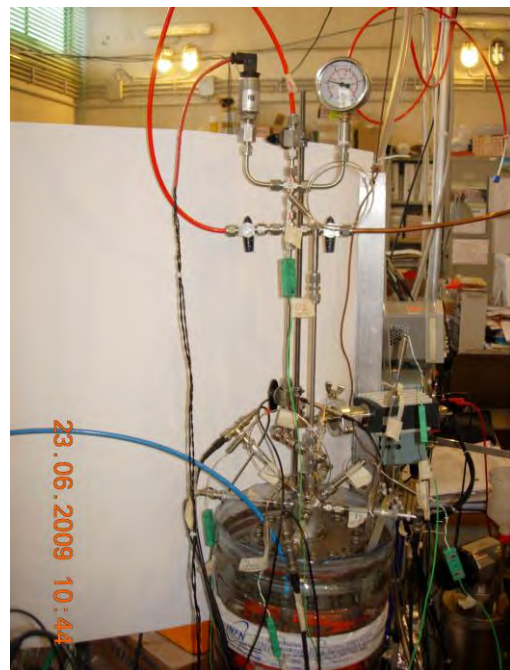


Fig. 1. - Photo of the 3 wires with thermal insulation. Fig. 2. - Photo of the experimental setup.

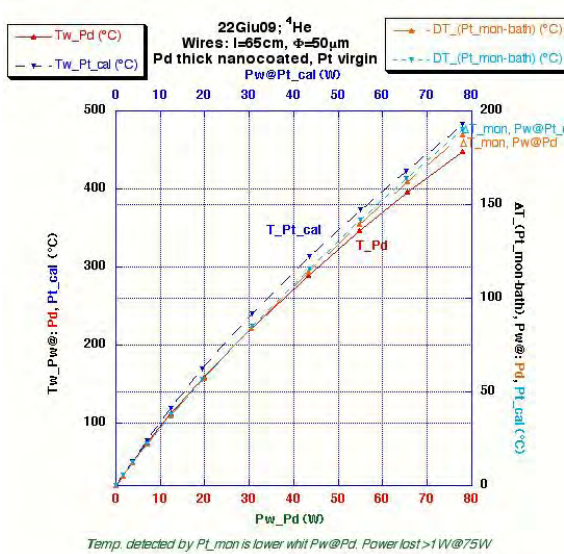


Fig. 3. - Calibration by ⁴He.

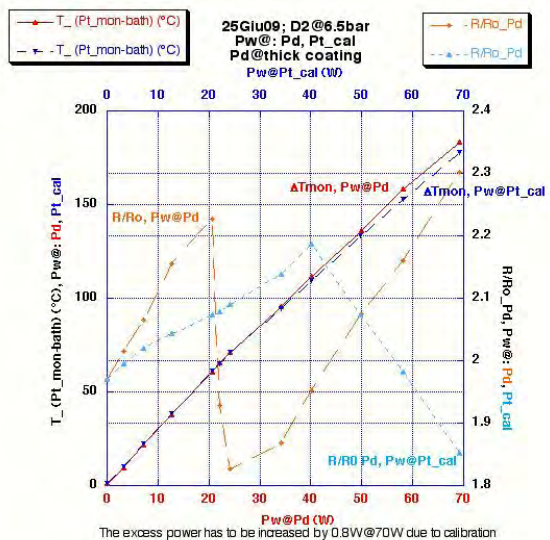


Fig. 4. - Experiment with D₂ pure at 6.5 bar.

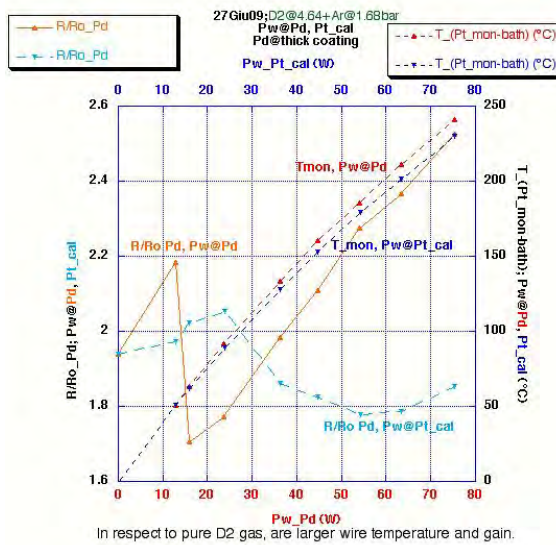


Fig. 5. - Experiment with D₂-Ar mixture.

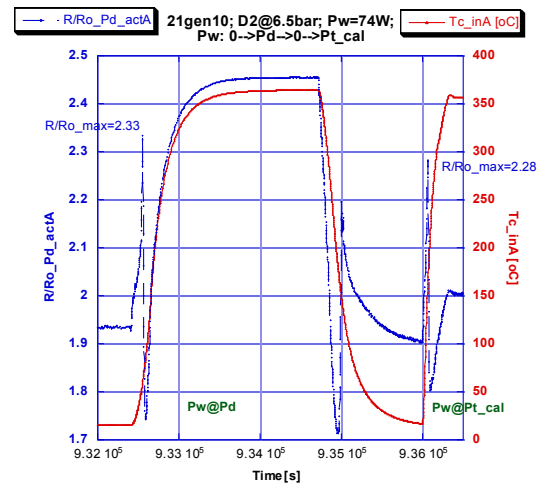


Fig.6. - R/Ro versus kind of power applied.

5. Conclusions

According to the experimental results we can argue that:

- 1) The data presented at ICCF14 were reconfirmed/reinforced (experiment with D₂+Ar mixture);
- 2) There are indications that increasing the temperature (e.g. the experiment with pure D₂ against the mixing D₂+Ar: at 70W of input power the Pt calibration temperature was 460°C in pure D₂ and 560°C in Ar+D₂) and (probably) the pressure on nanocoated Pd wires can be possible to increase the gain. We hope that our improved (multi-layer: SS&Cu 3N) high temperature and pressure reactor (in construction) will allow to overcome the problem of “poisons” coming out from the reactor wall (at least, we identified the S, at 300-700 ppm concentration, that is always present in the typical SS AISI 304 and 316 used for pressurized vessel). The general problem of S was introduced in same details, in the CMNS experiments, by Tatsumi Hioki (and Collaborators) from Toyota Company [9] since 2007 during ICCF13 (Sochi, Russia).
- 3) The new specific nanocoating of Pd wires improved their overall stability against “aging” effects due to loading-deloding cycles (the length of wire is weakly affected by such effect).
- 4) The well know, deleterious, effect of decreasing the amount of excess heat production after the “first” cycle seems not to be present in our experimental materials, set-up and operating conditions. *We can imagine that the continuous flowing of “fresh” Deuterium inside and through the Pd surface “clean up” the ashes of CMNS reactions.*
- 5) Because there are several indications that the system, in our experimental operating conditions, can have behaviour of “positive feedback” versus the temperature, some efforts have to be done to find a procedure to keep the “reactor” under **full control**, specially at temperatures of 700-850°C where the theoretic Carnot efficiency is quite high (of the order of 70%). The Carnot efficiency is the quality factor for practical applications: conversion of heat to “noble” energy.
- 6) Y. E. Kim (Purdue Univ., USA) suggested that the experimental, fully reproducible, evidence of a R/Ro values of Pd larger with direct heating (i.e. power applied, or better to say current-voltage, to Pd wire) in respect to indirect one (e.g. Fig. 4, 5, 6), can be explained as a proof of *Bose-Einstein Condensation* in Pd-D system [10]. F. Premuda (Bologna Univ., Italy) introduced since 1993 the BEC as possible explanation of anomalies in D-Pd systems [11]. Our opinion is that such experimental evidence (if reproduced also in other Laboratories) is the result of several combined conditions: a) voltage drop (and/or large current flowing: e⁻) along the long and thin Pd wire; b) large temperatures that reinforce the D flowing; c) effect of nanomaterials at the surface of the Pd wire (we experienced D/Pd ratio in nanomaterials even >1).
- 7) More work is needed both to increase the anomalous heat generation and identify the nuclear channels of the reaction (e.g. ⁴He, transmutations, isotope changing, ...).

Acknowledgments

* We are indebted to vacuum technologies group at INFN-LNF (headed by Mr. Valerio **Lollo**) for their help during the HT vacuum cleaning and conditioning of our SS reactor vessel.

* The welding group (Mr. Urbano **Martini**, Aldo **Olivieri** and Alessandro **Cassarà**), at INFN-LNF, made very patient and accurate work during the soldering of SS vessel: operations both in vacuum and pressure.

* We can't forget the continuous support/advice of the INFN-LNF Director Prof. Mario **Calvetti**.

* As quoted in the introduction, our work was also "inspired" by the experiments with nano-Pd (up to the recent Pd₃₅Zr₆₅ and Zr₆₅-Ni₃₀-Pd₅) absorbing Deuterium, as pioneered by Academician Yoshiaki **Arata** (Osaka University, Japan). Replication experiments (with Pd₃₅Zr₆₅ produced by Santoku Company at Kobe tanks to joint collaboration University-Industry), performed by Akito **Takahashi**-Akira **Kitamura** group (respectively at Technova Inc., Tokyo and Kobe University, Japan), reinforced both the Y. Arata results and our decision to pursue the nano-material "route" [12]. The pioneering work on multi-layer Pd-CaO, performed by Yasuhiro **Iwamura** group (at MHI, Yokohama, Japan), give some hints to develop our simplified "Atomic Layer Deposition" process made by chemical-thermal-mechanical procedures. Obviously, the system operated in tunneling regimes because of small dimensionality and the expertise/comments of Nobel Laureate Brian **Josephson** were important for us. The experiments performed independently by Prof. **Li Xing Zhong** (Tsinghua University, China; from 2002) and Jan Paul **Biberian** (Marseille University, France; from 2006) using Pd tubes (with even surface oxidized) reconfirmed the importance of surfaces/nanomaterials to promote anomalous thermal effects, although not stable versus time (surface damaged by the reaction itself). In deep discussions with the previous Scientist helped us to avoid mistakes and optimize our operations: we are deeply indebted with them.

* Last but not least, the partial and timely financial support by Eng. Luigi **Barbero** and Adriano **Bassignana**, both at Lam.Ba. Srl (Caluso, Turin-Italy) allowed, among others (like in deep technical discussions on the experimental set-up), to some of the Authors to attend the (quite expensive) ICCF15.

6. References

- [1] Y. Arata and Y. C. Zhang. Proc. Japan Acad. **70B**, 106 (1994). See also: Yoshiaki Arata "*Toward the Establishment of Solid Fusion as a Perpetual Energy for Humankind*", ISBN 888-6062-066-X (2008). Translated from Japanese to English (by M. Nakamura).
- [2] Y. Iwamura, T. Itoh et al. *Jpn. J. Appl. Phys.* **41**, 4642-4648 (2002)
- [3] E. Del Giudice, ...G. Preparata et al: "*The Fleischmann-Pons effect in a novel...*" Proc. ICCF8 (21-26 May 2000, Lerici-Italy). Edited by Italian Phys. Soc. **70**, 47-54 (2000). ISBN 88-7794-256-8.
- [4] F. Celani, A. Spallone et al. *Physics Letters A* 214 (1996), 1-13. See also ICCF5 (1995), F. Celani.
- [5] F. Celani, A. Spallone et al. "*High Hydrogen Loading into Thin....*" Proc. ICCF8 (21-26 May 2000, Lerici-Italy). Edited by Italian Phys. Soc. **70**, pg. 181-190 (2000). ISBN 88-7794-256-8.
- [6] A. Spallone, F. Celani et al. "*New Electrolytic Procedures for...*" Proc. ICCF8 (21-26 May 2000, Lerici-Italy). Edited by Italian Phys. Soc. **70**, pg. 191-198, (2000). ISBN 88-7794-256-8.
- [7] F. Celani et al. "*Deuteron electromigration in thin Pd wires coated...*" Proc. ICCF14 (2008), by WS. Allowable also at: [http://www.lnf.infn.it/sis/preprint/pdf/LNF-09-1\(P\).pdf](http://www.lnf.infn.it/sis/preprint/pdf/LNF-09-1(P).pdf)
- [8] R. S. Gambhir and S. C. Saxena, *Physica*, **32**, 2037-2043, (1966).
- [9] Tatsumi Hioki, Naoko Takahashi, Tomoyoshi Motohiro. "*XPS study on surface....*" Proc. ICCF13 (June 25-July 1, 2007, Sochi-Russia), pg. 518-528, ISBN 978-5-93271-428-7.
- [10] Y. E. Kim, "*Theory of Bose-Einstein condensation mechanism.....in micro/nano-scale metal grains and particles*". *Naturwissenschaften*, **96**, 803-811, (2009).
- [11] F. Premuda, "*Coulomb.. by Bose-Einstein Condensed..*" *Fusion Technology* **33**, 350-366, (1998).
- [12] Akira Kitamura, ...Akito Takahashi et al. "*Anomalous effects in charging of Pd powders...*" *Physics Letters A* **373** (2009), 3109-3112.

Hydrogen/Deuterium Absorption Property of Pd Fine Particle Systems and Heat Evolution Associated with Hydrogen/Deuterium Loading

T. Hioki¹, H. Azuma¹, T. Nishi¹, A. Itoh¹, J. Gao¹, S.Hibi¹, T.Motohiro¹, and J. Kasagi²

¹Frontier Research Center, Toyota Central R & D Laboratories, Inc., Nagakute, Aichi, Japan

²Research Center for Electron Photon Science, Tohoku University, Mikamine, Sendai, Japan

E-mail: hioki@mosk.tytlabs.co.jp

Abstract. Hydrogen absorption capacity and heat evolution upon loading with hydrogen/deuterium gas were measured for Pd-ZrO₂ nanocomposite obtained from Santoku Corporation. In order to examine the influence of oxidized Pd on both hydrogen absorption capacity and heat evolution, the measurements were performed three times repeatedly. Prior to each measurement, the samples were heat treated in vacuum at 523K for more than 2 hours. The first time measurement gave an apparent H/Pd ratio of 2.6 and a heat evolution of 2.6eV/Pd. During the first time measurement, the oxidized Pd was reduced to metallic Pd. It was found that the H/Pd ratio at 1MPa was slightly smaller than that of Pd bulk. It was also noted that Pd nanoparticles grow significantly during the cycles of absorption and desorption of hydrogen. When the sample was loaded with deuterium, intermittent heat evolutions as small as at most 0.1W were observed in the second stage where heat evolutions arising from chemical reactions were hardly expected.

1. Introduction

A very simple solid nuclear fusion reactor has recently been proposed by Arata and Zhang [1]. They have used a material of nano-sized (~5nm) Pd particles dispersed in ZrO₂ matrix. By simply pressurizing the material with deuterium gas, they have observed a long lasting difference in the temperature between the center of the sample powder and the outside surface of the sample vessel. When the sample was loaded with hydrogen gas, no such temperature difference was observed. Furthermore, by using a quadrupole mass spectrometer, they have observed a significant increase of ⁴He for the gas sampled from the powder pressurized with deuterium gas. From these facts, they have claimed a heat evolution arising from a deuteron-deuteron nuclear fusion reaction yielding ⁴He as ash.

Kitamura et al. [2] have constructed a flow calorimeter and measured quantitatively the heat evolution associated with loading of hydrogen or deuterium gas for Pd-ZrO₂ nanocomposite with Pd particle size of ~10nm. The material was obtained from Santoku Corporation and was different from those used by Arata and Zhang. Kitamura et al. have clearly observed a difference in the heat evolution between the loadings with deuterium and hydrogen in the second phase where heat evolution due to chemical reactions is not expected [2]. What seems to be important in the Arata and Zhang's experiment is that they have attained a very high value of hydrogen absorption capacity per Pd atom, i.e. D/Pd or H/Pd ratio, by using nano-sized Pd material. It has been known that attaining a D/Pd ratio larger than 0.88 is favorable to observe an excess heat in the electrochemical loading of Pd with deuterium [3]. Actually, a high value of hydrogen absorption capacity has been reported for nanoscale Pd particles embedded in ZrO₂ matrix prepared from Zr-Pd amorphous alloys [4]. Kitamura et al. [2] also reported a D/Pd or H/Pd ratio of 1.1 for the Santoku's Pd-ZrO₂ composite material, which far exceeds the reported value [5] of 0.74 for Pd bulk.

We have started to investigate the relationships between Pd particle size, hydrogen/deuterium absorption capacity and heat evolution upon loading with hydrogen/deuterium gas for nanoPd materials.

The results for Pd nanopowder and Pd- γ Al₂O₃ composite have been reported elsewhere [6]. In this paper, a similar study has been extended to Pd-ZrO₂ composite obtained from Santoku Corporation.

2. Experimental

2.1 Materials

The material used in this study was a composite of nanoPd and ZrO₂ (Pd-ZrO₂) synthesized by Santoku Corporation. The X ray diffraction pattern for the as-received sample showed that it consisted from PdO and ZrO₂. The contained amount of PdO was 35.4wt%. The crystal phases of the ZrO₂ component were monoclinic and tetragonal. The contained amount of each phase was roughly equal. The specific area was 38m²/g. As a reference for Pd bulk, Pd foils (99.95%, The Nilaco Corporation) with dimensions of 8mm × 30mm × 0.025mm were used.

2.2 Hydrogen storage capacity

A pressure-composition (PC) isotherm apparatus (Suzuki Shokan Co. Ltd) was used to measure hydrogen absorption capacity as a function of pressure up to about 1MPa at room temperature (300K). The purity of hydrogen and deuterium was 99.99999% and 99.995%, respectively.

2.3 Calorimetry

The heat evolution associated with loading of hydrogen isotope gas was measured with a flow calorimeter. The difference in the temperature between the inlet and outlet of the cooling water was measured with thermocouples of alumel-chromel. The flow rate of water was measured by using a Coriolis-force type flow meter. The temperature difference and the flow rate of water were registered every 30 seconds and used to calculate the heat power. An electric heater was mounted at the center of the sample vessel and used to determine the recovery rate of heat, i.e. the ratio of the calculated heat power with the measured temperature difference and the flow rate of water to the heat power supplied by the electric heater. A value of 0.55 was used as the recovery rate, which was almost independent on the species of the used gas (H₂, D₂, He), the gas pressure in the range 0 ~1 MPa, and the electric heater power in the range of 1~5W. In order to suppress the fluctuation and the drift of the measured output power, the calorimeter system was thermally insulated from the ambient atmosphere by using a thermal insulation material. The accuracy of the calorimeter was \pm 50mW. The gases were supplied into the sample vessel through a needle valve and a mass flow controller. The flow rate of gas was about 20ml/min.

3. Results and discussion

3.1 Hydrogen absorption capacity

The as-received Pd-ZrO₂ composite sample of about 10g was mounted in the sample vessel of the PC isotherm apparatus. First, in order to remove absorbed gases or molecules, the sample was evacuated for a day, heated up to 523K in vacuum and maintained at the temperature for about 2 hours, followed by natural cooling to room temperature. After these pre-treatments, hydrogen gas was supplied to the sample until the pressure of the sample vessel reaches a given value. At around the given pressure, about 30minutes were needed to achieve an equilibrium pressure. Thus, the hydrogen pressure was increased step by step up to 1MPa. After the course of this first time measurement, the sample was again evacuated for a day, heated up to 523K and maintained at the temperature for about 2 hours, followed by natural cooling to room temperature. Then, the second time measurement was performed following the same procedure as those of the first time.

In Fig.1, the relationship between pressure and composition (H/Pd) are shown for three times successive measurements. It is seen that in the first time measurement, H/Pd ratio at 1MPa reaches a value of 2.6, while this value decreases greatly to a value of 0.70 in the second and third measurements. This difference is attributed to the fact that the Pd particles are initially oxidized and reduce to metallic Pd during the first time measurement. Then, in the first time measurement both of the following chemical reactions occur :



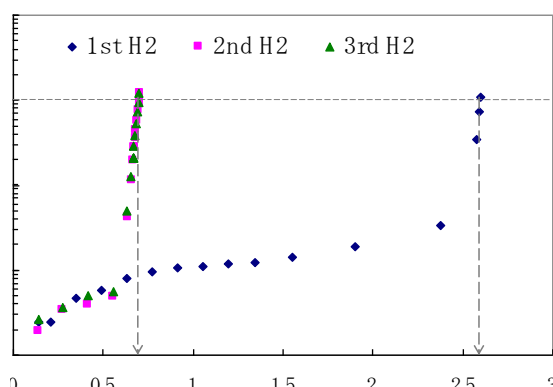


Fig.1 - Pressure- composition isotherms for Pd-ZrO₂ composite. The results of three times repeated measurements are shown.



The water formation reaction (1) gives an apparent H/Pd ratio of 2.0, and the hydride formation reaction (2) gives a true value of hydrogen absorption capacity x . The value of x is obtained from the experiment in the second or the third time measurement and x is 0.70 as seen in Fig.1. Therefore, when the Pd particles are nearly 100% oxidized, an apparent H/Pd ratio of ~ 2.7 is obtained. The observed value of 2.6 indicates that 95% of Pd in the as- received sample is in the chemical state of PdO.

The PC isotherms were also measured for Pd foil samples of about 3g. The measurements were repeated two times. For this sample, no difference in the H/Pd ratio at 1MPa was seen between the two measurements, indicating that the foil sample was nearly 100% metallic. The H/Pd ratio for this sample was 0.74. This value agrees with the literature value [5] for Pd bulk. Therefore, the H/Pd value of 0.70 for the Pd-ZrO₂ composite sample is slightly smaller than the value of Pd bulk. This is contrary to the expectation that the hydrogen absorption capacity for nano-sized Pd particles is increased compared to that for Pd bulk. Similar results have been observed for Pd nanopowder and Pd- γ Al₂O₃ composite, as reported elsewhere [6].

3. 2 STEM observation

In order to examine the size and distribution of the Pd particles, scanning transmission electron microscope (STEM) observations with an electron beam focused to less than 1nm were performed for the samples as-received and after the three times PC isotherm measurements. From Fig.2 (a), it is seen that the size of the Pd particles (white spot) for the as-received state is roughly about 10nm. Fig.2 (b) and (c) show the lateral distribution of characteristic Zr(L) and Pd(L) X-ray intensity, respectively. It is seen from Fig.2 (b), (c) or from Fig.3 (b), (c) that the Pd particles do not distribute uniformly in the ZrO₂ matrix. From Fig.3(a), it is seen that the size of the Pd particles after the PC measurement is 15-20nm, which is significantly larger the initial value. This fact indicates that Pd particles grow during the hydrogen absorption and desorption cycles. Similar growth of Pd nanoparticles during the cycles of absorption and desorption of hydrogen has also been reported for nanoPd powder and Pd- γ Al₂O₃ composite [6]. It should be mentioned that the measured H/Pd ratio, i.e. 0.70, is for Pd particles with a size significantly larger than the initial value determined for the as-synthesized sample.

3.3 Heat evolution upon loading with hydrogen isotope gases

The as-received Pd-ZrO₂ composite sample of 51.4g (Pd :15.6g) was mounted in the sample vessel of the calorimeter. The sample was first evacuated for two days and heated up to 523K in vacuum and maintained at the temperature for about 2 hours, followed by natural cooling to room temperature. Then, deuterium gas was supplied to the sample at a flow rate of 20ml/min with a mass flow controller up to 0.4MPa. From 0.4MPa to 1.0MPa, the flow rate was controlled manually with a needle valve, and the

flow rate was in the range 20–40ml/min. When the pressure reached the value of 1MPa the gas supply was stopped and the sample was maintained under the fixed pressure of 1MPa. Here, we define the first stage as the period where the pressure was raised from 0 to 1 MPa, the second stage as the period where the sample was maintained under the constant pressure of 1MPa. As in the case of hydrogen absorption capacity measurements, the measurement of heat generation upon loading of deuterium /hydrogen gas was repeated three times. Prior to each measurement, the sample was heat treated in the same way as the first time measurement. In Fig.4 (a), (b) and (c), the heat power as a function of time is shown for the first time loading with D₂, the second time loading with D₂ and the third time loading with H₂, respectively. The variation of pressure with time is also shown in Fig.4. It is clearly seen that the heat evolution in the first stage is remarkable in the first time measurement while it decreases greatly in the second or third time measurement. This behavior is quite similar to that of hydrogen absorption capacity, suggesting that the heat evolution in the first stage is related with the chemical reactions (1) and (2). In fig.5, the variation of the heat evolution in the first stage with the order of measurement cycle is shown. The experimental values are compared to the estimated ones. The estimation was made assuming that in the first time measurement, both of the reactions (1) and (2) contribute to the heat evolution while only the reaction (2) in the second and third time measurements. The values of $\Delta H(\text{water})=-178\text{kJ/molPd}$ [7] and $\Delta H(\text{hydride})=-40\text{kJ/molH}_2$ [8] were used. It was further assumed that $\Delta H(\text{hydride}) = \Delta H(\text{deuteride})$ and the ratio of the oxidized Pd to the total Pd before the first time measurement was 95%. It is seen in Fig.5 that the heat generated in the first stage is largely explained by the chemical reactions (1) and (2). Therefore, in the first stage it is difficult to identify the heat evolution from nuclear origin, if any. However, in the second stage, any chemical reactions are hardly expected to occur. In Fig.6, the same figure as Fig.5 is shown with the vertical axis magnified by ten times. It is noted that in the second stage a small heat evolution is observed intermittently for the first and second time loadings with D₂ while no such heat evolution is observed in the third loading with H₂. Similar behavior of heat evolution in the second stage has also been reported for nanoPd power and Pd- γ Al₂O₃ composite [6]. The heat evolution of the second stage observed in the present study seems to be considerably smaller compared to that reported by Kitamura et al. [2]. It is required to enhance the heat power in the second stage in order to clarify the origin of the observed anomalous heat evolution.

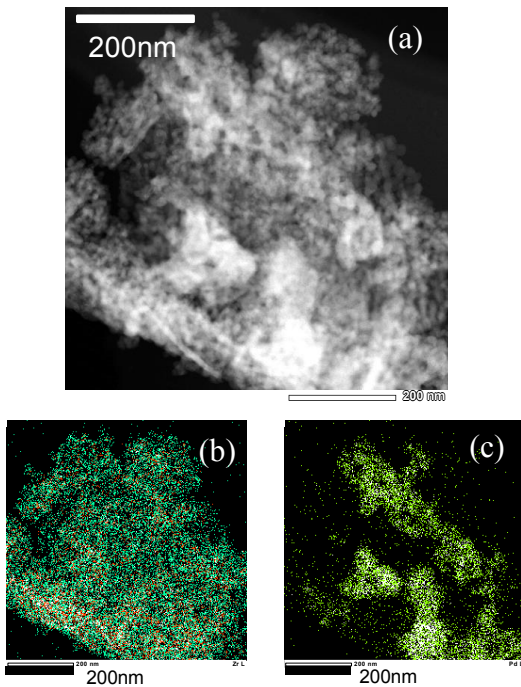


Fig.2 - (a)STEM image of the as-received sample, (b) Zr(L) image, (c) Pd(L)image

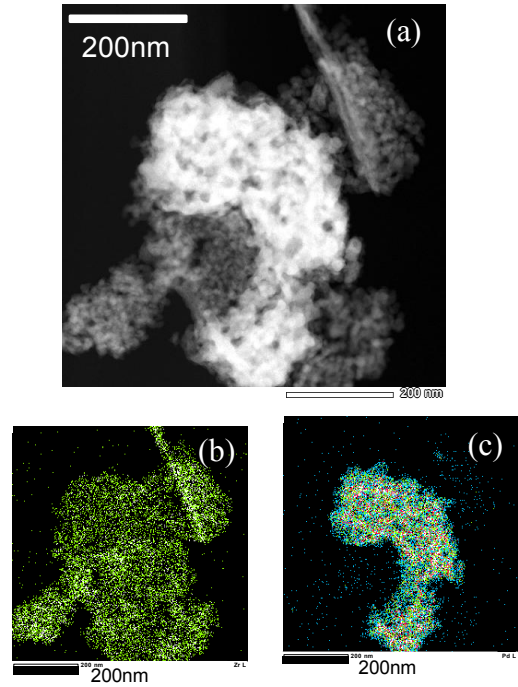


Fig.3 - (a)STEM image after measurements of H/Pd, (b) Zr(L) image, (c) Pd(L) image

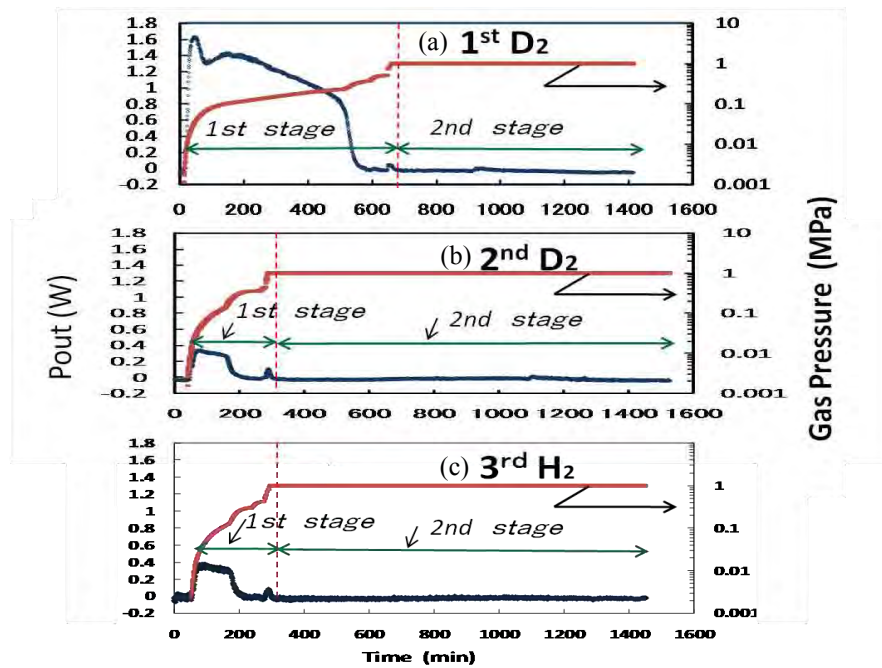


Fig.4 - Heat power and gas pressure as a function of time for Pd-ZrO₂; (a) the first cycle loading with D₂, (b) the second cycle loading with D₂, (c) the third cycle loading with H₂.

4. Summary

Hydrogen absorption capacity and heat evolution with loading of hydrogen isotope gases were measured for composite samples of Pd-ZrO₂ obtained from Sankoku Corporation. The followings were found.

- (1) The chemical state of Pd in the as received powder was 95% PdO. As a result, the first time loading with hydrogen gave an apparent hydrogen absorption capacity at 1MPa as large as H/Pd = 2.6 and heat evolution in the first stage as large as 2.6eV/Pd. These values are largely understood by taking into account the two chemical reactions; the water formation reaction and the hydride formation reaction. The PdO was reduced to metallic Pd during the first time measurement.
- (2) In the second or third time measurement of hydrogen absorption capacity, a true value of H/Pd = 0.70 was obtained. This value is slightly smaller than the value of Pd bulk.

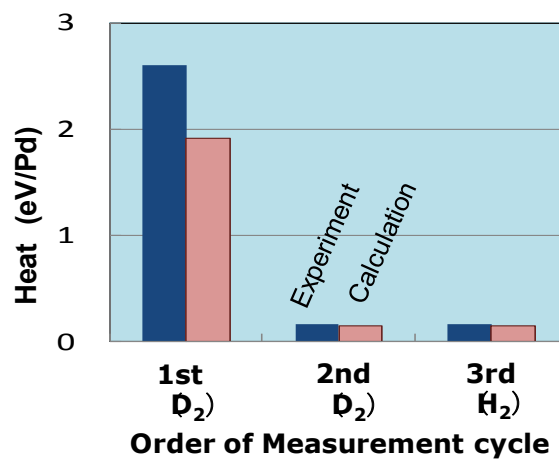


Fig.5 - The variation of the heat generated in the first stage with the order of measurement cycle. The experimental values are compared to the calculated ones.

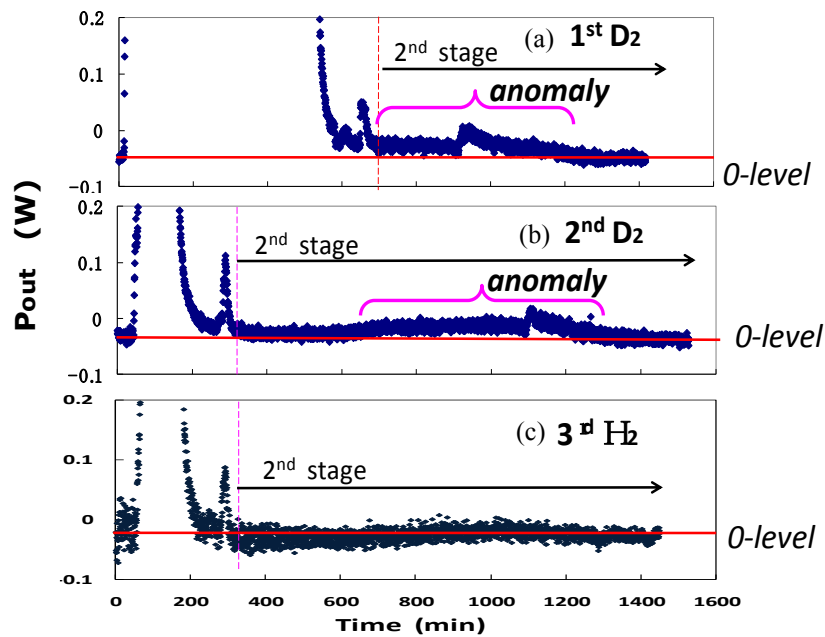


Fig.6 - Heat evolution in the second stage. The vertical axis of Fig.3 is magnified by ~ 10 times.
 (a) the first cycle loading with D₂, (b) the second cycle loading with D₂, (c) the third cycle loading with H₂.

(3) The size of the Pd particles was found to be increased significantly during the repeated measurements of hydrogen absorption capacity.

(4) When the sample was loaded with D₂ gas, a very small heat power was observed intermittently in the second stage where chemical reactions are hardly expected to occur.

Acknowledgement

We greatly thank N. Suzuki for the STEM observations.

References

- [1] Y. Arata and Y. Zhang, *Journal of High Temperature Society* **34**, 85-93 (2008).
- [2] A. Kitamura, T. Nohmi, Y. Sasaki, A. Taniike, A. Takahashi, R. Seto, and Y. Fujita, *Physics Letters A* **373**, 3109-3112 (2009).
- [3] M. McKubre, F. Tanzella, P.L. Hagelstein, K. Mullican, and M. Trevithick, *Proceedings of the 10th International Conference on Condensed Matter Nuclear Science*, edited by P. Hagelstein and S. Chubb, Cambridge, Massachusetts, 2003, pp.199-212.
- [4] S. Yamaura, K. Sasamori, H. Kimura, A. Inoue, *J. Mater. Res.* **17**, 1329-1334 (2002).
- [5] E. Wicke and H. Brodowsky, in *Hydrogen in Metals II*, edited by G. Alefeld and J. Volkl, Springer, 1978, p.81.
- [6] T. Hioki, H. Azuma, T. Nishi, A. Itoh, S. Hibi, J. Gao, T. Motohiro, and J. Kasagi, AIP Source Book, edited by J. Marwan, submitted.
- [7] HSC Chemistry 6.1, "Chemical Simulation and Reaction software with Extensive Thermo-chemical Database", Outokumpu Research, Oy, Finland, (2007).
- [8] Y. Fukai, K. Tanaka, Y. Uchida, *Suiso to Kinzoku*, Uchida Rokakuho Publishing Co. Ltd., Tokyo, 1998, p.38.

Anomalous Heat Generation in Charging of Pd Powders with High Density Hydrogen Isotopes, (I) Results of absorption experiments using Pd powders

Y. Sasaki¹, A. Kitamura¹, Y. Miyoshi¹, T. Nohmi¹, A. Taniike¹,
A. Takahashi², R. Seto², and Y. Fujita²

¹*Division of Marine Engineering, Graduate School of Maritime Sciences, Kobe University, Higashinada-ku, Kobe 6580022, Japan*

²*Technova Inc, Chiyoda-ku, Tokyo 1000011, Japan*

E-mail: 088w508w@stu.kobe-u.ac.jp

Abstract. A twin system for hydrogen-isotope absorption experiments has been constructed to replicate the phenomenon of heat and ⁴He generation by D₂ gas absorption in nano-sized Pd powders reported by Arata and Zhang, and to investigate the underlying physics. For Pd-Zr oxide nano-powders, anomalously large energies of hydrogen isotope absorption, 2.4 ±0.2 eV/D-atom and 1.8 ±0.4 eV/H-atom, as well as large loading ratio of D/Pd = 1.1 ±0.0 and H/Pd = 1.1 ±0.3, respectively, were observed in the phase of deuteride/hydride formation. The sample charged with D₂ also showed significantly positive output energy in the second phase after the deuteride formation. For comparison, results for 0.1-μmφ Pd powder samples and Pd-black samples are also shown..

1. Introduction

Arata and Zhang recently reported that highly pure D₂ gas charging of Pd nano-powders in the form of Pd/ZrO₂ nano-composite induced significantly higher temperatures inside the reactor vessel than on the outside wall for more than 50 hours, while runs with H₂ gas showed almost no temperature difference.¹⁾ To verify that the excess heat originated in a nuclear process, a QMAS was employed to show the existence of ⁴He as nuclear ash in the vessel and in the powder after the charging. The charging system is a sophisticated and simplified version of the previous-generation DS reactor²⁾. Replication experiments using systems similar to the DS reactor with Pd-black seem to be successful^{3,4)}. It is extremely important to confirm the phenomenon of heat and ⁴He generation with fully quantitative confidence.

In the present work we constructed an experimental system to replicate the phenomenon and to investigate the underlying physics. Two lots of oxide samples of mixture of Pd (34.6 %) and Zr (65.4 %) were fabricated by Santoku Corporation, Kobe, Japan. The first sample had an average particle size of 7.7 μm, a specific surface area of 37.1 m²/g, and had an average Pd grain size of 10.7 nm, while the second sample had 8.5 nm Pd grain size. If we assume perfect oxidation of the metal elements, 10 g of the sample contains 3.0 g of Pd.

2. Experimental system

The D₂/H₂ absorption system is composed of two identical chambers (an A₁·A₂ twin system): one for a D₂ gas foreground run, and the other for H₂ gas background run. As shown in Fig.1 and Fig.2 each part has an inner reaction chamber containing Pd powder and an outer chamber that is evacuated to provide thermal insulation for calorimetry. A sheath heater and a cooling water pipe (copper) are wound on the outer surface of the reaction chamber for baking the sample powder and for flow calorimetry to estimate the heat production rate, respectively. A pair of thermocouples is provided for the flow calorimetry by measuring the temperature difference between the inlet and the outlet of the cooling water.

The D_2 gas is nominally 99.5 % pure and the H_2 is 99.998 % pure. Flow rate control of D_2/H_2 gas purified through a liquid-nitrogen cold trap is made either with a Pd membrane filter or a ‘SuperNEEDLE’ valve. The gas flow rate is controllable between 1 and 1000 sccm at 1MPa by the latter. All parameters measured are stored in a PC with an acquisition period of 1 min.

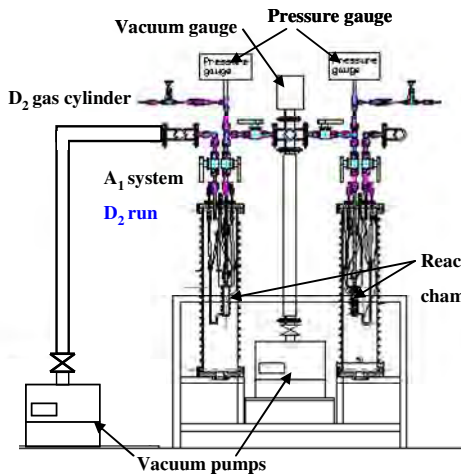


Fig. 1. - Reduced view of the A_1 - A_2 twin system

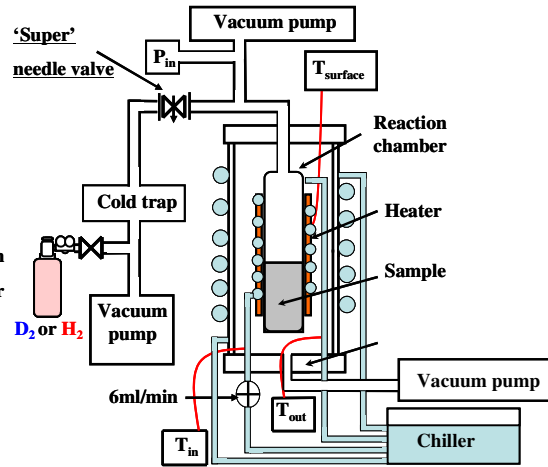


Fig. 2. - Functional view of A_1

3. Preliminary experiments

As a calibration of the flow calorimeter, we measured the heat recovery rate under a variety of conditions; with input power of 1, 3, 6 and 10 W, and D_2 gas pressure of 0, 0.1, 0.3 and 1.0 MPa in the reaction chamber. The coolant flow rate was 6 ml/min in all cases. The heat recovery rate was found to be almost independent of the pressure and the input power, and the averaged value is $(63.1 \pm 5.8) \%$. Temperature response to a stepwise variation of the input power was found to be expressed as a simple exponential function with a time constant of 5.2 min.

We examined temperature uncertainty and drift, with no sample powder put in the A_1 chamber filled with H_2 gas at a pressure of 1MPa. The inlet-outlet temperature difference and the output power deduced from it showed short-term fluctuation as shown in Fig.3. If we regard an experimental error in the present system as the standard deviation of the longitudinal data, the error or the uncertainty for the output power and the integrated output energy measured for the A_1 - A_2 system is evaluated to be 0.014 W and 0.83 kJ for 1000-min acquisition. In the prototype system A_0 , which had the larger time constant and smaller sensitivity of heat measurement, and was used in the 1st stage experiments with the 0.1- $\mu\text{m}\phi$ Pd powder and the Pd-black⁵⁾, a temperature drift observed sometimes resulted in the larger error of 4.0 kJ for 1000-min run.

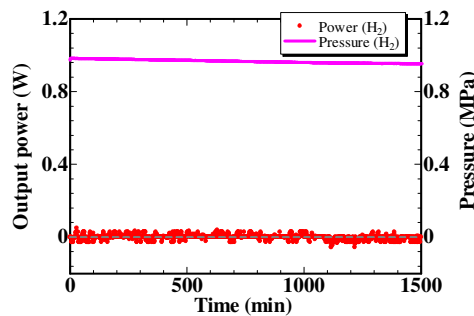


Fig.3. - Blank run with no sample powder.

4. Samples

We used three kinds of samples—PP (Pd powder with particle diameter of 0.1 μm and a purity of 99.5 %), PB (Pd-black with a particle size of “300 mesh”) and PZ (purity of 99.9 %, and mixed oxides of Pd·Zr). Figure 4 shows TEM images of the second lot PZ sample taken by courtesy of Prof. R. Duncan *et al.*, the Nuclear Science and Engineering Institute and Particulate Systems Research Center at the University of Missouri-Columbia.

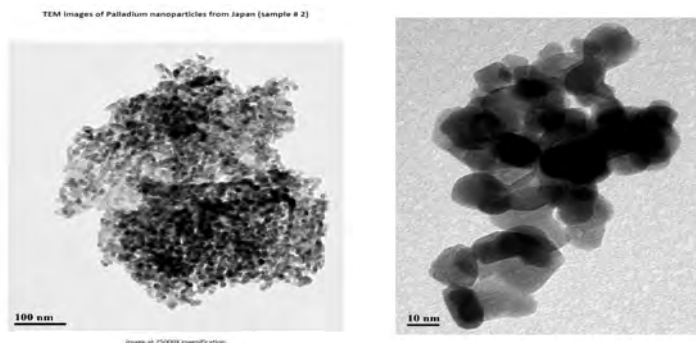


Fig.4. - TEM images of the PZ sample (the second lot).

In the following, the run number is designated by “G-PN#M”, with G, P, N and M being the gas species, the powder species, powder ID, and the number of repeated use, respectively. For example, “D-PB2#3” represents the third absorption run with D_2 using a Pd-black sample “2” following evacuation and baking after two cycles of evacuation-baking-absorption.

5. Results

5.1 Results by $\phi 0.1\mu\text{m}$ -Pd powder

First, we describe absorption runs using the A_0 system for five gram of 0.1- $\mu\text{m}\phi$ Pd powder. The reaction chamber filled with the powder was evacuated and heated for baking at 430 K. Then highly pure D_2 or H_2 gas was introduced into the reaction chamber through the Pd membrane filter. The results for the case of D_2 and H_2 absorption are compared in Fig.5. After the gas was introduced, pressure did not begin to rise for a while. During this phase (the first phase) the Pd powder absorbed almost all of the D_2 (H_2) gas atoms as they flowed in, and heat was released as a result of adsorption and formation of deuterides (hydrides). After about 30 minutes, the powder almost stopped absorbing gas; the gas pressure began to rise, and the heat release from deuteride (hydride) formation subsided. This is the beginning of the 2nd phase, and the gas flow rate in the 1st phase is evaluated from the rate of the pressure increase. From the flow rate multiplied by the duration of the 1st phase, loading was estimated to reach $\text{PdD}_{0.43}$ ($\text{PdH}_{0.44}$).

The output powers are integrated over the 1st phase to give the output energies of 0.10 kJ/g-Pd(D) and 0.08 kJ/g-Pd(H), which are divided by the loading ratio of 0.43 and 0.44 to give the heat of solution ΔH_s ,

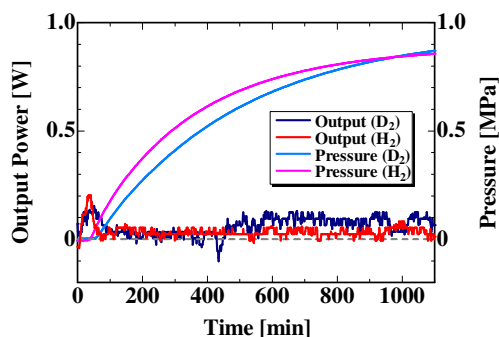


Fig. 5 - Evolution of heat and pressure in the vessel after introduction of D_2 gas (blue/light blue) or H_2 gas (red/pink) to 0.1- $\mu\text{m}\phi$ Pd powder (D-PP1#1 and H-PP2#1). Power is slightly higher for D than H after 500 min.

of 0.24 eV/atom-D and 0.20 eV/atom-H, respectively. The values appear to be somewhat larger than those found in literatures⁶⁻¹⁰. However, they are consistent with each other, when we take into account that the differential heat of solution is a decreasing function of the loading ratio; $\Delta H_s = 0.15, 0.12, 0.070,$ and 0.061 eV/H for H/Pd ratio of 0.5, 0.55, 0.6 and 0.65^{9,10}. The difference between D and H, the isotope effect, is rather large, but is not considered to be anomalous, since we find $\Delta H_s(D)/\Delta H_s(H) = 1.25$ in ref. [9]. On the other hand, the output energies in the 2nd phase, *i.e.*, the output powers integrated over the 2nd phase with duration of 1,400 min, are smaller than the experimental error mentioned above, and “excess heat” is not meaningful in this case. The results are summarized in Table I, which includes those for the Pd-black and the Pd-Zr mixed oxide samples.

5.2 Results by Pd-black

The second kind of the sample tested is commercially available 300-mesh Pd-black whose surface has a kind of nano-scale fractal structure finer than the $0.1\text{-}\mu\text{m}\phi$ Pd powder. The performance of Pd-black absorption of D₂ using the A₀ system is compared with that of H₂ in Fig. 6. It is very interesting to note that: (1) much higher loading to PdD_{0.88} or PdH_{0.79} is realized, and (2) the output energies in the 1st phase, $E_{1st} = (0.67 \pm 0.12)$ eV/atom-D and (0.62 ± 0.11) eV/atom-H, are 2 - 3 times larger than those for the $0.1\text{-}\mu\text{m}\phi$ Pd powder and those found in the literatures⁶⁻¹⁰. On the other hand, the output energy of 8.3 ± 4.5 kJ (2.6 ± 1.4 kJ/g-Pd) in the 2nd phase of D₂ absorption appears to be larger than that in the case of H₂. The difference is only marginal compared with the above-mentioned error due to the temperature drift of 5.5 kJ in the present case.

Using the improved twin system A₁-A₂, we compared the performance of the Pd-black sample PB3 with a prolonged duration of the 2nd phase of 4,500 min, which was subjected to repeated use with the sample baking before absorption made at 440 K for 3 h (#2), or at 570 K for 1 h (#3). The results are shown in the 6th row through the 8th in Table I.

First we notice that the first run (D-PB3#1) has essentially the same D/Pd ratio and the energy output E_{1st} as those with the A₀ system. Second the repeated use retains almost the same or even higher energy output E_{1st} in spite of the significantly smaller D(H)/Pd ratio. This interesting fact could be related to some structural change of the sample.

As for the 2nd phase, we have little to discuss, when we take into account that they are comparable to the error of 4.0 kJ/1000-min mentioned above for the A₀ system.

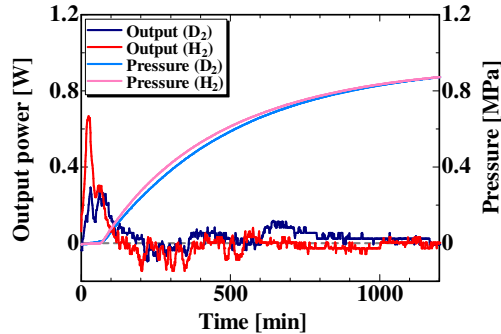


Fig.6. - Evolution of heat and pressure in the vessel after introduction of D₂ gas (blue/light blue) or H₂ gas (red/pink) to 300-mesh Pd-black (D-PB1#1 and H-PB2#1). Power is slightly higher for D than H in the 2nd phase.

5.3 Results by Pd-Zr oxide compounds

Now we describe the performance of the mixed oxides of Pd-Zr that are thought to have even finer mesoscopic structure. The results of 8 runs using virgin PZ samples are summarized in the last 8 rows in Table I. Those of runs with repeated use of the PZ sample will be discussed in the next paper¹²) together with the above-mentioned PB samples. Using the A₁-A₂ twin system, the runs H-PZ(2n)#1 were performed simultaneously with D-PZ(2n-1)#1, where $n = 1, 2, 3,$ and 5 . The A₁ subsystem was used for D-PZ1#1, D-PZ3#1, H-PZ6#1, and D-PZ9#1. In all runs, the PZ sample used was 10 g, and the baking

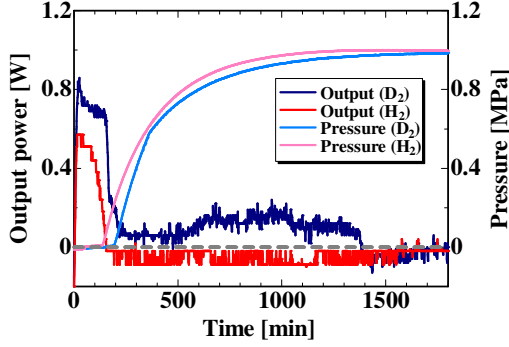


Fig. 7 - Evolution of heat and pressure in the vessel after introduction of D₂ gas (blue/light blue) or H₂ gas (red/pink) to Pd-Zr oxide compounds (D-PZ1#1 and H-PZ2#1). Heat-power level by D is larger than that by H in the 1st phase and also in the 2nd phase.

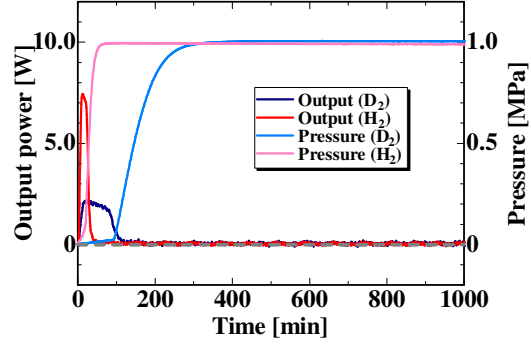


Fig. 8 - Evolution of heat and pressure in the vessel after introduction of D₂ gas (blue/light blue) or H₂ gas (red/pink) to Pd-Zr oxide compounds (D-PZ9#1 and H-PZ10#1).

temperature was 570 K for 3 h. The output energy in the 2nd phase is the power integrated over 1,600 min. In PZ1~6, we use the 10.7-nm sample, while in PZ9 and 10, we use the 8.5-nm sample. Examples of the evolution of the output power and the pressure for runs D-PZ1#1 and H-PZ2#1 are shown in Fig. 7. And D-PZ9#1 and H-PZ10#1 are shown in Fig. 8.

Table I. Comparison of absorption runs for the 0.1- $\mu\text{m}\phi$ Pd powder (PP), the 300-mesh Pd-black (PB), and the Pd-Zr nano-composite (PZ).

run	weight [g]	flow rate [sccm]	Output energy[kJ]		Specific output energy[kJ/g]		D/Pd or H/Pd	E per D/H atom
			1st phase	2nd phase	1st phase	2nd phase		
D-PP1#1	5	3.5	0.5±0.4	2.5±4.1	0.10±0.07	0.52±0.83	0.46	0.24
D-PP1#2	5	4.3	0.5±0.2	4.0±4.4	0.10±0.05	0.79±0.88	0.43	0.26
H-PP2#1	5	6.8	0.4±0.2	2.6±3.9	0.08±0.003	0.53±0.8	0.45	0.20
D-PB1#1	3.2	3.5	1.7±0.3	8.3±4.5	0.54±0.1	2.6±1.4	0.85	0.69
H-PB2#1	3.6	5.6	1.6±0.3	-2.2±4.6	0.45±0.08	-0.62±1.3	0.78	0.63
D-PB3#1	20	2.9	9.3±1.1	1.1±0.5	0.47±0.06	0.06±0.02	0.78	0.66
D-PB3#2	20	0.8	3.3±0.5	3.4±2.6	0.17±0.03	0.17±0.13	0.23	0.79
H-PB4#2	20	1.9	3.2±0.2	14±4.6	0.16±0.01	0.68±0.23	0.22	0.80
H-PB4#3	20	1.5	16±2.4	-4.8±8.1	0.79±0.01	-0.24±0.40	0.20	4.42
D-PB3#3	20	1.1	14±1.7	-2.2±1.1	0.68±0.01	-1.1±0.54	0.22	3.51
D-PB3#4	20	1.1	3.1±0.4	0.3±4.7	0.16±0.02	0.02±0.23	0.24	0.71
D-PZ1#1	10	1.76	7.0±0.2	6.8±1.3	1.3±0.04	1.9±0.31	1.08	2.39
H-PZ2#1	10	2.29	3.6±0.1	-5.1±1.4	1.0±0.03	-1.5±0.32	1.00	1.33
D-PZ3#1	10	1.85	6.4±0.2	5.5±0.8	2.13±0.0	1.2±0.2	1.07	2.20
H-PZ4#1	10	2.93	5.1±0.1	1.1±0.9	1.70±0.0	-1.3±0.2	0.86	2.18
D-PZ3#2	10	1.66	0.17±0.03	9.89±1.48	0.03±0.07	2.3±0.35	0.29	0.13
H-PZ4#2	10	2.79	0.58±0.05	1.68±1.46	0.17±0.01	0.39±0.34	0.31	0.59
D-PZ3#3	10	1.69	0.29±0.04	-3.47±0.34	0.07±0.09	-0.81±0.35	0.25	0.29
H-PZ4#3	10	2.99	0.37±0.02	0.75±0.35	0.01±0.01	0.17±0.34	0.26	0.42
D-PZ5#1	10	2.02	7.14±0.15	1.26±1.36	2.37±0.04	0.29±0.32	1.04	2.51
H-PZ6#1	10	6.23	7.07±0.07	-0.23±1.44	2.33±0.02	-0.05±0.33	1.41	1.82
D-PZ5#3	10	9.93	0.54±0.03	0.23±1.51	0.18±0.01	0.08±0.50	0.25	0.74
H-PZ6#3	10	10.69	0.92±0.03	4.18±1.51	0.31±0.01	1.39±0.50	0.30	1.10
D-PZ9#1	14	6.42	10.23±0.10	3.81±1.51	2.44±0.02	0.91±0.36	1.41	1.87
H-PZ10#1	14	22.55	9.56±0.03	3.82±1.51	2.28±0.01	0.91±0.36	1.02	2.46

We notice the following five facts in the 1st phase: (1) very large output energies that are more than 3 times greater than those for the Pd-black samples, (2) very large D/Pd (H/PD) ratios of 1.1 ± 0.0 (1.1 ± 0.3) that are even higher than those for the PB samples, (3) surprisingly large $E_{1st} = (2.4 \pm 0.2)$ eV (D) and (1.8 ± 0.4) eV (H) on the average, and (4) larger isotope effect in E_{1st} compared with those for 0.1- $\mu\text{m}\phi$ powder and Pd-black; the difference just exceeds the error range determined from standard deviations, (5) the output energy increases with increasing flow rate.

For the 1st phase heat data of D-PZ9#1 and H-PZ10#1, we observed that power levels increased almost proportionally to the increase of flow rates. In the 2nd phase, D-PZ9#1 has no positive net output heat. The sample size and the flow rates are thought to be causally related to this phenomenon. In the PZ9 and 10, the flow rates might have been set too large to get the positive net output heat, because the faster formation of the saturated pressure condition might affect the dynamic condition. We need further study by changing the flow rate to this respect.

In two runs using H₂, we have negative integrated values for the specific output energies in the rather stable 2nd phases. This should be considered to be due to a slight shift in the zero point of the thermocouple signal.

Finally, it should be mentioned that we observed nothing other than steady background in the neutron counter and the scintillation probe located just outside the outer chambers.

Further discussions and conclusions on the results and a possible underlying physics are given in the succeeding paper¹²⁾ in this Proceedings.

6. References

- [1] Y. Arata and Y. Zhang: The special report on research project for creation of new energy, J. High Temperature Society, 2008, No. 1.
- [2] Y. Arata, and Y. Zhang: *Condensed Matter Nuclear Science, Proc. 12th Int. Conf. on Cold Fusion* (ed. A. Takahashi, Y. Iwamura, and K. Ota, World Scientific, 2006) pp.44-54.
- [3] V. A. Kirkinskii, A. I. Kumel'nikov: *Proc. ICCF13, Sochi, 2007* (Publisher Center MATI, Moscow, ISBN 978-5-93271-428-7) pp.43-46.
- [4] J. P. Biberian and N. Armanet: *ibid.* pp.170-180.
- [5] T. Nohmi, Y. Sasaki, T. Yamaguchi, A. Taniike, A. Kitamura, A. Takahashi, R. Seto, and Y. Fujita: <http://www.ler-canr.org>; to be published in Proc. 14th Int. Conf. Condensed Matter Nuclear Science (ICCF14), Washington DC, 2008.
- [6] *Hydrogen in Metals II -Topics in Applied Physics*, 29, ed. G. Alefeld and J. Voelkl (Springer, 1978).
- [7] A. Koiwai, A. Itoh, and T. Hioki: Japan Patent 2005-21860 (P2005-21860A).
- [8] C. P. Chang, *et al.*: *Int. J. Hydrogen Energy*, 16 (1991) 491.
- [9] M. M. Antonova: *Sboistva Gidriedov Metallov* (Properties of Metal-hydrides) (Naukova Dumka, Kiev, 1975; translated by NissoTsushinsha, Wakayama, 1976) [in Japanese].
- [10] Y. Fukai, K. Tanaka, and H. Uchida: *Hydrogen and Metals* (Uchida Rokakuho, Tokyo, 1998) [in Japanese].
- [11] H. Fujita: *J. High Temperature Society* 24 (1998) 272.
- [12] A. Takahashi, A. Kitamura, Y. Sasaki, Y. Miyoshi, A. Taniike, R. Seto, and Y. Fujita: Anomalous Heat Generation in Charging of Pd Powders with High Density Hydrogen Isotopes, (II) Discussions on Experimental Results and Underlying Physics, this Proceedings
- [13] S. Rossi and H. Morkoc: *J. Vac. Sci. Technol. B* 10 1237 (2000)
- [14] A. Kitamura, T. Nohmi, Y. Sasaki, A. Taniike, A. Takahashi, R. Seto, Y. Fujita: Anomalous effect in charging of Pd powders with high density hydrogen isotopes, *Physics Letters A*, 373 (2009) 3109-3112

Yes, Virginia there is Heat, but It is Likely of Chemical Origin

D. A. Kidwell¹, D. L. Knies², K. S. Grabowski², and D. D. Dominguez¹

¹Chemistry Division, Naval Research Laboratory, Washington, DC 20375

²Materials Science and Technology Division, Naval Research Laboratory, Washington, DC 20375

E-mail: David.Kidwell@nrl.navy.mil

Abstract. Gas loading of palladium particles <2 nm in size produces anomalous amounts of heat in a reproducible manner. This heat is produced in the presence of deuterium but not in the presence of hydrogen. Control experiments have ruled out the excess heat was due to impurities in the deuterium that were absent in the hydrogen. Because the system is simple and mostly reversible, all extra heat must be of chemical or some other origin. Neither radiation nor nuclear “ash” was found to correlate with the anomalous heat. In some matrices, the likely source of the anomalous heat is D-H exchange with the water present in the matrix, where an approximate third increase of the expected energy from calculations can account for most of the excess heat. In other matrices, no simple explanation of the excess heat can be made.

1. Introduction

Palladium electrochemically loaded with sufficient amounts of deuterium has been reported to produce anomalous amounts of heat that may be nuclear in origin.¹ The complete requirements for heat production have not been determined. However, one criterion for having a high likelihood of producing heat appears to be that the D-Pd ratio must be above 0.9.² Electrochemical loading of palladium can reach these high levels, which correspond to 10⁵ to 10⁶ atmospheres³ of deuterium overpressure in bulk palladium – a challenge for simple gas pressurization. Pressure alone appears to be insufficient, because Isaac, *et al.* had pressurized palladium with deuterium in a diamond anvil cell and saw no radiation emitted.⁴ Although a temperature change was observed, it was attributed to instrumental drifts.

Most of these claims of excess heat have been dismissed as experimental error rather than nuclear chemistry because almost any conventional nuclear event, such as D-D fusion, should produce some form of radiation (X-rays, neutron, gamma rays) or transmuted atoms (nuclear “ash”). Given the amount of heat claimed, these should be easily detectable.⁵ No convincing evidence of radiation nor transmutations have been reported⁶ and the calorimetry results are sometimes called into question.⁷

As unidentified sources of anomalous heat appear to be the major signature of this process, we investigated the heat production in a gas loading system - a simpler system than electrochemical loading - with the goals of: (1) reproducible heat production, (2) careful attention to heat measurements and energy losses and inputs, and (3) understanding of substrate matrix preparation and instrumentation.

Gas loading experiments have the advantage that the system can be reversible – the heat generated upon pressurization due to the work of pressurization of the gas and the uptake of hydrogen/deuterium into the palladium matrix and spillover of that hydrogen to the support is subsequently taken-up upon evacuation. Any net energy (endothermic or exothermic) from a pressurization/depressurization cycle must come from an irreversible event such as a chemical reaction. Typical reactions and processes that must be considered are the initial reduction of PdO to Pd metal and water, water absorption by the matrix,⁸ oxidation of the hydrogen/deuterium by adventitious oxygen in the gas or absorbed on surfaces, water in the gas binding to the matrix, the Joule-Thompson effect⁹, a change in the matrix lattice with pressure, or D-H exchange with water in the matrix or surface hydroxyls. Most chemical reactions produce gaseous materials that can be monitored by sampling the gas in the cell, or they consume the pressurization gas and cause a pressure drop and thereby signal their presence. Thus, all the reactions listed above should make themselves known, or their effect (such as a change in lattice structure) should quickly be lost during

pressurization/depressurization cycles. Additionally, except for D-H exchange, pressurization with deuterium should produce similar amounts of heat as pressurization with hydrogen *i.e.* any chemical isotope effect should be small.

The consideration that the D/Pd ratio must be near 0.9 for anomalous heat to appear² puts constraints on the size of the palladium particles for gas loading at reasonable pressures. In 1908, Paal and Gerum reported H/Pd of 0.98 measured volumetrically at atmospheric pressure using palladium black prepared with hydrazine.¹⁰ Since that report, most H/Pd ratios on pressurized palladium particles fall in the range of 0.6-0.8 at room temperature (similar to bulk palladium) – increasing at lower temperatures and decreasing at higher temperatures.³ Recently, two groups have reported that they can reach H/Pd ratios near one by decreasing the particle size on certain supports, but this ratio appears to be highly size dependant.^{18,19} A summary of data calculated from Huang, *et al.*, is shown in Table 1.

Table 1. Estimated particle sizes and H/Pd ratios as calculated from the data in reference 19. Note the sensitive dependence of the loading ratio with particle size and the rapid increase in particle size with percent Pd. The more chemically accessible particles (> 5 nm) show a loading similar to bulk palladium of 0.6.

Preparation	Estimated Particle Size (nm)	Heat of Hydrogen Adsorption (kJ/mole)	Ratio H:Pd @ 0.2 bar
Pd Powder	9	94	0.55
1.86% Pd/SiO ₂ (IW)	~4	92	0.68
1% Pd/SiO ₂ (SG)	1.1	131	0.9
0.5% Pd/SiO ₂ (SG)	1	183	1.05

It is difficult to prepare palladium colloids less than 5 nm in diameter as palladium tends to catalyze its own growth.^{11,12} Possibility, Paul and Gerum had a procedure to prepare sufficiently small palladium particles that they absorbed large amounts of hydrogen.¹³ Rather than prepare palladium colloids with their inherent irreproducibility, we focused on preparing nanoparticles in an oxide matrix where the growth is limited by the pore size and availability of atoms. We focused on zeolites because the pore size is about 1 nm and should allow growth of more uniform particles. Also, zeolites are thermally stable so that the high temperatures potentially reached by the particles during pressurization do not degrade the support and the zeolites should help isolate the particles and prevent their coalescence with pressure/temperature cycling.

This paper describes the preparations of some matrices that show an anomalous amount of irreversible heat produced in gas loading and discusses that this heat could be due to Deuterium-Hydrogen (D-H) exchange. Trace levels of neutrons and tritium above background have been seen in some gas loading experiments by other authors.¹⁴ Long term heat also has been reported by other authors that is difficult to explain using conventional chemistry.^{15,16,17} We have been unable to confirm any of these observations in our gas-loading systems.

2. Experimental

We constructed our own data acquisition interface so that we had control over all the design parameters. Two basic systems were designed (GC oven and Hart calorimeter) with a common data acquisition interface. Each component and some of the design parameters will be discussed elsewhere. The deuterium gas was from various suppliers over the course of this project and of varying cylinder ages (which affect the tritium impurity concentrations). The main suppliers were Cambridge Isotope Laboratories, Inc., Praxair, and Matheson. The source of the gas did not appear to affect the results. In earlier experiments, the deuterium was passed through Supelco gas purifiers to remove water and oxygen and produced comparable results to unpurified gases. For the results reported here, all gases were used directly. Weak X-Rays and intense light emission has been observed from these matrices during pressurization, which will be discussed elsewhere. Briefly, these have been shown to be artifacts of the measurement technique or uncorrelated to heat production and therefore likely of chemical origins.

Preparation of the palladium-loaded matrices.

The majority of the matrices were made using zeolite 13X from Aldrich (cat #283592) and chromatography grade Alumina from Fischer (cat #A-540). Other zeolites were purchased from Zeolyst International. High Alumina

Zeolite (Code name NaKX(2.0)) was a gift from Praxair, Inc. As these other zeolites produced similar data to 13X, they will not be reported here.

Two variations were employed to prepare the palladium loaded matrices – wet impregnation for alumina^{18,19} and ion exchange for zeolites.^{20,21,22} Palladium chloride came from several sources but for large scale preparations, it was synthesized by dissolving Suisse 99.95% Pd in *aqua regia* and evaporating to dryness. The palladium-amine solution was prepared fresh each time by dissolving 1 g PdCl₂ in 16 mL of water + 4 mL of concentrated HCl and warming. To this deep red solution was slowly added 20 mL of concentrated ammonium hydroxide (an excess ammonia is used but the reaction is in an open beaker so some ammonia is lost). A pink precipitate formed that slowly redissolved upon warming to generate the light yellow Pd(NH₃)₄Cl₂. If the ammonia concentration is too low, Pd(NH₃)₂Cl₂ may form instead.²³ The percentage palladium is based on palladium metal where PdCl₂ is assumed to be 60% Pd metal by weight. Typically 100 g of zeolite powder was placed in a 500 mL flask with 200 mL of distilled water and the required amount of palladium solution. The flask was refluxed overnight. The zeolite was filtered and washed three times with warm water. The material was either air dried overnight then dried at 120°C or dried at 120°C directly. Air drying overnight appeared to produce material with the best characteristics especially when the palladium concentration was decreased below 0.25%. Allowing the water to be slowly lost may preserve the zeolite crystalline structure. The palladium loaded alumina was made by wet impregnation. Alumina (100 g) was placed in a 500 mL flask and slurried with water. The palladium solution was added and the excess water removed on a RotoVapor system under aspirator pressure to a semi-dry, flowing powder. This was air dried overnight and then dried at 120°C for varying lengths of time. Upon oven-drying, the zeolites lost approximately 15% of their weight and the alumina about 11%.

When samples were dried at 450°C they initially were pink and quickly became yellow when cooled in air or in a desiccator. The palladium in these samples reduced to the nanoparticles faster than the matrix dried at 120°C, but drying the matrix at higher temperatures (450°C) appeared to be detrimental for excess heat production.

Higher loading appears to decrease the percentage of heat produced (see Figure 1), likely by growing larger particles. This particle size effect sets apart our approach from that of Kitamura, *et al.*, where he employed high loading 6-30% and high heat that produces multi-nanometer palladium particles.^{16,24} We have tested material produced using Kitamura's recipe¹⁶ with our protocols. Although the heat generated is large because the percentage of palladium is large, we see neither excess heat nor long-term heat. Why our results should differ from that of Kitamura is unknown but similar results to ours have been presented by Hioki and colleagues.²⁵ However if the hypothesis is correct that <2 nm particles are necessary for anomalous heat generation, their production can be difficult and may depend on the exact sample preparation conditions or impurities in a given preparation.

Pressurization and Depressurization Cycles.

A picture of the manifold and peripheral equipment used with the Hart calorimeter is shown in Figure 2. The automated valves are controlled by a custom LabView program that is managed by macros. A summary of the macros for the pressurization and depressurization of the sample cell are given in Table 2.

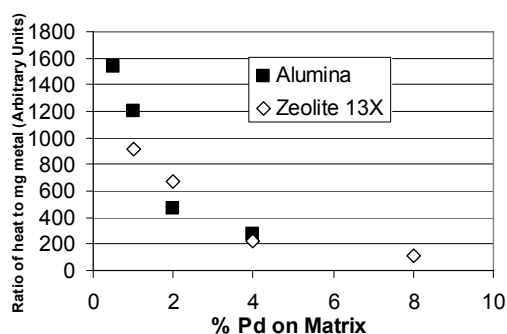


Fig. 1 – Effect of palladium loading of the matrix on excess heat produced. These samples were tested in the GC oven system, which produces relative heats only. The second pressurization cycle with deuterium was used in the calculations. Because these samples were run at different times, direct comparison between matrices is not possible. The percentage Pd on zeolite may vary from the nominal value depicted due to losses during washing.

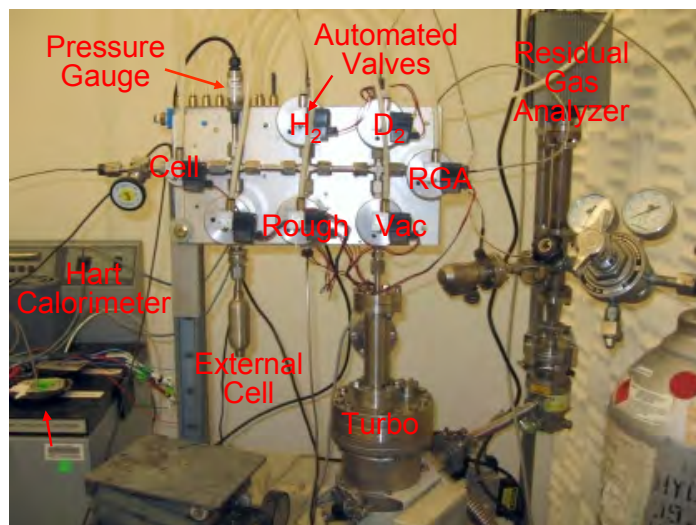


Fig. 2 – Photograph of the manifold and peripheral equipment.

Table 2- Pseudo-macros used to control the automated valves. The timing is in ticks x10, which are acquisition cycles somewhat over a second in length and related to time. The macros in this table were simplified for illustration purposes. The depressurization cycle was done in steps to more accurately measure the D-H exchange. This measurement will be discussed in a subsequent paper.

Pressurization Macro	
Ticks x10	Action
0-120	Close all valves
140	Open RGA
160	Open D2 into manifold
180	Open Cell and fill
1080	Close Cell
1100	Close RGA
1120	Close D2

Depressurization Macro	
0-120	Close all valves
140	Open RGA
160	Open Cell
960	Close Cell
1000	Rough-out the manifold
3000	Close Rough
3020	Open Cell
3100	Close Cell
7000	Rough-out the manifold
9000	Close Rough
9020	Open Cell
9100	Close Cell
13000	Rough-out the manifold
15000	Close Rough
15020	Open Cell

3. Results and Discussion

Figure 3 shows a reversible gas-loading system - five pressurization/depressurization cycles with helium on a Pd-alumina matrix. Integration of all five cycles gives a total heat of $0 \pm 1\text{J}$. The average measured heat of pressurization from the five cycles is $-13.4\text{J} \pm 0.1\text{J}$, whereas the calculated heat of pressurization from PV work is -13.4J .²⁶ This example shows that our approach can have good accuracy and precision. In some matrices, we can directly observe the heat of pressurization because the chemical reduction and subsequent uptake of deuterium is delayed. The delayed chemical reduction is also seen in the pressure recordings, where a pressure drop is observed when the reduction occurs. Like helium, if matrices are initially pressurized with hydrogen, the hydrogen also shows reversible chemistry, where $\text{heat}_{\text{in}} = \text{heat}_{\text{out}}$.²⁷

In contrast to the reversible heat from pressurization with helium (Figure 3) or hydrogen (Figure 4a), is pressurization by deuterium as shown in Figure 4b. With deuterium, the heat released during pressurization (-76.6J) is not equal to that absorbed during evacuation (26.4J) for a difference of -50.2J .²⁸

In one test series, the matrix was cycled many times and the integrated heat ($\text{heat}_{\text{in}} + \text{heat}_{\text{out}}$ and thus excess heat) is shown in Figure 5. The heat from the first pressurization was large due to chemistry occurring. The abrupt decrease in heat after 11 cycles has an unknown cause but it may be due to depletion of a chemical reactant or growth of the palladium nanoparticles above a certain size where anomalous heat is no longer generated.

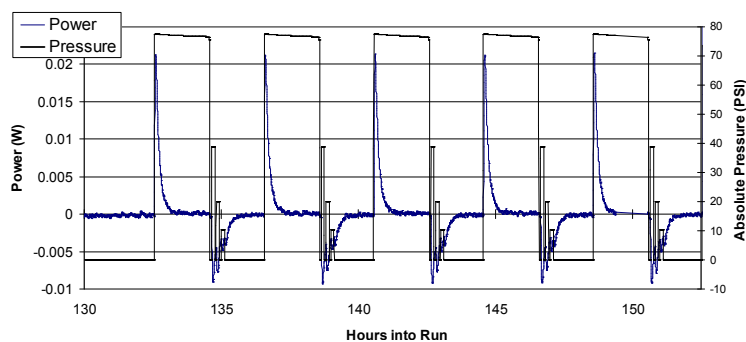


Fig. 3 – Pressurization/Depressurization Cycles Showing Reversible Heat. Pressurization of Pd on alumina with helium: $\text{heat}_{\text{in}} = \text{heat}_{\text{out}}$. The pressurization and depressurization cycles are given in Table 2. The automatic, membrane valves leak deuterium slightly if the pressure is reversed from the normal flow path. To minimize this leakage in the sample cell, the sample cell valve is closed after pressurization and the manifold pressurized. The slight decrease in pressure in the manifold, which is read by the pressure transducer, is due to a leak from the manifold into the turbo system, not due to consumption of the helium in a chemical reaction.

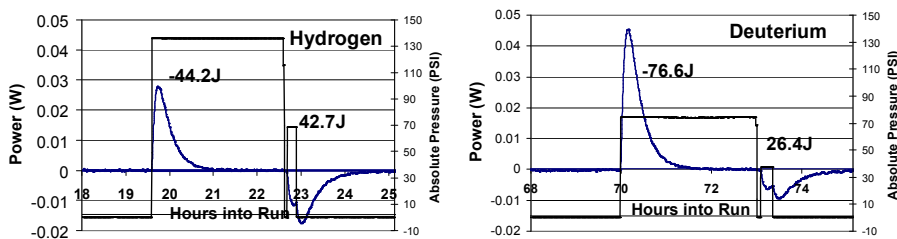


Fig. 4 – Comparison of Hydrogen and Deuterium pressurization cycles. The matrix was 0.5% Pd on zeolite 13X. The hydrogen was pressurized first to avoid possible reverse D-H exchange. Deuterium pressurization shows irreversible heat whereas hydrogen pressurization integrates to near zero (-2.5J). The pressure for hydrogen was larger, but this extra PV work is recovered in the depressurization cycle. In this case, the depressurization cycles were done in two steps rather than four as in Figure 3.

Figure 6 shows a pressurization/depressurization series ($\text{heat}_{\text{in}} + \text{heat}_{\text{out}}$) using zeolite 13X with 1% palladium loading. In this case, the pressurization and depressurization cycles were rapid, which was detrimental to production

of excess heat (see below). The heat decayed with time in a fairly linear manner. More importantly, pressurization with hydrogen produced an endothermic reaction rather than zero (recall that all reversible heat from PV work and hydrogen uptake by the matrix is accounted). This indicates that chemistry must be occurring and, in the case of pressurization with hydrogen, H-D exchange

Consider the reactions in Scheme 1. Palladium-loaded zeolites are known to catalyze D-H exchange.^{29,30} If D-H exchange was occurring in our system, then the chemistry would be exothermic until all the protons in the H₂O and zeolite hydroxyl groups were exchanged. Then, this irreversible energy (due to chemistry) would stop. Pressurization with hydrogen would reverse the exchange making normal water and be endothermic (reverse reactions in Scheme 1). Upon restarting deuterium pressurizations, heat should be produced as the H₂O present would be reconverted to D₂O. Partial restoration of heat appears to occur, as illustrated in Figure 6.

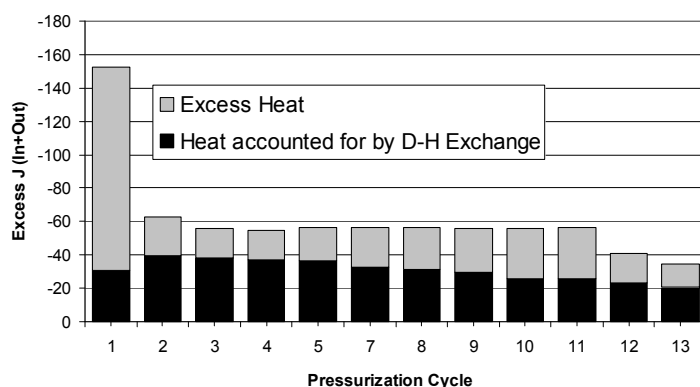
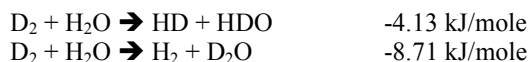


Fig. 5 – Integrated heat for each cycle for 15.42 g of 1% Pd on alumina. The alumina was dried at 120C for 3 hr before use. Note that the calculated heat from D-H exchange (dark bars) is not a constant fraction of the total heat. From step 9 and on, the evacuation time was increased to 10 hr from 6 hr.

D-H exchange should produce a signature in the gas phase because the excess gas overpressure (cells were typically filled to ~5 bar) would be enriched in HD or H₂. This enrichment should be observable using the in-line RGA (see Figure 2). When we first took gas samples, very little D-H was observed. Given the amount of deuterium present and the percentage of HD formed, we concluded that at most 7 J of excess heat could come from D-H exchange. However, later we sampled the gas in pulses (see Table 2 and Figure 5) that allowed sampling at various pressures.³¹ The lower pressure samples were enriched in HD and H₂ and these percentages were used in calculating the excess heat shown in Figures 5 and 6. With these updated numbers, D-H exchange can account for 60-62% (average for initial FDeuterium 7-16 60.7% ±0.56%, n=10) of the heat as calculated from the heats of formation in the pressurization series shown in Figure 6. Other sources (or sinks) of heat can come from the hydrogen bonding of the water and hydroxyls in the zeolite. One complication is that normal water forms stronger hydrogen bonds than does D₂O.^{32,33} Converting normal water to D₂O should absorb heat and make the discrepancy even larger. Thus, the source of this discrepancy is unknown.

Scheme 1. Possible D-H exchange reactions and the calculated enthalpy. Exchange of the hydroxyls on surfaces should have similar thermochemistry.



Although the calculations of the energy from D-H exchange using the values in Scheme 1 do not quantitatively agree with the measurements, D-H exchange is the dominant mechanism to explain Figure 6 because: (1) the percentages of excess are constant, (2) the hydrogen is negative – also by a constant amount, although slightly different (64.3% ±0.87%, n=15) than that of the deuterium, (3) after the hydrogen pressurization/depressurization cycles, the deuterium returns to similar heat and similar percentage of D-H exchange (after = 60.9% ±0.33% n=4) as was observed initially, and (4) the total heat from D-H exchange of the first 22 pressurization cycles is consistent with the amount of water possible in the zeolite (total = -288 J, 0.6 g water, 4.4% water).

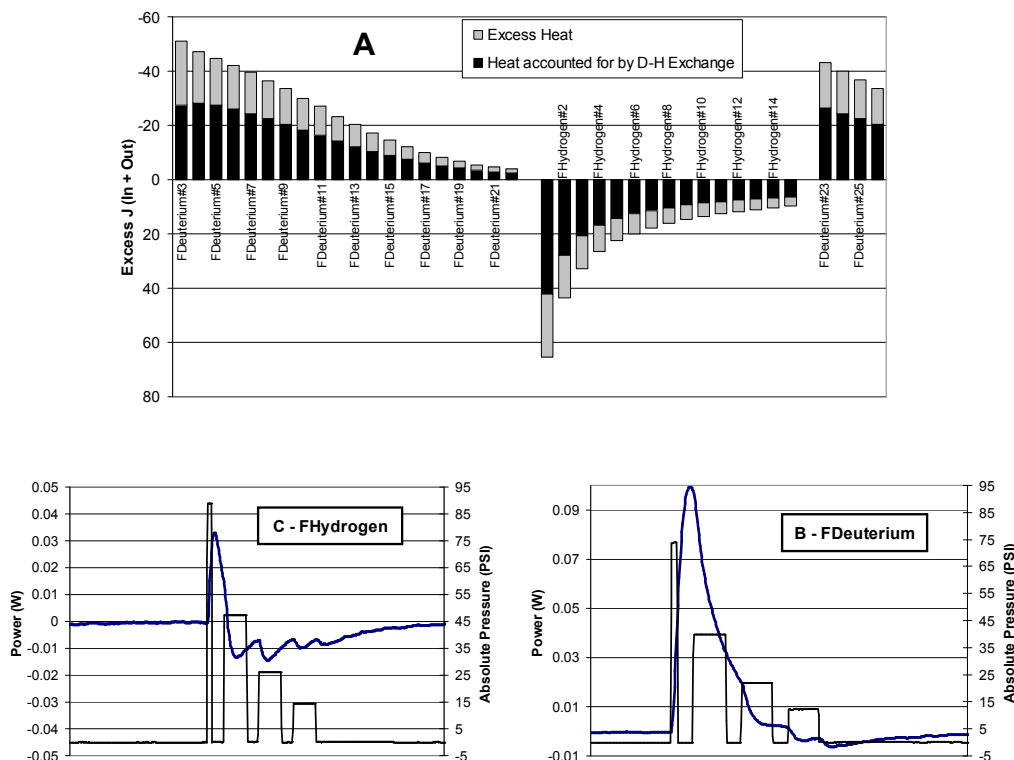


Fig. 6 - (A) Integrated heat for each pressurization/depressurization cycle for 13.5 g of 0.5% Pd on zeolite 13X. This series was started after two normal cycles. The letter F indicates a fast pressurization cycle, which are rapid in-out pulses (which was later hypothesized to be detrimental) where the depressurization period overlaps the pressurization period. Any net positive or negative peak measured is irreversible energy. The depressurization is done in steps (see B & C light lines) to better sample the excess gas with the RGA for calculating the amount of D-H exchange. For an inert gas, the net heat is almost zero. Figure 6 B and C show the cycles for deuterium (cycle FDeuterium #7) and hydrogen (cycle FHydrogen #2). The deuterium cycle is mostly above the baseline – exothermic – whereas, the hydrogen cycle is mostly below the baseline – endothermic. The D-H exchange appears to have a rapid time constant otherwise the heat of pressurization pulse in C should be more evident.

The structure of palladium inside zeolites is complex and depends on preparation conditions.³⁴

We have tried to dry the matrix before the pressurization. However, Type X zeolites contain up to 30% water and can retain considerable water (and OH groups on the surface), except under severe conditions.^{8,35} Also, water and ammonia (left-over from the preparation) may be important to observe anomalous heat generation (they would certainly be important for D-H exchange), as these species can coordinate to the nanoparticles and modify their electronic structure. Heating the zeolites in air to 450°C for 8 hr and adding D₂O reduced the excess heat but did not eliminate it. However, the exchange may have been incomplete and normal water still could have been present.

What is interesting is that the explanation for D-H exchange does not account for the excess heat observed in FDeuterium#3 and FDeuterium#4 (Figure 6). Statistically, FDeuterium#4 at 59.8% of the heat accounted for by D-H exchange is two standard deviations from the mean expected of 60.7%, whereas FDeuterium#3 at 53.8% is 12 standard deviations from the mean. The initial chemical reactions of reduction of the PdO to Pd nanoparticles may take several cycles. Therefore, the excess heat observed in FDeuterium#3 and FDeuterium#4 MAY be due to an incomplete reduction of the PdO rather than unusual chemistry.

Referring to Figure 5, the D-H exchange heat decreases as was observed in Figure 6. This decrease would be expected as the H₂O gets converted to D₂O. However, the excess heat stays the same out to pressurization cycle 11. Thus, in this pressurization series, the D-H exchange is NOT a constant percentage of the total heat, and is not as easily explained as the pressurization series shown in Figure 6. One possibility is that the surface is changing as it becomes more deuterated, and the amount of heat released as H₂O goes to D₂O somehow increases with surface coverage. The major difference between Figures 5 and 6 is in the timing of the pressurization pulses. After many

tests, it appears necessary to restore the particles to their original form without deuterium. This takes considerable time at room temperature given the poor vacuum pumping speed to the cell (Figure 2). Even the 6 hr evacuations used in Figure 5 did not remove all the deuterium from the sample.³⁶ Faster pressurization cycles (2 hr intervals) as used in the sample depicted in Figure 6 would not be sufficient to remove much of the deuterium. Thus, any excess heat due to other causes would no longer be apparent and the D-H exchange reaction would dominate, as in Figure 6.

There may be two reasons for why low deuterium levels in the nanoparticles are necessary to observe anomalous heat: (1) upon absorbing deuterium, small particles heat (but this heat is reversible). One can estimate the expected temperature rise. For example, assume that the enthalpy of formation of nanoparticles of PdD is approximately 100 kJ/mole.³⁷ If all this energy were deposited in one second³⁸ and not transferred quickly to the matrix (as the matrix is an oxide insulator), each particle could heat to 3849°C³⁹ – substantially above the melting point of palladium (1554°C). This high temperature would help catalyze conventional chemical reactions, such as D-H exchange, or it may catalyze an anomalous heat production. and (2) some authors have suggested that anomalous heat production is flux driven.² This could require a particle without much deuterium/hydrogen present each time to reach sufficient flux into the particle during pressurization.

These two hypotheses also suggest why small particles are necessary for this effect to be observed. Larger particles would not load to as high of deuterium levels AND would not load as quickly and thereby not reach as high of temperatures.

4. Conclusions

Low concentrations of palladium in oxide matrices appear to produce sub-nanometer palladium particles which allow high and rapid deuterium gas loading at easily reachable pressures. Gas loading produces anomalous amounts of heat in a reproducible manner in the presence of deuterium but not in the presence of hydrogen. This anomalous heat appears to be sensitive to the size of the palladium particles and rate of loading. The excess heat is reduced during repeated pressurization-depressurization cycles, pointing towards a source of chemical energy that is diminished. Alternatively, the particles may grow with repeated cycling beyond a range that is easily loaded with the parameters employed. In some matrices and pressurization conditions, the likely source of the anomalous heat is D-H exchange with the water present in the matrix. In other cases, this explanation is incomplete and other sources of heat must be considered.

Acknowledgements

Funding from the Defense Threat Reduction Agency is gratefully acknowledged. We would like to thank Graham Hubler, Albert Epshteyn, and Andrew Purdy for helpful discussions and suggestions.

References and Notes

- [1] Martin Fleischmann and Stanley Pons, "Electrochemically Induced Nuclear Fusion of Deuterium", *Journal of Electroanalytical Chemistry*, **261** (1989) 301–308.
- [2] G.K. Hubler, "Anomalous Effects in Hydrogen-Charged Palladium - A Review", *Surface and Coatings Technology*, **201** (2007) 8568–8573.
- [3] P.L. Levine and K.E. Weale, "The Palladium + Hydrogen Equilibrium at High Pressures and Temperatures", *Transactions of the Faraday Society*, **56** (1960) 357-362.
- [4] Isaac F. Silvera and F. Moshary, "Deuterated Palladium at Temperatures from 4.3 to 400 K and Pressures to 105 Kbar: Search for Cold Fusion", *Physical Review B*, **42** (1990) 9143-9146.
- [5] Although they never reached the critical D/Pd loading of 0.9, an early attempt at replication was: N. S. Lewis, C. A. Barnes, M. J. Heben, A. Kumar, S. R. Lunt, G. E. McManis, G. M. Miskelly, R. M. Penner, M. J. Sailor, P. G. Santangelo, G. A. Shreve, B. J. Tufts, M. G. Youngquist, R. W. Kavanagh, S. E. Kellogg, R. B. Vogelaar, T. R. Wang, R. Kondrat, and R. New, "Searches for low-temperature nuclear fusion of deuterium in palladium", *Nature*, **340** (1989) 525-530.
- [6] Although we find the data problematic for various reasons, examples of reported transmutations and nuclear "ash" are: Yasuhiro Iwamura, Mitsuru Sakano, and Takehiko Itoh, "Elemental Analysis of Pd Complexes: Effects of

- D2 Gas Permeation", *Japanese Journal of Applied Physics*, **41** (2002) 4642–4650. W. B. Clarke, "Search for 3He and 4He in Arata-Style Palladium Cathodes I: A Negative Result," *Fusion Sci. Technology*, **40** (2001) 147-151. Brian Clarke, Brian M. Oliver, Michael C. H. Mckubre, Francis L. Tanzella, and Paolo Tripodi, "Search for 3He and 4He Nuclear Reactions in Arata-Style Palladium Cathodes II: Evidence for Tritium Production", *Fusion Sci. Technology*, **40** (2001) 152-167.
- [7] Gordon M. Miskelly, Michael J. Heben, Amit Kumar, Reginald M. Penner, Michael J. Sailor, and Nathan S. Lewis, "Analysis of the Published Calorimetric Evidence for Electrochemical Fusion of Deuterium in Palladium", *Science*, **246** (1989) 793-796.
- [8] Y. Erten, A. Günes-Yerkesikli, A. E. Çetin and F. Çakicioğlu-Özkan, "CO2 Adsorption and Dehydration Behavior of LiNaX, KNaX, CaNaX and CeNaX Zeolites", *Journal of Thermal Analysis and Calorimetry*, **94** (2008) 715–718.
- [9] The calculated Joule-Thompson effect for Hydrogen and Deuterium is essentially the same and small (< 1J) for the volumes and pressures used. It is ignored in the data analysis. For values, see: Herrick L. Johnston, Irving I. Bezman, and Charles B. Hood, "Joule-Thomson Effects in Hydrogen at Liquid Air and at Room Temperatures", *J. Am. Chem. Soc.*, **68** (1946) 2367-2373. Herrick L. Johnston, Carroll A. Swanson, and Henry E. Wirth, "Joule-Thomson Effects in Deuterium at Liquid Air and at Room Temperatures", *J. Am. Chem. Soc.*, **68** (1946) 2373-2377.
- [10] C. Paal and Josef Gerum "Über Palladiumwasserstoff", *Berichte*, **41** (1908) 818.
- [11] Ting-Hao Phan and Raymond E. Schaak, "Polyol synthesis of Palladium Hydride: Bulk Powders vs. Nanocrystals", *Chem. Commun.*, (2009) 3026–3028.
- [12] Kirti Patel, Sudhir Kapoor, Devilal Purshottam Dave, and Tulsi Mukherjee, "Synthesis of Pt, Pd, Pt/Ag and Pd/Ag nanoparticles by microwave-polyol method", *J. Chem. Sci. (Indian)*, **117** (2005) 311–316.
- [13] Given how early this work was, it is possible that their reagents had impurities that limited colloid growth. What these impurities could be would be difficult to determine.
- [14] M.S. Krishnan, S.K. Malhotra, D.G. Gaonkar, V.D. Nagvenkar, and H.K. Sadhukhan, "Evidence for Production of Tritium via Cold Fusion Reactions in Deuterium Gas Loaded Palladium", BARC Studies In Cold Fusion, BARC Report 1500, Dec. 1989, p. B4. Available at: <http://www.lenr-canr.org/Collections/BARC.htm>
- [15] Yoshiaki Arata and Yue-Chang Zhang, "Observation of Anomalous Heat Release and Helium-4 Production from Highly Deuterated Palladium Fine Particles", *Japanese Journal of Applied Physics Part 2-Letters*, **38** (1999) L774-L776
- [16] A. Kitamura, T. Nohmi, Y. Sasaki, A. Taniike, A. Tahahaski, R. Seto, and Y. Fujita, "Anomalous effects in charging of Pd powders with high density hydrogen isotopes", *Phys. Lett. A*, **373** (2009) 3109-3112.
- [17] V.A. Kirkinskii, V.A. Drebuschak, and A.I. Khmel'nikov, "Excess Heat Release During Deuterium Sorption-Desorption by Finely Powdered Palladium Deuteride", *Europhysics Letters*, **58** (2002) 462-467.
- [18] Shu-Chin Chou, Shu-Hui Lin, and Chuin-Tih Yeh, "Isosteric Heat of Sorption of Dihydrogen on Alumina-supported Palladium", *J. Chem. Soc. Faraday Trans.*, **91**(1995) 949-951.
- [19] Sheng-Yang Huang, Chin-Da Huang, Boh-Tze Chang, and Chuin-Tih Yeh, "Chemical Activity of Palladium Clusters: Sorption of Hydrogen", *J. Phys. Chem. B*, **110** (2006) 21783-21787.
- [20] K.P. Prasanth, Renjith S. Pillai, Sunil A. Peter, H.C. Bajaj, R.V. Jasra, H.D. Chung, T.H. Kim, and S.D. Song, "Hydrogen uptake in palladium and ruthenium exchanged zeolite X", *Journal of Alloys and Compounds*, **466** (2008) 439–446.
- [21] Kh. M. Minachev, A. N. Detyuk, R. V. Dmitriev, and P. I. Slyunyaev, "Deuterium Exchange with the Surface of Zeolite Catalysts 5. Palladium-Containing Zeolites", Academy of Sciences of the USSR, Moscow. Translated from *Izvestiya Akademii Nauk SSSR, Seriya Khimicheskaya*, No. 12, pp. 2678-2682, December, 1978.
- [22] J. Michalik, M. Narayana, and Larry Kevan, "Studies of the Interaction of Pd³⁺ and Pd⁺ with Organic Adsorbates, Water, and Molecular Oxygen in Pd-Ca-X Zeolite by Electron Spin Resonance and Electron Spin-Echo Modulation Spectroscopy", *J. Phys. Chem.*, **89** (1985) 4553-4560.
- [23] George Irving Kemmerer, Thesis - Presented to the Faculty of the Department of Philosophy of the University of Pennsylvania in Partial Fulfillment of the Requirements for the Degree of Doctor of Philosophy, 1908.
- [24] Shin-ichi Yamaura, Ken-ichiro Sasamori, Hisamichi Kimura, and Akihisa Inoue, "Hydrogen absorption of nanoscale Pd particles embedded in ZrO₂ matrix prepared from Zr–Pd amorphous alloys", *J. Mater. Res.*, **17** (2002) 1329-1334.
- [25] T. Hioki, H. Azuma, T. Nishi, A. Itoh, J. Gao, S. Hibi, T. Motohiro, and J. Kasagi, "Hydrogen/Deuterium Absorption Property of Pd Fine Particles Systems and Heat Evolution Associated with Loading of

Hydrogen/Deuterium”, 15th International Conference on Condensed Matter Nuclear Science, Rome, Italy October 5-9, 2009

[26] The heat from PV work for expanding He, D₂, or H₂ into a vacuum container of 30 mL can be estimated from the equation Heat = 0.2058(pressure) + 0.1558. The heat is proportional to the size of the container inside the calorimeter (25 mL in this case).

[27] Interestingly, the Zeolite matrices absorb large amounts of Argon and Nitrogen (but not likely to be enough to be useful commercially) at room temperature so that these gases cannot be used to measure chamber volumes.

[28] Heat is reported using the chemical convention where exothermic reactions are negative and endothermic reactions are positive.

[29] Jana Novakova, Ludmila Kubelkova, and Pavel Jiru, "Isotopic Exchange of Deuterium in Zeolites", *J. Chem. Soc. Faraday Trans. 1*, **77** (1981) 1331-1339.

[30] C. Kemball and R. McCosh, "Hydrogen-Deuterium Exchange Reactions on Ion-Exchanged X-Type Zeolites", *Proceedings of the Royal Society of London. Series A, Mathematical and Physical Sciences*, **321** (1971) 249-257.

[31] Apparently the produced HD and H₂ was bound to the surface and exchanged only slowly with the gas phase. Lower pressures sampled the surface and gave a truer picture of the amount of D-H exchange.

[32] Melvin C. Alvin, Jan Hermans Jr., and Harold A. Scheraga, "Effect of Deuterium on the Strength of Hydrogen Bonds", *J. Am. Chem. Soc.*, **81** (1959) 5048-5050.

[33] Surjit Singh and C.N.R. Rao "Deuterium Isotope Effects On Hydrogen Bonding", *Canadian Journal of Chemistry*, **44** (1966) 2611-2614.

[34] E. Garbowski, M. Primet, and M. V. Mathieu, "UV Spectroscopic Study of Oxidized and Reduced Palladium Loaded Zeolites", *Reaction Kinetics and Catalysis Letters*, **8** (1978) 515-520.

[35] K. M. Miedzinska and B. R. Hollebone, "A study of chromium-exchanged zeolites as potential catalysts for thermolysis of water", *Can. J. Chem.*, **64** (1986) 1382-1388.

[36] The pressure is typically in the 10⁻⁵ to 10⁻⁶ torr range after 6-10 hr of evacuation. However, Deuterium evolution is still evident as measured by the RGA, and the time it takes to remove the Deuterium depends on the matrix. Alumina appears to be faster than Zeolites. We considered reacting the trace Deuterium with oxygen to remove it faster, but this could introduce additional chemistry that may confuse the pressurization cycles.

[37] Pen Chou and M. Albert Vannice, "Calorimetric Heat of Adsorption Measurements on Palladium I. Influence of Crystallite Size and Support on Hydrogen Adsorption", *Journal of Catalysis*, **104** (1987) 1-16.

[38] Unlike some other authors, we pressurize quickly. Modeling suggests that the heat pulse evolved has three components. Based on the appearance of the heat curves from hydrogen pressurization of deuterated matrices, we suggest that the fastest component is the PV work, the next component is D-H exchange and that the slowest component is deuterium absorption by the nanoparticle and spillover onto the surface.

[39] (100 kJ/mole)/(Specific heat capacity of 25.98 J·mol⁻¹·K⁻¹) provides a ΔT of 3849K. This assumes that the heat capacity is constant and heat transfer to the matrix is at a rate much less than the heat production. Both are unlikely situations so this calculation provides an upper limit.

Low Temperature Gas Loading of Deuterium in Palladium

F. Scaramuzzi

LNF/INFN, Frascati, Italy

E-mail: frascara@lnf.infn.it

Abstract. One of the most established features of the phenomenon known with the name of “Cold Fusion”, with reference to the system palladium (Pd) – deuterium (D), is that a condition necessary (even though not sufficient) to be satisfied in order for these phenomena to take place is that the content of D in Pd, called also the D/Pd ratio X , approaches the value of 1 (understanding by this quantity the atomic ratio between the two species in the Pd lattice). In order to reach such a high value of X , extensive use of electrolysis of heavy water with a Pd cathode has been made.

The present experiment is aimed at obtaining high loading ratios of deuterium in palladium without using electrolysis. The idea is to have deuterium gas in contact with palladium. The use of low temperatures has the purpose of increasing the equilibrium loading ratio for a given gas pressure.

A first test experiment, performed at ENEA Frascati in 2002, showed that it was possible to have D/Pd ratios as high as 1 at 150 K with a pressure lower than 1 bar [1]. The experiment has been rebuilt at LNF/INFN and the first results are reported here.

An anomaly in the loading dynamics will be also reported.

1. Introduction

The idea is to realize a conceptually simple experiment, reproducible, and with straightforward answers:

- To start with, measuring the D/Pd ratio, aiming to high values.
- Possibly detecting excess heat.
- Analyzing the gas, looking for ^4He .
- Studying the loading dynamics.

We refer to Ref. [1] for the description of the apparatus and the report of the first results. Here we will limit ourselves to describe the calorimetric technique and to report preliminary results on the loading dynamics.

2. The calorimeter

In Fig. 1 is reported the general scheme of the apparatus. The cell containing the sample is surrounded by a shield: both are made out of copper, and can be considered isothermal. With the help of a Cryodyne closed-cycle refrigerator [2], both can be kept at a constant temperature, from a minimum of 20 K to almost room temperature. The thermoregulator [3] assures a temperature constant within ± 1 mK.

The cell is held at a temperature higher than the shield: thus, heat power has to be dissipated in the cell heater in order to keep the assigned temperature. This power is measured and recorded with the help of a LabVIEW data acquisition system. Should an independent heat source become active within the cell, the thermoregulator has to reduce the amount of energy fed to the cell heater. This decrease, with the opposite sign, gives the value of the heat produced by the independent source.

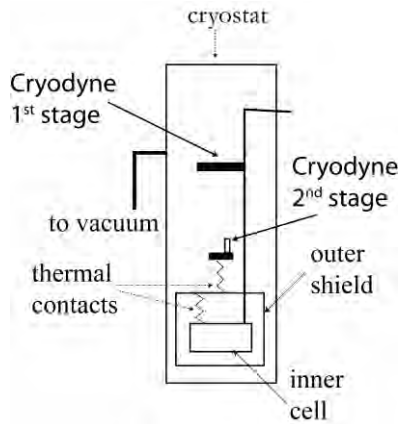


Fig.1 - Schematic view of the apparatus.

In order to validate this method, tests have been performed by mounting within the cell a dummy heater (an evanohm wire in which to create Joule heating), and the power sent into the dummy heater is compared with that detected by the calorimeter. A typical example is shown in Fig. 2. Note the oscillation of the signal of W_c (the power sent by the thermoregulator into the cell heater), both when the heat starts and when it stops. However, when the oscillation is quenched, the agreement between the calculated power (W_{calc}) and the experimental one (W_{exp}) is quite satisfactory, on the order of 1 %.

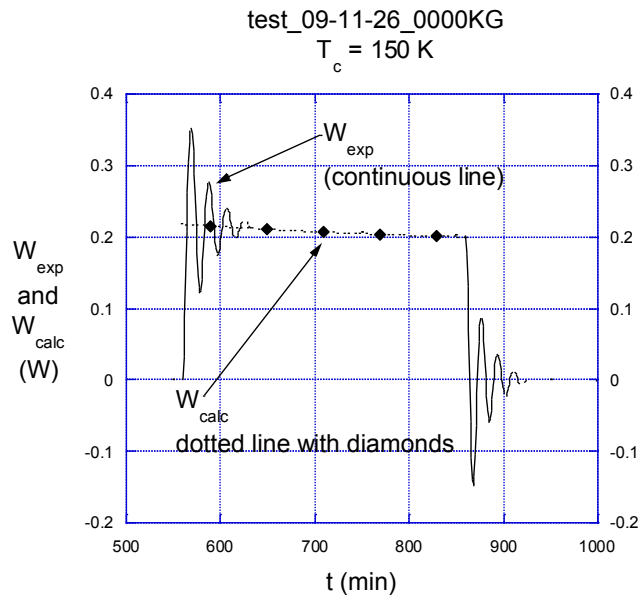


Fig. 2 - Validation of the calorimeter.

It is also possible to measure the total heat produced by the independent heater, by integrating the W_c graph versus time.

3. Preliminary tests of loading dynamics

The geometry of the first samples used for this experiment – the same used in [1] - is shown schematically in Fig. 3a.

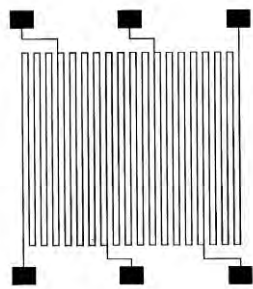


Fig. 3a - The sample used for loading dynamics tests.

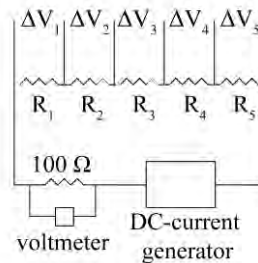


Fig. 3b - The circuit used to measure the resistances R_i .

The real sample is constituted by a Pd film, of thickness 0.5 to 3.5 μm , 80 μm large, and 2.5 m long, deposited on a glass support, 1 mm-thick, 25 x 35 mm^2 area. Its resistance can vary, as a function of thickness, temperature and loading ratio, from a few hundreds to many thousands ohms.

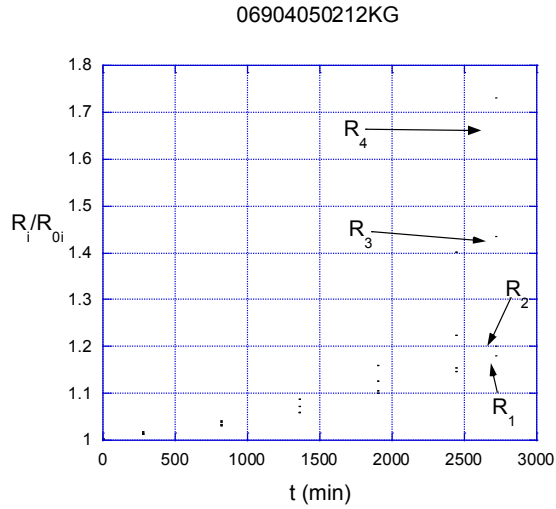
The geometry is such that the total resistance is divided in 5 sections, all in series. In Fig. 3b is reported the scheme of the circuit used to measure the five resistances R_i . The voltmeter in the figure permits measuring the current circulating in the sample, and thus the measurement of the ΔV_i 's, made by the LabVIEW system, gives the resistances. They are measured and recorded as a function of time, at the rate of one value every minute.

Bearing in mind also the suggestion by Giuliano Preparata, the “Preparata Effect” [4], which envisages the possibility that the loading ratio can be influenced by the value of the electric potential on a Pd cathode (in an electrolysis experiment), we have looked at the behavior of the 5 resistances described above during the loading of Deuterium gas. In our case the “electric potential” was that used to measure the resistances. The results are at present quite poor, because of the difficulty of having good Pd samples (“bad” ones tend to detach themselves from the glass support when absorption starts), but nevertheless they are quite suggestive. We will report them here.

The first run we consider is that performed in 2002 [1], at the temperature of 150 K. In order to keep track of the changes of loading ratio, the value of the resistance is considered: it is well known that the resistance grows linearly with increasing X [5]. At room temperature, when $X \approx 0.75$, the resistance is doubled (it increases by a factor 2.6 in the same interval at 150 K).

In Fig. 4 the behavior of the ratio between the value of the resistance while absorbing deuterium (R) and the value of the unloaded sample (R_0) is shown as a function of time for the various sections of the sample during the first phase of the absorption process. Note that R_5 was broken after about one day, and then short-circuited, so that this measurement is reported only for the remaining four sections of the sample.

Table 1. The loading ratio (X) reached by the four sections of the sample.



	R/R ₀	X
R ₁	1.18	0.13
R ₂	1.20	0.14
R ₃	1.42	0.29
R ₄	1.75	0.52

Fig. 4 - R_i/R_{0i} vs t (2002, 150 K)

The behavior of the four resistances almost two days after starting loading is quite dramatic. In Table 1 the final values of the R_i/R_{0i} are listed, together with the corresponding values of X = D/Pd. In this run R₄ was the most negative and R₁ the most positive among the four sections. The absolute value of the voltage used was 0.2 V.

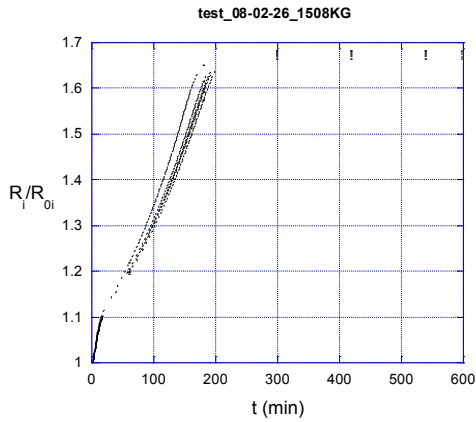


Fig.5a

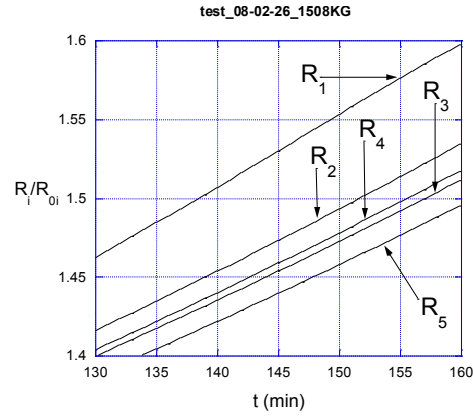


Fig. 5b

The different behavior among the sections becomes much smaller when approaching the maximum value of the loading. This is shown in a Fig. 5a, where another run, this time at room temperature, is considered. In

Fig 5b the same results are reported, by emphasizing the effect at the beginning of the loading. Here R_1 the most negative, R_5 is the most positive. The absolute value of the voltage used was 8 V.

Thus, it seems that a negative potential favors the absorption, at least at the beginning of the loading process.

The data are scarce, even though suggestive. More tests are needed and will hopefully be performed. The main problem is having good quality samples, in the sense that they do not detach from the support when they absorb deuterium. A collaboration is under way with this purpose with David Knies of the NRL of Washington DC, USA.

Acknowledgements

Since 2006 this experiment was hosted at the LNF of INFN: thanks are due to the Direction of the Laboratory and to Commission 5 of INFN for its support.

The Author is deeply grateful to his colleague and friend Ivo Modena for continuous scientific support in conducting the experiment.

He thanks warmly Arturo Moleti, Alessio Rocchi and Filippo Sanjust, who took care of the LabVIEW data acquisition system.

Thanks are due to Antonio Frattolillo and Antonella De Ninno of ENEA, and to Alberto Clozza and Angelo Viticchié of INFN, for permitting the use of valuable scientific instruments.

The experiment reported here would not have been possible without the skillful help of Franco Campolungo, Mauro Iannarelli, Livio Bettinali and Lorenzo Martinis: also to them goes the Author's gratitude.

4. References

- [1] F. Scaramuzzi, *Journal of Alloys and Compounds*, 385, 19 (2004).
- [2] CTI-Cryogenics, model 1020c, Cryodyne cryocooler.
- [3] Lake Shore Cryotronics, model 340 Temperature Controller
- [4] M. Cola, E. Del Giudice, A. De Ninno, G. Preparata, *Proceedings of the 8th International Conference on Cold Fusion, Atti di Conferenze SIF n. 70*, 349 (2001).
- [5] T.B. Flanagan, *J. Phys. Chem.*, 65, 280 (1961); G. Bombakidis, R.J. Smith, D.A. Otterson, *Phys. Rev.*, 177, 1044 (1969).

Proposal of an Experiment Aimed at Charging Deuterium in Palladium at the Temperature of Liquid Nitrogen

F. Scaramuzzi
LNF/INFN, Frascati Italy

E-mail: frascara@lnf.infn.it

Abstract. One of the most established features of the phenomenon known with the name of “Cold Fusion”, with reference to the system palladium (Pd) – deuterium (D), is that a condition necessary (even though not sufficient) to be satisfied in order for these phenomena to take place is that the content of D in Pd, called also the D/Pd ratio X, approaches the value of 1 (understanding by this quantity the atomic ratio between the two species in the Pd lattice).

In order to reach such a high value of X, extensive use of electrolysis of heavy water with a Pd cathode has been made. An alternative line that has been followed by the Author [1] consists of trying to obtain high values of X by the direct interaction of Pd with D₂ gas. The use of low temperatures has the purpose of increasing the equilibrium loading ratio for a given gas pressure.

The proposal of an experiment which requires little attention is presented here.

1. Introduction

When facing the task of loading deuterium (or hydrogen) in palladium, with the aim of reaching high values of the loading ratio $X = D/Pd$, the following parameters have to be considered:

- temperature: X increases as temperature decreases;
- pressure: X increases as pressure increases;
- minimum linear size of the sample: diffusion regulates the distribution of D within the lattice of Pd, and the coefficient of diffusion decreases as temperature decreases; conversely using low linear size samples shortens the diffusion times;
- as a consequence of the latter, time becomes an important parameter when planning an experiment.

To give an idea, in the quoted experiment [1] a value of $X = 1$ was obtained with a pressure slightly lower than 1 bar, at the temperature of 150 K, with a sample 3.6 μm thick. The time necessary in order to reach thermodynamic equilibrium starting from the moment in which D₂ went in contact with Pd, was in the order of one week.

The idea at the base of this proposal is to have a much simpler experiment, able to run for a long time substantially unattended, in order to handle long lasting runs. It consists of using a sample of larger mass and lower dimensionality than the one used in [1], held at the temperature of liquid nitrogen (LN₂), while in touch with D₂ gas at a rather high pressure, and realizing a very simple calorimeter, so that the possible excess heat be the only parameter to be measured and recorded. In this way, it would be possible to perform very long runs, lasting weeks, or even months.

It has been said that another necessary condition to satisfy in order to have cold fusion phenomena, is to have a motion of the D ions in the lattice of Pd: in the system presented here diffusion should be able to provide this kind of dynamic regime.

The calorimeter will be described here.

2. The calorimeter

The calorimeter is based on the use of an “old style” Supairco dewar, designed to contain either liquid helium or liquid hydrogen. It is well known that these liquids have a very low latent heat of evaporation; thus, in order to keep them in liquid form, their container has to be well protected from heat inlets of various types. In particular, in order to reduce the heat inlet by radiation coming from the outer envelope at room temperature, modern dewars have both MLI (MultiLayer Insulation) and metallic shields cooled by the evaporating He/H₂. However, till the years ‘sixties these techniques were not yet applied: the way in which the radiation heat inlet was cut down consisted of having a liquid nitrogen dewar (77 K) surrounding the liquid helium (hydrogen) container, of course both in a good insulating vacuum. The reduction in heat power inlet due to radiation was thus cut by a factor $300^4/77^4 \approx 230$. In Fig. 1 a schematic drawing of such a dewar is shown.

For the calorimeter described here the idea is to put liquid nitrogen (LN₂) also in the inner dewar, the one designed to contain liquid He/H₂. In this way the radiation heat coming from the surrounding container is cut to zero. The only heat inlet remaining is that by conduction through the stainless steel pipe sustaining the inner dewar, which is quite small, since a thin-walled pipe is used.

This remaining heat will produce a small constant evaporation of nitrogen from the inner dewar. Should any independent source of heat appear, there will be an increase in the evaporation rate, which will take place at a substantially constant temperature. The measurement of the increase of the evaporation rate will be easily transformed into heat inlet, since the latent heat of nitrogen is well known.

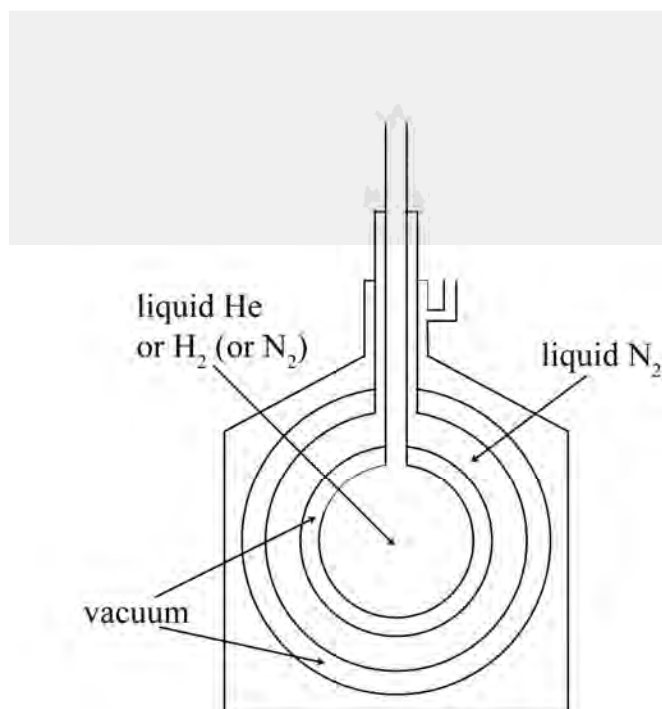


Fig. 1 - Schematic drawing of a Supairco “old style” liquid He/H₂ dewar.

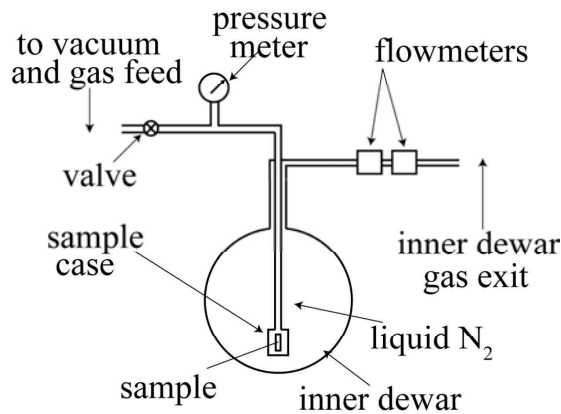


Fig. 2 - Scheme of the experimental set-up.

Thus, provided that the the nitrogen evaporation from the inner dewar is measured and recorded, the experiment can be run substantially unattended. The only operation to perform is, from time to time, to refill LN2 in the outer dewar.

3. The proposed experimental set-up

In Fig. 2 a scheme of the experimental set-up proposed is shown.

The sample is in a vacuum-tight case immersed in LN2 in the inner dewar. In the case high pressure (tens of bars) D_2 gas is put. Evaporation from the inner dewar is measured by a series of two flow meters of different full scale range and recorded with the help of a LabVIEW data acquisition system. Care is taken that the outer dewar be always at least half-full of LN2.

Excess heat in the sample will produce an increase in the evaporation rate of LN2, and will be detected by the flow meters. It will be easy to transform these data into heat or power.

4. A preliminary test

A test was performed, using gas meters, rather than flow meters. The outer dewar was filled with LN2, only 3 liters of LN2 were put in the inner dewar (this was a Supairco 10-liters dewar).

The (residual) heat input in the inner dewar, calculated from the evaporated gas, was constant in time, and amounted to 10 mW (it would take about 19 months to evaporate all the 3 liters of LN2).

The two flow meters in series that will be used will have 20 and 500 sccm (standard cubic centimeters per minute) range full scale. The first will give a reading of 2.47 sccm (the 10 mW quoted above) in the absence of heat excess. The second would give a reading of 240 sccm in the presence of a heat excess of 1 W.

5. References

- [1] F. Scaramuzzi, *Journal of Alloys and Compounds*, 385, 19 (2004).

Wave Nature of Deuterium Flux Permeating through the Palladium Thin Film with Nanometer Coating Layers --- (I) Experimental Observation

B. Liu^{*} , **J. Tian** , **X.Z. Ren** , **J. Li** , **Q.M. Wei** , **C.L. Liang** , **J.Z. Yu** , **X.Z. Li**
Department of Physics, Tsinghua University, Beijing 100084, CHINA
**R & D Dept., China Shenhua Energy Company Ltd., Zhouji Tower, No.16 Andelu, Dongcheng District, Beijing, 100011, CHINA*

E-mail: liub01@shenhua.cc

Abstract. Wave nature of deuterium flux permeating through the palladium thin film is revealed using nanometer coating layers. Three sets of experimental data [1,2,3] agree with wave in multiple-layer theory quantitatively or qualitatively. Other than granular particle diffusion model and surface catalyst model, the wave nature of deuterons inside the coating layers must be included in order to explain the experimental phenomena.

1. Introduction

The anomalous deuterium flux permeating the thin wall of palladium tube showed a peak while the temperature of Pd tube was monotonically decreasing through 150°C to 120°C [1]. It was a hint that other than the diffusion there must be some different mechanism governing the deuterium flux permeating the thin Pd film, otherwise diffusion coefficient was supposed to be a monotonic function of temperature. When deuterium molecule dissociated into 2 atoms, and entered the Pd surface as if a granular particle, it would be reflected by the single surface layer only. However, if its behavior was similar to that of a wave; then, it would feel more layers behind the surface layer. The reflecting wave from the surface would be determined not only by the surface layer, but also by the layers behind the surface. Then the reflection of wave should depend on the interference of several reflecting waves from several layers, and manifest itself a peak-wise behavior. This distinct feature might be tested by a deuterium flux permeating through a palladium thin film with multiple nanometer coating layers.

2. Experimental results

Fig.1 shows the schematics of the apparatus. We loaded deuterium gas to Pd film through coating layers while pumping on other side, and then heating the Pd film. Thus deuterium flux formed in Pd had to go through multi-coating layers on the surface of Pd first. By the analysis of the experimental data, we can identify relationship between deuterium flux and coating layers on Pd film.

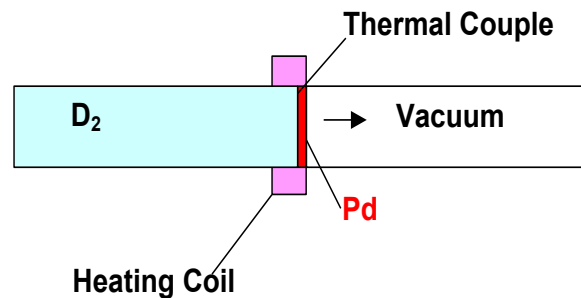


Fig. 1 – Schematics of the deuterium flux apparatus.

The following plots show some results of observation. Under the same conditions, the Pd film with

coating layers (Pd-TiC-Pd) has greater deuterium flux than Pd film without coating layers has unexpectedly.

Fig. 2 and Fig. 3 show a set of comparative results of the experiment. These two experiments have almost the same gas-loading procedure, and the only difference between these two experiments is the sample of Pd film. The first sample is a Pd film ($\phi 20\text{mm} \times 0.1\text{mm}$) without coating layer, while the second one was coated with a layer of titanium carbide (Pd / TiC). The substrate is a Pd film of $\phi 20\text{mm} \times 0.1\text{mm}$, while the Pd / TiC coating layer is 20/2nm. In two experiments, we were first using mechanical pumps to evacuate both sides of the Pd film, and then turned off the pumps. After that we loaded deuterium gas into Pd film from the side with coating layer. At that time deuterium gas pressure reached 80kPa, right in the measuring range of pressure gauge. We heated Pd films in a stepwise way, (changing the heating power every 80 minutes, such that the temperature rose to 120°C thermal equilibrium first; then to 200°C thermal equilibrium, and then dropped back to 120°C thermal equilibrium and room temperature thermal equilibrium)(see temperature curves in Fig. 2 and Fig. 3).

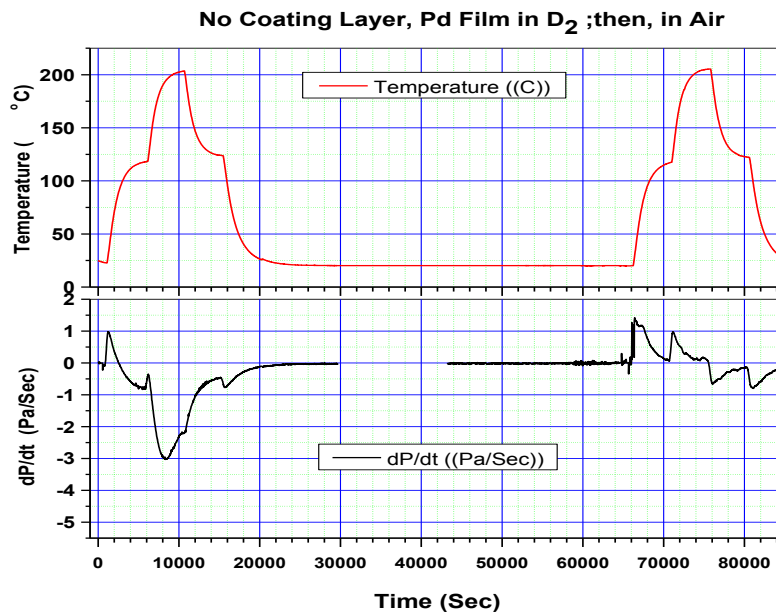


Fig. 2 – Pd film without coating layer.

At the same time we used the multi-channel data acquisition system (Keithley 2700) to record the pressure data. In order to analyze data of pressure change, we calculate deuterium gas chamber pressure derivative to get pressure change rate. The negative peak of pressure change rate represents the rapid decrease of deuterium gas pressure (lower plots in Fig. 2 and Fig. 3 for dP/dt). After deducting the pressure changes caused by temperature, we use the curve to watch deuterium flux.

In order to compare with loading deuterium gas, we loaded air instead of deuterium gas with the same procedure. After heating and cooling in air, we also got temperature and pressure change rate in air as well (Fig. 2 and Fig. 3).

On both figures data after 45,000 seconds are loading air procedure. The positive and negative peaks of dP/dt curves indicate pressure change rate accompanied with temperature changes. We can see from the loading air part, every time Pd film temperature changes, there will be a correspond peak on the pressure change rate curve.

The heating and cooling corresponds separately to the positive peak and negative peak, regardless of the Pd film with or without coating layer. What's more, at the loading air part the positive peak shape of pressure change rate curve is almost the same as the negative peak shape, and peaks height are roughly equal. This shows the air inside chamber acts as the ideal gas isochoric change following the gas state equation. The air does not permeate through the Pd film. However, loading deuterium gas procedure is completely different. After thermal equilibrium pressure change rate is larger than that of loading air, and positive and negative peak are not asymmetric. A wider and higher negative peak indicates more reduction of deuterium gas pressure. Deuterium flux appears. The puzzle is that Pd film with coating might have much more deuterium flux than Pd film without coating at the same temperature, although Pd film with one coating layer is thicker than Pd film without coating layer. This phenomenon conflicts with classical diffusion theory. (In Fig. 2 the peak of deuterium flux reaches -3.0Pa/s, while in Fig. 3 it reaches

-5.0Pa/s).

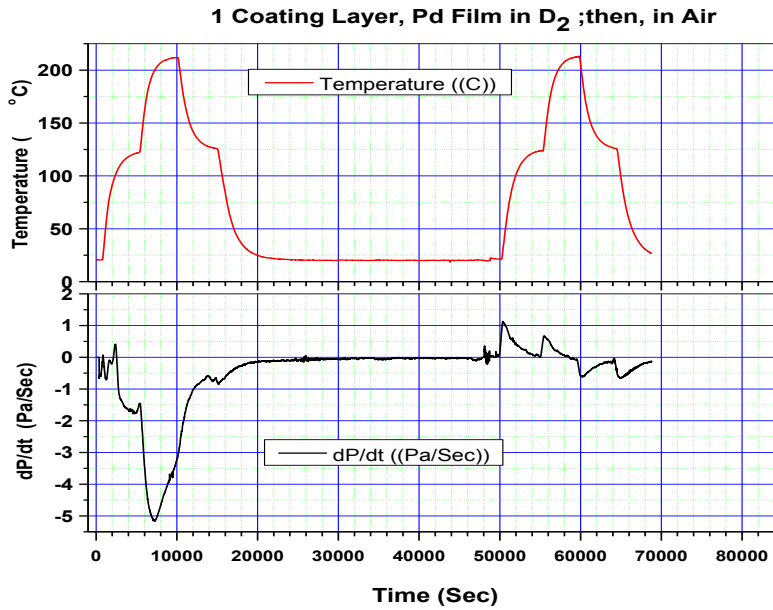


Fig. 3 – Pd film with coating layer.

Further more, we use different numbers of coating layer Pd film to run the same loading procedures. The results show the deuterium flux with different coating layer numbers is not monotonic. Fig. 4 indicated that at the different number of Pd/TiC layers on Pd film with the same experimental conditions, the peak value of deuterium flux changes. All the experiments run with the same deuterium gas pressure (80kPa), and the substrate of Pd film was $\phi 20\text{mm} \times 0.1\text{mm}$, each Pd/TiC layer thickness was 20/2nm. We repeated experimental procedures as abovementioned experiments. Different coating layer number Pd film reaches the peak deuterium flux at slightly different temperature. We found that the deuterium flux through the multilayer films was not monotonic with the number of coating layers, and there comes the peak in a certain layer.

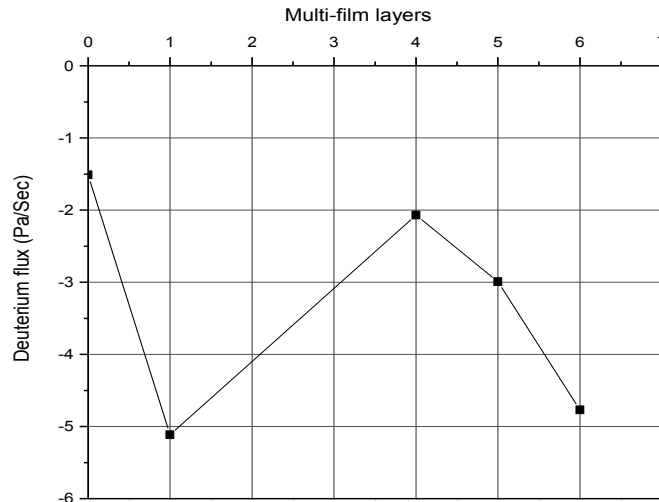


Fig. 4 – Deuterium flux in different coating layer number.

3. Discussion

In 1858, reference to the Fourier thermal equation in 1822, Fick established the quantitative formula to describe the matter migration from high-density area to low-density areas. [4] With low concentration, during unit time and through unit area, material quality (flux) determined by the concentration gradient:

$$\vec{J} = -D\vec{\nabla}n \quad (1)$$

Here D is constant coefficient, called the diffusion coefficient. The concentration n can be expressed as the number of diffusion atoms per unit volume, or other physical quantity represents amount of material like gram atoms. (diffusion flux also takes the appropriate units) Equation (1) is often called as Fick's first law. Equation (1) shows that, keeping the Pd film with the same pressure, the diffusion of deuterium flux through the Pd film usually monotonously decreases when thickness of Pd film increases.

The work of this experiment shows that, accompanied with the variation of the number of coating layers The peak of deuterium flux appears. That is to say, the deuterium flux reaches peak value at the certain number of coating layers. According to the wave nature of deuteron motion, although individual reflected waves on each scattering body is not zero, the summation of reflected waves may be smaller than that of single scattering body. In another words, with the appropriate number of coating layers the different reflected waves might have destructive-interference which would lead to a very small reflectivity. Deuterium flux peak would occur at this condition.

Based on above discussion, permeating characteristics of Nano-system materials can not be fully explained by traditional diffusion theory. The wave nature of deuteron motion can qualitatively describe some anomalies in D-Pd/TiC/Pd multi-layer systems.

Acknowledgments

This research is supported by the Natural Science Foundation of China(#10475045), the China Association of the Science and Technology, The Ministry of Science and Technology (Fundamental Research Division, and (2009CB226113).), Tsinghua University (Basic Research Fund (985-III)).

References

- [1] X.Z. Li, B. Liu, J. Tian, et al. *J. Phys. D: Appl. Phys.* **36** 3095–3097(2003).
- [2] X.Z. Ren, *Thesis for Master Degree of Science at Tsinghua University* (2003).
- [3] J. Li, *Thesis for Bachelor Degree at Tsinghua University* (2006).
- [4] D. Brogioli and A. Vailati, *Diffusive mass transfer by nonequilibrium fluctuations: Fick's law revisited*, *Phys. Rev. E.* **63**, 012105/1-4 (2001).

Wave Nature of Deuterium Flux Permeating through Palladium Thin Film with Nanometer Coating Layers --- (II) Theoretical Modeling

Xing Z. Li, Bin Liu, Jian Tian, Xian Z. Ren, Jing Li, Qing M. Wei ,
Chang L. Liang, Jin Z. Yu

Department of Physics, Tsinghua University, Beijing 100084, CHINA

E-mail: lxz-dmp@tsinghua.edu.cn

Abstract. Two sets of experimental results are analyzed using the wave nature of the deuterons inside the palladium film. An identity for the ratio of absorption to transmission rate is derived to qualitatively explain the correlation between the deuterium flux and heat flow in experiments. In addition, a peak-wise behavior is shown for the permeation of deuterium flux through the palladium thin film as a function of the number of nanometer coating layers in experiments and in theory. This peak-wise variation is the characteristic behavior due to the wave nature of the deuterons.

1. Introduction

The studies on deuterium/palladium system have been conducted for more than 20 years in order to search for the anomalous phenomena. One of the subjects has been if we should treat the deuterons inside the palladium as granular particles or as a wave. S. Chubb and T. Chubb proposed early in 1990 that the deuterons inside the palladium should be treated as a wave based on the similarity with the electrons and the experimental facts [1, 2]. In 1995, the selective resonant tunneling model was proposed to explain the tunneling of Coulomb barrier between deuterons based on the wave mechanics [3, 4]. This wave model explained also why there was no accompanied commensurate neutron and gamma radiation for excess heat. Indeed the hot fusion data for 6 major fusion cross sections justified this wave model [5, 6] as well. The verification of three deuteron fusion reactions [7, 8, 9] has further supported this wave resonance model inside the metal-hydrides. In this paper, we provide two additional analyses of experimental data which show the wave nature of the deuterons inside the palladium thin film.

The correlation between deuterium flux and heat flow provides the first set of experimental data [10]. The permeation of the deuterium through the palladium thin film with nanometer coating layers provides the second set of experimental data [11, 12, 13]. Two theoretical derivations are presented accordingly to explain these two sets of data, and show clearly the wave nature of deuterons.

2. The identity of (A/T) and correlation between deuterium flux and heat flow

A, the absorption rate, and T, the transmission rate, are two important rates to describe the permeation process of deuterons through palladium film. A is defined as the ratio of the number of absorbed deuterons to the number of injected deuterons. T is defined as the ratio of the number of permeated deuterons to the number of injected deuterons. If the deuterons are treated as granular particles, we may expect that the transmission rate might decrease when the absorption rate increases while the injected number is fixed.

However, the experimental result showed differently. The deuterium flux (solid line in upper plot of Fig.1 (blue, right coordinate)) increased when the heat flow (dash-dotted line (red, left coordinate)) increased. Since the deuterium flux and heat flow are supposed to be related to transmission (T) and absorption (A), respectively, the summation of (T+A) is supposed to be equal to (1-R). Here R is the reflection rate which is defined as the ratio of the number of reflected deuterons to the number of injected deuterons. If the deuterons are treated as granular particles and the permeation is treated as a diffusion process of random walking particles; then, the number of the reflected deuterons on the palladium surface is fixed or increases slowly when temperature decreases (the solid line (pink) in the lower plot of Fig.1). Thus, we might expect (T+A) is fixed or decreases slowly. Then any peak up in T would be accompanied a spike down in A. In contrary, the experimental data showed that peaks in T are accompanied by peaks up in A. It implied that (T+A) has a peak there, or more deuterons are entering palladium there. This conflicts with the diffusion model which implies less diffusion flux through palladium when temperature goes down.

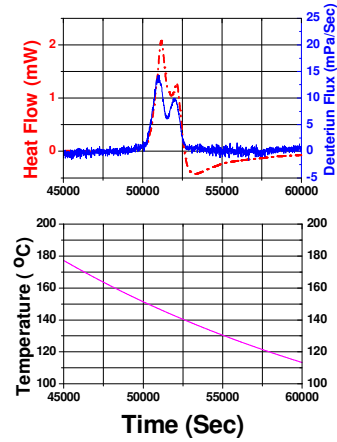


Fig.1—Correlation between deuterium flux and heat flow

In a word, diffusion model allows only a monotonic decreasing deuterium flux when palladium is cooling down, and allows only a negative correlation between the deuterium flux and heat flow. It does not allow such a peak-wise behavior of deuterons permeating through the thin film of palladium, and does not allow a positive correlation between the deuterium flux and heat flow. We have to modify the diffusion model in order to explain this phenomenon. That is to say: deuterons are not random walking granular particles in permeation through the thin palladium film.

A slab model based on the wave nature of the deuterons is proposed to describe the interface between deuterium gas and palladium surface in Fig.2. A thin layer (PdO or any coating layer) is assumed on the surface of palladium. Two sets of rates, (T_0, A_0) and (T_1, A_1) are defined to describe the surface layer and the palladium substrate, respectively.

An identity has been proved to calculate the transmission and absorption rates of compound system (see Appendix A):

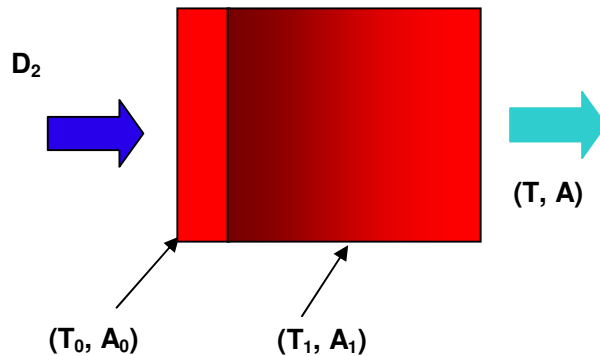


Fig. 2. - Slab model for coating layer on surface of Pd substrate

$$\frac{A}{T} \equiv \frac{A_0}{T_0} + \frac{A_1}{T_1} + \frac{A_0}{T_0} * \frac{A_1}{T_1} \quad (1)$$

It is a direct result of wave property: (1) The injected wave may be reflected not only by the first layer, but also by the interface between the first layer and the Pd substrate; (2) the total reflection is determined by the summation of these two reflected waves; (3) the wave phase angle between these two reflected waves may lead to a zero summation of wave amplitude and greatly reduce the total reflection. As a result, the ratio of $\frac{A}{T}$ is always greater than each individual ratio ($\frac{A_0}{T_0}$ or $\frac{A_1}{T_1}$), because the multiple reflections in the interface between the first layer and the Pd substrate always enhance the total absorption (A) and reduce the total transmission (T). On the contrary, if the deuterons act as the granular particles, the total reflection, (1-(T+A)), is always greater than each individual reflection; then, (T+A) must be reduced. Thus any peak in T must lead to a spike downward in A.

Consequently, the positive correlation between the deuterium flux and the heat flow just denies the simple diffusion model of granular particles and reveals the wave nature of the deuterons permeating through the thin film of palladium. A series of experiments were designed to further verify this wave nature [11, 12, 13].

3. The permeation of deuterons through palladium film with nanometer multiple coating layers

In order to verify this wave nature of deuterons permeating through palladium film, we may add more coating layers on the surface of palladium substrate (Fig.3). Instead of changing temperature, we may change the number of coating layers and see if the total reflection might be reduced by interference of reflected waves from several interfaces. If the wave model is correct; then, at certain number of coating layers, we are supposed to see the total transmission would be enhanced to higher than the transmission with no coating layers.

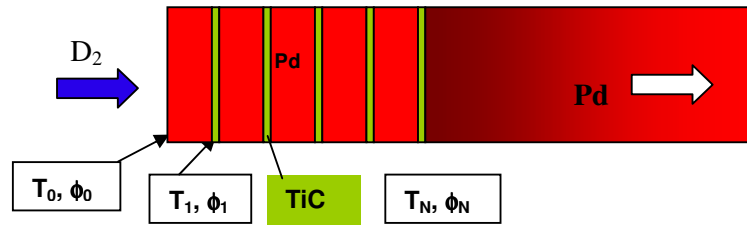


Fig. 3. - Multiple coating layers on the surface of Pd substrate

On the palladium substrate a TiC layer of 2 nm is coated first by ion sputtering. Then a palladium layer of 20 nm is coated. These alternatively coated Pd-TiC-Pd films were used to measure the deuterium flux near 120°C [13]. Since the phase angle plays key role in the wave phenomena, we assign the change of the phase angle (ϕ) for each Pd-TiC-Pd compound layer. The transmission rate (T) is assigned also to describe the feature of each Pd-TiC-Pd compound layer. The task is to find the total transmission rate (T_N) for a palladium substrate with N Pd-TiC-Pd compound layers, and compare it with the experimental data.

Based on the matrix algebra(Appendix B), we may reach 3 conclusions:

(1) The Transmission rate of the palladium coated with nanometer TiC-Pd layers is

$$T_{0N} = \frac{T_0 * T_N}{1 + (1-T_0)(1-T_N) + 2\sqrt{(1-T_0)(1-T_N)}\text{Cos}(\phi_0 + \phi_N)}. \quad (2)$$

Here, (T_0, ϕ_0) is assigned for the first palladium layer facing deuterium gas. (T_N, ϕ_N) is assigned for the N compound layers TiC-Pd facing the first palladium layer (see Appendix B.)

(2) (T_N, ϕ_N) can be written as an explicit function of the number of compound layers TiC-Pd...TiC-Pd:

$$T_N = \left| \frac{\text{Sin} \alpha_1}{\sqrt{\frac{1}{T_1} e^{-i\phi_1} \text{Sin}(N\alpha_1) - \text{Sin}[(N-1)\alpha_1]}} \right|^2 \quad (3)$$

$$\phi_N = -\text{Arg}\left[\left(\sqrt{\frac{1}{T_1}} e^{-i\phi_1} \text{Sin}(N\alpha_1) - \text{Sin}[(N-1)\alpha_1]\right) / \text{Sin} \alpha_1\right] \quad (4)$$

(3) An eigen angle, α_1 , is introduced in eqs.(3) and (4) based on the (T_1, ϕ_1)

$$\alpha_1 = \text{ArcCos}\left[\sqrt{\frac{1}{T_1}} \text{Cos} \phi_1\right] \quad (5)$$

Here, N is the number of nanometer coating layers.

Using 4 input parameters, T_0, ϕ_0, T_1, ϕ_1 , it reproduces the experimental data, the ratio of $\left(\frac{T_{0N}}{T_0}\right)$. In

Fig.4, the red stars are the results of the experimental measurement, and the open circles are the result of calculation using eqs. (3), (4), (5) for $T_0 = 0.0031$, $\phi_0 = 0.1123$, $T_1 = 0.7629$, $\phi_1 = 2.4026$. These open circles are connected by dotted lines because N is supposed to be integers only. The predominate

feature is that: (1) This ratio $\left(\frac{T_{0N}}{T_0}\right) > 1$ at N=1, and N=6. It implies the reduction of reflection due to

interference of several reflected waves.

This is the characteristics of wave model.

(2) A peak-wise behavior of $\left(\frac{T_{0N}}{T_0}\right)$

versus N implies the failure of diffusion model of random walking granular particles in palladium.

4. Discussion

This wave model is originally based on the similarity between electrons and deuterons in the palladium-deuterides. However, the de Broglie wavelength of deuteron is much smaller than that of electron. Can we still apply the wave model to deuteron? The low energy electron diffraction (LEED) experiments show that the electron

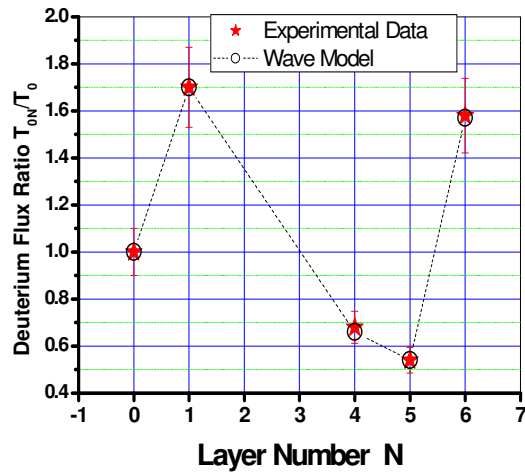


Fig. 4. - Comparison between experiment and slab model

diffraction pattern appears even if the electron energy reaches 267 eV [14]. The electron wave length at this energy is similar to that of a deuteron at thermal energy. Hence, we might expect the characteristics of deuteron waves in the palladium deuteride at room temperature. Indeed we checked once and once

again this peak-wise dependence of $\left(\frac{T_{0N}}{T_0}\right)$ versus N by different experiments: measure the changing

rate of deuterium pressure in vacuum side of palladium film[12], and in the high pressure side of palladium film[13]; compare the behavior of air and deuterium to assure the peak-wise characteristics of deuterium flux[13]. All these experiments have confirmed the peak-wise behavior in Fig. 4. Hence, the wave nature of deuterium flux permeating through palladium thin film is confirmed.

The great success in superwave triggering, and in ultrasonic wave work has implied the wave nature of metal deuterides as well [15,16,17] although we need to figure out the underlined mechanism. Chemical catalyst model failed in this peak-wise feature because its effect depends only on the first surface layer.

The ratio $\frac{A}{T}$ may be enhanced by multiple nanometer coating layers on the surface of palladium. If we increase the transmission T by certain number of coating layers; then, we may increase the absorption of deuterons inside the palladium deuteride. In this way we may enhance the loading ratio and the possibility of having “excess heat”. Indeed, this is using the reflection waves among interfaces to enhance the confinement of deuterons inside the palladium.

Acknowledgments

This research is supported by the Natural Science Foundation of China(#10475045), the China Association of the Science and Technology, The Ministry of Science and Technology (Fundamental Research Division, and (2009CB226113).), Tsinghua University (Basic Research Fund (985-III)).

References

- [1]. S.R. Chubb and T.A. Chubb, *Proceedings of the First Annual Conference on Cold Fusion*, March 28-31,1990, Salt Lake city, Utah, p.119 (National Cold Fusion Institute, 1990)
- [2]. R. Nieminen, *Nature* **356** 289 (1992)
- [3]. X.Z. Li: *Proceedings of ICCF-5*, 9-13 April, 1995, Monte Carlo, Monaco, p.285(1995)
- [4]. X.Z. Li: *J. of New Energy*, **1** No.4 44 (1996)
- [5]. X.Z. Li: *Fusion Science and Technology* **41** 63(2002)
- [6]. X.Z. Li, Q.M. Wei, B. Liu: *Nuclear Fusion* **48** 125003(2008)
- [7]. J. Kasagi, et al., *J. Phys. Soc. Japan* **64** (3) 778 (1995)
- [8]. A. Takahashi, et al., *Fusion Tech.* **34** 256 (1998)
- [9]. G.K. Hubler, Private communication (2009)
- [10]. X.Z. Li, B. Liu, J. Tian, et al. *J. Phys. D: Appl. Phys.* **36** 3095(2003)
- [11]. X.Z. Ren, *Thesis for Master Degree of Science at Tsinghua University* (2003)
- [12]. J. Li, *Thesis for Bachelor Degree at Tsinghua University* (2006)
- [13]. B. Liu, et al., *Proceedings of ICCF-15*, (2009)
- [14]. J.B. Pendry, *Low Energy Electron Diffraction*, Academic Press (London and New York, 1974), p.20.
- [15]. I. Dardik, *Proceedings of ICCF-15*, (2009)
- [16]. V. Violante, et al., *Proceedings of ICCF-15*, (2009)
- [17]. Y. Toriyabe, et al., *Proceedings of ICCF-15*, (2009)
- [18]. X.Z. Li, *Condensed Matter Nuclear Science, Proceedings of 9-th International Conference on Cold Fusion*, May 19-24,2002, Beijing, CHINA, edited by X.Z. Li, p.202(2002)

Appendix A, Identity of $\frac{A}{T} \equiv \frac{A_0}{T_0} + \frac{A_1}{T_1} + \frac{A_0}{T_0} * \frac{A_1}{T_1}$

A useful identity may be derived just based on the wave properties. The wave mechanics may be expressed by matrix algebra as follows.

The injected wave coming from the left-hand-side of the slab. Part of it is reflected, and part of it penetrates the slab. We may use the 2 plane waves as the base functions to describe the outgoing wave and the incoming wave. Then the outgoing wave on the right-hand-side may be assigned as a wave vector:

$$\Psi_0 = \begin{bmatrix} 1 \\ 0 \end{bmatrix}$$

The wave on the left-hand-side may be written as

$$\Psi_1 = M\Psi_0$$

$$M = \begin{bmatrix} m_{11} & m_{12} \\ m_{21} & m_{22} \end{bmatrix}$$

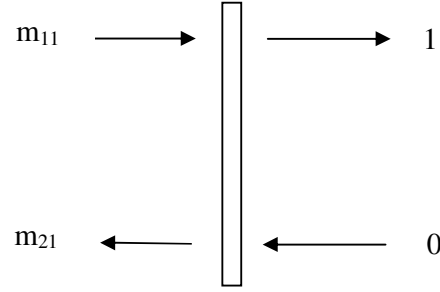


Fig. A1. - Slab model

M is the matrix to describe the slab. Because of the conservation of the probability current, and the symmetry of the slab, we have:

$$M = \sqrt{\frac{1}{T}} \begin{bmatrix} e^{-i\phi} & -i\sqrt{1-T-A} \\ i\sqrt{1-T-A} & e^{i\phi} \end{bmatrix};$$

Here, $T \equiv \frac{1}{|m_{11}|^2}$ is the transmission rate, $R \equiv \frac{|m_{21}|^2}{|m_{11}|^2} = (1-T-A)$ is the reflection rate, and A is the absorption rate, respectively. M is defined as the compound layer composed of layer 1 and 2. Similarly, M_1 and M_2 are defined for individual layer 1 and 2, respectively.

$$M_1 = \sqrt{\frac{1}{T_1}} \begin{bmatrix} e^{-i\phi_1} & -i\sqrt{1-T_1-A_1} \\ i\sqrt{1-T_1-A_1} & e^{i\phi_1} \end{bmatrix}; \quad M_2 = \sqrt{\frac{1}{T_2}} \begin{bmatrix} e^{-i\phi_2} & -i\sqrt{1-T_2-A_2} \\ i\sqrt{1-T_2-A_2} & e^{i\phi_2} \end{bmatrix}.$$

ϕ, ϕ_1 and ϕ_2 are defined as the change of phase angle of the wave across the corresponding layer, respectively.

This leads to the identity directly using $M=M_1*M_2$ and matrix algebra.

$$\frac{A}{T} \equiv \frac{A_0}{T_0} + \frac{A_1}{T_1} + \frac{A_0}{T_0} * \frac{A_1}{T_1}$$

Appendix B, Permeation through multiple coating layers

$$T_{0N} = \frac{T_0 * T_N}{1 + (1 - T_0 - A_0)(1 - T_N - A_N) + 2\sqrt{(1 - T_0 - A_0)(1 - T_N - A_N)} \cos(\phi_0 + \phi_N)}. \quad (\text{B.1})$$

Same matrix algebra may be applied to show: The transmission rate, T_{0N} , of a compound layer composed of layer 0 and layer N, may be expressed by the individual parameters, (T_0, A_0, ϕ_0) and (T_N, A_N, ϕ_N) as eq.(B.1). (T_0, A_0, ϕ_0) defines the first layer on the surface (Fig. B1). (T_N, A_N, ϕ_N) defines the compound layer behind the first layer. It is composed of N layers, each of which is same with the parameters (T_1, A_1, ϕ_1) . In reality, each individual layer was composed by a thin TiC layer (2nm) and a thick Pd layer (20nm) in our experiments. (T_N, ϕ_N) may be expressed by (T_1, ϕ_1) and N as well (A_0, A_1 are assumed zero in calculation because it is negligible in our experiments).[18]

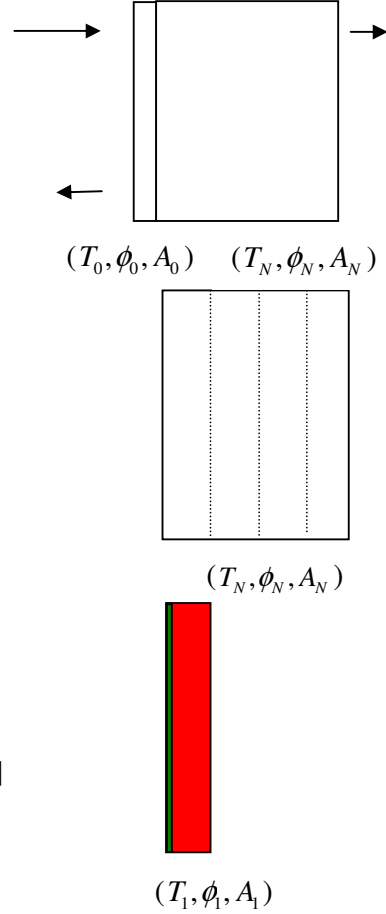


Fig. B1. - Multiple coating layers on the surface of Pd substrate

$$T_N = \left| \frac{\sin \alpha_1}{\sqrt{\frac{1}{T_1} e^{-i\phi_1} \sin(N\alpha_1) - \sin[(N-1)\alpha_1]}} \right|^2,$$

$$\phi_N = -\text{Arg}\left[\left(\frac{1}{T_1} e^{-i\phi_1} \sin(N\alpha_1) - \sin[(N-1)\alpha_1]\right) / \sin \alpha_1\right],$$

$$\alpha_1 = \text{ArcCos}\left[\sqrt{\frac{1}{T_1}} \cos \phi_1\right].$$

Self-Polarisation of Fusion Diodes: Nuclear Energy or Chemical Artefact?

F. David & J. Giles

*Deuo Dynamics, Moss Side House, East Blairdaff, Aberdeenshire, AB51 5LT.
(UK)*

E-mail: davidfa@altern.com

Abstract. The authors discuss the results of the testing of a new fusion device : the “Fusion Diode”.

The cold fusion community has been trying to justify cold fusion on the basis of empirically produced excess heat for nearly two decades. [1], [2] The science world has continually resisted the possibility, citing the heat as not conclusive. Some problems of chemical reactions can interfere with calorimetry. [3]

The authors have sought a different approach, whereby the device has no input energy, relying on the only energy produced from the device. We are using diodes, made of palladium as the metal, and silicon as the semiconductor. We have also tried other semiconductors. But we describe here our experiments with silicon. The palladium is loaded with deuterium simply by the gas-loading method. We don't know the effective loading value, but it is probably rather high, because of the micrometer size of the palladium powder.

A diode is basically a surface of contact with a metal (electronic conductor) and a semiconductor (hole conductor).

We think that the deuterium nuclei which are in the palladium will be driven in the direction of the electric field. Once these deuterium cores will arrive at the interface between palladium and the semiconductor, they will accumulate there. The probability of fusion probably will increase. [4]

Better: if reactions of fusion take place into the junction, an excitation of the electrons will occur at this level (as in the junction zone of a photovoltaic cell). A solar cell is a diode with a large surface. When photons fall on the junction zone, certain atoms are excited, and electrons pass from a low energy level to a higher energy level. A spontaneous electric voltage thus will appear. It is what we observed.

In order to get a surface of junction as large as possible, our fusion diodes are made as powder diodes, with a large surface junction made up of a semiconductor powder in contact with palladium powder charged with deuterium. (Fig. 1) [5] The weight of palladium powder is comprised between 1 g and 2 g by diode.

The suspected fusion reactions take place in the junction between the semiconductor and the Palladium powder, which produces an excitation which is transmitted to the electrons. This excitation increases their energy and allows them to cross the bandgap of the semiconductor and pass into the conduction band, as in a photovoltaic cell. This energy very quickly appears as a spontaneous potential difference which can reach over 0.5 volt per junction. (open circuit)

Diodes comprising of a stack of junctions were made, making it possible to obtain over 1 volt at the poles of a very compact device of a few centimeters length. The released power remains very low for the moment, (in the nanowatt range) but it should be noted that it is presented in the form of directly usable electrical energy, and not of thermal energy.

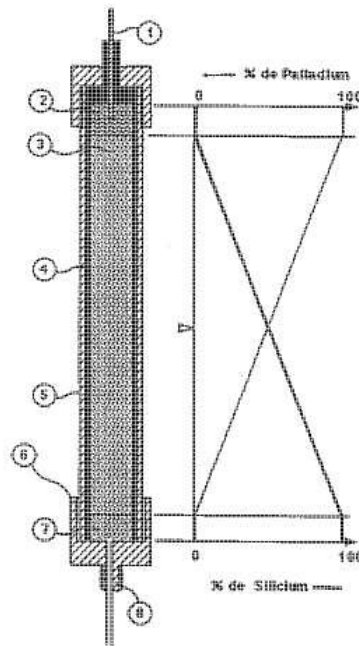


Fig. 1 - Our fusion diode : 1 Electrical connection; 2 End cap with threading; 3 Mix of silicon and palladium powder (at the bottom pure palladium and then an increasing concentration of silicon; at the middle of the diode: 50% silicon, 50% palladium; at the top: pure silicon. The result is a very large surface rectifier diode); 4 Plastic tube for insulation; 5 Aluminum or machined nylon container; 7 End cap; 8 Swagelok valve.

Of course, we have made blank and control experiments. We have built three diodes, one filled with pure deuterium (1.5 bar) another filled with hydrogen at the same pressure, and another filled with pure argon (Fig. 2). The black plastic tubes are 6 cm long.

We observed no voltage with argon filling, a little voltage with hydrogen, twice the voltage with deuterium. We think that the observed voltage with hydrogen is generated by the little amount of deuterium in the hydrogen. (0.015%)



Fig. 2 - Three diodes, one filled with pure deuterium (1.5 bar) another filled with hydrogen at the same pressure, and another filled with pure argon.

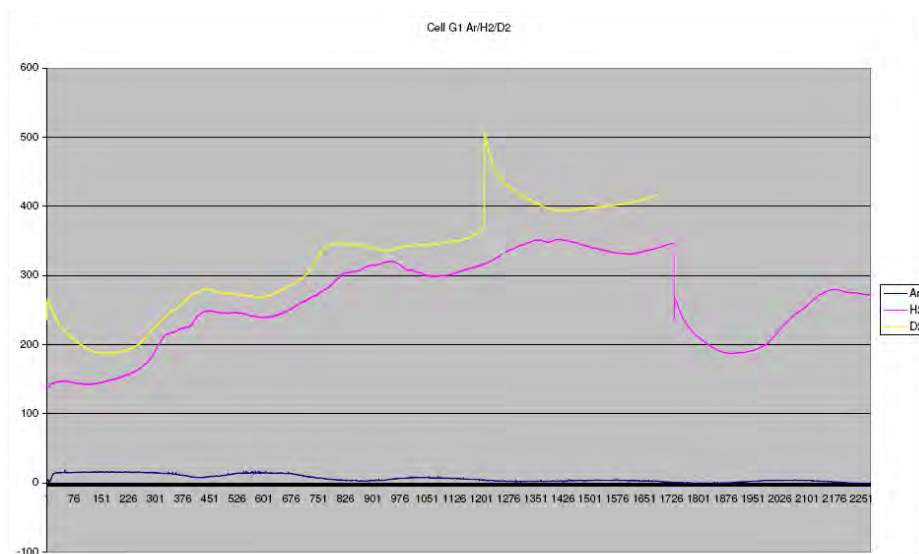


Fig. 3 - Yellow line : voltage at the ends of the deuterium filled diode; Cyan Line : voltage at the ends of the hydrogen filled diode; Blue line : voltage at the ends of the argon filled diode. Vertical axis: millivolts; Horizontal axis: minutes.

Our lab is not air-conditioned : the diurnal oscillation of the voltage is probably caused by the variation of the temperature of our lab, so we can exclude a “Allais Effect”.

Is the observed release of energy due to the fusion of the deuterium nuclei, or is it an electrical voltage produced by an electrochemical reaction? (For example, oxidation of deuterium by the little amount of adsorbed oxygen on the powder) The authors plan to prove the origin of the energy measured over several months with the help of various methods. First of all, we plan to seal our fusion diodes inside glass containers, to avoid leak of deuterium.

References

- [1]. M. Fleischman and S. Pons: *J. Electroanal. Chem.*, 1989, **261**, 301.
- [2]. S. E. Jones, E. P. Palmer, J. B. Czirr, D. L. Decker, G. L. Jensen, J. M. Thorne, S. F. Taylor and J. Rafelski: *Nature*, 1989, **338**, 737–740.
- [3]. David, F., Giles, J. *Materials Research Innovations*, 2008, 12, **4**, 173-174
- [4]. FP n° FR2662537, 1991-11-29, F. David
- [5]. FP n° FR2729249, 1996-07-12, F. David

***In Situ* Energy-Dispersive X-ray Diffraction Study of Thin Pd Foils at D/Pd and H/Pd ~1**

D.L. Knies¹, V. Violante², K.S. Grabowski¹, J.Z. Hu³, D.D. Dominguez¹, J.H. He⁴, S.B. Qadri¹ and G.K. Hubler¹

¹*U.S. Naval Research Laboratory, Washington, DC*

²*ENEA, Frascati, Italy*

³*NSLS, Brookhaven National Laboratory, Brookhaven, NY*

⁴*Nova Research, Alexandria, VA*

david.knies@nrl.navy.mil

Abstract. Time resolved, *in-situ*, energy dispersive x-ray diffraction was performed in a modified Fleishman-Pons electrolytic cell during electrochemical loading of palladium foil cathodes with hydrogen and deuterium. Concentrations of H:Pd (D:Pd) up to 1:1 in 0.1 M LiOH (LiOD) in H₂O (D₂O) electrolyte were obtained, as determined by both the Pd lattice parameter and cathode resistivity. In addition, some indications on the kinetics of loading and deloading of hydrogen from the Pd surface were obtained. The alpha-beta phase transformations were clearly delineated but no new phases at high concentration were determined.

1. Introduction

Since the discovery in 1886 by Graham [1] that Pd can absorb relatively large amounts of hydrogen, palladium hydrides and deuterides have been extensively studied. Metal hydrides have generated much interest among a variety of scientific disciplines, particularly in hydrogen storage in recent years [2-3], because of the limited supply of fossil fuels and growing worldwide demand for energy. Palladium and its alloys are also materials extensively used for hydrogen purification [4], which is applicable to fuel cells. Although current research on hydrogen storage has shifted from transition metals to light elements to gain a high gravimetric density of hydrogen, palladium still plays an important role in the study of metal hydrides.

The phase diagram of Pd-H shows this system to have two phases, α and β , separated by a miscibility gap for temperatures below about 300°C and a hydrogen pressure below about 20 bar. At room temperature, the solubility limit for H in the dilute α phase is about 0.03 H/Pd, while the lower limit for the concentrated β phase is 0.58 H/Pd. In between is a two-phase region with a mixture of α and β at these H concentration limits. Both α and β are FCC interstitial solid solutions, but with different lattice parameters. In both, hydrogen atoms randomly occupy the four octahedral interstitial sites present per FCC unit cell containing four palladium atoms. So, when fully loaded with H, stoichiometric PdH forms the B1, or rocksalt structure. The Pd lattice parameter increases from 3.889 Å for pure Pd up to 4.102 Å for PdH at room temperature, an increase over 5.5%.

However, deviations from this simple structural model have been reported. For nanocrystalline palladium, a narrowing of the Pd-H miscibility gap has been observed using *in-situ* synchrotron x-ray diffraction measurements [5]. The phase boundary change is associated with a larger ratio of the value of the entropy of mixing to that of the enthalpy of mixing in nanocrystalline samples than in coarse-grained samples. At low temperature (50-80K) in the concentrated β phase of PdH, there is the so-called 50-K anomaly, associated with a structure change [6]. At high hydrogen pressures, a hydrogen-induced superabundant-vacancy phase can be produced in the palladium metal lattice [7] and stabilized at room temperature and normal pressure [8].

At high H (D) concentrations, there is some evidence for additional structure changes. Tripodi et al. suggested a new γ phase to explain the temperature coefficient of resistance (TCR) increase for electrochemically loaded palladium when the composition H/Pd approached one [9]. Recently, they showed the TCR decreases when H/Pd exceeds one [10]. In the Pd-D system, new phases were reported from deuterium thermal desorption spectra taken from Pd samples [11]. In addition, there was a report showing oscillating resistivity for palladium hydrides at a high concentration range of H/Pd > 0.9 [12].

All these recent experiments suggest that something must happen in palladium with a ratio of H/Pd approaching unity or above, which is currently not understood. Moreover, these proposed phase transitions are only based on indirect experimental data and have not been structurally determined yet. In fact, while loadings of H and D approaching 1:1 D:Pd and H:Pd have been measured *in situ* at 77K on Pd powder [13] the highest loading of D/Pd that has been measured at room temperature by *in-situ* x-ray diffraction is 0.76 [14,15]. For these reasons, we have undertaken this *in situ* x-ray diffraction (XRD) investigation of Pd highly loaded with H and D at near room temperature.

2. Experimental Procedure

Fig. 1 shows a schematic representation of the experimental geometry used with the wiggler beam line X17C at the National Synchrotron Light Source, Brookhaven National Laboratory.

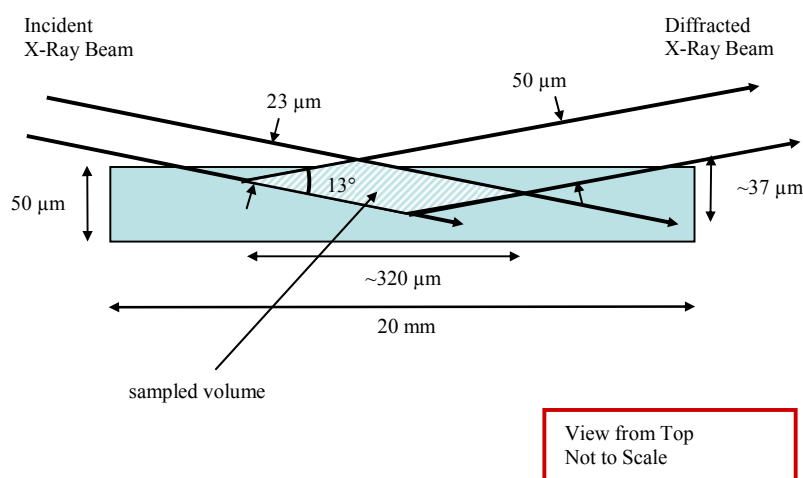


Fig. 1. - Schematic representation of experimental geometry used. Beam widths collimated to dimensions shown, with an incident beam height of 12-15 μm , resulting in a sampled volume of ~ 70 pL, with maximum dimensions as shown. A high resolution Ge detector was positioned at a diffraction angle of 13° (2θ).

A collimated, high-intensity, white-radiation x-ray beam with energies of 10-100 keV entered from the left and impinged upon the center of a sample stage that provided x-y-z translation and two axes of rotation, ω for the sample and 2θ for the detector. The incident x-ray beam was collimated to a shape 12-15 μm tall and 23 μm wide. The diffracted beam was collimated to 50 μm width by tungsten slits, and detected by a high resolution Ge x-ray detector. Nominally symmetric reflection diffraction conditions were used with $\omega \approx \frac{1}{2} 2\theta = 6.5^\circ$, meaning grazing incidence and a shallow sampling volume applied. As a guide, the x-ray path length in Pd is almost 18 times its depth of penetration with this geometry. For energies just above the Pd K absorption edge at 24.35 keV, the short absorption length in Pd (i.e., $1/\mu$) of about 14 μm limits sensitivity to depths very near the surface. Just below the Pd K edge and up at 47 keV, $1/\mu$ is 83 μm , allowing sensitivity to the top 10 or so μm of the foil. Only for energies > 80 keV (where $1/\mu = 335$ μm) is the entire thickness of the foil accessible, as selected by positioning the sampling volume within the foil. We employed the Pd K_α x-ray fluorescence at 21.13 keV ($1/\mu = 55$ μm) to position the sample surface in the diffraction sampled volume, based on the intensity of this x-ray fluorescence. Diffraction data from high energy x-rays was sometimes obtained even when the Pd K x-ray was not observed, because it would be totally absorbed by the cathode at depths greater than ~ 30 μm ($10 \times 1/\mu \div 18$). The original Pd grain size of the cathodes averaged 100 μm , so that most spectra sampled a mixture of two or three grains that the sampled volume straddled during the measurement.

The 2θ diffraction angle was set to 13 degrees to transmit the x-ray beam between the cathode and anode, and to enable diffraction from a broad range of d spaces. The diffraction angle was calibrated using a gold target substituted for the cell. The experimental procedure was to take x-ray spectra prior to beginning electrolysis, and to

also establish the starting resistance to enable measurement of R/R_0 , where R is the measured resistance and R_0 is the starting value. The x-y-z stage and ω were used to align the cathode within the sampled volume and to establish the Bragg diffraction condition.

The electrochemical cell, fabricated at ENEA, consisted of a 26-mm-OD glass tube with 1-mm-thick walls and an electrolyte volume of 25 mL. The x-rays passed through the glass wall and about 12 mm of electrolyte to reach the cathode and another 12 mm of electrolyte and the glass wall before emerging from the cell. This limited the detection of diffracted x-rays to energies greater than ~ 20 keV. The cathode was positioned at the center of rotation of the sample stage and initial alignment was performed with a microscope. The parallel-plate, dual-anode-geometry electrochemical cell is illustrated in Fig. 2. The two anodes were 50- μm -thick Pt foils and the cathodes were nominally 50- μm -thick Pd foils. All electrodes were 20 mm wide and 40 mm in height. The anodes and cathode were separated by 4-mm-thick Teflon spacers, used to clamp the electrodes together at each end.

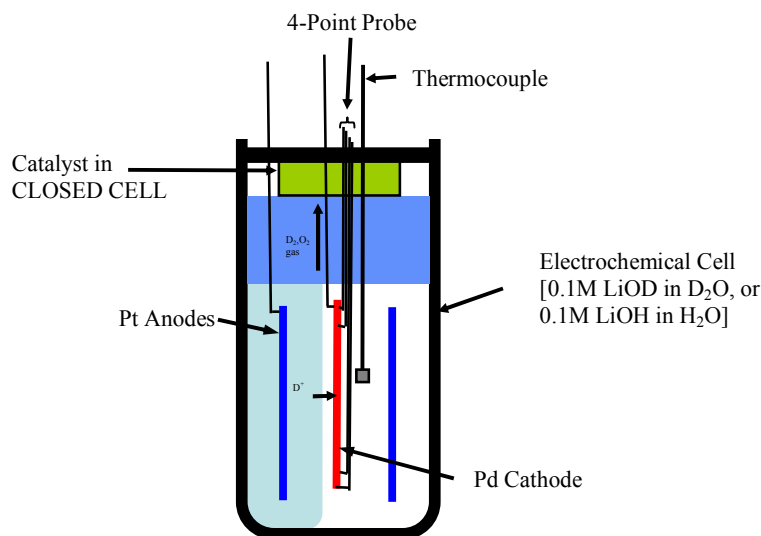


Fig. 2. - Schematic representation of the modified Fleischman-Pons electrolysis cell. This was a closed cell with self-contained catalyst for H_2 and O_2 recombination, and was instrumented to measure cathode resistance and cell temperature and pressure.

Five Pt wires were spot-welded to the Pd foil: one contact for the cathode current and four for the four-point probe measurement of resistivity at a frequency of 1 kHz. Initial resistance of the Pd was a few m Ω . The cell was hermetically sealed, and had a Pt basket containing a catalyst in the upper region to recombine the evolved hydrogen and oxygen generated by electrolysis. A valve was set to release at 1.4 bar to ensure safety from explosion, and a temperature-controlled, high-precision pressure sensor monitored cell pressure and enabled termination of electrolysis if the pressure reached 1.4 bar. The measured pressure was very stable throughout the experiments, indicating that the catalyst performed well.

The electrolyte was composed of either 18M Ω H_2O containing 0.1M LiOH or 98+ atomic% D_2O with 0.1M LiOD. Thermocouples measured the electrolyte temperature and the temperature of the x-ray cabinet at 5 different positions. Input electrolysis power to the cells varied but never exceeded 14 watts. The electrolyte temperature was highly correlated to the input power. The cell electrolyte temperature increased to as much as 51 $^\circ\text{C}$ from a starting temperature of 29 $^\circ\text{C}$ during experiments due to this heat source.

Electrolysis was begun using 0.2 to 1.2 mA/cm 2 current density under current control and required a starting voltage of about 2.2 V to drive the current. The voltage steadily increased with the degree of loading as the chemical potential of the PdH system increases with loading. The degree of loading was estimated using the resistance ratio R/R_0 calibration curves for H or D shown in Fig. 3. Spectra were collected during ~ 5 -minute intervals. The error in the R/R_0 measurement is estimated to be $<1\%$.

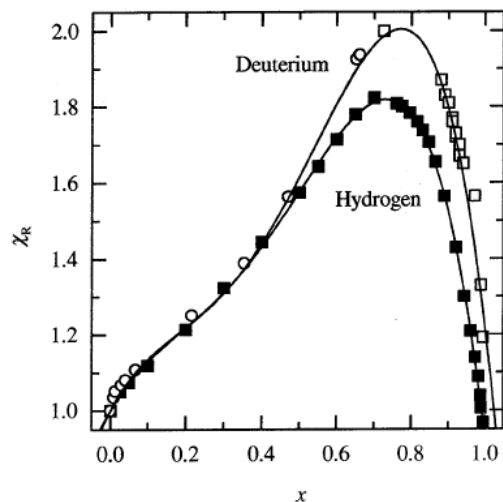


Fig. 3. - Resistance ratio R/R_0 or χ_R versus H(D)/Pd ratio x . Data taken from Zhang et al. [16], and references therein. Data was digitized then fit using fifth order polynomials.

However, the Pd resistance changed during a run from factors other than just hydrogen content, such as changes in dislocation density, grain size, and lattice strain, so that when the resistance ratio peak is retraced, the maximum can unpredictably change by as much as 6%. Therefore, the R/R_0 measurement is considered a semi-quantitative *in-situ* indicator of loading of the foil. Additionally, R_0 was always measured at room temperature, but the temperature upon reaching the peak in resistance was always higher due to the input power into the cell. Therefore, the peak value of R was temperature corrected to room temperature prior to forming the R/R_0 ratio, using a temperature coefficient of resistance value of 0.004 K^{-1} taken from the value for pure Pd. Nevertheless, the peak value of the R/R_0 ratio generally differed from literature values (1.8 for H and 2.0 for D), due to extraneous factors as mentioned above. Consequently, the peak value was scaled to the literature value by multiplying R_0 by an appropriate factor.

When R/R_0 approached the peak in Fig. 3, the current was increased in stages to produce a higher loading ratio. At appropriate times when the loading stalled, either the current was increased, or the current set to zero for several minutes and then restarted at a current 20% greater than prior to shutting off the current. These procedures sometimes resulted in a new surface condition where the loading would increase.

Due to the large lattice expansion of Pd when it is loaded with hydrogen (up to 5% lattice parameter increase, 16% volume increase), the cathode began to warp and move immediately upon initiation of electrolysis. This required continuous use of the x - y - z stage and ω to reengage the cathode, since it moved as much as 2 mm as it adjusted to the strain from loading. The problem was less acute at high loadings due to the slower change in H/Pd value and lattice constant with time. The problem was so severe that little data was taken at low loading ratios. In the last run with H_2O , the cathode was deloaded in steps by lowering the current systematically so that some x-ray spectra could be taken at smaller H/Pd ratios.

During each run, additional x-ray fluorescence lines appeared in the spectra that were identified as Sn and Pb. The origin of these impurities was most likely from solder used in wire connections to the feed-through at the top of the cell. Conceptually, the solder dissolved in vapor condensed onto the solder, then dripped back into the electrolyte. The surface of the cathode became coated with impurities from the electrolyte, because metallic ions in the electrolyte will plate out on the cathode during electrolysis. This was confirmed by visual observation of the cathode when the cathodic current was removed. Immediately a cloud of material came off of the cathode turning the electrolyte black in color. Then, the electrolyte cleared in only a few seconds as the material dissolved back into the strong base.

Four cathodes prepared at ENEA were run in the cell. Details of their preparation are described elsewhere [17]. Briefly, cathodes of 0.9995 purity were rolled to 50- μm thickness, annealed at 850°C for 1 hours, etched in Aqua

Regia, and recleaned with alcohol and DI water just prior to insertion into the cell. In one case, a cathode (B) was reused with another batch of electrolyte, after first deloading and recleaning.

All x-ray spectra were least-squares-error fit to obtain peak positions, widths, and intensities. These were analyzed to obtain d spacings and hkl values, then lattice parameter a. At the beginning of loading, few diffraction peaks were found, consistent with few grains being sampled, and the Bragg diffraction condition not readily being satisfied. As the loading progressed, more peaks were observed, consistent with subgrains being formed due to the large lattice strains generated by the hydrogen loading of Pd. In many cases, a single lattice parameter could match all the diffraction peaks observed. However, in some cases the loading was heterogeneous, typically resulting in pairs of peaks at the same hkl value. In those spectra we identified two different lattice parameters.

The D (H) composition of the cathode in the β phase of PdD_x (PdH_x) was determined from the measured lattice parameter using the 77K composition versus lattice parameter data from Schirber and Morosin [13], combined with an extrapolation of the thermal expansion data of Hemmes, Geerken and Griessen [18] provided from 10-250K.

3. Results

Table 1 summarizes results for the four cathodes run over a 9-day period. Table 1 shows that high maximum loadings ($0.86 < \text{H(D)}/\text{Pd} < 0.98$) were obtained from the lattice parameter a for all four cathodes; that the thinnest cathodes (with larger R_0) loaded to the highest H(D)/Pd ratios; and that the R/R_0 method slightly underestimated the maximum loading fraction for the D case, but overestimated it for the H case. The discrepancy was about 2%. Fig. 4 shows the current, voltage and power values needed to obtain the minimum R/R_0 for a D loaded cathode, plotted versus the minimum R/R_0 . Higher values of all 3 parameters promote better loading, but the strongest correlation is for input power and input current. For all cathodes, higher powers were attempted after the minimum R/R_0 (max. loading) was reached, but the cathodes deloaded and never returned again to the lowest R/R_0 values. For 3 of the 4 cathodes, the electrolyte temperature clearly decreased upon initial loading, caused by the endothermic heat of water hydrolysis combined with the dissolution of D (H) in Pd and the creation of orphan oxygen, preventing their recombination at the catalyst. For the fourth, very low current was initially used so that the thermal signal was below the sensitivity of the measurement.

Table 1. Cathode Loading Descriptions.

Cathode	Electrolyte	R_0 (m Ω)	Time (h:min)	Charge (C)	Energy (kJ)	Maximum	Maximum
						D(H)/Pd From R/R_0	D(H)/Pd From a
NRL#2	D ₂ O	3.69	46:15	6337	22.14	0.85	0.856
L23	D ₂ O	3.82	30:15	5974	18.32	0.87	0.893
B2	D ₂ O	10.08	48:22	110947	783.24	0.95	0.977
L5	H ₂ O	5.24	09:56	4354	18.19	0.97	0.946

Figs. 5a and 5b show x-ray spectra for Cathode B2 (D loaded) and cathode L5 (H loaded), respectively. The intensity falls off at low energy due to absorption in electrolyte and at high energy due to x-ray beam intensity fall-off. Diffraction from multiple hkl orientations are identified in the plots, and indicate that the incident x-ray beam intercepted multiple subgrains within the nominal 3 original grains inside the sampled volume. The D/Pd ratio in (a) is 0.913 from the lattice parameter, while R/R_0 indicated a ratio of 0.936 for cathode B2/spectra_154. From (b), the H/Pd ratio is 0.933, which matches the value obtained from R/R_0 for cathode L5/spectra_229. Pd, Sn, and Pb fluorescence peaks are also identified in the spectra, as are satellite escape peaks from the escape of Ge x rays from the detector, and diffraction peaks likely from Sn deposited on the surface in (a).

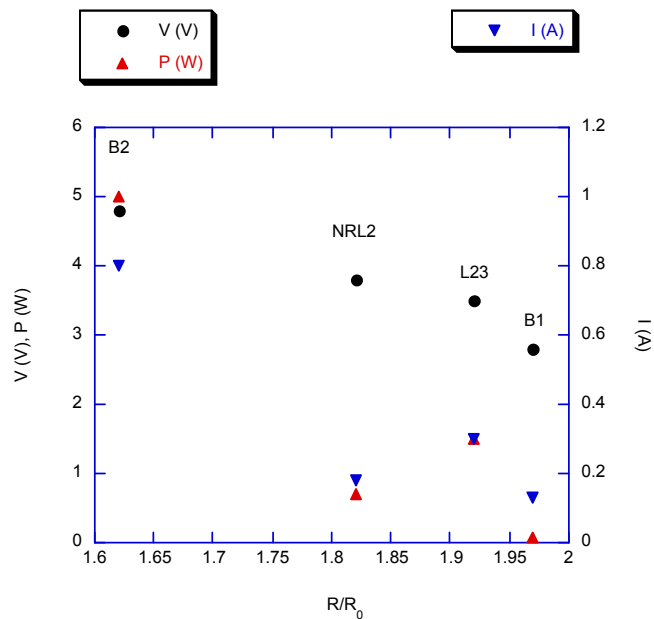


Fig. 4. - Cathode operating conditions to obtain the minimum R/R_0 at the highest D loading: current, voltage, and power, versus the minimum R/R_0 obtained.

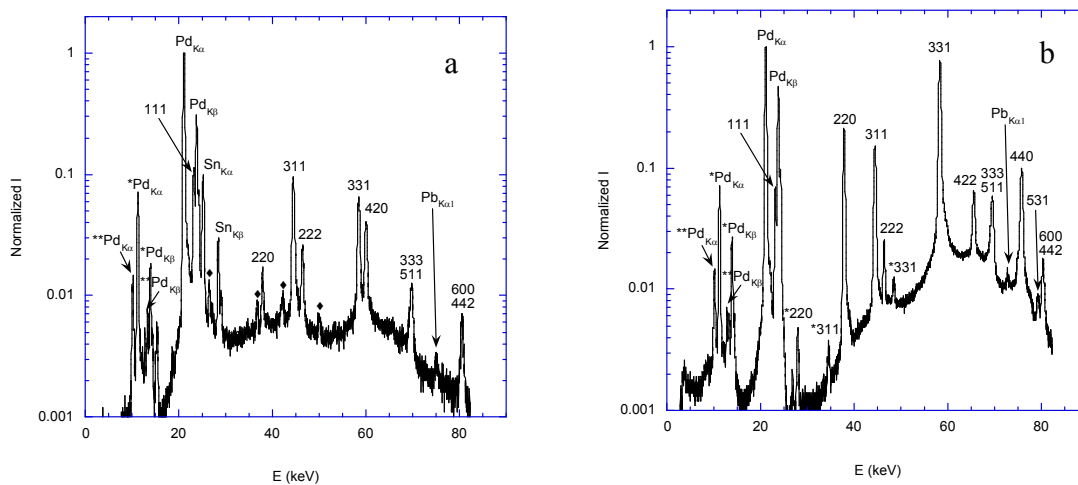


Fig. 5. - Typical x-ray diffraction spectra obtained, a) from cathode B2 (D loaded, spectra 154), and b) from cathode L5 (H loaded, spectra 229). Besides diffraction peaks marked by their hkl values, there were also fluorescence peaks from Pd, Pb, and sometimes Sn present in spectra, as well as escape peaks caused by escape of $Ge_{K\alpha}$ or $Ge_{K\beta}$ x rays from the detector (marked by * or **, respectively). Extra diffraction peaks from white Sn deposited on the cathode could sometimes be observed, as indicated by the diamond symbols shown in a).

Figs. 6a and 6b display a time history of the lattice constant, R/R_0 , and cell current for Cathode B2 (D loaded) and cathode L5 (H loaded), respectively. A general observation is that the deuterium-loaded cathodes displayed variability in the lattice constant upon large current changes (Fig. 6a, 4E4 s and 1.0 E5) while the one hydrogen-loaded cathode did not show this variability (Fig. 6b, 2.2 E4 s). The highest D/Pd ratios occur at the beginning of the electrolysis, and in one case occurred when the R/R_0 ratio had not yet even reached the peak (not shown). A possible explanation is that some orientations of the crystallites have faster kinetics than others and may load to high values

unconstrained by neighboring grains. Eventually, the other grains equilibrate, but by then compression prevents all the grains from obtaining the highest value. A second possible explanation is that the Pb and Sn surface impurity build-up over time may reduce the H fugacity and therefore the chemical potential pressure on the surface. This behavior was not observed in the one cathode run with H₂O.

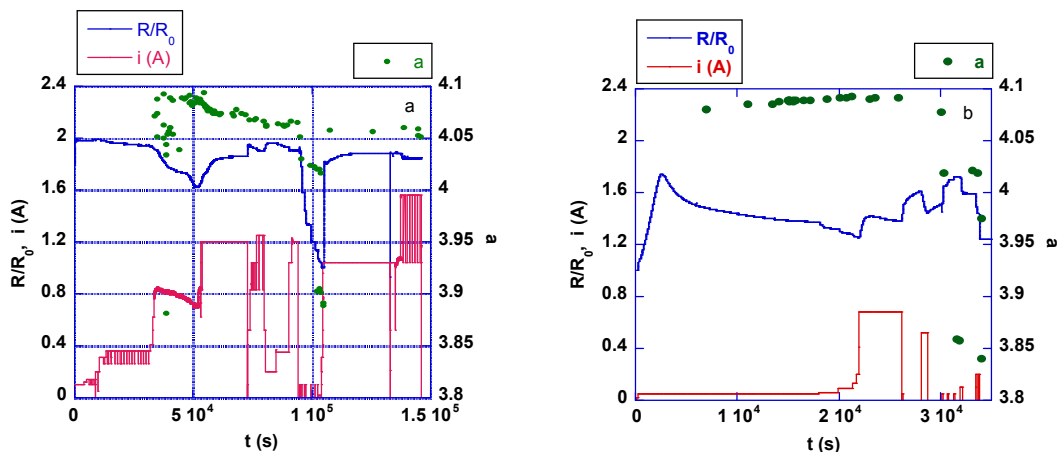


Fig. 6. - Time history of (a) cathode B2 loaded with D, and (b) cathode L5 loaded with H. R/R_0 , cell current, and measured lattice parameter a are shown.

Figs. 7a and b plot the R/R_0 ratio versus lattice constant for Cathode B2 and Cathode L5, respectively. These data have several features to note. First, there is a very clear delineation between the lattice constants for the α phase ($a \sim 3.9$) and the β phase ($a > 4$). Second, the collection of data does not appear to follow a smooth curve, especially near the peak in R/R_0 for the B2 cathode. This is largely caused by the heterogeneous loading of subgrains in the Pd foil. While R/R_0 is a bulk average for the foil, XRD was measuring individual subgrains, whose composition varied from subgrain to subgrain during some measurements. In those cases, the diffraction spectra showed multiple peaks for a given hkl for PdD_x, leading to multiple lattice parameters corresponding to the single R/R_0 value. These multiple values of a are plotted in Fig. 7. These cases were most common when the current changed by a large amount.

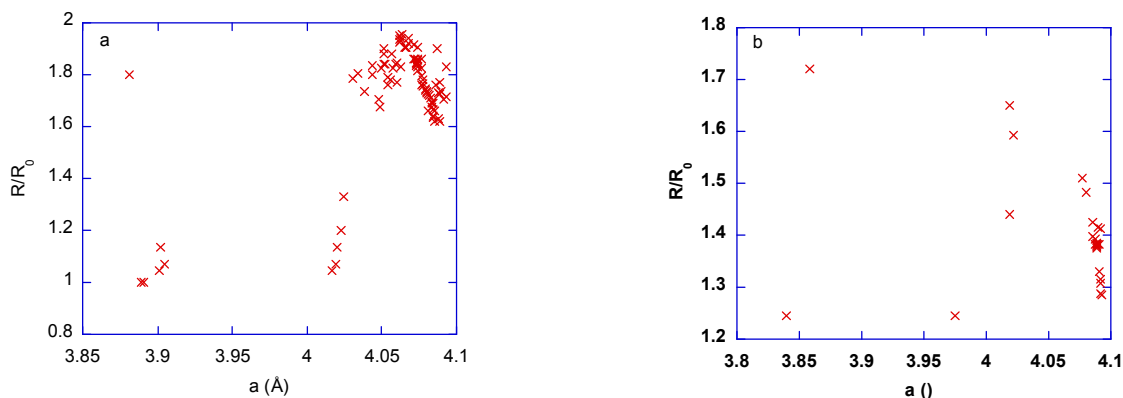


Fig. 7. - Comparison of measured R/R_0 with lattice parameter for (a) cathode B2 loaded with D, and (b) cathode L5 loaded with H.

4. Summary

For the first time, time resolved, *in-situ*, energy-dispersive x-ray diffraction was performed on modified Fleishman-Pons electrolytic cells during electrochemical loading of palladium foil cathodes to high levels with hydrogen and

deuterium. Concentrations of H/Pd (D/Pd) up to nearly 1 in 0.1 M LiOH (LiOD) in H₂O (D₂O) electrolytes were obtained with lattice parameter data monitored throughout the range of concentrations.

A number of observations regarding the electrolysis of F-P cells were consistent with the literature. These include: it is more difficult to load deuterium than hydrogen into palladium, large amounts of impurities are deposited on the cathode from the electrolyte, the *in-situ* relative-resistance measurement of the cathode provides only a semi quantitative guide to the hydrogen concentration, and once a cathode has been loaded to high hydrogen concentration, it is difficult to repeat this high concentration upon subsequent loading. Potential new observations in the electrolysis of FPE cells include: higher starting resistivity foils (thinner foils) loaded to higher D concentration, the highest loading fractions occurred during times of large current and/or concentration change, and all 4 cathodes produced at ENEA loaded very well.

Observations regarding *in situ* XRD during electrolysis in F-P cells were consistent with the literature in that only the well-known alpha-beta phase transition was observed. New observations from the *in situ* XRD during electrolysis in F-P cells include: data obtained for high D/Pd ratios up to 0.98, the relative resistivity measurement R/R_0 slightly underestimates the XRD measurement of the maximum D/Pd ratio by ~ 2%, there is no obvious new PdD phase at D/Pd~1, and nonuniform loading of hydrogen can occur. Tentative new observations from the XRD data include evidence of rapid loading and deloading (~minutes) of the surface while R/R_0 was virtually unchanged, and very few x-ray spectra contained both alpha and beta phases together. This implies that the phase change snaps from Alpha to Beta, and vice versa, within the time resolution of the data, or about 5 minutes.

The research work demonstrated for the first time with *in situ* XRD that a loading near D(H)/Pd = 1 may be achieved at room temperature, and can be reasonably controlled.

Acknowledgments

Use of the National Synchrotron Light Source, Brookhaven National Laboratory, was supported by the U.S. Department of Energy, Office of Science, Office of Basic Energy Sciences, under Contract No. DE-AC02-98CH10886. Additional support was provided by ONR Global for V. Violante travel.

5. References

- [1] T. Graham, *Proc. Roy. Soc.*, **17**, 212 (1869).
- [2] L. Schlapbach and A. Züttel, Hydrogen storage materials for mobile applications, *Nature*, **414**, 353 (2001).
- [3] D. Chandra, Reilly, R. Chellappa, Metal hydrides for vehicular applications: The state of the art, *JOM* **58**, 26 (2006).
- [4] S. Adhikari and S. Fernando, Hydrogen membrane separation techniques, *Ind. Eng. Chem. Res.* **45**, 875 (2006).
- [5] J.A. Eastman, L.J. Thompson, and B.J. Kestel, Narrowing of the palladium-hydrogen miscibility gap in nanocrystalline palladium, *Phys. Rev. B*, **48**, 84 (1993).
- [6] J.K. Jacobs and F.D. Manchester, *J. Less-Common Metals*, **49**, 67 (1976).
- [7] Y. Fukai and N. Ōkuma, Formation of superabundant vacancies in Pd hydride at high hydrogen pressure, *Phys. Rev. Lett.* **73**, 1640 (1994); S. Miraglia et al, *J. Alloys Comp.* **317**, 77 (2001).
- [8] D.S. dos Santos, S. Miraglia, D. Fruchart, *J. Alloys Comp.* **291**, 1 (1999).
- [9] P. Tripodi et al, Temperature coefficient of resistivity at compositions approaching PdH, *Phys. Lett. A*, **276**, 122 (2000).
- [10] P. Tripodi, D. DiGiacchino, and J.D. Vinko, Magnetic and transport properties of PdH: Intriguing superconductive observations, *Brazilian J. Phys.*, **34**, 1177 (2004).
- [11] V.F. Rybalko, A.N. Morozov, I.M. Neklyudov, and V.G. Kulish, Observation of new phases in Pd-D systems, *Phys. Lett. A*, **287**, 175 (2001).
- [12] G.H. Miley, G. Selvaggi, A. Tate, M. Okuniewski, M. Williams, D. Chicea, H. Hora, J. Kelly, in Proceedings of the ICCF-8, Villa Marigola, Lerici (La Spezia), Italy, 2000, p. 169.

- [13] R. Felici, L. Bertalot, A. DeNinno, A. Labarbera, and V. Violante, *In situ* measurement of the deuterium (hydrogen) charging of a palladium electrode during electrolysis by energy dispersive x-ray diffraction, *Rev. Sci. Instrum.* **66**, 3344 (1995).
- [14] E.F. Skelton, P.L. Hagans, S.B. Qadri, D.D. Dominguez, A.C. Ehrlich, and J.Z. Hu, *In situ* monitoring of crystallographic changes in Pd induced by diffraction of D, *Phys. Rev. B*, **58**, 14775 (1998).
- [15] J. E. Schirber and B. Morosin, *Phys. Rev. B*, **12**, 117 (1975).
- [16] W.-S. Zhang, Z.-F. Zhang, and Z.-L. Zhang, *J. Electroanal. Chem.*, **528**, 1 (2002).
- [17] V. Violante, et al. *Joint Scientific Advances in Condensed Matter Nuclear Science*. in *8th International Workshop on Anomalies in Hydrogen / Deuterium Loaded Metals*. 2007. Sicily, Italy.
- [18] H. Hemmes, BA.M. Geerken and R. Griessen, *J.Phys. F: Met. Phys.*, **14**, 2923 (1984).

Material Database for Electrochemical Loading Experiments at ENEA

S. Lecci, E. Castagna, M. Sansovini, F. Sarto and V. Violante RdA

ENEA, Frascati Research Center, Technical Unit for Nuclear Fusion, Via Enrico Fermi, 45 - 00044 Frascati (Rome) ITALY

E-mail: stefano@lecci.it

Abstract: A large number of palladium cathodes have been crafted, in many years, to perform chemical loading experiments. These cathodes underwent, very often, different production processes, characterization procedures and experimental conditions. The need to keep trace of all the steps of the “life” of a cathode was the starting point for the creation of a database. The information stored in this useful archive puts us in condition of easily compare different cathodes and try to correlate their experimental behavior with their history.

1. Introduction

The research activity carried out in ENEA on the field of the Fleischmann and Pons (F&P) effect includes different aspects regarding the palladium cathodes used in the electrochemical experiments. One of these concerns the best way to sort and classify the huge quantity of information produced by the large number of experiments carried out and by the enormous number of variables that can be introduced in the manufacture process and in the characterization of each cathode. An efficient method to do so could both easily allow to run through the steps that led to the generation of a cathode again, and help correlating one or more peculiar characteristic with the results of an experiment.

2. The Database

Each electrode undergoes, during its “life”, different processes, some of which are needed for its manufacture (figure 1), and others for its characterization (figure 2). Each detail of the manufacture of the cathodes has to be recorded into a database.

A lot of data, result of the characterization procedures used on the cathodes before and after the electrolysis process, needed as well to be stored in the database.

The first thing to do in order to classify different electrodes, and all the information about them, is to give to each one a name that will allow to:

- Discriminate it from all the others.
- Discriminate different stages of its own (temporal) manufacturing path.

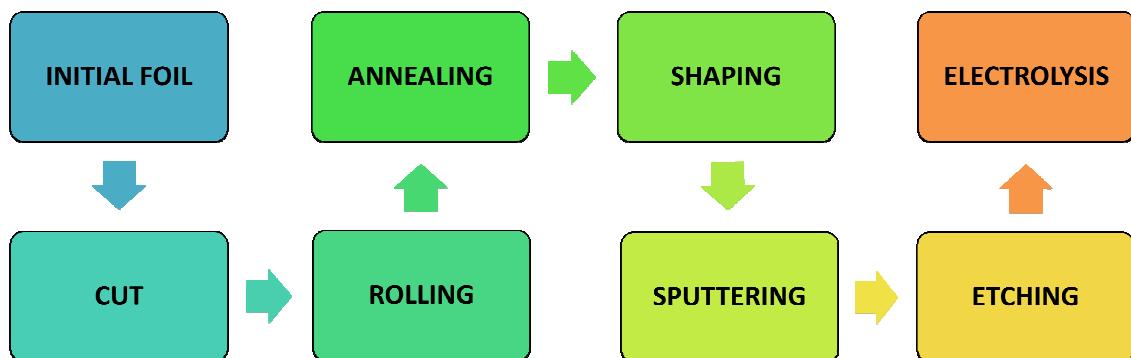


Fig. 1 – Example of some of the processes a cathode can undergo during its manufacture.

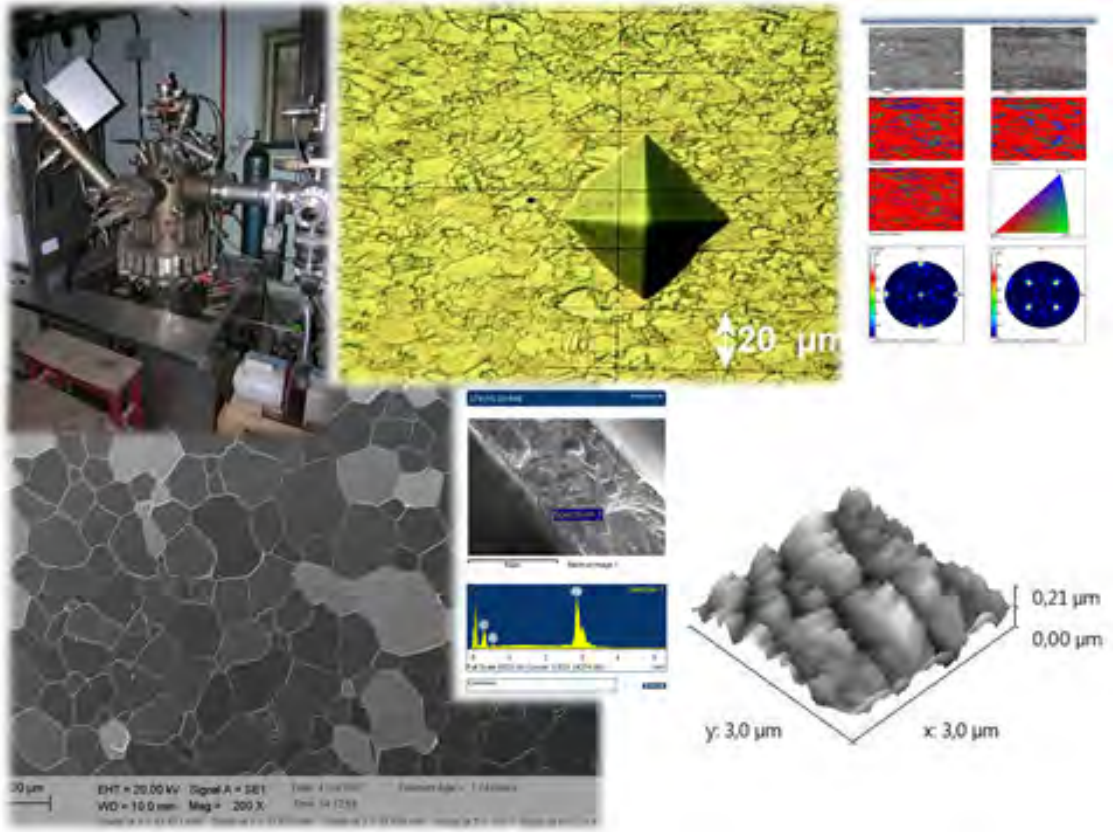


Fig. 2 – Example of some of the techniques used to characterize the cathodes. Starting from the upper left corner, moving clockwise: S.I.M.S., Vickers indenter, E.B.S.D., S.E.M., E.D.X., atomic force microscope.

To do so we thought up a very efficient nomenclature that matches these two requirements and consists in naming each cathode with an abbreviation that increases as the electrode goes on through its manufacturing process. Each cathode name is unique and contains information on which production processes the electrode underwent, and on the position the electrode took up on the rolled foil. Such nomenclature allows to discriminate each stage of the cathode “life” and to store information stage-related. An example is shown in Figure 3.

The database has been made using Microsoft® Access®. Its structure is time organized, newer cathodes are added sequentially from top to bottom and newer operations done on them are added from left to right in the corresponding row. A scheme of its structure and contents is shown in figure 4. All the information stored for each electrode can easily be accessed through a simple interface as shown in figure 5.

L54 (189-227) RAEF					
L54: means that the electrode comes from a certain rolling process	{189-227}: shows the point of the rolled foil, in millimeters, the cathode was cutted from	R: means that the rolling process has been recorded into the database	A: means that the annealing process has been recorded into the database	E: this letter can change and represent the etching process	F: this letter can change and represent the cell in wich the cathode was electrolyzed

Fig. 3- Example of a cathode’s name.

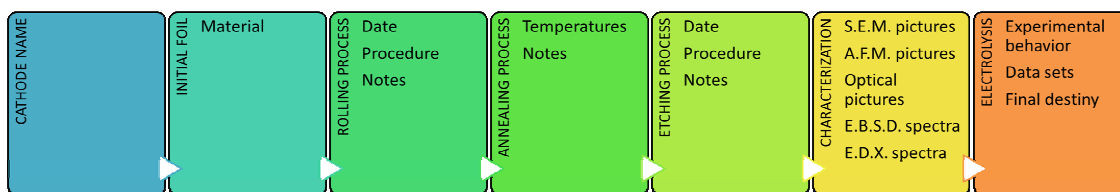


Fig. 4 – Structure of the database.

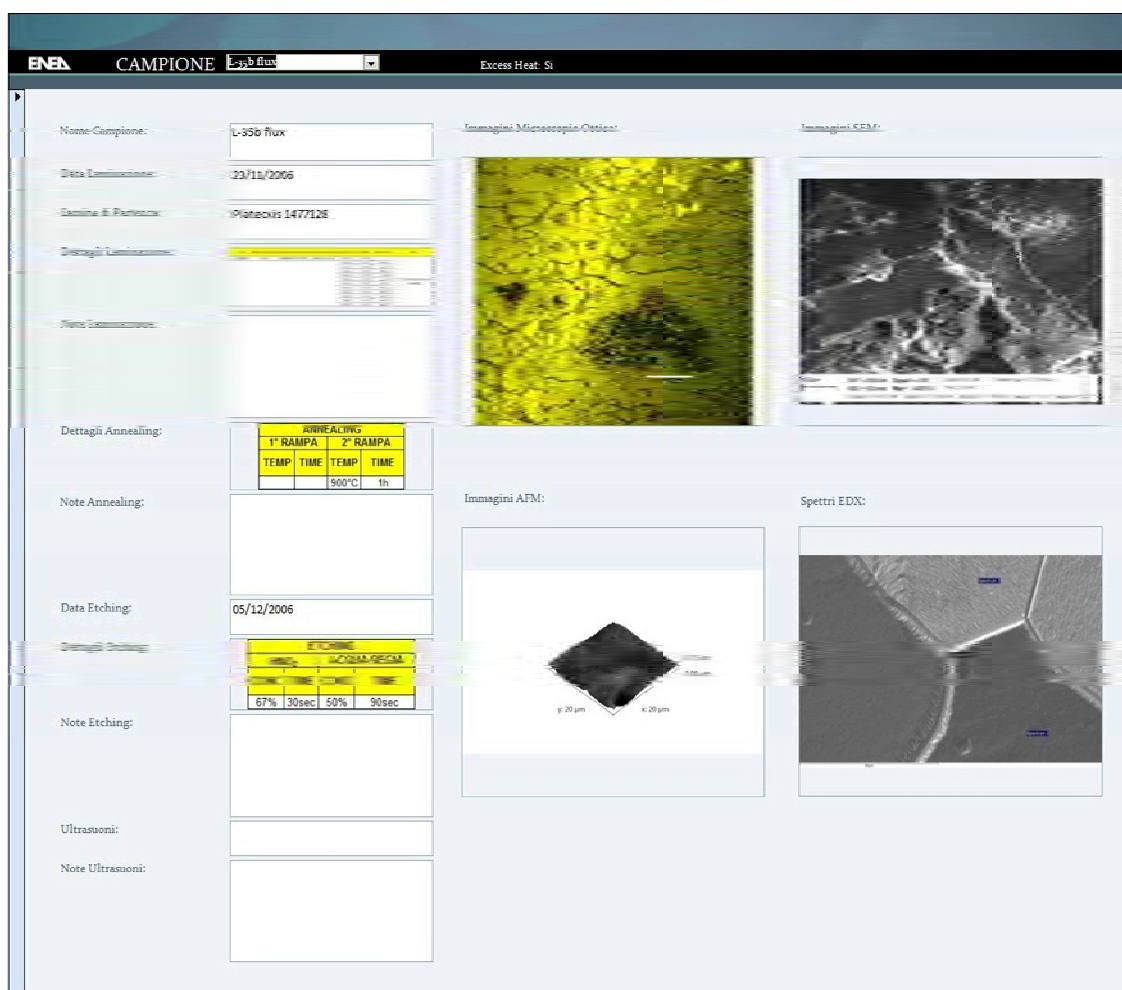


Fig. 5 – Database interface.

3. Conclusions

Our database holds, until now, over 550 records and is updated almost daily, the oldest entry is from the 29th of June 2005 and since the 21th of November 2007 the cathodes were named using the new nomenclature. The large number of information, spanning over a wide period of time, have put us in conditions, as done in other works, to try to statistically correlate the experimental behavior of the cathodes with their measured properties or with the production processes they underwent. However a lot of additional work is still required to improve it, both in terms of variety of information stored and in terms of capability to sort the electrodes who share one or more characteristics. Time will allow us to increase the number of information and to ameliorate our database so that it could become, more than it is today, an absolutely necessary tool for a systematic approach to the problem we try hard to solve.

Interaction of the Electromagnetic Radiation with the Surface of Palladium Hydride Cathodes

E. Castagna, S. Lecci, M. Sansovini, F. Sarto and V. Violante RdA

ENEA, C. R. Frascati, Nuclear Fusion and Fission and Related Technologies Department, Via Enrico Fermi, 45 - 00044 Frascati (Rome) ITALY

E-mail: emanuele.castagna@enea.it

Abstract. The change of the electronic density of metallic Pd due to the hydride formation and to the build-up of the double layer, rising at the metal-dielectric interface when an electric field is applied, is involved in the variation of the metal dielectric function. A model including also metal surface roughness has been developed to take into account such modifications.

1. Introduction

The dissolution of hydrogen within a metal lattice and the formation of a metal hydride greatly perturb the electrons and phonons of the host material. Several are the relevant observed effects:

- The generally observed expansion of the lattice, often including a change in the crystal structure, involves a modification of the symmetry of the states and a reduction of the band width
- The attractive potential of the protons affects those metal wave-functions which have a finite density at the H site and leads to the so called metal hydrogen bonding band below the metal d-band
- The additional electron brought by the H atoms into the unit cell produces a shift of the Fermi level
- H-H interactions leads new features in the lower portion of the electron density of states.

One can affirm that the *1s* electron bonded with the hydrogen ion enters into *s* and *d* bands of the considered material, thus modifying the states density on Fermi surface and the energy bands structures itself^[1].

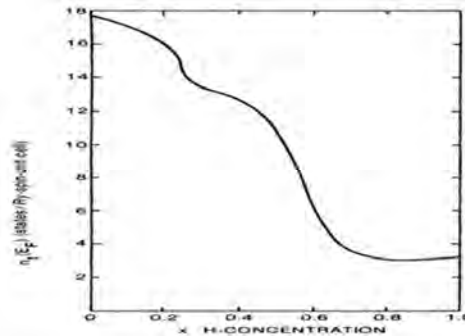


Fig. 1 - Total Density of States at the Fermi level plotted versus hydrogen concentration in Pd.

In Ref. [2] the total density of states (DOS) of palladium versus hydrogen concentration is shown, expressed for unit cell, spin and Rydberg (1 Rydberg, R_y , ~ 13.6 eV).

To estimate the electrons concentration n_e at Fermi energy for pure Pd and for $\text{PdH}_{x=1}$ we have to integrate the DOS with respect to such energy.

By considering that the volume of the unit cell in the reciprocal lattice is

$$V_{cell} = \frac{a^3}{4} \quad (1)$$

Where a is the lattice parameter, we can write for n_e the expression:

$$n_e \approx \frac{2DOS \cdot KT}{Ry} \frac{1}{V_{cell}} \quad (2)$$

Where K is the Boltzmann constant and T is the room temperature. By assuming a lattice parameter of 0.348 nm for pure Pd and of 0.406 nm for $\text{PdH}_{x=1}$ we obtain $n_{ePd} = 6.5 \cdot 10^{21} \text{ cm}^{-3}$ and $n_{ePdH_{x=1}} = 6.8 \cdot 10^{20} \text{ cm}^{-3}$. As expected, the electron concentration at Fermi energy strongly decreases in palladium hydride.

2. Electrochemical Surface Model

In the considered system, an electrochemical interphase has to be taken into account, as the hydrogen is introduced into metal lattice via electrolysis by a cathodic polarization of the metal.

The chemical interface is characterized by the presence of a strong electric field.

Recently, techniques based on the resonant excitation of surface plasmons (SPR) have been developed in order to study the effect of the electrochemical double layer electric charges redistribution on the thin metallic film dielectric properties^[3].

Substantially, the application of a electric potential modifies the dielectric properties near the metal-liquid interphase, and consequently the SPR signal is modified.

It has been demonstrated that the Helmholtz double layer formation deeply influences the SPR answer.

A model has been developed to take into account such modifications^[4].

Several effects, rising at a metal-dielectric interface when an electric field is applied, are involved in the angular shift of the SPR. In particular, the electronic density variations due to double layer and to the hydride formation are taken into account.

Modification in Palladium real and imaginary dielectric function components after deuterium solubilisation in metal lattice are shown in Fig.2 e Fig.3

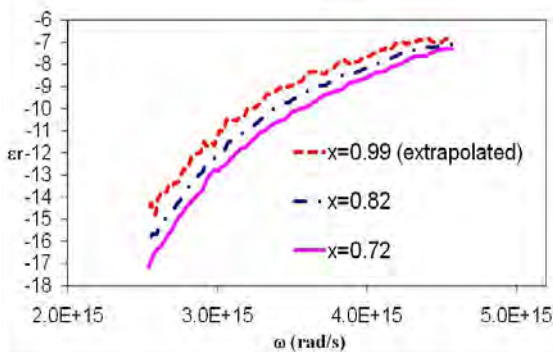


Fig.2 - Dielectric function real component, palladium

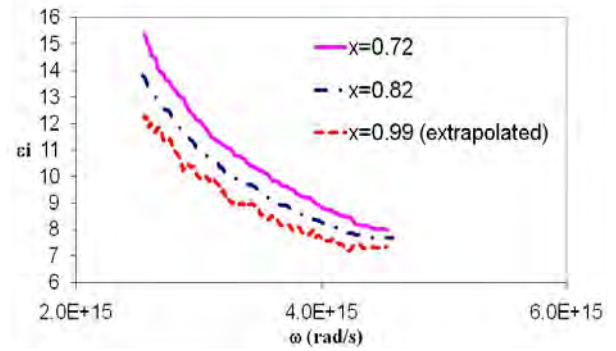


Fig.3 - Dielectric function imaginary component, palladium hydride.

Surface charge density σ , which can be calculated by the Stern's theory^[4], by varying the electronic configuration of the material, affected dielectric function value too^[5].

The dielectric function variation $\Delta\epsilon_{PdH_x}$ related to surface charge density is

$$\Delta\epsilon_{PdH_x} = \left(\epsilon_{x_{free}} - 1 \right) \frac{\Delta Ne \sigma_{PdH_x}}{Ne_{PdH_x}} \quad (3)$$

Where $\epsilon_{x_{free}}$ is palladium hydride dielectric function free electrons contribute, Ne_{PdH_x} is the free electrons concentration in palladium hydride bulk and $\Delta Ne \sigma_{PdH_x}$ is the free electrons excess on its surface, defined as:

$$\Delta Ne \sigma_{PdH_{0.99}} = \frac{\sigma^m}{q \cdot d} \quad (4)$$

Where q is the electron electric charge modulus and d the electric field penetration inside metal, defined in c.g.s. units as^[6]

$$d = \frac{c}{\sqrt{8\pi\mu_{0Pd}\rho_{PdH_{0.99}}^{-1}}} \quad (5)$$

Where c is light velocity in vacuum, $\rho_{PdH_{0.99}} \approx 5 \cdot 10^{-5} \Omega cm$ is palladium hydride samples resistivity and $\mu_{0Pd} = 1$ is palladium magnetic permeability.

The total surface palladium hydride dielectric function in electrochemical condition ϵ_{PdH_xTOT} can be expressed as:

$$\epsilon_{PdH_xTOT} = \epsilon_{PdH_x} + \Delta\epsilon_{PdH_x} \quad (6)$$

Where ϵ_{PdH_x} is palladium hydride dielectric function if no excess of charge is on the metal surface, i.e. no electrochemical processes are running.

In Fig.4 and Fig.5 the profile of PdH_x dielectric function real and imaginary components versus angular frequency is presented, in the range of validity of the proposed approximation. Also the total dielectric function, obtained taking into account the presence of an excess of electric charges due to electrochemical operating conditions is shown. As expected, the presence of surface charge density makes the material to acquire a more metallic behaviour.

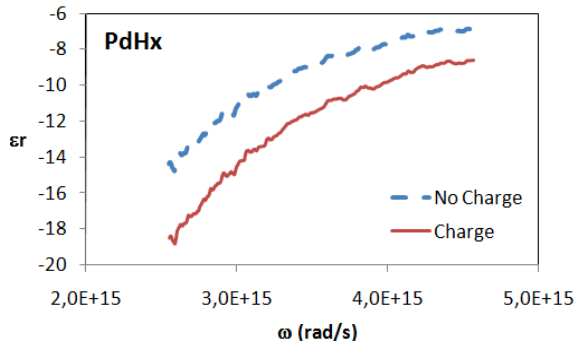


Fig.4 - Dielectric function real component, palladium hydride under cathodic polarization.

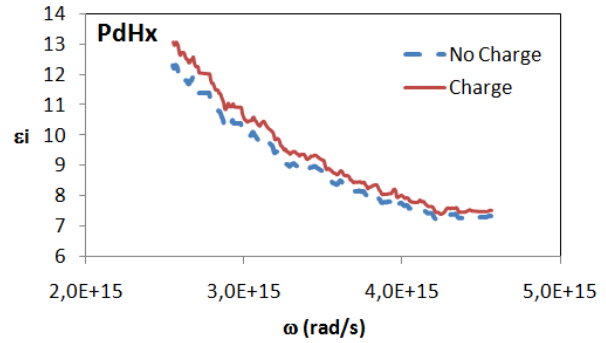


Fig.5 - Dielectric function imaginary component, palladium hydride under cathodic polarization.

Surface Plasmons resonance could give rise to a huge local field enhancement, due to a focusing effect: a broad e.m. wave is confined in a surface. Enhancement of about 10^2 factor could be obtained in this classical calculation. Using appropriate structures and quantum mechanical computation the enhancement factor could be equal to several magnitude orders. No matching condition results to be possible between light lines and surface plasmon dispersion curve at an air-Pd interface: the matching condition can not be satisfied on smooth surface, because the interaction between photons and plasmons can not simultaneously satisfy the energy and momentum conservation^[7]. It is possible to obtain s.p. excitation both using a corrugation lattice or by corrugating the metal surface itself: such a corrugation increases the surface parallel component of the laser beam wave vector, making thus possible the coincidence with s.p. wave vector^[7].

As Pd cathode are chemically etched before electrolysis, their surface is quite rough, with roughness parameters highly depending both from etching procedure and starting material properties. In Fig.6 and Fig.7 Atomic Force Microscope (AFM) three-dimensional images of two Pd etched samples are shown. The differences in surface morphology are quite evident.

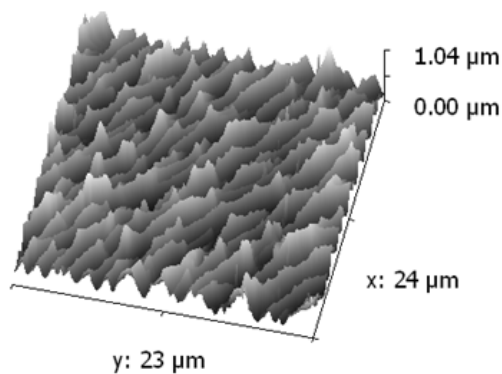


Fig.6 - Dielectric function real component, palladium hydride under cathodic polarization.

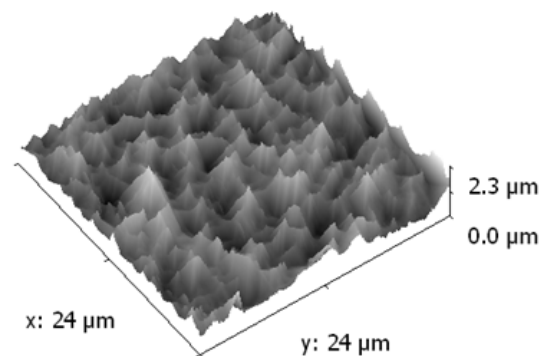


Fig.7 - Dielectric function real component, palladium hydride under cathodic polarization.

3. References

- [1] J. Zbasnik et al., *The Electronic Structure of Beta-Phase Palladium Hydride*, Z. Phys.B, vol.23, pp.15, 1976.
- [2] D.A. Papaconstantopoulos et Al., Coherent-potential-approximation calculations for PdHx, Physical Review B, vol.18, n. 6, pp.2784-2791, 1978.
- [3] J.E. Garland et al., *Surface plasmon resonance transients at an electrochemical interface: time resolved measurements using a bicell photodiode*, Analitica Chimica Acta 475, 47-58; 2003.
- [4] Vladimir Lioubimov et al., *Effect of Varying electric potential on surface-plasmon resonance sensing*, Applied Optics, Vol.43, No.17, p. 3426, 2004.
- [5] J. McIntyre, Electrochemical modulation spectroscopy, Surf. Sci. 37, 658–682 ,1973.
- [6] Born, E. Wolf, Principles of optics, Pergamon Press, 1982.
- [7] Heinz Raether, *Surface Plasmons on Smooth and Rough Surfaces and on Gratings*, Springer-Verlag Berlin Heidelberg, 1988.
- [8] J. Isidorsson et al., Optical Properties of MgH2 measured in situ by ellipsometry and spectrophotometry, Phys. Rev. B 68, 115112, 2003.

The Role of Cathode's Surface Properties in the Electrochemical Deuterium Loading of Pd Foils

F. Sarto, E. Castagna, S. Lecci, M. Sansovini and V. Violante RdA

*ENEA, Frascati Research Centre, Technical Unit for Nuclear Fusion
Via Enrico Fermi, 45 - 00044 Frascati (Rome) ITALY*

E-mail: francesca.sarto@enea.it

Abstract. Recent experimental evidences clearly indicate that the reproducibility of excess heat production is correlated with the cathode surface properties. To support the results, a theoretical frame has been also developed, that suggests that a relevant role in the excess heat production is played by the electro-dynamics processes at the cathode interface. In particular, one of the mechanisms involved is the enhancement and spatial localization of the electro-magnetic field at the metal/electrolyte interface, promoted by proper surface roughness and morphology.

A further point to be considered is the dynamic character of the metal/electrolyte interface during electrochemical deuterium loading, that derives from the coupling between the different interface characteristics. Surface reconstruction of the metallic cathode is expected to happen, due to corrosion-deposition mechanisms, D/H transport, stress relaxation and defect production, and so on. All these mechanisms both affect and are affected by the surface properties, such as the morphology of the metal/electrolyte interface, the metallurgical and crystal structure of the cathode and the presence of contaminants.

1. Introduction

In the last years, an increasing amount of experimental evidences has been reported, pointing out the correlation between the material properties of the palladium cathodes used in the Fleischmann and Pons (F&P) excess heat experiments and the reproducibility of the effect [1-3]. Replication of calorimetric results in different laboratories was achieved according to the fact that the cathodes had undergone the same manufacturing process and were belonging to the same commercial Pd lot [4]. Some cathodes features have been preliminarily identified to be relevant to the occurrence of the effect, in particular the polycrystalline structure and the surface morphology on micrometer scales.

Recently, a systematic study has been carried out by the authors, aimed to characterize the surface properties of the cathodes and to correlate them with the excess heat occurrence [3]. The results supported the preliminary observations, showing further evidence of the dependence of the anomalous heat effect on the crystallographic orientation, impurity contamination and microscopic features of the cathodes' surface. As concerning this last observation, an extended characterization of the surface morphology at the microscopic scale have been carried out by Atomic Force Microscopy (AFM) [2]. This study was also inspired by a theoretical frame suggesting that electro-dynamical effects (plasmons excitation) could be involved the excess heat production of F&P experiments [5,6].

Based on these recent experimental results and considerations, in this article we analyze some possible scenarios through which the microscopic surface morphology of the Pd cathodes could affect the electric field distribution at the metal/electrolyte interface during the electrochemical deuteride formation.

2. Experimental methods

The Pd samples used as cathodes in the electrolysis experiments were obtained from different commercial lots of pure Pd, having nominal purity above 99.95%. They have been processed by

mechanical, thermal and chemical treatments, well described elsewhere [3], in order to reduce foil thickness and to improve metallurgical properties and surface morphology. The typical manufacturing procedure consists in the following steps: 1) cold rolling of the raw 1 mm thick material to produce foils thinner than 50 microns; 2) annealing at temperatures ranging from 800 to 900°C for about 1 hour, to relax defects and induce re-crystallization into a proper polycrystalline structure, optimized for achieving maximum deuterium loading; wet chemical etching by nitric acid and aqua regia, to remove impurities and native oxide, and to produce a specific surface roughening.

Atomic Force Microscopy was used to investigate the surface morphology of the samples. AFM gives a direct measurement of the tri-dimensional (3-D) surface height profile. For each sample, several images have been taken at different points on the surface, excluding grain boundaries. Details of the AFM instrument used can be found elsewhere [2]. To make easier the comparison between different samples, the images were acquired on the same length scale (typically $24 \times 24 \mu\text{m}^2$) and with the same number of pixels (typically 257×257). Scanning of the same sample zone on different scale was also performed, in order to select the magnification factor more convenient to observe the surface features of typical samples.

The height profiles of the investigated samples were generally characterized by random fluctuations superimposed on periodic or quasi-periodic patterns. These surface features are hard to recognize in direct space, but can be effectively revealed in reciprocal space of the spatial frequencies (k_x, k_y), by computing the Power Spectral Density (PSD) of the height profile, that provides a decomposition of the surface profile into its spatial wavelength. Although the computation of the PSD is a quite common practice in isotropic random surface characterization, because of the anisotropic texture of our samples, we have defined a dedicated set of (1-D) PSD functions, which were more appropriate to extract the more relevant patterns embedded in the surface profiles, without missing the information relative to surface anisotropy. Details of image processing and analysis can be found in previous publication [2].

3. Results and discussion

It's well known that nano-metric surface features of a metal/dielectric interface can induce collective oscillations of the free electron gas (surface plasmon polaritons (SPP) or localized surface plasmons (LSP)), which can be associated to strong amplification of the local electromagnetic field [7].

The electromagnetic (EM) field can be enhanced close to a metal-dielectric interface via the excitation of surface plasmon (SP) modes. Surface roughness and isolated surface features make it possible the coupling of a EM field source with the SP modes, because they provide additional wave-vector to the source EM field that is necessary to fulfill the required momentum conservation. Thus, the role of the surface morphology in the electric field enhancement is played by the wave-vector content of the surface morphology. The Power Spectral Density is just a tool to quantify such a "wave-vector content" of the height profile, since it represents the distribution of the intensity of the sinusoidal components of the surface morphology. The correlation between the shape and intensity of the PSD curves and the anomalous thermal behavior of the Pd cathodes, observed in ref. [2], supports this scenario.

SPP modes can be excited on rough metal surfaces by electromagnetic radiation of suitable frequency and polarization to fulfill simultaneously energy and momentum conservation laws. In the specific case of a plane wave of wavelength λ impinging on a sinusoidal corrugated metal surface of wave-vector \mathbf{G} , this condition implies that

$$\mathbf{G} = \mathbf{K}_{sp} - \mathbf{K}_i \quad (1)$$

where \mathbf{K}_{sp} is the wave-vector of the SP mode given by

$$\mathbf{K}_{sp} = (2\pi/\lambda)^2 \text{Real}(\epsilon_m / (\epsilon_m + \epsilon_d)) \quad (2)$$

where \mathbf{K}_i is the projection of the incident wave-vector into the surface plane, ϵ_m is the metal dielectric constant and ϵ_d is the dielectric constant of the adjacent dielectric medium (see for example, ref. [7] pag.8).

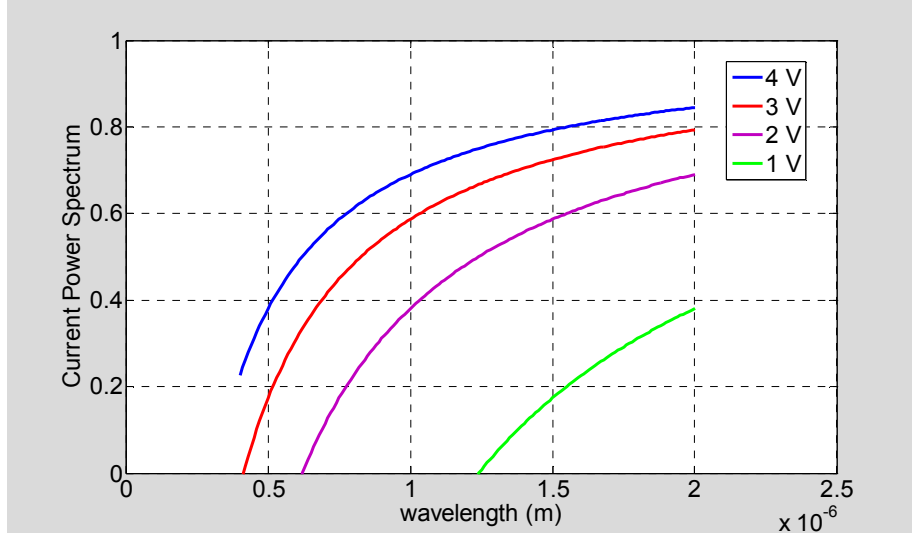


Fig. 1 Power Spectrum of the DC Current fluctuations at the interface of a DC polarized tunnel junction; different colored lines refers to different values of the DC polarizing voltage.

Typical experiments have been performed by using laser radiation to excite surface plasmons modes confined on the surface of thin metal films during electrolysis [8]. Electrochemical F&P experiments have been also carried out, in which laser irradiation of the metallic cathode was performed during deuterium loading [9]. Anyway, most of the F&P-type electrolytic experiments do not usually employ external sources of electromagnetic radiation, because they operate under direct current (DC) control.

An interesting case that presents some similarities with the typical situation occurring in the F&P experiments is the SPP excitation by microstructures on tunnel metal/insulator (or metal/semiconductor) rough junctions [10]. The effect was well known from the literature since more than 30 years ago and it consisted in the observation of light emission by tunnel junctions DC polarized, when the metal/dielectric interface presented a rough morphology. A DC bias voltage across a tunnel junction causes a DC tunnel current to flow across the dielectric barrier. Although this current is continuous, its time dependent fluctuations have a frequency spectrum ($C(\omega)$) extending from DC to a cutoff frequency (ω_c); then, such time fluctuations can drive SPP modes. In ref. [10] the tunnel current spectrum and cutoff frequency were reported:

$$C(\omega) = \frac{eV}{2\pi R_0} \left(1 - \frac{\hbar\omega}{eV}\right). \quad (3)$$

where e is the electron charge, R_0 is the DC junction resistance, \hbar is the Planck's constant V is the DC voltage across the junction and $\omega_c = eV/\hbar$.

In a typical F&P experiment we could depict the double layer zone at the metal/electrolyte interface as the equivalent of the metal/dielectric interface of a tunnel junction. Under the DC current flow across the junction, the SPP modes localized at the metal interface can be excited by the time dependent fluctuations of the electric current. The frequency spectrum of the fluctuations depends on the particular type of noise by which they are produced: in the case of the tunnel junctions described above it was assumed to be that typical of "shot" noise, due to the discrete nature of the electrons flow, which has been shown in fig. 1; in the case of an electrolysis experiment different sources of noise can be imagined to be involved, such as "thermal noise" or "bubble noise".

Once a driving EM field is available to excite SPP, the amplitude and frequency spectrum of the SPP field depends on the coupling between the source spectrum and the characteristic modes of the rough surface. The linear theory [11] offers a simple approach to compute the total field enhancement due to SPP.

We have followed this approach in order to get an approximate estimate of how much the SPP effect can be relevant to the surface morphology of our investigated samples.

In the following section, we briefly illustrate the linear method and its main assumptions and we report the results of the calculations of the electric field enhancement relative to the surface profiles of the cathodes measured by AFM technique.

3.1 The linear model

The surface profile z of the metallic cathode is described as the superposition of several sinusoidal diffraction gratings [11]:

$$z = \zeta(x, y) = \sum_{\vec{G}} \zeta_G e^{i\vec{G} \cdot \vec{R}} \quad (3)$$

where \mathbf{R} is the position vector of Cartesian coordinates (x, y) , the average value of the profile is zero (i.e. $\langle \zeta(x, y) \rangle = 0$), \mathbf{G} is the wave vectors of the surface profile, belonging to the reciprocal space of the Cartesian plane.

Under the hypothesis of “small roughness“, (i.e. $\sigma \ll \lambda$, where $\sigma = [\langle \zeta^2(x, y) \rangle]^{1/2}$ is the surface roughness and λ is the wavelength of the electromagnetic field) the first order approximation can be assumed to be valid, in which the electromagnetic field scattered by a surface having the specific profile $\zeta(x, y)$ of eq. (1) is reduced to the linear superposition of many fields, each scattered by a sinusoidal diffraction grating characterized by an amplitude ζ_G of eq. (1).

Consequently, SPP modes can be excited on the rough metal surface if eq. (1) and eq. (2) are fulfilled, being \mathbf{G} the wave vectors of the surface profile defined by eq. (3) and $|\mathbf{K}_i| = (2\pi/\lambda) \cos(\theta_i)$, where θ_i is the incidence angle of the electromagnetic radiation.

In the same hypothesis, it can be shown that the SPP excitation probability (ΔR_{sp}) is given by:

$$\Delta R_{sp} = (2\pi/\lambda) 4 \cos(\theta_i) \int PSD(\mathbf{G}) \Phi(\mathbf{G}, \theta_i, \epsilon_m, \epsilon_d) \delta(|\mathbf{G}|^2 - |\mathbf{K}_{sp} - \mathbf{K}_i|^2) d\mathbf{G} \quad (4)$$

where $PSD(\mathbf{G})$ is the power spectrum of the surface profile; $\Phi(\mathbf{G}, \theta_i, \epsilon_m, \epsilon_d)$ is a factor that does not depend on the surface profile; $\delta(x)$ is the Dirac δ function, whose effect in the integration of eq. (4) is to reduce the integration domain to the ensemble of wave-vectors \mathbf{G} which fulfill the matching conditions stated by eq. (1) and (2).

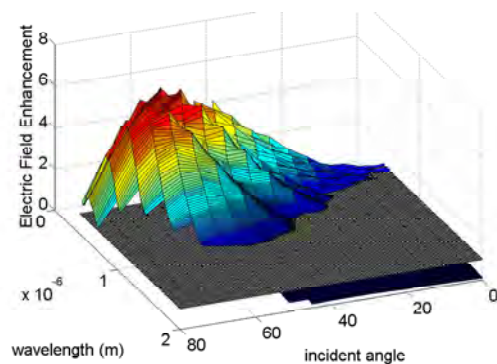
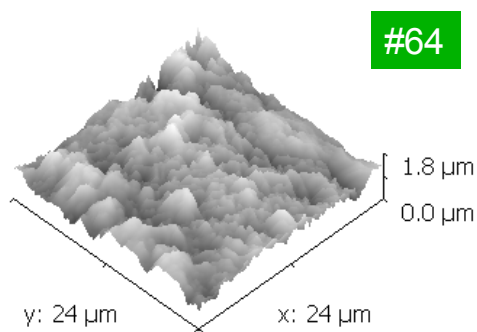
The electric field associated to the SPP charge oscillation is enhanced because of its spatial confinement close to the interface. The enhancement ratio ($|E_{sp}|^2/|E_{inc}|^2$) is given by [12]

$$|E_{sp}|^2/|E_{inc}|^2 = \cos(\theta_i) \Psi(\lambda, \epsilon_m, \epsilon_d) \Delta R_{sp} \quad (5)$$

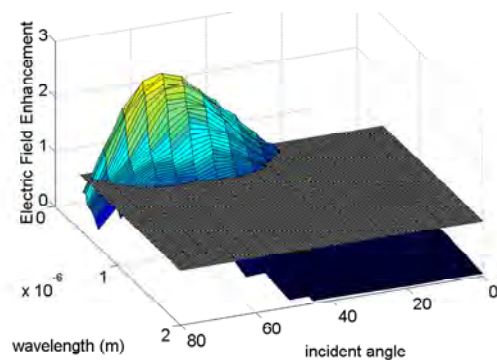
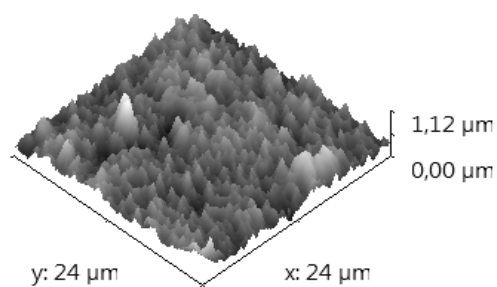
where $\Psi(\lambda, \epsilon_m, \epsilon_d)$ is a factor that does depend only on the dielectric constant of the metal and of the adjacent dielectric and on the wavelength.

3.2 Computation results

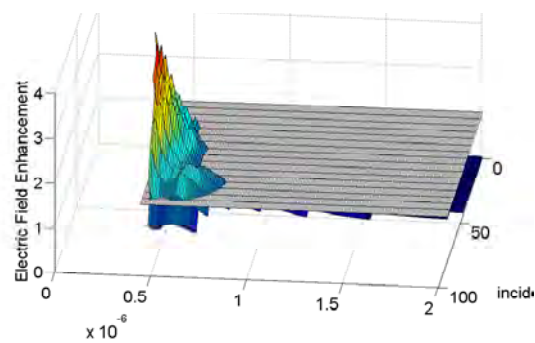
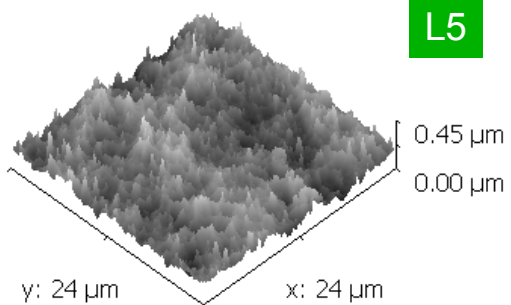
The surfaces of the Pd cathodes used in F&P experiments have been scanned by atomic force microscopy and the collected data have been numerically processed to compute the corresponding bi-dimensional PSD spectra. Such PSD spectra were used to calculate the enhancement ratio of the electric field,



ET-US3-05



L5



L46

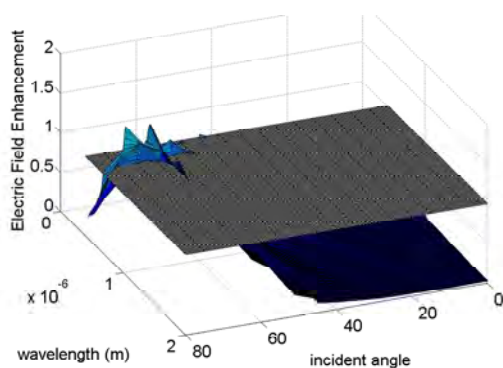
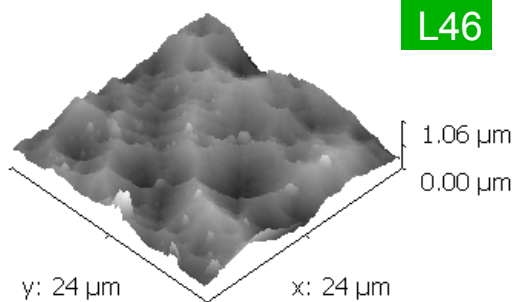


Fig. 2 AFM images (left) and corresponding electric field enhancement (right), computed according to the linear approach described in the text, of samples which gave anomalous excess heat production; the horizontal plane outlines the region in which the enhancement factor is higher than 1.

according to the linear theory described above, by means of eq. (4) and eq. (5), in which the values of the dielectric constants of the metal and the dielectric have been taken from ref. [13] and set to be 1, for the PdH and the electrolyte, respectively.

In fig. 2 the AFM images (left) and the results of the calculations of the enhancement ratio (right), relative to a set of samples which showed anomalous thermal behavior, have been reported; it can be observed that this ratio is higher than 1, in a selected domain of the incident electromagnetic radiation parameters (angle and wavelength). In particular, in going from the top to the bottom of the figure, the measured amount of excess heat produced by the corresponding samples decreased, as expected on the basis of the results reported in ref. [2], showing a correlation between the amount and reproducibility of excess heat and the maximum value of the PSD spectrum (see table I of ref. [2]). In addition, it can be noted that the max values of the field enhancement correspond to values of the incident wavelength in the range of a fraction of to a few microns.

4. Conclusions

The surface morphology of Pd cathodes used in electrochemical experiments has been characterized by atomic force microscopy, after electrochemical loading of deuterium. The electric field enhancement due to surface plasmons excitation has been estimated on the basis of the AFM images and the Power Spectral Density function, following the approach of the first order perturbation theory of the interaction of electromagnetic radiation with a random moderately rough metal surface. The results indicate that the surface morphology of the samples giving anomalous heat production can sustain SPP modes at wavelengths in the range of a fraction to some microns, thus enhancing the electric field at the metal/electrolyte interface up to a factor ten.

5. References

- [1] F. Sarto, E. Castagna, M. Sansovini, S. Lecci, V. Violante RdA, D.L. Knies, K.S. Grabowski, G.K. Hubler, "Material Science on Pd-D System to Study the Occurrence of Excess Power", Proc. of *14th Int. Conf. Condensed Matter Nuclear Science (ICCF14)*, Washington D.C., USA (2008).
- [2] F. Sarto, E. Castagna, M. Sansovini, S. Lecci, V. Violante, D. L. Knies, K. S. Grabowski, G. K. Hubler, "Electrode Surface Morphology Characterization by Atomic Force Microscopy", Proc. of *14th Int. Conf. Condensed Matter Nuclear Science (ICCF14)*, Washington D.C., USA (2008).
- [3] E. Castagna, M. Sansovini, S. Lecci, A. Rufoloni, F. Sarto, V. Violante, D. L. Knies, K. S. Grabowski, G. K. Hubler, M. McKubre, F. Tanzella, "Metallurgical characterization of Pd electrodes employed in calorimetric experiments under electrochemical deuterium loading", Proc. of *14th Int. Conf. Condensed Matter Nuclear Science (ICCF14)*, Washington D.C., USA (2008).
- [4] M. McKubre, F. Tanzella, I. Dardik, A. El Boher, T. Zilov, E. Greenspan, C. Sibilina and V. Violante, "Replication of Condensed Matter Heat Production", *American Chemical Society National Meeting Chicago 2007, Conference Proceedings* (Oxford University Press).
- [5] V. Violante, *Fusion Technology* **35**, 361-368 (1999);
- [6] V. Violante, A. Torre, G. Selvaggi, G. H. Miley, *Fusion Technology* **39**, 266-281(2001)
- [7] H. Raether, in "*Surface Plasmons on Smooth and Sough Surfaces and on Gratings*", edited by Springer-Verlag, Berlin Heidelberg New York London Paris Tokyo (1986)
- [8] V. Lioubimov, A. Kolomenskii, A. Merzhin, D. V. Nanopoulos and H. A. Schuessler, *Applied Optics* **43**, 3426-3432 (2004).
- [9] D. Letts and D. Cravens, "Laser stimulation of deuterated palladium: Past and present, Proc. *10th Int. Conf. on Cold Fusion (ICCF10)*, Cambridge, Massachusetts, USA (2003), p. 159.
- [10] R. W. Rendell and D. J. Scalapino, *Phys. Rev.* **B 24**, 3276 (1981)
- [11] A. Marvin, F. Toigo, V. Celli, *Phys. Rev.* **B 11**, 2777 (1975)
- [12] W. H. Weber, G. W. Ford, *Optics Lett.* **6**, 122 (1981)
- [13] E. Castagna, S. Lecci, M. Sansovini, F. Sarto, V. Violante RdA, "Interaction of the Electromagnetic Radiation with the Surface of Palladium Hydride Cathodes", in this Proceedings.

Concentration polarization in Pd-based membranes for hydrogen separation: modeling and simulation

A. Caravella¹, G. Barbieri^{2*}, E. Drioli^{2,3}

¹Research Institute for Innovation in Sustainable Chemistry – National Institute of Advanced Industrial Science and Technology, ISC-AIST, Central 5, 1-1-1 Higashi, Tsukuba (Ibaraki) 305-8565, Japan.

²Institute on Membrane Technology – National Research Council, ITM-CNR, c/o University of Calabria, Via P. Bucci, Cubo 17C, 87036, Rende (CS), Italy.

³Department of Chemical Engineering and Materials – University of Calabria, Via P. Bucci, Cubo 44A, 87036, Rende (CS), Italy.

*E-mail: giuseppe.barbieri@cnr.it

Abstract. In this study, a new hydrogen permeation model through Pd-based membranes is developed and used to analyze the role of the concentration polarization. According to this new model, the entire hydrogen permeation process is divided into several elementary steps: multicomponent mass transport in the feed and permeate side, adsorption and desorption on/from the membrane surface, absorption and de-absorption into/from the metal lattice, diffusion through the Pd-based bulk and multicomponent mass transport through an asymmetric multilayered porous support. Each of these steps is modeled by means of some equations whose solution provides as result the value of transmembrane flux and the hydrogen partial pressure profile through the membrane. The influence of each step is evaluated as a function of several operating conditions (membrane thickness, temperature, fluid-dynamic conditions, hydrogen partial pressure on feed and permeate side). The effect of the mass transfer in the feed and permeate side is evaluated in terms of concentration polarization effect by defining an opportune coefficient and analyzing its behaviour in different conditions. As results, the investigation shows that the influence of the polarization can be appreciable even for not so thin membranes and provides some “polarization maps”, which are diagrams where the polarization level (in terms of CPC) can be directly visualized and simply estimated once knowing the external operating conditions. Hence, these maps can be very useful in order to predict better the membrane performances and, consequently, reduce the uncertainty during the design step of the membrane modules.

1. Introduction

It is well-known that Pd-based membranes show an infinite selectivity towards hydrogen with respect to the other chemical species. Thus, they are usually employed in processes requiring the selective removal of hydrogen from the reactive zone. In order to optimize their usage, in this work, the H₂ permeation and the concentration polarization phenomena are described by a complex model taking into account all the mass transfer phenomena involved in the H₂ transport through such membranes.

2. Description of the model

The schematic representation of the target system are shown in Fig. 1, where a) an SEM photo of a multilayered Pd-based membrane, b) the scheme of membrane considered here and c) the mechanism rate of each elementary step involved in the permeation, are reported. The Pd-based layer is supported by an asymmetric support characterized by several (five) layers, each one having different thicknesses and pore sizes (Table 2). The whole permeation mechanism has been divided into the following elementary steps: mass transfer in the fluid phase of the film just near the interface on retentate and permeate side; dissociative adsorption and recombinative desorption on the Pd-based layer; atomic hydrogen transition from Pd-alloy surface to Pd-alloy bulk and vice-versa (named “Surface-to-Bulk” and “Bulk-to-Surface”, respectively); diffusion of atomic hydrogen through the Pd-alloy bulk; mass transfer in the multilayered porous support. The detailed mathematical form of such a model can be found elsewhere [1].

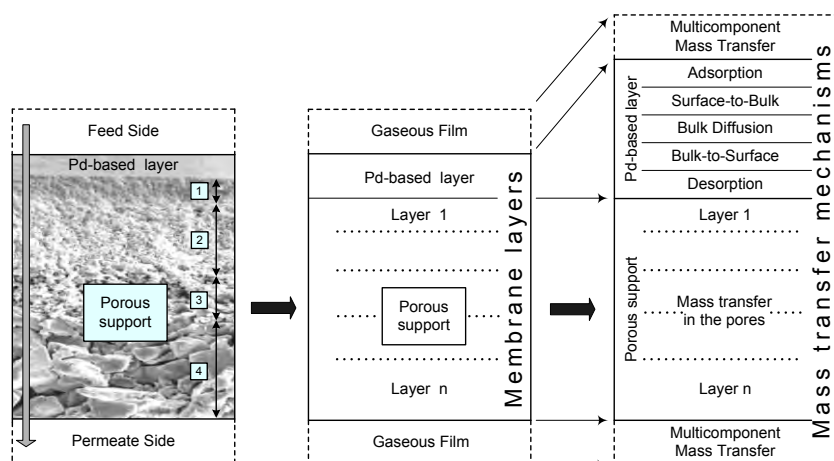


Fig. 1. – Scheme of the multilayered membrane considered and mass transfer mechanisms of all the elementary steps involved in the permeation process.

Table 1. Operating conditions considered.

Side	Pressure, kPa							Reynolds' Number	Total flow rate, mmol/s
	H ₂	N ₂	O ₂	CO ₂	H ₂ O	CO	Total		
Feed	600	75	75	50	50	25	875	1700 - 800	100
Permeate	100	80	20	-	-	-	200	1900 - 950	20

Temperatures, °C = {250; 300; 350; 400; 500; 600}

Table 2. Geometrical data of the Pd-alloy supported membrane considered.

Porous Support Layers	Pd-alloy layer thickness, μm = {1, 10}			Porosity, -	Tortuosity, -
	Thickness, μm	Mean pore Diameter, nm			
1	1	5			
2	50	100			
3	100	1,000		0.5	1.2
4	500	10,000			
5	850	50,000			

3. Results and discussion

Fig. 2 shows the transmembrane hydrogen partial pressure profile at different temperatures for a thickness of 1 μm. At 300°C a quite significant pressure drop is found for hydrogen profile in the upstream film. In the adsorption and desorption steps the pressure drop is low but non-negligible, whilst both “surface-to-bulk” and “bulk-to-surface” do not show any appreciable contribution. The diffusion in Pd-bulk and transport in porous support provide important pressure drops, especially in the first two porous layers, which show important resistances even if their thicknesses are very thin. The effect of external mass transfer is also appreciable in permeate side. At higher temperatures, the mass transfer influence becomes more relevant in both gaseous film and in the support, whereas the surface phenomena (adsorption and desorption) and diffusion in the Pd-based layer got to be more rapid steps.

In Fig. 3, the overall resulting flux is plotted together with the step-limited fluxes (dashed-line), each of which is calculated considering a certain step as the only rate-determining one and all the others at the equilibrium. The adsorption and desorption steps have a decreasing slope larger than diffusion, but

obviously in both cases the temperature has a positive effect on the flux. The slopes related to these steps are proportional to their respective activation energies. On the contrary, the curve of the transport in the film on the retentate side is almost flat and the one relative to the transport in the support has even an increasing profile. This means that this last step is not favoured by the temperature and, hence, that Knudsen-type transport prevails on the Poiseuille-type one and on ordinary diffusion, the Knudsen diffusivity decreasing with temperature.

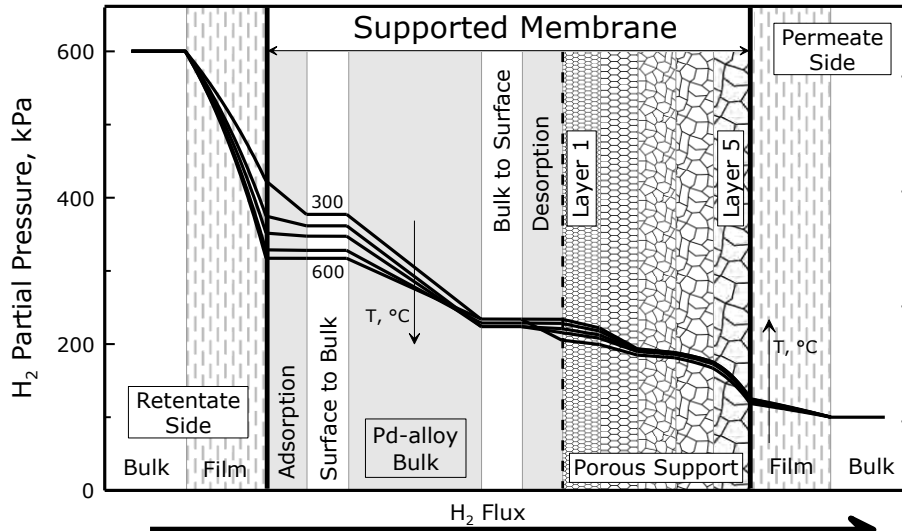


Fig. 2. – Calculated hydrogen partial pressure profiles through the membrane and in the fluid phases adjacent to the membrane for different temperatures in laminar regime at a membrane thickness of 1 μm. The lengths of the permeation steps are not to scale.

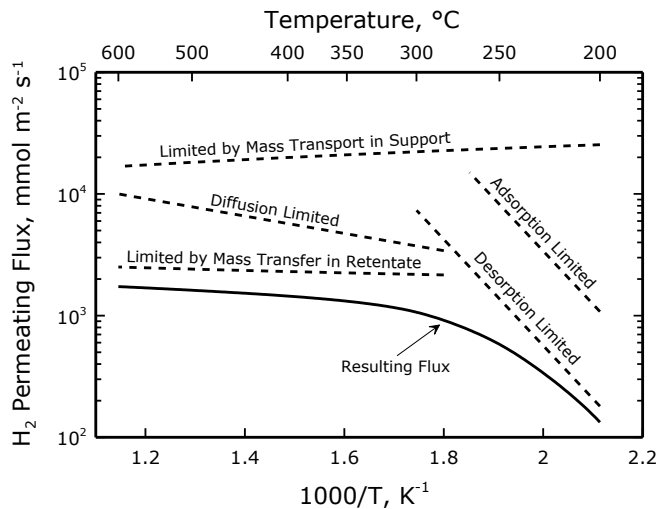


Fig. 3. – Step-limited fluxes (dashed lines) and overall resulting flux (continuous line) as functions of temperature in laminar conditions. Membrane thickness of 1 μm.

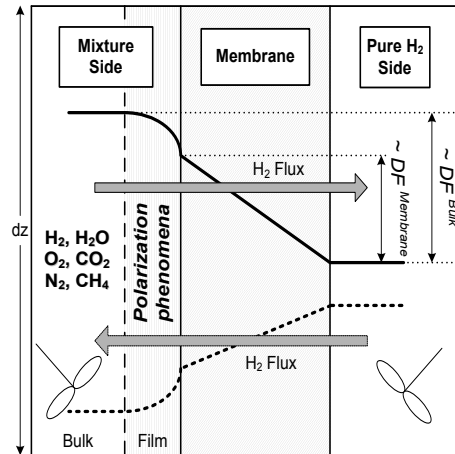


Fig. 4. – Sketch of the system to analyze the concentration polarization phenomenon.

Fig. 4 shows the system considered to analyze the concentration polarization phenomena. In this case, the presence of the support has not taken into account in order to focus the attention on the external mass transfer. Furthermore, in the permeate side, only hydrogen is considered to be present. The Concentration Polarization Coefficient (CPC) is defined as shown in Eq. 1, where the value of the flux is calculated by means of the model described above. Further details about its definition are reported elsewhere [2]. The so-defined CPC approaches to zero when the polarization is negligible and to one in the opposite case.

$$CPC = 1 - \frac{H_2 \text{ Flux (ElementarySteps)}}{\pi^{Membrane} \Delta \sqrt{P_{H_2}}^{Bulk}} \quad (1)$$

Fig. 5 shows the effect of the operating conditions on *CPC* is analyzed in details, developing some “polarization maps” useful to determine the level of the polarization in some situations. The influence of six different system variables is considered: 1) temperature, 2) membrane thickness, 3) total pressure of mixture, 4) total pressure in pure H₂ side, 5) hydrogen molar fraction in mixture. In the first plot, considering molar fractions from one to zero, the level of polarization on one hand tends to increase for the larger composition of other components, but, on the other hand, it tends to decrease for the smaller hydrogen permeating flux. Until the first tendency prevails, the curve is convex, whilst it is concave in the opposite situation. This inflection point can be found in correspondence of a higher abscissa as lower temperature is considered. At high contents of hydrogen in mixture (close to unitary value), the polarization tends to be zero, even for high fluxes, because of the absence of other species creating a composition gradient. The other two plots show similar behaviour as regards the effect of mixture and pure H₂ side pressure.

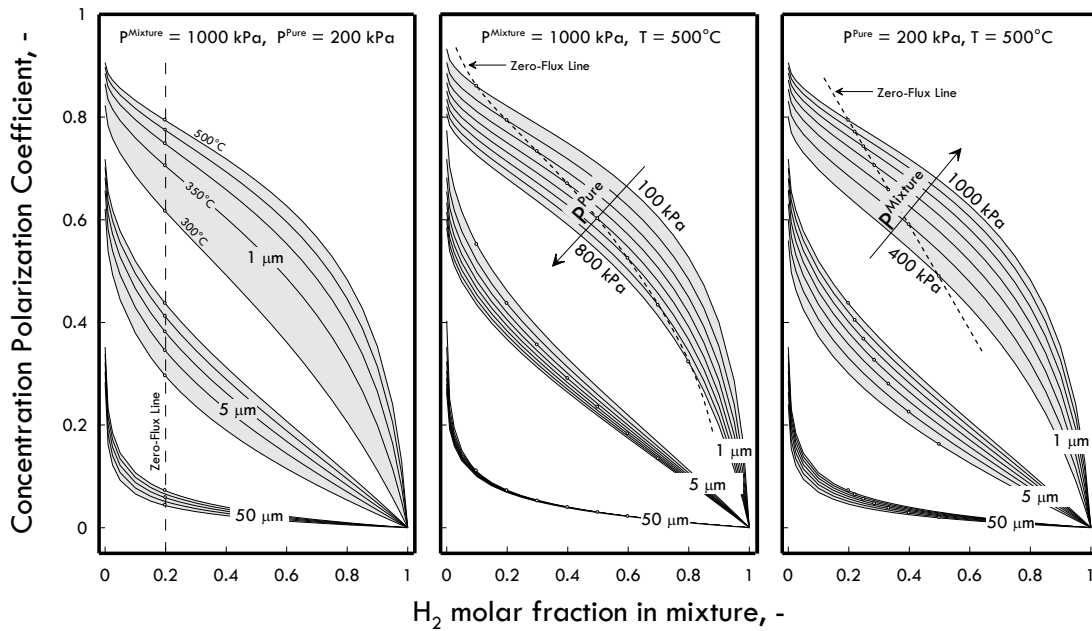


Fig. 5. – Polarization maps in different operating conditions (temperature, feed and permeate pressure).

4. Conclusions

The hydrogen permeation through supported Pd-alloy membranes is described by means of a detailed model involving several elementary steps, among which the external mass transfer on feed and permeate side. After describing this model, the concentration polarization phenomenon is studied in terms of an opportune coefficient, which is evaluated as a function of several operating conditions. This analysis is summarized in some “polarization maps”, which can be built once the fluid-dynamic conditions and the membrane permeation parameters are known. These diagrams can be very useful to avoid as much as possible the inefficiencies of a membrane separation process by minimizing the uncertainty in the step of the membrane-based system design.

References

- [1] Caravella A., Barbieri G. and Drioli E., 2008. *Chem. Eng. Sci.*, **63**: 2149-2160.
- [2] Caravella A., Barbieri G. and Drioli E., 2009. *Sep. Pur. Tech.*, **66**: 613-624.

Electrical resistivity and linear expansion of a hydrogenated Pd/Ag permeator tube

A. Santucci^{1,2}, F. Borgognoni¹ and S. Tosti¹

¹ENEA, Dip. FPN, C.R. ENEA Frascati, Via E. Fermi 45, Frascati (RM) I-00044, Italy.

²Dept. of Chemical Science and Technology, Via della Ricerca Scientifica, 00133 Roma, Italy.

E-mail: alessia.santucci@enea.it

Abstract. The Pd-Ag-H system is of particular importance with respect to the separation and purification of the hydrogen gas. Pd-Ag alloys have high selectivity for hydrogen gas permeation and thus are suitable for manufacturing hydrogen selective membranes. Accordingly, among the technological properties many authors have studied the electrical resistivity and linear expansion of the Pd-Ag-H system, but no data are available in a wide range of temperature and hydrogen pressure. During this activity, the solubility, the linear expansion, the resistivity and the permeability of a Pd/Ag (with Ag 25% wt) permeator tube has been measured in both hydrogenated and non-hydrogenated conditions. The experiments have been carried out in a temperature and in a lumen hydrogen partial pressure range of 50-400 °C and 0-400 kPa, respectively.

1. Introduction

Hydrogen selective membranes are important for technological processes such as separation of hydrogen from gaseous mixtures, purification of hydrogen for fuel cell applications and chemical reactions in membrane reactor [1]: they are even used in hydrogen isotope storage, extracting, purification and separation processes [2].

Palladium membranes have been development for ultra-pure hydrogen separation because of their high selectivity. However, they have problem of hydrogen embrittlement, a phenomena in which dissolved hydrogen tends to cause an elongation of the metal lattice as a consequence of the hydrogen uploading thus leading to the membrane failure after repeated thermal and hydrogenation cycles. In order to avoid the embrittlement, alloying of Pd with group IB metals such as silver is generally made. Another advantage of alloying is that the mechanical strength in pure hydrogen atmosphere is higher [3]. In general, a Pd-membrane becomes brittle after certain cycles of $\alpha \rightarrow \beta$ transformations due to the accompanied lattice expansion. For example in palladium-silver alloys, the lattice has already been expanded by the silver atoms, and the Pd-Ag lattice is less influenced by hydrogen uploading and then less brittle than the pure Pd lattice [4]. An optimal value of the hydrogen permeation rate is reached for a silver content around 25 wt. %.

During this activity the electrical resistivity and the linear expansion of a 25 % wt Pd/Ag permeator tube has been measured under both hydrogenated and non-hydrogenated conditions. The experimental measurements have been carried out in a temperature and in a lumen hydrogen partial pressure range of 50-400°C and 0-400 kPa, respectively.

2. Experimental

A Pd-Ag tube of wall thickness 200 μm and length of 12.8 cm has been produced by extrusion. The hydrogen permeator has been obtained by joining via brazing at the ends of the Pd-Ag tube a stainless steel tube and a steel plug. The obtained permeator was assembled inside a membrane module in a finger like configuration (Fig. 1): the membrane tube was gas tight fixed to one end of the module in order to permit its elongation and contraction due to the hydrogenation cycles. In this way, any mechanical stress on the thin wall tube was avoided. In the finger like configuration the feed stream entered the membrane lumen via a stainless steel tube inserted inside the Pd-Ag membrane.

The experimental apparatus used to characterize the membrane is shown in the scheme of figure 2. A mass flow controller sends the hydrogen feed stream into the lumen side, while a nitrogen flux of 500 $\text{N cm}^3 \text{ min}^{-1}$ is used as sweep gas in the shell side. The membrane module is heated by a direct current supply system; the elongation and the resistivity are measured with an optical microscope and a multimeter, respectively.

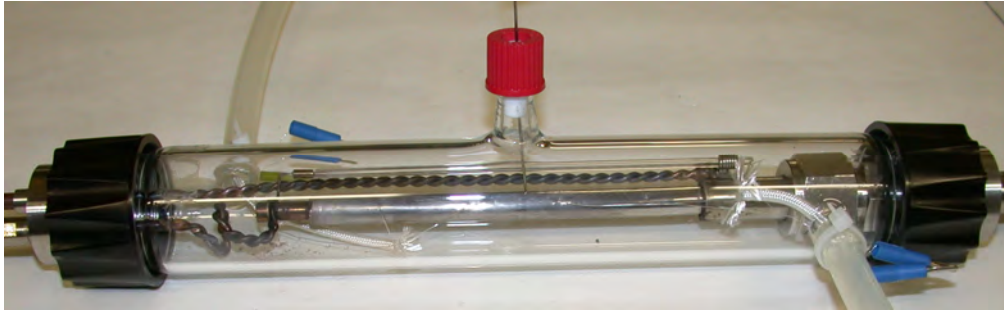


Fig. 1. - Pd-Ag permeator tube.

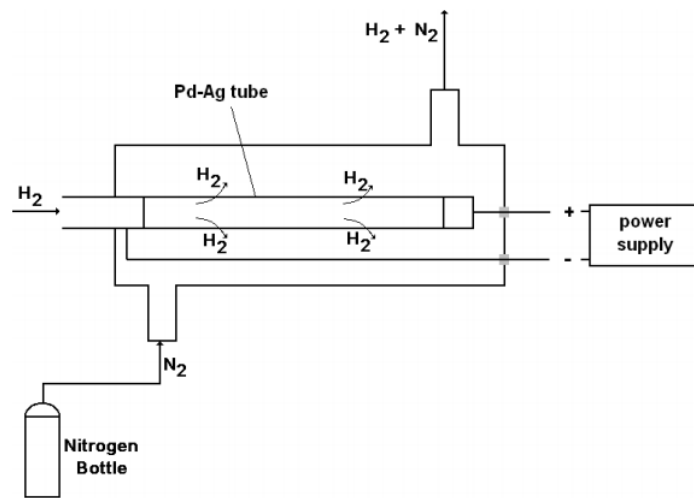


Fig. 2. - Scheme of the experimental apparatus.

3. Results and discussion

3.1 Hydrogen Solubility

The hydrogen solubility, in the investigated operative conditions, has been assessed by applying the Sieverts' law:

$$S = K_s p^{0.5} \quad (1)$$

where K_s [5] is the solubility constant:

$$K_s = 0.182 \exp\left(\frac{19598}{RT}\right) \quad (\text{mol m}^{-3} \text{ Pa}^{0.5}) \quad (2)$$

and p the hydrogen partial pressure into the metal lattice, assessed as the arithmetic mean between the hydrogen partial pressure in the lumen side ($p_{\text{H}_2, \text{lumen}}$) and the hydrogen partial pressure in the shell side ($p_{\text{H}_2, \text{shell}}$).

In figure 3 the effects of temperature and hydrogen lumen pressure on the solubility are reported. By increasing the temperature, the hydrogen solubility decreases for all the hydrogen lumen pressures investigated, although the solubility gap between the various lumen pressures is much larger at low temperature. Particularly, these results show that the hydrogen loading into the Pd-Ag membrane significantly occurs below 150-200 °C where the hydrogen permeation is quantitatively modest as reported below (section 3.4).

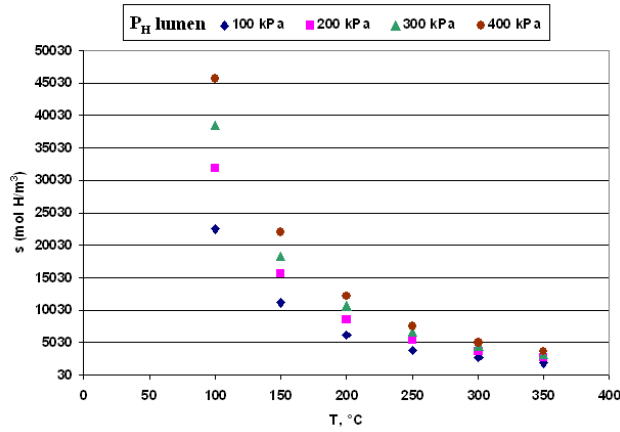


Fig. 3. - Hydrogen solubility in Pd-Ag membrane versus temperature for different hydrogen lumen pressure.

3.2 Linear Expansion

To measure the linear expansion of the membrane a metal cylinder sustained in a pyrex tube has been attached on the free-end of the membrane: the metal cylinder was able to move inside the pyrex tube. In this way the movement of the metal cylinder followed the elongation of the membrane, while the pyrex tube having negligible thermal expansion coefficient has been used as a reference. An optical microscope fixed on the described experimental apparatus has been used to measure the displacement of the metal cylinder, i.e. the linear expansion of the membrane. Figure 4 represents a particular of the experimental set-up viewed by the microscope.

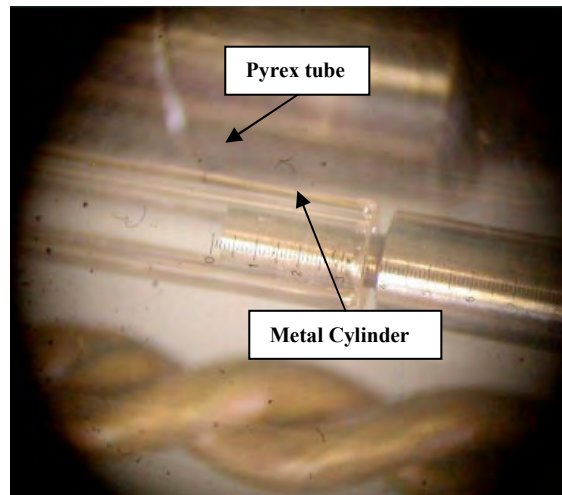


Fig. 4. - Particular of the membrane viewed by the optical microscope.

Figure 5 described the linear expansion ε of the Pd-Ag membrane in different conditions.

$$\varepsilon = \frac{\Delta l}{l_0} \quad (3)$$

Where Δl is the difference between the final and the initial (l_0) length of the membrane tube.

In particular the linear expansion can be considered by the sum of two contributions: the thermal and the hydrogen uploading contribution. In order to put into evidence these contributions, in figure 5 the grey points are referring to the linear expansion measured under nitrogen atmosphere (hydrogen partial pressure equal to zero), that means only thermal contribution, while the other points are related to the total linear elongation (both thermal and loading contribution).

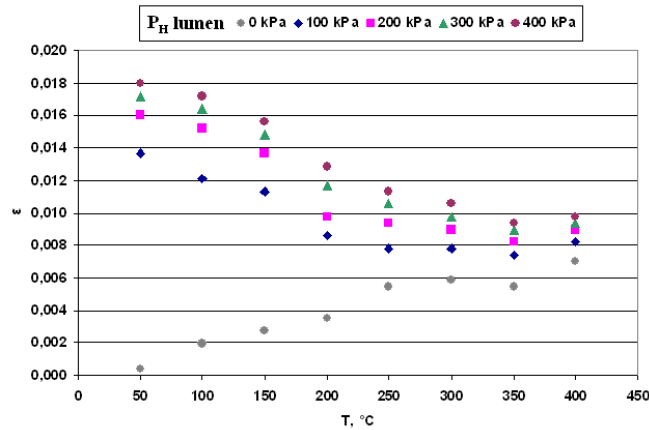


Fig. 5. - Linear elongation of the Pd-Ag membrane tube in a temperature range between 50-450 °C at different lumen hydrogen partial pressures, from 0-400 kPa.

According to the literature, the linear expansion related to the thermal contribution increases by increasing the temperature: in particular at 50 °C the elongation is almost zero, while at 400 °C it is about 0,7%. Under the hydrogenated conditions, the linear elongation decreases by increasing the temperature for each lumen hydrogen partial pressure investigated. Even in this case the gap between the measurements at low temperature is larger than the gap related to the measurements at high temperatures, in particular at 400 °C the gap is almost negligible.

This phenomenon agrees with the assessed hydrogen solubility values: at low temperature maximum hydrogen solubility (uploading) corresponds to the maximum elongation.

3.3 Electrical Resistivity

The electrical resistivity is a Pd-Ag property alloy affected by the hydrogen loading: measurements of this parameter have been carried out under different hydrogenation conditions and temperatures. A DC current has been applied to the ends of the membrane tube through a power supply (HP 6573A) while a multimeter (HP 3458A) has been used in order to measure the voltage in different points of the membrane. The electrical resistivity has been then assessed via the Ohm law.

The connection between the multimeter and the membrane has been realized with Pt wires attached on the membrane surface (Fig. 6).

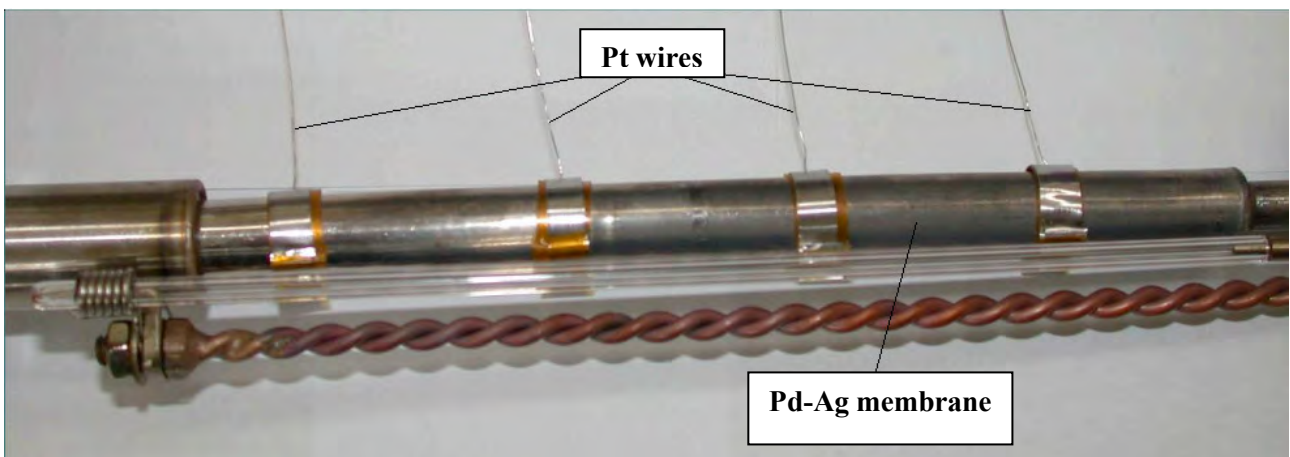


Fig. 6. - Particular of the palladium wires attached onto the membrane surface for the resistivity measures.

Figure 7 reports the values of the Pd-Ag electrical resistivity in the range temperature between 100 and 400 °C, for different lumen hydrogen partial pressure. Especially, for a given temperature the electrical resistivity values change slightly for the hydrogenated material.

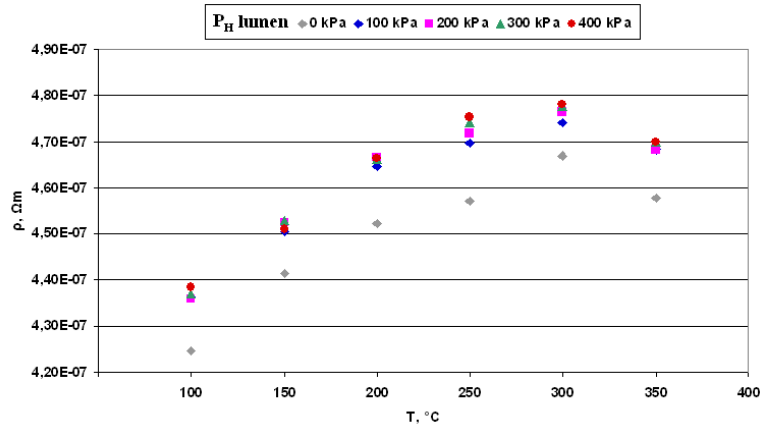


Fig. 7. - Pd-Ag electrical resistivity in temperature range between 100-400 °C for different lumen partial hydrogen pressure.

3.4 Hydrogen Permeability

Permeation tests of the Pd-Ag tube have been carried out under controlled temperature and transmembrane differential pressure conditions: pure hydrogen was fed in the lumen side in the pressure range between 100-400 kPa, while the hydrogen permeated through the membrane was collected in the shell side at atmospheric pressure by a nitrogen stream of $500 \text{ Ncm}^3 \text{ min}^{-1}$, the investigated temperature range was 100-400 °C.

The hydrogen permeability through the Pd-Ag membrane was calculated by the formula:

$$Pe = \frac{Fd}{(\sqrt{p_{H_2, \text{lumen}}} - \sqrt{p_{H_2, \text{shell}}})A} \quad (4)$$

where Pe is the hydrogen permeability ($\text{mol m}^{-1} \text{ s}^{-1} \text{ Pa}^{0.5}$), F is the hydrogen permeating flow rate (mol s^{-1}), d the wall tube thickness (m), $p_{H_2, \text{lumen}}$ the hydrogen pressure inside the membrane (Pa), $p_{H_2, \text{shell}}$ the hydrogen partial pressure in the shell side (Pa), and A is the permeation surface area (m^2).

The permeability data have been collected according to the Arrhenius law:

$$Pe = Pe_0 \exp\left(\frac{-E_a}{RT}\right) \quad (5)$$

where Pe is the hydrogen permeability, Pe_0 the pre-exponential factor, E_a the activation energy, R the gas constant and T the absolute temperature.

By considering the hydrogen permeability values reported in figure 8, there are some considerations to underline. In fact, the activation energy (that can be visualized by the slope of the permeability values line) presents two different values, as reported in table 1. In particular the activation energy at low temperature is higher than the activation energy at high temperature thus meaning that significant hydrogen permeation through the membrane can occur only at temperature over 200 °C. As another important result, despite of the large membrane wall thickness (200 μm) the high hydrogen permeation fluxes measured demonstrated the applicability of such a membrane tube for separating ultra pure hydrogen in laboratory and industrial processes.

Table 1. Hydrogen permeability through Pd-Ag.

Temperature, K	Pressure, kPa	Pe_0 , $\text{mol m}^{-1} \text{ s}^{-1} \text{ Pa}^{-0.5}$	E_a , kJ mol^{-1}
373-423	100-400	3.38×10^{-5}	19.7
474-673	100-400	3.43×10^{-7}	3.4

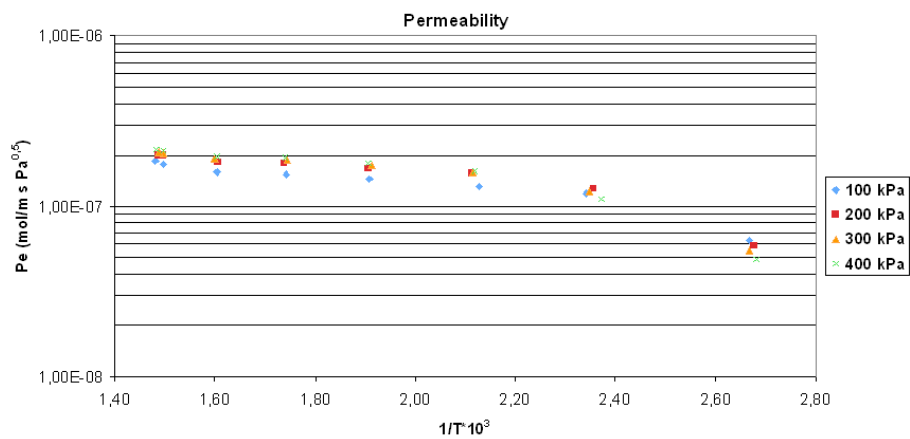


Fig. 8. - Hydrogen permeability through Pd-Ag.

4. References

- [1] A. Petersen, C.S. Nielsen and S.L. Jorgensen, *Catalysis Today* **46** 193 (1998).
- [2] S. Wieland, T. Melin, A. Lamm, *Chem. Eng. Sci.* **57** 1571 (2002).
- [3] D. Fort and I. R. Harris, *J. of Less-Common Metals* **41** 313 (1975).
- [4] O. Hatlevik, et al., *Separ. Purif. Technol.* Doi:10.1016/j.seppur.2009.10.020
- [5] E. Serra, M. Kemail, A. Perujo, and D.K. Ross, *Metallurgical and materials transactions* **29A**, 1023 (1998)

Synthesis and characterization of $\text{BaCe}_{1-x}\text{Y}_x\text{O}_{3-\delta}$ protonic conductor

A. Santucci^{1,2}, V. Esposito², S. Licoccia² and E. Traversa²

¹ENEA, Dip. FPN, C.R. ENEA Frascati, Via E. Fermi 45, Frascati (RM) I-00044, Italy.

²Dept. of Chemical Science and Technology, Via della Ricerca Scientifica, 00133 Roma, Italy.

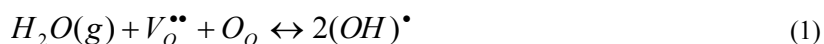
E-mail: alessia.santucci@enea.it

Abstract. In recent years, doped perovskites such as barium cerates (BaCeO_3), strontium cerates (SrCeO_3) and barium zirconates (BaZrO_3) have been studied as ceramic proton conductors for several technological applications: protonic membranes, hydrogen separation, catalytic support and solid oxides fuel cell components. Among those compounds, yttrium doped barium cerates have the best performances in terms of protonic conductivity at lowest temperature.

In this activity, doped BCY oxide powders was synthesized via novel soft chemical route. The method is based on the formation of a metallorganic xero-gel at room temperature. The structural phase of powders and dense pellets were analyzed using X-ray diffraction (XRD), while the morphology was investigated by field emission scanning electron microscope (FE-SEM). Electrochemical impedance spectroscopy (EIS) measures were performed on dense pellet under synthetic air flux and hydrogen atmosphere in a temperature range between 200-750 °C with a frequency range of 10mHz-10MHz.

1. Introduction

Several oxide with the ABO_3 perovskite structure have shown protonic conductivity between 500-1000 °C [1-4]. These oxides are doped on the B-site by lower valence elements, typically a trivalent rare-earth metal (M), to introduce oxygen defects. The exposure of the doped material to humid atmospheres results in the formation and incorporation of hydroxyl groups to oxygen vacancies followed by the migration of the lone protons by hopping between oxide ions via a Grotthus-like mechanism. The formation of the hydroxyl defects may be written using Kröger-Vink notation (1).



According to Irvine et al. [5] the most technologically promising moderate-temperature proton conductors are those perovskites based upon the cerates or zirconates of barium doped with yttria or lanthanide oxides. Barium cerates generally exhibit the highest proton conductivities; but these materials are unstable at high temperature in the presence of CO_2 and steam, while the zirconates are much more resistant to degradation. The zirconates do not sinter easily, and the highest conductivities are only obtained when sintering occurs at or approaching 1700 °C, in fact the highest conductivities are influenced by some form of phase transformation or segregation or, as suggested by Snijkers et al. by a slow kinetic process of water absorption. The stability of doped BaCeO_3 is improved by the introduction of Zr at the B site, but the typical sintering temperature of Zr-replaced BaCeO_3 is still above 1550 °C. However, very significant differences exist in reported values of conductivities, which seem to be related to the synthesis procedure.

In general, the BaCeO_3 powders were synthesized by the conventional solid state reaction, in which oxide precursors are repetitively milled and calcined at high temperature. However, these conventional ceramic powder processes can have several drawbacks such as relatively large and varied grain sizes, inhomogeneities in the chemical composition [6,7], and of course high cost related to the high sintering temperature.

In this view, one possible approach to overcome these difficulties is to employ a soft chemical process which has the following advantages: lower sintering temperature, shorter processing time, and the possibility of obtaining high purity and ultrafine powders. Essentially, these methods can produce nanocrystalline materials, which appear to be a promising approach to combine the superior characteristics of these nanoscaled ceramics with the proton conducting properties of doped perovskite [8].

In this activity a new synthesis route for the $\text{BaCe}_{0.8}\text{Y}_{0.2}\text{O}_{3-\delta}$ (BCY20) called sol gel combustion, has been investigated. The method is based on the autocombustion reaction of the gel resulting from a novel sol gel process. The technique involves three different steps: the preparation of a stable and homogenous sol, the formation of a gel, and the

combustion of the so-formed gel. This synthesis procedure allows us to obtain the requisite phase for BCY20 at lower temperature and dense pellet with high conductivity.

2. Experimental

The novel synthesis method consists of the formation of a gel of the nitrate solution using agar powder. The metal nitrates were dissolved in water in the correct stoichiometric ratio, and then the solution was heated to 80 °C. At that temperature the agar powder (20% of weight) was added. Agar is a polysaccharide and it works as a gelling agent. The dissolution process of the agar in the solution was completed by several minutes of stirring at 80 °C. The agar induced the complete gelation at 4 °C in a few minutes. During cooling the viscosity increased rapidly and there was the formation of a self-sustaining gel, then the gel was burned in a reactor. The reactor had two different holes that allowed the continuous flux of air that was essential to ensure the complete combustion of the gel inside. The precursor powders were ground into an agate mortar and calcined at the appropriate temperature in order to have a pure perovskite phase. Then the powders were uniaxially pressed at 4 tons in order to form a 3 mm diameter pellet. The discs were sintered in air in a tubular furnace. The sintering temperature required for the agar method was 1450 °C. After sintering the surface of the pellet were polished and stripped off with a thermal etching.

The precursor powder obtained with the agar method was characterized by simultaneous thermogravimetric-differential thermal analysis (TG/DTA) performed on a NETZSCH STA 409. The sample was held in a platinum holder under air atmosphere. The phase composition was analyzed by X-ray diffraction (XRD). X-ray diffraction data were acquired using a Philips X'PertMPD using $\text{CuK}\alpha$ radiation. The phases present in the BCY20 sample at different stage of calcination were analyzed in the Bragg angle range $20^\circ < 2\theta < 85^\circ$. The microstructure of the sample was then characterized by field emission scanning electron microscopy (FE-SEM LEO 1530) after polishing and thermal etching. The densification rate has been determined with samples of 10,40 mm length and a diameter of 8,02 mm, it was sintered in a dilatometric up to 1600 °C using a constant heating rate of 5 K min^{-1} and cooled down to a room temperature with a rate of 10 K min^{-1} . The shrinkage was recorded during heating and cooling. Finally conductivity measurements on the BCY20 agar sample were performed in order to investigate the electrical property of the material. The BCY20 pellet was assembled in a cell (Fig. 1): the cell apparatus was connected with a frequency response analyzer to measure the conductivity across the electrolyte. The measurements have been performed in a frequency range between 10mHz-10MHz, and in a temperature range between 200-750 °C.

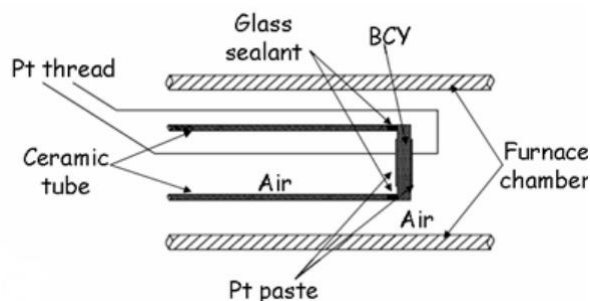


Fig. 1. – Scheme of the cell apparatus.

3. Results and discussion

3.1 TG/DTA

The powders obtained after burning the gels at 200 °C were characterized by Thermogravimetric/Differential Thermal Analysis (TG/DTA), in order to study the crystallisation process and choose the suitable temperature range for calcination. The TG (Fig. 2) revealed that the weigh loss, for a heating rate of 5 °C/min, was completed at 1150 °C with a total weigh loss less than 10%. The results showed two plateaux: between 700-800 °C and over 1200 °C. According to the DTA, from 600-700 °C, the reaction is exothermic, associated with the initial decomposition stage of the organic species involved in the gel.

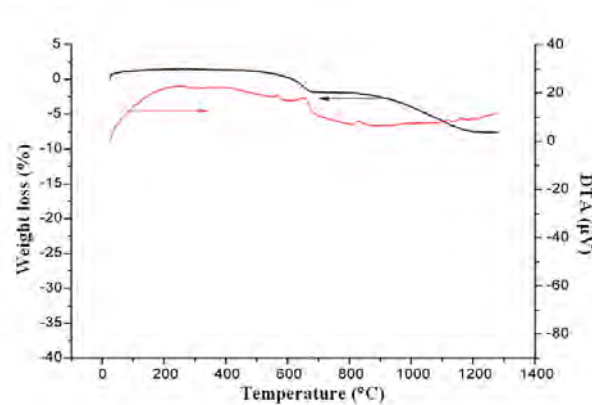


Fig. 2. – TG/DTA of the BCY 20 precursor synthesized with the agar method.

3.2 XRD Measurements

The X-ray diffraction patterns of BCY20, powder and pellet, obtained with the Agar synthesis are shown in figure 3.

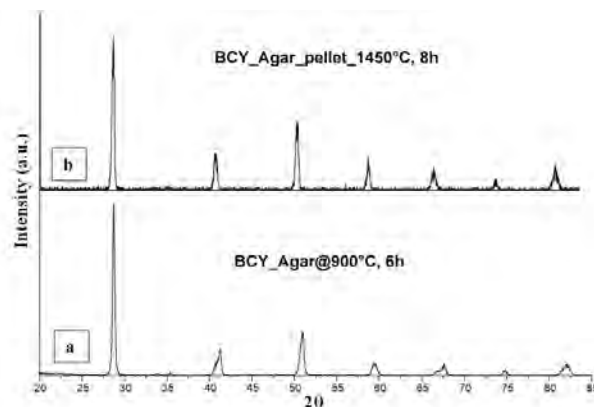


Fig. 3. - XRD patterns of the BCY20 obtained with the agar synthesis method, a) powder calcined at 900 °C for 6 h, and b) pellet sintered at 1450°C for 8 h.

The XRD reveals that, with this method, a pure perovskite phase is reached at 900 °C while, with the standard synthesis procedure, the phase was pure only when temperature approached 1100 °C.

Another relevant aspect is related to the sintered pellet: in fact, the BCY20 pellet (90% of the theoretical density) was obtained with a sintering treatment carried out at 1450 °C for 6 hours. The decrease of the sintering temperature (usually around 1600 °C) avoids the presence of secondary phases related to aggregation processes caused to barium evaporation.

3.3 Dilatometric measurements

To better understand the sintering behaviour of the BCY20 obtained with the described synthesis procedure, dilatometric measures have been performed on two BCY20 samples: one sample was prepared with the Agar synthesis method, and one sample was realized using a traditional ethylene glycol method.

Figure 4 reports the dilatometric behaviour of the two BCY20 samples. From the results it is possible to observe that in the sample prepared with the agar method the shrinkage starts between 900-1000 °C, while in the sample prepared with the EG method the shrinkage starts at 1200 °C. Another important difference in the sintering behaviour of the two samples is recorded in the temperature range between 1100-1200 °C. At that point, in fact, the sample prepared with the EG method expands and then the shrinkage starts. The different dilatometric behaviour between the two BCY20 samples has a macroscopic effect as reported in figure 5 which shows the samples after the dilatometric measurements. From that picture it is clear that both samples are cracked, but in the EG sample the cracks are more.

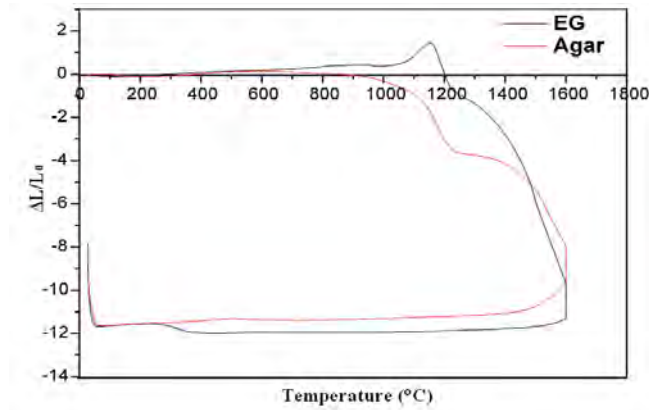


Fig. 4. - Dilatometric shrinkage of the two BCY20 samples obtained with the Agar synthesis (red line) and with the EG synthesis (black line).

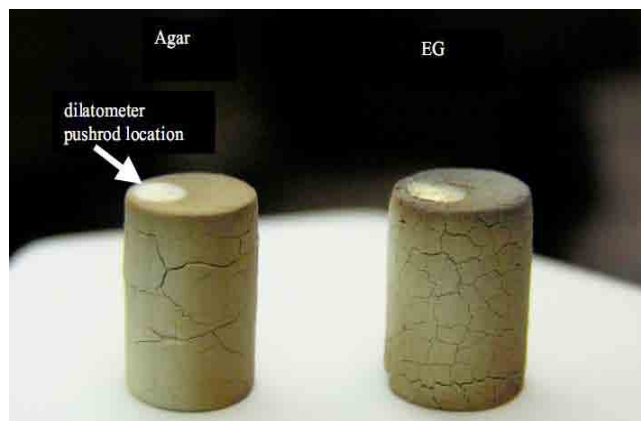


Fig. 5. - Picture of the two BCY20 samples after the dilatometric measurement.

3.4 SEM micrographs

The SEM micrographs reveal what the dilatometric measures have already shown. In fact, as figures 6 and 7 report, the BCY20 powders and pellets have a different microstructures according to the used synthesis procedures.

In particular figure 6 shows the SEM micrograph of the calcined BCY20 powder obtained with the agar method (a) and with the EG method (b), respectively. The main differences between the two BCY 20 powders are related to the dimension of the particles and to the different phases of the two powders. In fact, the particles obtained with the agar synthesis route are smaller than the other while the different shapes of the powders reveal different phases. In figure 7 the surface micrographs of the two BCY20 sintered pellet are reported. Even in this case, a difference in the particles size is observed. In fact, in the agar sample, the average grain size is around 100 nm, while in the EG sample, the average grain size is about 1-2 μm. Also the density of the two samples is different, in particular the BCY20 pellet obtained with the agar method, sintered at 1450 °C, is more dense than the EG sample, sintered at 1600 °C.

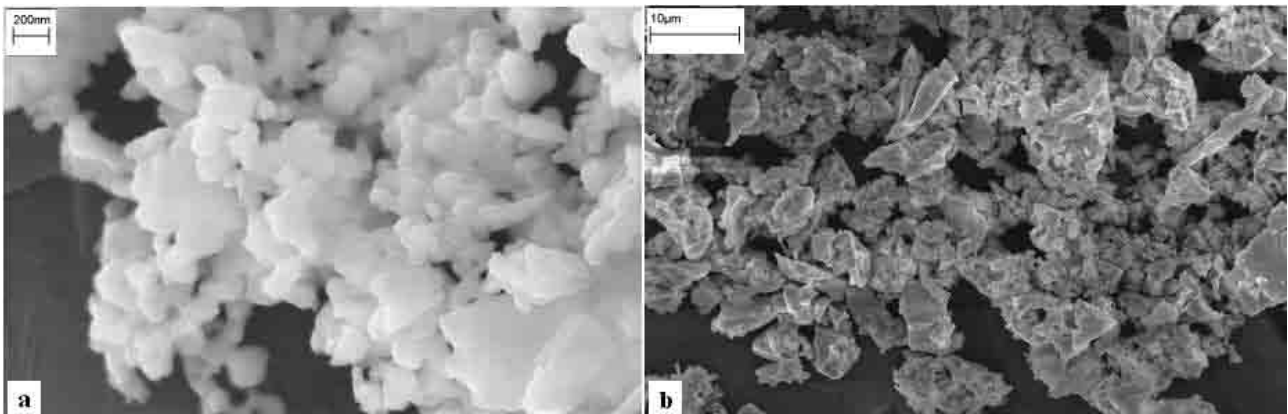


Fig. 6. - FE-SEM micrographs of the BCY20 powder, a) Agar method, b) EG method.

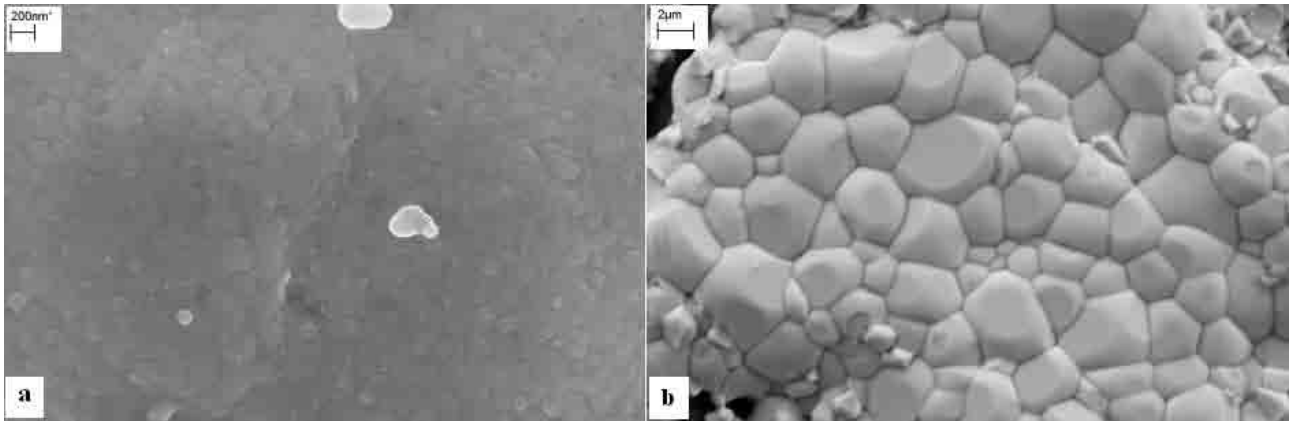


Fig. 7. - FE-SEM micrographs of the BCY20 pellet, a) Agar method, b) EG method.

3.5 Conductivity measurements

The electrolyte BCY20 pellet made with the agar method was placed into a single chamber reactor. The reactor was installed into a horizontal tube furnace and the cell was connected with a frequency response analyzer to measure the AC impedance spectra across the electrolyte. The conductivity of the perovskite sample with increasing temperature was measured and recorded in the range between 200-750 °C with steps of 25 °C intervals in air and wet hydrogen atmosphere. The activation energy of the proton conduction mechanism can be determined from an appropriate Arrhenius plot. In this way, the slope is equal to $-E/k$, where E is the activation energy and k is the Boltzmann constant. The Arrhenius plot for BCY20 is shown in figure 8. The activation energy for BCY20 is 0.40 eV, in agreement with the values reported in literature.

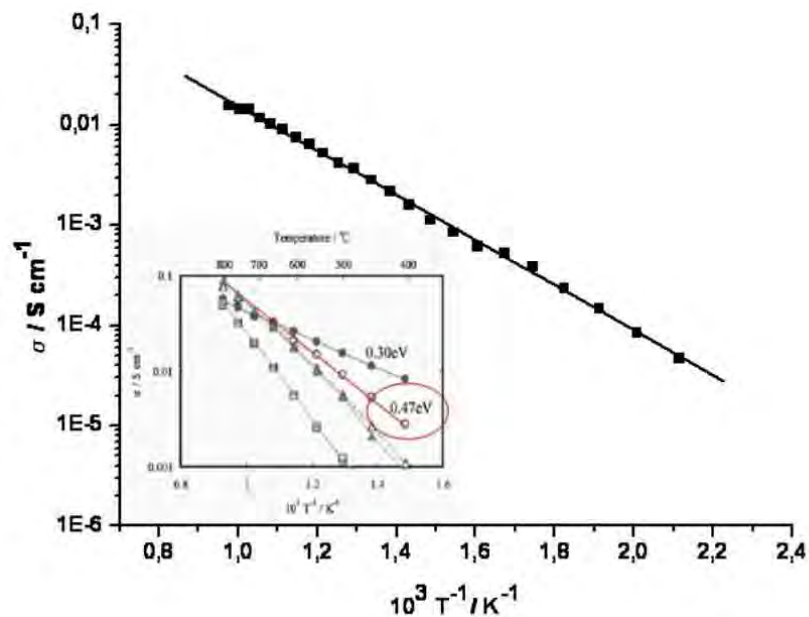


Fig. 8. - Arrhenius plot for BCY20 compared with literature data [9].

Acknowledgments

This work was supported by the Ministry of University and Research (MIUR) as part of a PRIN project. We gratefully thank Dr. Sean Bishop for the dilatometric measures.

References

- [1] Bin Zhu, Xiangrong Liu, *Electrochemistry Communications*, 2004, 6, 378.

- [2] J. Van Herle, T. Horita, T. Kawada, *Solid State Ionics*, 1996, 86, 1255.
- [3] H. Iwahara, T. Esaka, H. Uchida, N. Maeda, *Solid State Ionics*, 1981, 3-4, 359.
- [4] H. Iwahara, H. Uchida, K. Ono, K. Ogaki, *J. Electrochem. Soc.* 1988, 135, 529.
- [5] John T.S. Irvine, *Adv. Mater.* 2006, 18, 1581.
- [6] Hsin-Lung Lin, Kay-Kuang Chiang, *Journal of Non-Crystalline Solids*, 2007, 353, 1188.
- [7] J. Luo, R.J. Ball, R. Stevens, *Journal of Material Science*, 2004, 39, 235.
- [8] C. Savaniu, J.T.S. Irvine, *solid State Ionics*, 2002, 150, 295.
- [9] A. Tomita, T. Hibino, *Journal of Materials Science*, 2006, 39, 2493.

Characterization of materials by means of laser-based techniques

L. Caneve

ENEA, CR Frascati, Rome, Italy

E-mail: luisa.caneve@enea.it

Abstract. Laser-based techniques are more and more used in the field of materials processing and analysis. In particular, laser spectroscopic techniques as the Laser Induced Breakdown Spectroscopy (LIBS) and Laser Induced Fluorescence (LIF) have been applied to investigate the chemical-physical properties and the morphological structure of several kinds of materials. Some results in different fields of application are reported.

1. Introduction

The application of laser-based techniques as analytical tools in materials science is widespread and very promising by now, also due to the continuous development of the laser technology. In this work, in particular, the attention will be focused on two spectroscopic laser techniques: Laser Induced Breakdown Spectroscopy (LIBS) and Laser Induced Fluorescence (LIF).

Laser induced breakdown spectroscopy (LIBS) is an atomic emission spectroscopic technique. It is based on the spectral analysis of the radiation emitted by a plasma generated by the interaction of an intense laser radiation with a material sample. The elemental composition of the investigated sample can be determined from the analysis of the emission spectrum [1] and the element concentrations theoretically deduced [2]. LIBS is particularly suitable for rapid on-line analysis. Nowadays, LIBS has reached a mature stage for analytical applications on a wide range of materials in solid, liquid and gas phase [3]. Good results have been obtained by LIBS on surface and sublayers analysis.

The emission of radiation by luminescent materials is observed whenever an absorption of energy sufficient to activate allowed electronic transitions occurs. Laser induced fluorescence (LIF) is a molecular spectroscopy based on the interaction of the ultraviolet radiation emitted by a laser with the matter [4]. This technique, for a surface analysis, is fast, remote, non invasive and specific. Through the study of the fluorescence emission spectrum is possible to obtain information of analytical and qualitative interest [5]. Both techniques have been used in many fields of application.

2. Experimental

In the laboratory of laser applications of ENEA Frascati, LIBS and LIF experimental equipments have been developed.

2.1 LIBS apparatus

The LIBS apparatus has fully described in its general configuration elsewhere [6], here the main characteristics will be recalled. In 'Fig.1' a scheme is reported. The radiation source is a Nd:YAG laser (Handy Quanta System) working usually at the fundamental wavelength of 1064 nm and focalized by a lens on the surface of the studied sample. The plasma emissions were collected by suitable receiver optics and the optical signal was carried by an optical fiber to the entrance slit of monochromator (Jobin Yvon model TRIAX550) equipped with three different gratings.

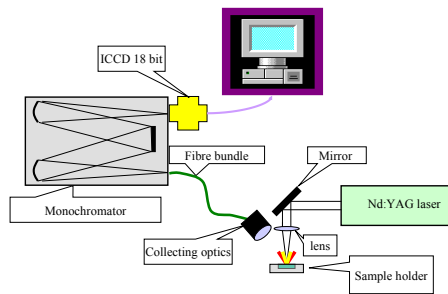


Fig. 1- Scheme of LIBS apparatus

The LIBS spectra were detected and recorded by a multichannel analyzer based on a gated ICCD, model Insta Spec IV. The experimental and acquisition parameters (energy laser, laser shots number, acquisition delay from the laser pulse, acquisition temporal gate) depend on the specific application. Stratigraphic analysis [7] with the identification of the chemical elements present at different depth is possible recording the LIBS spectra from the same point of the sample at increasing laser shots number.

Some advantages offered by LIBS make it very useful in many different applications: no sample pre-treatment is required, measurements can be performed directly in situ, in hostile environment too, on line data analysis is possible. Furthermore, LIBS is a fast spectroscopic method.

2.2 LIF apparatus

An innovative compact scanning LIF system has been developed at the ENEA of Frascati, based on a previous instrument's version [8]. The layout of the system is given in 'fig. 2'. The radiation source is a Thomson DIVA diode pulsed Nd:YAG laser, able to produce laser pulses both at 266 and 355 nm with a time duration of 10 ns at a fluence from 1 to 50mJ/cm². The main advantages of this new version are its reduced size, all the mechanical and optical elements have been installed in an aluminum box of 58×43×36 cm³ for less than 15kg, its small size and light weight that allow for an easy transfer of the system, and its operation from scaffoldings, in case of surfaces out of the current maximum range for remote operation (10 m). The spectrometer entrance is protected from the intense backscattered radiation by means of an appropriate dichroic filter. The digitized spectrum is transferred to a portable computer where a LabView program allows the user to set experimental parameters, to control data acquisition, and to perform a preliminary data analysis.

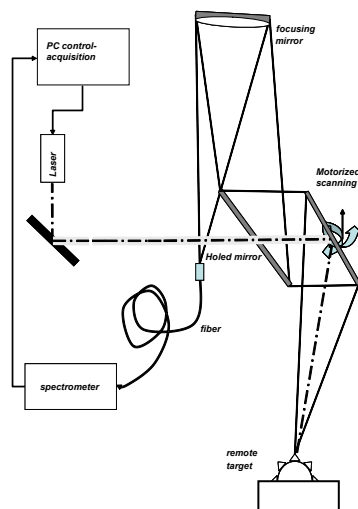


Fig. 2 – Scheme of LIF apparatus

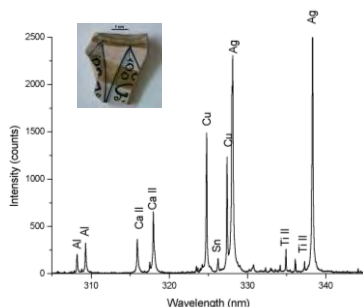


Fig. 3 - LIBS spectrum of ancient ceramic

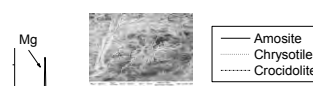


Fig. 4 - LIBS spectra of asbestos

The main advantages offered by this technique are the possibility to perform measurements in real time, in-situ without sample preparation, besides its minimum invasiveness.

3. Applications

Laser Induced Breakdown Spectroscopy and Laser Induced Fluorescence present several advantages with respect to other spectroscopic techniques and can be utilized for a variety of prompt analytical applications on different materials. Some applications will be reported on the following.

3.1 LIBS applications

LIBS has found in the Cultural Heritage preservation a fertile field of application due to its minimally invasive and only micro-destructive feature, the availability of portable instruments and the possibility of stratigraphy with on-line monitoring cleaning processes. These characteristics makes the technique suitable for qualitative and quantitative multi-elemental analyses on a large variety of samples surfaces in most different stages of preservation. Analysis of pigments [9] and different kinds of ancient materials as copper based alloys [10], ceramics [11,12] and marbles [13], for examples, has been performed by LIBS.

In ‘Fig.3’ a typical spectrum of gold lustre with silver and copper lines, emission line from Sn is coming from the underlying glaze, from a decorated Renaissance umbrian ceramic is shown.

LIBS has been successfully applied in laboratory analyses of soils and sediments, in order to trace the presence of heavy metals as pollutants [14] or to investigate sedimentation processes in natural ecosystems (Ross Sea, Antarctica) [15]. Among the environmental applications, the possibility of detecting and identifying asbestos by LIBS technique (‘Fig.4’) in samples of different kind, as for example building materials, has been demonstrated [16].

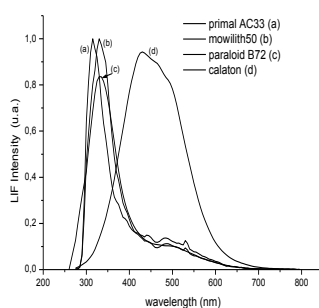


Fig. 5 - Fluorescence spectra at $\lambda_{exc} = 266\text{nm}$ of acrylic resins

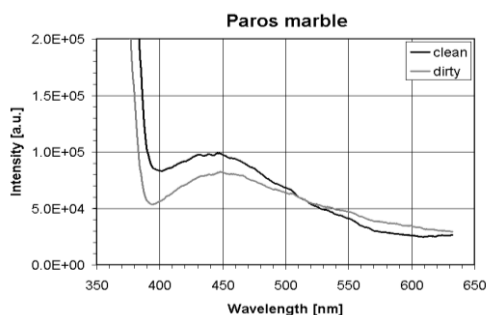


Fig. 6 – LIF spectra at $\lambda_{exc} = 355$ nm of Paros marbles clean and with crust

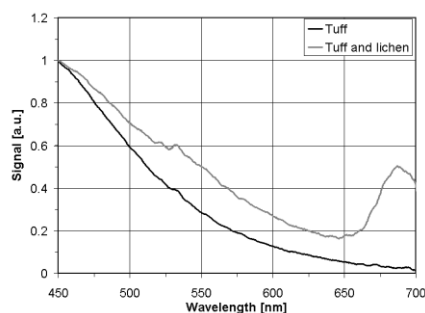


Fig. 7 – LIF spectra at $\lambda_{exc} = 355$ nm of tuff and deteriorated tuff.

The LIBS applicability in situ makes it one of the most interesting techniques to carry out remote measurements inside a tokamak vacuum chamber directly, without any removal of the internal coverings.

A recent study aimed to assess the diagnostic potentialities of the LIBS technique for the qualitative and quantitative determination of superficial contaminants deposited and/or adsorbed on the superficial coating of a tokamak reactor, has been led [17].

3.2 LIF applications

The performance of laser induced fluorescence (LIF) as a diagnostic tool for cultural heritage has been evaluated by exploiting the ENEA scanning LIF system to investigate different materials relevant in this field of application. The possibility to detect and discriminate different acrylic resins on fresco has been demonstrated both on laboratory samples and on original wall paintings by in situ measurements [18,19]. In 'Fig.5' the fluorescence spectra corresponding to four different resins are reported.

The effect of deteriorating agents on different materials has been investigated. The presence of a detrimental crust on a marble from Paros due to the external exposure has been well emphasized by the LIF signal, as can be seen in 'Fig.6'.

The detrimental effects on tuff surfaces of biodegrading agents, as fungi and lichens, has been detected by LIF allowing to observe characteristics invisible with the naked eye while avoiding to move sample from their original location. In 'Fig.7' the chlorophyll fluorescence emission at 680 nm from a deteriorated area respect to a clean one reveals the presence of a biodegradation process.

In conclusion, laser-based techniques can be used in the field of materials analysis with good results and many fields of application are possible. The experimental conditions need to be optimized according to the specific application.

Acknowledgments

All activities reported in this paper have been developed with my colleagues: F. Colao, R. Fantoni, L. Fiorani, V. Lazic, A. Palucci.

4. References

- [1] R. Wisbrun, I Schechter, R. Niessner, H. Schroeder: *SPIE* **1716** 2-14 (1992)
- [2] E. Tognoni, V. Palleschi, M. Corsi, G. Cristoforetti: *Spectrochimica Acta B* **57** 1115-1130 (2002)
- [3] J.D. Winefordner, I.B. Gornushkin, T. Correll, E. Gibb, B.W. Smith, N. Omenetto: *J. Anal. At. Spectrom.* **19** 1061-1063 (2004).
- [4] J. L. Kinsey: *Ann. Rev. Phys. Chem.* **28** 349-372 (1977)
- [5] D. Lognoli, G. Lamenti, L. Pantani, D. Tirelli, P. Tiano, L. Tomaselli: *Appl. Opt.* **41** 1780-1787 (2002)

- [6] F. Colao, R. Fantoni, V. Lazic, L. Caneve, A. Giardini, V. Spizzichino . *J. Anal. At. Spectrom.*, **19** 502-504 (2004).
- [7] D. Anglos, S. Couris, C. Fotakis: *Appl. Spectrosc.* **52** 1025-1030 (1997).
- [8] F. Colao, L. Caneve, R. Fantoni, L. Fiorani, A. Palucci: "Lasers in the Conservation of Artworks" *Proceedings of LACONA 2007, Madrid, 2007*, Marta Castillejo, Pablo Moreno, Mohamed Oujja, Roxana Radvan, Javier Ruiz Eds. (CRC Press).
- [9] M. Castillejo, M. Martin, D. Silva, T. Stratoudaki, D. Anglos, L. Burgio, R.J. Clark: *J. Mol. Struct.*, **550-551** 191-198 (2000).
- [10] L. Caneve, F. Colao, R. Fantoni, V. Spizzichino: *Appl. Phys. A*, **85** 151-157 (2006).
- [11] J.M. Anzano, M.A. Villoria, I.B. Gomushkin, B.W. Smith, J.D. Winefordner: *Can. J. An. Sc. Spec.* **47** 134-140 (2002).
- [12] V. Lazic, F. Colao, R. Fantoni, A. Palucci, V. Spizzichino, I. Borgia, B. Brunetti, A. Sgamellotti: *J. Cultural Heritage* **4** 303s-308s (2003).
- [13] P. Maravelaki-Kalaitzaki, D. Anglos, V. Kilikoglou, V. Zafirooulos: *Spectrochimica Acta B* **56** 887-903 (2001).
- [14] Capitelli, F., Colao, F., Provenzano, M.R., Fantoni, R., Brunetti, G., Senesi N.: *Goederma*, **106** 46 – 62. (2002)
- [15] Barbini, R., Colao, F., Lazic, V., Fantoni, R., Palucci, A., Angelone M.: *Spectrochimica Acta B* **57** 1203-1218 (2002).
- [16] L.Caneve, F.Colao, R.Fantoni, V.Spizzichino: *Spectrochimica Acta B* **60** 1115-1120 (2005).
- [17] L.Caneve, F.Colao, R.Fantoni: *ENEA RT/2008/52/FIM*
- [18] L.Caneve, F. Colao, R. Fantoni, L. Fiorani, L. Fornarini: *Proceedings of the 2nd OSAV International Conference, Saint Petersburg, 2008*, 57-63.
- [19] F. Colao, R. Fantoni, L. Fiorani, A. Palucci *ENEA RT/2006/FIM*

Integrated approach for high resolution surface characterization: coupling focused ion beam with micro and nano mechanical tests.

Edoardo Bemporad¹, Marco Sebastiani¹, V. Palmieri^{2,3}, S. Deambrosis^{2,3}

¹ University of Rome "ROMA TRE", Mechanical and Industrial Engineering Dept, Via della Vasca Navale 79 – 00146 Rome Italy

² Laboratori Nazionali di Legnaro, ISTITUTO NAZIONALE DI FISICA NUCLEARE, Viale dell'Università 2 -35020 Legnaro, PADOVA - Italy

³ Science Faculty, University of Padua, via Jappelli, 1 - 35121 Padova – Italy

E-mail: e.bemporad@stm.uniroma3.it

Abstract. In the present paper, we will give a brief overview about the synergic use of two high resolution techniques with focus on applications on thin coatings: Focused Ion Beam (coupled with electron beam) imaging, milling and deposition technique (briefly called FIB) and Nanoindentation. After a basic description of both techniques (architecture, probe-sample interaction basics and operation modes), we will demonstrate effectiveness of this approach for microstructural investigation on very small samples without any sample preparation or pre-processing by presenting two case studies:

(i) *Analysis of residual stresses of engineered surfaces by coupling focused ion beam controlled material removal and nanoindentation testing, and*
(ii) *Nano-mechanical characterization of sputtered niobium thin films for application in accelerating cavities.*

1. Introduction

At present, mechanical characterisation of engineered surfaces is gaining more and more interest for the growing industrial application of surface modification and coating techniques, which are usually applied to improve either surface mechanical or functional performances (i.e hardness, load bearing capacity, wear resistance, surface free energy and chemical reactivity, electrical resistivity, thermal conductivity) [1].

Furthermore, it has to be considered that the development of nanostructured materials and the growing use and application of nano-systems and nano-structures make the use of advanced procedures for nano-scale mechanical characterisation strictly necessary [2]; in other cases, mechanical behaviour can be strongly influenced by microstructural and size effects (grain size, defects, interfaces, porosity,...), so multi-scale characterisation procedures [3] are strongly needed for a determination of the correct correlation function among process parameters, surface properties and in-service performances.

It is therefore clear that a comprehensive, statistically reliable, economically sustainable procedure for the characterisation of engineered surfaces has not yet been developed in literature, especially when a strong microstructure and size dependent behaviour is observed.

In the present work, a new developed characterisation procedure for the mechanical characterisation of engineered surfaces is presented, based on the combined use of high resolution microscopy (FIB-SEM, TEM, AFM) and surface mechanical characterisation techniques (nanoindentation, scratch testing).

Mechanical characterization activities are essentially based on nanoindentation testing, which at present is the prime technique used in nanomechanics to investigate the mechanical properties of the materials on the sub-microscale. It has long been used to study the elastic, plastic and fracture properties on the surfaces of bulk samples, as well as for thin-films [4-6]. More recently, it became possible to perform controlled compression, shear, and bending tests on nanostructures smaller than a micron, such as nanospheres, nanowires and nanopillars [7-8].

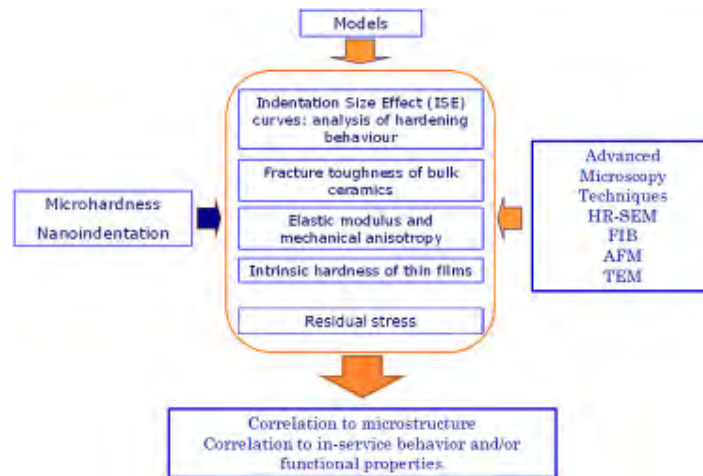


Fig. 1 – Concept scheme representing how the proposed integrated approach can be applied for improving the understanding of mechanical behavior of nano-structured systems and then give the correlation to microstructure and functional properties.

On the other hand, focused ion beam techniques are used for advanced sample preparation and microstructural characterization. FIB systems [9] utilize a finely focused beam of gallium ions (Ga+) operating at low beam currents for imaging and at high beam currents for site-specific milling. By controlling the location, beam size and current density of the ion beam, material can be selectively removed from sub-micron areas. Most apparatus nowadays available in the market also contains in situ scanning electron microscopy (SEM) capabilities for real time imaging of the ion milling site and even 3D tomography. The capability of high-resolution imaging using both secondary electron and secondary ion signals has made the FIB microscope a unique imaging tool. Stress-free cross sectioning using the primary gallium ion beam provides valuable microstructure information beneath the specimen surface. FIB techniques can be also used for TEM specimen preparation: a finished electron transparent portion of the sample (usually 5 μm x 20 μm) is obtained by FIB micro-milling and then placed by a micromanipulator on a sample holder to be inserted into the TEM microscope: this procedure at present represents the one site-specific and artefact-less outstanding TEM sample preparation techniques.

One of the present challenges in the field of material science and surface engineering is represented by the development of new integrate methodologies which are based on the combined use of nanoindentation techniques and high resolution microscopy, with the main aim of investigating the structural and microstructural evolution during nano-mechanical testing of nano-scale systems [7-8].

Following this approach (see figure 1), results arise from the application of integrated methodologies (see figure 1), which start from indentation experiments and finally come to the evaluation of mechanical properties of investigated materials, by the support of modelling (both analytical and numerical) and high resolution morphological and microstructural characterisation activities, such as Scanning and transmission electron microscopy (SEM, TEM), Focused Ion Beam microscopy (FIB) and Atomic Force Microscopy (AFM) techniques.

In this paper, two case studies are reported, explaining how the combined use of FIB and nano-mechanical testing can be crucial for the correct evaluation of mechanical and functional performances of nano-structured systems:

- Analysis of residual stresses of engineered surfaces by coupling focused ion beam controlled material removal and nanoindentation testing;
- Nano-mechanical characterisation of sputtered niobium thin films for application in accelerating cavities;

2. Case study 1: Analysis of residual stresses of engineered surfaces by coupling focused ion beam controlled material removal and nanoindentation testing

Residual stresses play a crucial role in determining the deformation behaviour and performance of engineering components and materials, from bulk alloys and composites used in construction and manufacturing industries down to micro-mechanical studies of stresses in individual grains within polycrystalline aggregates, thin films and coatings, and MEMS/NEMS systems [10].

At present, one of the main challenges in the field of residual stress measurement in nanostructured systems is represented by the development of site-specific micro-scale evaluation techniques, which should be also semi-destructive method that allow routine determination of residual stress in engineered components.

In a previous work some of the authors [10], a new optimised method for the determination of residual stress at the microscopic scale was presented, based on focused ion beam (FIB) controlled material removal and relaxation strain mapping by Digital Image Correlation (DIC) techniques [11].

The newly proposed approach (figure 1) involves incremental focused ion beam (FIB) milling of annular trenches (ring-drill) at material surface, combined with high resolution SEM imaging of the pattern of markers previously deposited at the sample surface.

An optimised procedure for FIB milling is presented, allowing a complete automation of the procedure, also reducing the artefacts due to the ion milling of the stubs. Digital image correlation (DIC) analysis of the relative displacements between markers with respect to the undisturbed state provides a measure of strain relaxation.

The comparison of these strain relief measurements with finite element modelling (FEM) allows the evaluation of the residual stress state, in a manner similar to that used in macroscopic incremental hole drilling. Furthermore, the assessment of complete biaxial residual stress state is possible in this configuration, by measuring the relaxation strains along three different directions, in contrast with earlier studies that involve the machining of linear slots.

Results were presented [10] for residual stress evaluation of a 3.8 μm TiN coating on WC-Co substrate obtained by cathodic arc evaporation physical vapour deposition (CAE-PVD) techniques, showing an average compressive stress state of -5.63 GPa. This result was in good agreement with the estimate obtained by XRD ($\sin^2\psi$ method) analysis of -5,84 GPa on the same sample, adopting the same elastic constants [10].

Nevertheless, further studies are still needed in the sense of exploring potentialities of the new proposed technique in terms of strain resolution and sensitivity, by testing soft metallic coatings, which are also expected to be in a low tensile residual filed.

Here we present some original results on a 1,5 μm Au coating on silicon substrate deposited by DC sputtering PVD techniques (voltage 410 V, current 0.2 A). This coated system is particularly relevant for the fabrication of MEMS structure, where residual stress plays a significant role in determining the final shape of the structure. In this case, residual stress was measured both by the new FIB-DIC technique [10] and by curvature measurement and application of the Stoney equation [12].

On the basis of several repeated tests carried out in this study the value of residual stress in the coating was then found to be equal to $+270.64 \pm 88.62$ MPa for the DC sputtered Au coating. These results are in good agreement with the estimate obtained by curvature measurement $+280$ MPa for the Au coating.

These results also confirm that even low tensile residual stress states can be evaluated by the ring-drill technique, with a spatial resolution of the order of 1 μm , which is comparable with the resolution obtained by the use of synchrotron sources.

In addition, the combination of FIB milling and SEM imaging within a single experiment ensures the ease and efficiency of use of the present method, since it does not require the laborious and time-consuming transfer of samples between instruments. In fact, the current procedure can be successfully automated for systematic automatic residual stress mapping across significant areas.

This technique seems therefore to be absolutely relevant also in the case of stress analysis on MEMS structures, where an in-situ evaluation of residual stress should be strongly needed, and was not possible to be performed by the conventional XRD or curvature-based methods.

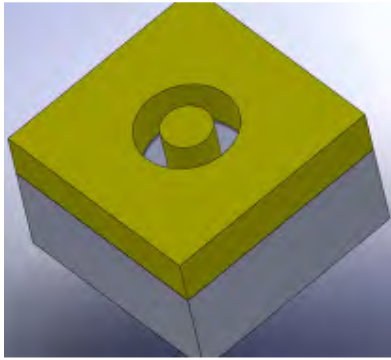


Fig. 2 – Illustration showing principle of ring-core milling, and the idealized geometry of the remaining “stub”

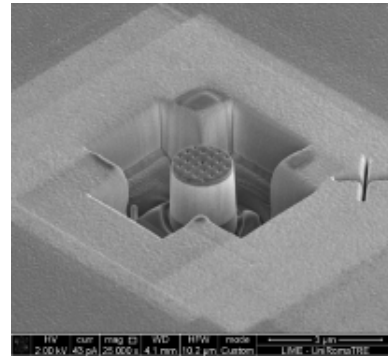


Fig. 3 – Example of one of the realized pillars on a PVD Au coating on Silicon substrate.

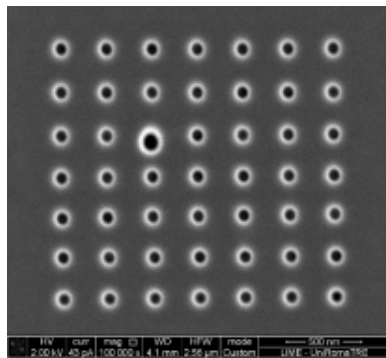


Fig. 4 – Example of the patterning realized over the surface before ring-drilling

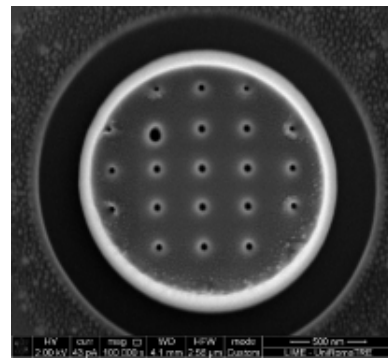


Fig. 5 –Micrograph of the patterning after ring drilling. The measured displacements of the milled dots gives the relaxation strain related to the stress relief process.

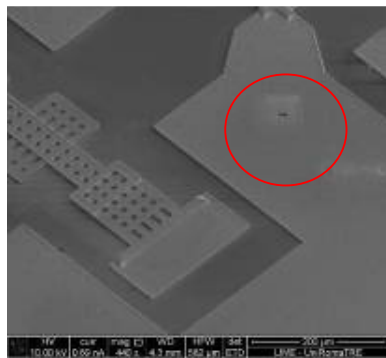


Fig. 6 – In-situ residual stress measurement in proximity of a MEMS structure (red circle) by the ring-drill method

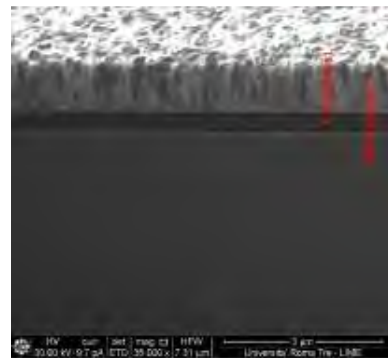


Fig. 7 – FIB cross section (imaging by using the ion probe) of the PVD Au coating under investigation

5. Case study 2: Nano-mechanical characterization of sputtered niobium thin films for application in accelerating cavities

Niobium films obtained by Magnetron Sputtering PVD have been used for many years in superconducting and RF cavity applications [13-14].

Several experimental studies have underlined the strong influence of coating thickness, microstructure and density, coating/substrate interface and surface oxide layer on its Residual Resistance and superconducting properties [13-14].

For these reason, a comprehensive surface chemical, morphological and mechanical surface characterisation is required, in order to find out the appropriate correlation functions among process parameters\microstructure\surface properties\RF performances, and an exhaustive and statistically well-founded procedure has not yet been developed.

The objective of this work [15] was to determine the influence of applied bias Voltage on morphological and Mechanical surface properties of MS-PVD Nb thin films on OFHC Cu substrate, and its correlation with their superconducting properties.

The idea at the basis is that the use of the developed advanced methodologies for surface mechanical characterisation could be successfully used also for acquiring information on microstructural and even functional behaviour of coatings

Experimental activities were focused on the analysis of the influence of the applied BIAS voltage during PVD deposition on mechanical and microstructural properties and functional performances of coatings, with the main aim of proposing indentation techniques as a complementary quality control tool for the indirect evaluation of coating performances.

Two sets of coatings were then realized, characterised by different values of applied bias voltage (100 V and 0 V, respectively) ; process parameters are reported in [15].

Cross-section coating investigations were performed by using Focused Ion Beam (FIB) techniques: SEM microstructural investigations have been performed after FIB sectioning, while interfaces structure and microstructure and thickness of the surface oxide layer have been investigated by TEM after FIB sample preparation. Surface mechanical properties (intrinsic hardness, elastic modulus, surface oxide layer properties) were analysed by means of nano-indentation testing: 25 tests (Agilent G200 Nanoindenter equipped with Continuous Stiffness Measurement). Test parameters and calculation procedures are reported in [15].

All microstructural and surface mechanical obtained information were then correlated to superconducting properties, evaluated by Critical Temperature T_C and Residual Resistance (RRR) measurements of coatings on Quartz substrate.

In fact, results of nano-mechanical testing on the BIASED and UNBIASED PVD Nb coatings showed significant and often unexpected differences, between coating on different substrate and obtained with or without an applied Bias voltage during deposition.

As shown in table 1, which summarises results of mechanical characterisation activities, significant differences in hardness and modulus were measured for the same **Biased** coating on Copper or Quartz substrate.

In particular, a much lower hardness and higher scatter of experimental data were observed in case of Biased coating on Quartz, compared to the same on Copper substrate.

As a confirmation of this, contrasting microstructural characteristics were observed on biased and unbiased coatings on different substrates: biased Nb films on copper showed higher roughness and finer

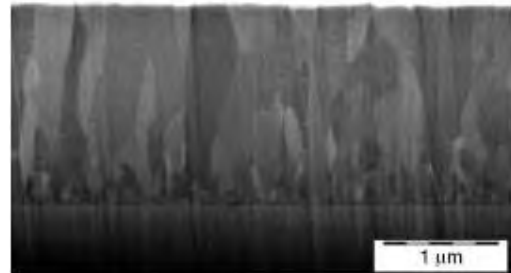
Table 1. Summary of mechanical characterization activities and comparison with T_C measurements

Sample code #	Description	Nanoindentation		Critical temperature measurement
		H (GPa)	E (GPa)	T_C (K)
796	Nb on Cu BIAS type	3,10 ± 0,58	101,5 ± 23,61	Not measured
797	Nb on Quartz BIAS type	1,63 ± 0,30	76,22 ± 48,99	9.45 ± 0.025
803	Nb on Cu CERN type (NO BIAS)	2,59 ± 0,35	108,68 ± 11,65	Not measured
804	Nb on Quartz CERN type (NO BIAS)	2,19 ± 0,31	95,95 ± 26,31	9.38 ± 0.05

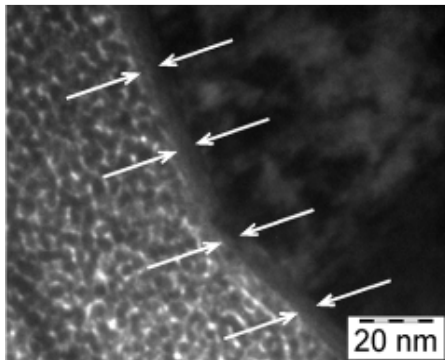
grain size, compared to the unbiased samples on the same substrate, while opposite results were obtained for coatings on quartz substrate. Such results suggest that attention should be paid to the use of RRR and T_C results (obtained for coatings on quartz substrate) for making conclusions on cavity performances. Focused ion beam (FIB) analysis confirms that biased films on copper have finer grain size than unbiased films, while the use of FIB techniques in sample preparation, coupled with TEM observation, gave a much deeper understanding of the coating microstructures at the nanoscale: in particular, the presence of the surface oxide layer was observed, and an estimation of its thickness was performed. It has to be



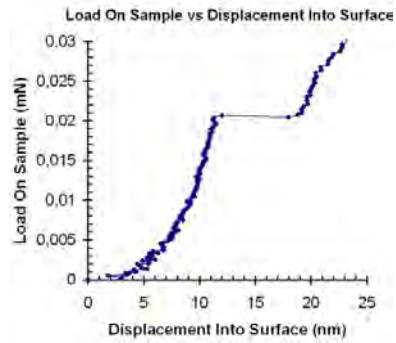
TEM lamella obtained by FIB milling and thinning. In-situ SEM-FEG observation (SE, 5 KV), 12000x



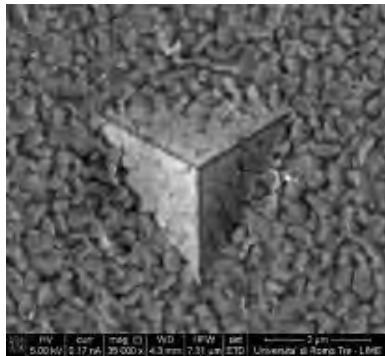
Microstructure of a Nb coating on Copper substrate. SEM-FEG (SE, 5 kV, 60000x) observation after FIB cross-section.



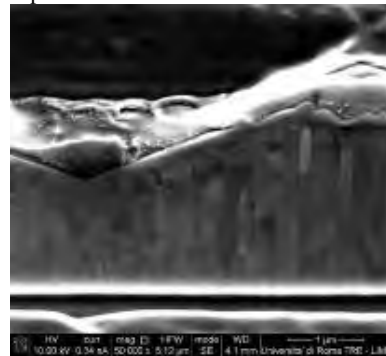
Detail of the surface oxide layer, Nb on Cu BIAS type (TEM BF 660000X after FIB lamella thinning)



Nanoindentation testing on Nb thin films: Detail of the L-d curve highlighting brittle failure of the surface oxide layer at depth 9-11 nm



SEM-FEG imaging of a Berkovich nanoindentation mark



FIB/SEM cross-section analysis of a Berkovich nanoindentation mark. Analysis of piling-up and deformation mechanisms of columnar grains during indentation

Fig. 8.

underlined that at present no other technique can give equivalent morphological and microstructural thin film characterization, including speed of analysis, site-specific morphology, and composition and crystal orientation.

In addition, nanoindentation testing also allowed an indirect (and cheaper compared to high resolution microscopy techniques) evaluation of the presence and thickness of this surface oxide layer (Figure 8), which has been already correlated to coating's superconducting performances.

All these considerations confirm how important and effective can be a comprehensive multiscale-multitechnique mechanical and microstructural characterisation procedure, also in case of functional coatings.

5. Conclusions

In this paper, the application of high resolution - multitechnique – multiscale procedures to the nano-mechanical characterisation of engineered surfaces is presented.

It is observed that only by the combination and synergic use of micro- and nano-hardness testing and SEM-TEM-FIB- AFM microscopy techniques a comprehensive characterisation of nanostructured coatings and complex structures can be achieved.

Two case studies are presented, both showing how nano-mechanical testing in combination with high resolution microscopy can be usefully applied to the characterization of coatings and nano-structured systems for functional (or non-mechanical) application.

In particular, (i) the use of FIB-DIC techniques for high resolution residual stress measurement on coatings for MEMS structures and (ii) the use of nano-mechanical testing for the investigation of microstructural effects of the functional performance MS-PVD Nb thin coatings are described and discussed.

These two applications gives an idea of how relevant can be the proposed procedure in many field of scientific and industrial interest, coming from coatings for applications in particle accelerators to thin films for wear resistant applications, up to in-situ microstructural and nano-mechanical characterization in MEMS structures.

Acknowledgments

Authors acknowledge Daniele De Felicis assistance during FIB characterization activities, carried out at the “Interdepartmental Laboratory of Electron Microscopy” (LIME), University ROMA TRE, Rome, Italy, <http://www.lime.uniroma3.it>.

7. References

- [1] P. H. Mayrhofer, C. Mitterer, L. Hultman, H. Clemens, *Progress in Materials Science* 51 (2006) 1032–1114
- [2] S. Zhang, D. Sun, Y. Fu, H. Du, *Surface and Coatings Technology* 167 (2003) 113–119
- [3] C. Bartuli, E. Bemporad, J.M. Tulliani, J. Tirillò, G. Pulci, M. Sebastiani, *Journal of the European Ceramic Society* 29 (2009) 2979–2989
- [4] W.C. Oliver and G.M. Pharr, *J. Mater. Res.*, Vol. 7, No. 6, June 1992
- [5] W.C. Oliver and G.M. Pharr, *J. Mater. Res.*, Vol. 19, No. 1, Jan 2004
- [6] S. J. Bull 2005 *J. Phys. D: Appl. Phys.* 38 R393-R413
- [7] Uchic MD, Dimiduk DM, Florando JN, Nix WD. *Science*, 2004; 305:986.
- [8] Beia H., Shim S., Miller M. K., Pharr G. M., George E.P., *Appl. Phys. Lett.*, 91, (2007), 111915.
- [9] Giannuzzi L A and Stenier F A 2005 *Introduction to Focused Ion Beams—Instrumentation, Theory, Techniques and Practice* (Berlin: Springer)
- [10] A. M. Korsunsky, m. Sebastiani, E. Bemporad, *Materials Letters* 63 (2009) 1961–1963
- [11] H Jin, W-Y Lu, J Korellis, *J. Strain Analysis* Vol. 43 (2008) 719-728
- [12] G.G. Stoney, *Proc. R. Soc. Lond. A* 82 (1909), p. 172.
- [13] C. Benvenuti, S. Calatroni, I.E. Campisi, P. Darriulat, M.A. Peck, R. Russo, A.-M. Valente, *Physica C* 316 (1999) 153–188.
- [14] H. Ji, G. S. Was, J. W. Jones, N. R. Moody, *J. Appl. Phys.* 81 (10), 15 May 1997.
- [15] E Bemporad, F Carassiti, M Sebastiani, G Lanza, V Palmieri, H Padamsee, *Supercond. Sci. Technol.* 21 (2008) 125026 (11pp)

Multifunctional Ion Beam Installation “HELIS” as a new instrument for advanced LENR research

A.S. Roussetski¹, M.N. Negodaev¹, A.G. Lipson²

¹ P.N. Lebedev Physics Institute of Russian Academy of Sciences, Moscow 119991, Russia

² A.N. Frumkin Institute of Physical Chemistry and Electrochemistry, Russian Academy of Sciences, Moscow 119991, Russia

E-mail: rusets@x4u.lebedev.ru

Abstract. The ion beam installation HELIS (P.N. Lebedev Physics Institute, Moscow, Russia) represents an ion accelerator of light elements with atomic number in the range $Z=1-54$ with ion energies ranging from 0.5 to 50 keV operating at deuteron current densities up to 2 A/cm^2 and intended to perform a wide spectrum of physical experiments related to LENR.

1. Introduction

The ion beam installation HELIS (P.N. Lebedev Physics Institute, Moscow, Russia) represents an ion accelerator of light elements with atomic number in the range $Z=1-54$ with ion energies ranging from 0.5 to 50 keV operating at deuteron current densities up to 2 A/cm^2 and intended to perform a wide spectrum of physical experiments: study of interaction of ion beam with various materials; preparing of thin-films of various materials (including films of high-temperature superconductors) by ion beam sputtering method; study of elementary and collective processes in ion-beam plasma, formed at interaction of intensive ion beam with gas medium; study of collisions of light nuclei with low energies.

- We propose to extend HELIS ability to wide spectrum of future physical experiments related to LENR: study of collisions of light nuclei with solid target at very low energies; study of DD-reaction enhancement down to $E_d = 1 \text{ keV}$ and multi-body (3D) reactions in metal targets; study of elementary and collective processes in ion-beam plasma, formed at interaction of intensive ion beam with gas and/or solid targets; preparation of thin-film coatings of various materials (including oxide films) by ion beam sputtering method; possibility of direct calorimetric measurements of excess heat *in-situ* during ion bombardment of metal targets; He-4 measurements during D-bombardment with quadrupole mass-spectrometer; direct X-ray measurements during metal target ion bombardment; four probe resistivity measurements of D-loading in Pd targets

2. Experimental

HELIS (Fig.1) is an accelerator of ions of various gases ($Z=1-54$, $E \leq 50 \text{ keV}$, $I \leq 50 \text{ mA}$) and consist of ion source (actually the accelerator) with an ion source gas system, LV and HV system; ion beam focusing system; vacuum system; ion beam diagnostic equipment for measurement of a current and energy of an ion beam.

The basic ion source HELIS is duoplasmatron (see Fig.2). It can produce the ion beam with characteristics presented in Tabl.1.

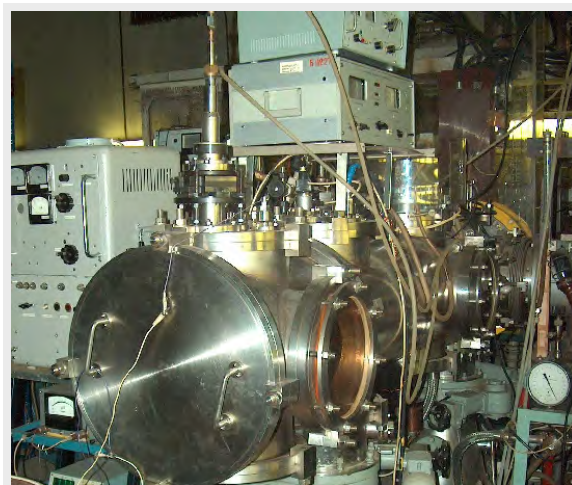


Fig.1 - General view of HELIS installation.

Table 1.

Total hydrogen beam current (at 50 keV)	≤ 50 mA
Energy range	1 -:- 50 keV
Energy spread	10 -:- 100 eV
Reduced emittance	$2 \cdot 10^{-5}$ -:- $5 \cdot 10^{-5}$ cm-rad

HELIS have two additional sources of ions: 1) high-frequency source with a current up to 1 mA and energy of ions ≤ 30 keV (emittance at 30 keV $\sim 1.5 \cdot 10^{-3}$ cm-rad); 2) high-frequency source with a current up to 8 mA and energy of ions 0,25-:-0,5 keV. For beam focusing the electromagnetic lens which provides focal length $f=11$ cm at $I=780$ A is used.

Fig.2. presents proposal of HELIS total experiment set up. Ion accelerator and detector holder need to fill up by different detecting systems. They include flow calorimeter, Q-mass-spectrometer, fast and slow neutron detectors (NE-213 and He-3), charged particle detectors (CR-39 track and dE/E SSB detectors), gamma and X-ray detectors (Ge and CdTe). Sample holder need to be add by four probe resistivity measurements of D-loading in targets and thermistor for target temperature control.

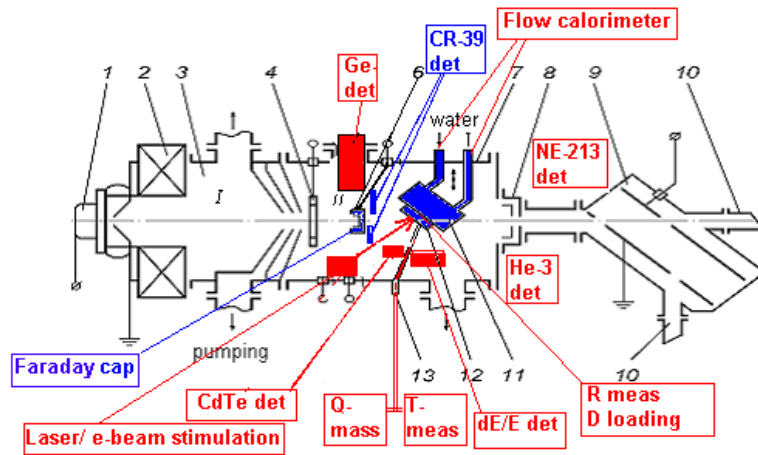


Fig. 2 - HELIS total experiment set up: 1 – ion source (duoplasmatron); 2 – electromagnetic lens; 3 – three-stage chamber of differential pumping; 4 – meter of a current of a transient-time type; 5 – auxiliary ion source; 6 - Faraday cap; 7 – chamber of targets; 8 – the device for calorimetric definition of a current of an ion beam; 9 – electrostatic analyzer; 10 – receivers of parsed fragments; 11 – water (or liquid gas)-cooled holder of the target; 12 - target; 13 – feeder of gas in an vacuum chamber. Detector blocks: ■ Blocks already existing. ■ Blocks needed to be add.

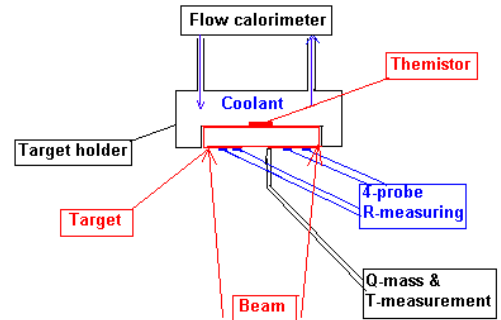


Fig. 3 - Target holders with water cooling.

3. Conclusion

The HELIS facility can be used for study of dd- and dT-reactions yields from various targets at low energy of deuterons and can be equipped by various nuclear detectors, including dE/E Surface Silicon Barrier detector pair, CR-39 plastic track, neutron and X-ray detectors. In general, the HELIS facility with additional installations mentioned above, will allow us to carry out full LENR experiment upon a deuterium implantation into metal targets, involving simultaneous measurements of excess heat, D-loading and He-4 emission, along with accompanying nuclear radiations.